A computational model to understand the relationship between cardiac microstructure and diffusion MRI

Joanne Bates

Lincoln College
University of Oxford

A thesis submitted for the degree of Doctor of Philosophy

Trinity 2016

Abstract

The normal microstructure of the heart is fundamental to its healthy mechanical and electrical function. In diseases such as hypertrophic cardiomyopathy or myocardial infarction there is remodelling of the microstructure which can lead to heart dysfunction and even death. Diffusion MRI measures the magnitude and direction of the diffusion of water molecules within tissue, and can therefore be used to infer structural information about biological tissue. There remains some uncertainty about the relationship between cardiac microstructure and the diffusion MRI signal that it produces. Monte Carlo models can be used to increase the understanding of this relationship as well as to design optimal MRI sequences and propose image biomarkers related to specific microstructural changes. This Thesis presents a computational framework for the simulation of diffusion MRI in cardiac tissue, including an anatomically realistic model of cellular geometry, a Monte Carlo method to simulate the diffusion of water molecules and the calculation of diffusion MRI signals. The model is shown to simulate diffusion MRI results which correspond well with experimental data from five ex vivo rat hearts over a range of gradient strengths and diffusion times. Neither introducing membrane permeability nor increasing the diffusivity in the extracellular space compared with that within the cells showed a marked effect. The introduction of type IB disarray into the model, as commonly found in hypertrophic cardiomyopathy, caused the diffusion to become less anisotropic while the amount of diffusion remained constant. This model will allow the investigation of the relationship between different types and degrees of remodelling and the diffusion MRI signal, which will further the use of diffusion MRI as a clinical tool in the detection and quantification of cardiac remodelling in disease.

A computational model to understand the relationship between cardiac microstructure and diffusion MRI

Joanne Bates

Lincoln College

University of Oxford

A thesis submitted for the degree of

Doctor of Philosophy

Trinity 2016

Abstract

The normal microstructure of the heart is fundamental to its healthy mechanical and electrical function. In diseases such as hypertrophic cardiomyopathy or myocardial infarction there is remodelling of the microstructure which can lead to heart dysfunction and even death. Diffusion MRI measures the magnitude and direction of the diffusion of water molecules within tissue, and can therefore be used to infer structural information about biological tissue. There remains some uncertainty about the relationship between cardiac microstructure and the diffusion MRI signal that it produces. Monte Carlo models can be used to increase the understanding of this relationship as well as to design optimal MRI sequences and propose image biomarkers related to specific microstructural changes. This Thesis presents a computational framework for the simulation of diffusion MRI in cardiac tissue, including an anatomically realistic model of cellular geometry, a Monte Carlo method to simulate the diffusion of water molecules and the calculation of diffusion MRI signals. The model is shown to simulate diffusion MRI results which correspond well with experimental data from five ex vivo rat hearts over a range of gradient strengths and diffusion times. Neither introducing membrane permeability nor increasing the diffusivity in the extracellular space compared with that within the cells showed a marked effect. The introduction of type IB disarray into the model, as commonly found in hypertrophic cardiomyopathy, caused the diffusion to become less anisotropic while the amount of diffusion remained constant. This model will allow the investigation of the relationship between different types and degrees of remodelling and the diffusion MRI signal, which will further the use of diffusion MRI as a clinical tool in the detection and quantification of cardiac remodelling in disease.

Acknowledgements

Firstly, I would like to express my thanks to my supervisor, Professor Vicente Grau, for his support and guidance throughout this project. Thanks are also due to Professor Jürgen Schneider and Professor Peter Kohl for their advice, and to Dr Irvin Teh and Dr Darryl McClymont for their data, suggestions and patience in the face of stupid questions. Thanks to all the members of 'Cake Club' for their solidarity in the face of deadlines and misbehaving Matlab, and for the weekly respite from this is the shape of delicious cake. Many thanks to my family and friends for not despairing *too* much at my slightly-early-mid-life-crisis decision to become a student again. I am very grateful to my parents, especially for their hospitality during the writing of this thesis. Special thanks to my mum for her excellent proof-reading.

Contents

List of Figures

List of Abbreviations

1D, 2D, 3D . . One-, two- or three-dimensional

ADC . . . . . Apparent Diffusion Coefficient, a measure of the amount of diffusion

ANG . . . . . Rate of change of helix angle

AR . . . . . Aspect ratio, of cell cross-section = thickness/width

b0 . . . . . Non-diffusion weighted image

BPR . . . . . Blood pressure response

CSA . . . . . Cross-sectional area, usually of cell

CT . . . . . Computer tomography (x-ray imaging)

$\mathbf{D}_{norm}$ . . . . . Diffusivity, normalised to free diffusion of water

DCM . . . . . Dilated cardiomyopathy

DIF . . . . . Diffusivity

dMRI . . . . . Diffusion Magnetic Resonance Imaging

DSI . . . . . Diffusion Spectrum Imaging

DT . . . . . Diffusion Tensor

DTI . . . . . Diffusion Tensor Imaging

DV1.5 . . . . . Vessels study with diffusivity of $1.5\,\mathrm{mm^2\,s^{-1}}$ in the vessels

DV2 . . . . . Vessels study with diffusivity of $2\,\mathrm{mm^2\,s^{-1}}$ in the vessels

DW . . . . . Diffusion Weighted

EC . . . . . Extracellular

ECG . . . . . Electrocardiogram

ev . . . . . Eigenvector of diffusion tensor

ev1, ev2, ev3 . Primary, secondary or tertiary eigenvector of diffusion tensor

FA . . . . . Fractional Anisotropy, a measure of the isotropy of diffusion

GPU . . . . . Graphics Processing Unit

HCM . . . . . Hypertrophic Cardiomyopathy

IC . . . . . Intracellular

L . . . . . Length, of cell

LV . . . . . Left ventricle

M . . . . . Number of molecules

MC . . . . . Monte Carlo

MD . . . . . Mean diffusivity, same as the mean ADC

MI . . . . . Myocardial infarction

MRI . . . . . Magnetic Resonance Imaging

NMR . . . . . Nuclear Magnetic Resonance

$\mathbf{N}_p$ . . . . . Number of pores

PGSE . . . . . Pulse gradient spin echo, MRI sequence

RF . . . . . Radio frequency

ROI . . . . . Region of Interest

RV . . . . . Right ventricle

$\mathbf{S}_0$ . . . . . MRI signal for non diffusion-weighted reference image

SCD . . . . . Sudden cardiac death

sd . . . . . Standard deviation

SEM . . . . . Scanning electron microscopy

SNR . . . . . Signal-to-Noise ratio

SV0 . . . . . Vessels study with no signal from the vessels

T . . . . . Number of timesteps

T1 . . . . . Time for longitudinal magnetisation to reach 63% of its maximum

T2 . . . . . Time for transverse magnetisation to reach 37% of its maximum

TBI . . . . . Traumatic brain injury

VF . . . . . Volume fraction. Usually of cells, i.e. the proportion of total volume consisting of myocytes

$\mathbf{VF}_{ves}$ . . . . . Volume fraction of vessels

α . . . . . Helix angle

Δ . . . . . Diffusion interval: the time between pulse onsets in the PGSE MRI sequence

δ	Diffusion pulse duration, in the PGSE MRI sequence
λ	Eigenvalue of the diffusion tensor
λ_1, λ_2, λ_3 . . .	Primary, secondary or tertiary eigenvalue of the diffusion tensor
μ / μ^*	The measure of importance of an input factor in the Morris / modified Morris method sensitivity analysis
σ	The measure of interactions and non-linearity in the Morris method sensitivity analysis

1 Introduction

1.1 The problem

Most people with hypertrophic cardiomyopathy (HCM) will live normal, healthy lives, but some will die from sudden cardiac death. Implantable defibrillators can be used to detect and stop the lethal arrhythmias, but for many patients the risk of surgery will outweigh the potential benefits. At the moment, some of the risk factors for sudden death have been identified, but these cannot completely reliably decide who should have a defibrillator implanted.

An additional risk factor or biomarker could be the extent or degree of myocardial disarray. Disarray has been found in HCM and has been linked with mechanical and electrical problems, but currently it can only be measured in post-mortem histology.

Diffusion MRI (dMRI) has been proposed as a way of measuring this disarray as it is sensitive to the amount and direction of water diffusion in the tissue and can therefore infer information about the underlying structure. To be able to use dMRI to measure disarray, we need to understand the relationship between the disarray and the signal changes that this produces. A computer model is a useful tool for

this research as it allows us to make controlled changes in the microstructure and determine how this affects the dMRI signal. There are several computer models of diffusion MRI available for the brain, but the structure of the heart is very different, as are the changes in disease, so we need a new model for the heart.

The aim of this work is therefore to create a model of cardiac tissue and the diffusion MRI signal it produces.

1.2 Contributions

The contributions of this work are:

- The development of a flexible model of diffusion MRI in cardiac tissue, and its validation by comparison with experimental acquisitions at a range of gradients and diffusion times. This model will streamline MRI sequence optimisation and exploration of parameter space beyond experimental limits.
- The investigation of the impact of parameter changes on the model outputs, determined by a sensitivity analysis. This shows that the diffusivity has the most marked effect on the diffusion MRI results, followed by the cross-section of the cells (both cross-sectional area and aspect ratio of the cross-section).
- The investigation of the effects of extracellular vs intracellular diffusivity, as well as membrane permeability, in the diffusion measurements as predicted by the model.
- The introduction of myocardial disarray into the model to quantify the effects of varying degrees and extents of type IB disarray on the output of diffusion MRI. This preliminary work demonstrates the use of the model to facilitate investigation of the effect of pathological changes in cardiac microstructure on the diffusion MRI signal.

- The introduction of blood vessels into the model to quantify the effect of the microvasculature on diffusion MRI results in the healthy heart.

Additionally, I made an attempt to validate the model with a specific geometry through the use of a phantom, which proved challenging due to practical difficulties related to phantom design and manufacture.

1.3 Thesis plan

In Chapter 2, I summarise the literature regarding heart microstructure, remodelling of the microstructure in disease, cardiac diffusion MRI, and modelling of diffusion MRI in biological tissue.

In Chapter 3, I introduce my Monte Carlo model of cardiac diffusion MRI. I explain the reasoning behind the modelling choices and the parameters chosen, with reference to the literature on myocardial tissue structure. I then carry out a sensitivity analysis of the model to investigate which of the input parameters have the largest effect on the diffusion MRI outputs, and which are less important.

In Chapter 4, I carry out two validations of the model compared with experimental data. Firstly, I compare the model results with experimental diffusion MRI data from five ex vivo rat hearts carried out at a variety of gradient strengths and diffusion times. This is to determine whether the model gives comparable results to the experimental data, and whether the results change in a similar way as the MRI sequence is changed. Secondly, I create a model of a cardiac fibre phantom and compare the model results with experimental data from the phantom. As for the heart data, this is done for a range of diffusion times and gradients strengths.

In Chapter 5, I investigate whether some of the differences seen between the model results and ex vivo heart data in Chapter 4 can be explained by changing two parameters: membrane permeability and extracellular diffusivity. These parameters

were chosen because membrane permeability has been shown in previous modelling work to have an effect on model results, while the sensitivity analysis in Chapter 3 showed diffusivity was the most important factor.

In Chapter 6, I introduce myocardial disarray into the model to investigate the effects of the degree and extent of type IB disarray on diffusion MRI results. This is the first step in understanding the effect of pathological changes on diffusion MRI and how diffusion MRI could be used to detect these changes in vivo.

In Chapter 7, I introduce small blood vessels into the model to determine whether these long thin capillaries affect the diffusion MRI results, which could be significant, especially in disease.

In Chapter 8, I summarise the findings and suggest directions for future work.

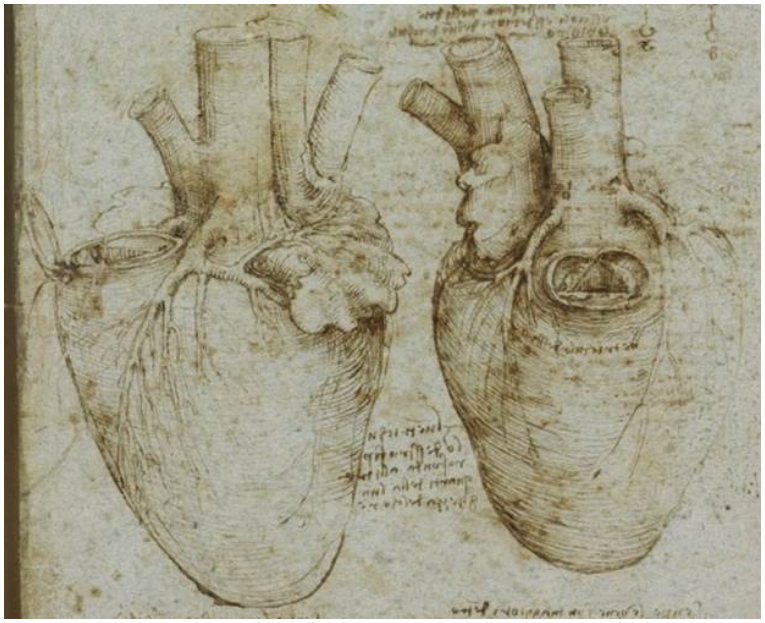

Figure 1.1: Illustration of the heart, by Leonardo da Vinci from c. 1511-13. Royal Collection Trust/© Her Majesty Queen Elizabeth II 2016

2

Background

In this chapter I summarise the structure and function of the healthy heart, and how this is affected by disease. I explain how diffusion MRI (dMRI) works and how it has been used in the heart. Finally, I summarise the literature on computational modelling of dMRI in biological tissue.

2.1 The healthy heart

The heart pumps blood around the body, providing oxygen and nutrients to all the body's cells and removing waste products. The heart has four chambers: the left and right atria and ventricles. Oxygenated blood flows from the lungs to the left atrium (LA), through the mitral valve to the left ventricle (LV), then through the aorta to the vascular system throughout the body. Deoxygenated blood flows from the body through the vena cava to the right atrium (RA), then through the tricuspid valve to the right ventricle (RV) then to the lungs. Ventricular contraction is called systole and forces the blood out of the ventricles and into the aorta and pulmonary artery. Ventricular relaxation is called diastole and corresponds to the

time when blood flows from the atria to the ventricles. A diagram of the heart chambers, and the blood flow through them, can be seen in Figure 2.1.

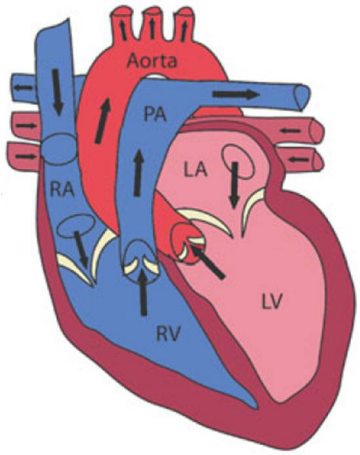

Figure 2.1: Anatomy of the heart. LV/RV = left/right ventricle; LA/RA = left/right atrium; PA = pulmonary artery. Arrows illustrate the direction of blood flow in normal heart function. Reproduced from Garside et al. [1], with permission.

The longitudinal axis of the LV is defined as pointing from the apex to the base of the LV. The radial-circumferential plane (or short-axis) is perpendicular to this, with the radial direction in this plane and pointing away from the longitudinal axis. The circumferential axis is perpendicular to both the longitudinal and radial axes. These can be seen in Figure 2.2.

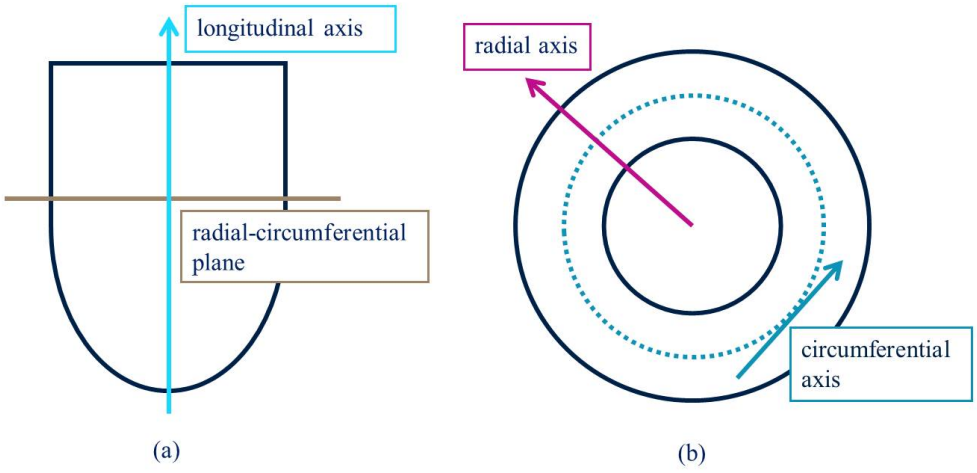

Figure 2.2: Axes of the heart. (a) Long axis view of the LV. (b) Short-axis / radial-circumferential plane view of the LV.

2.1.1 The structure of the myocardium

The LV wall of the heart is, by volume, predominantly composed of heart muscle cells (myocytes), along with connective tissue, fat, vasculature and nerves [2]. Capillaries are predominantly parallel to the myocyte orientation [3].

The orientation of the myocytes within the wall of the LV is complex; a visualisation of the 3D orientation of the myocytes in shown in Figure 2.3. Myocyte orientation can be described by its rotation from the radial-circumferential plane, where an anti-clockwise or right-handed rotation from the radial-circumferential plane is a positive helix angle and is shown in Figure 2.4.

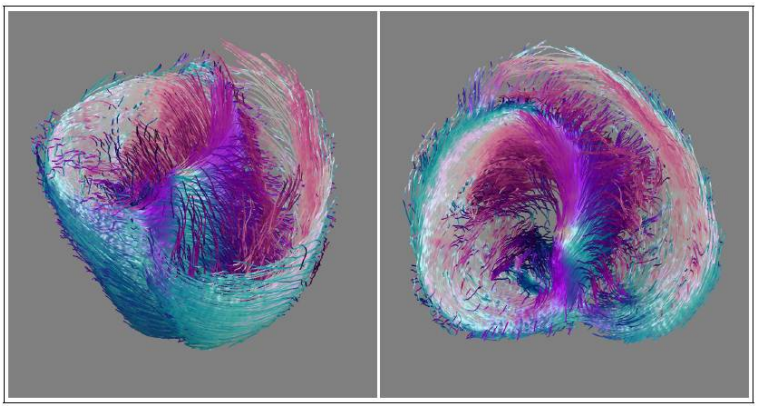

Figure 2.3: Myocyte orientations in the heart. Clockwise spiral orientations are in purple, horizontal parts of the fibres are in white; anticlockwise spiral orientations are in turquoise. Reproduced from Zhukov et al. [4] © IEEE

The orientation of the myocytes undergoes a gradual transition from a left-handed helical arrangement in sub-epicardial layers (those nearest the outer surface), to a circumferential alignment in mid-myocardium, to a right-handed helical direction in sub-endocardial tissue. The myocyte orientation is usually described by three angles [5]: the helix angle is the angle between the long axis of the myocyte and the radial-circumferential plane, the transverse angle is that between the projection of the long axis of the myocyte onto radial-circumferential plane and the circumferential axis, and the sheet angle is that between the sheets (described later) and the radial-circumferential plane. The relative directions of the helix and transverse angles are illustrated in Figure 2.4.

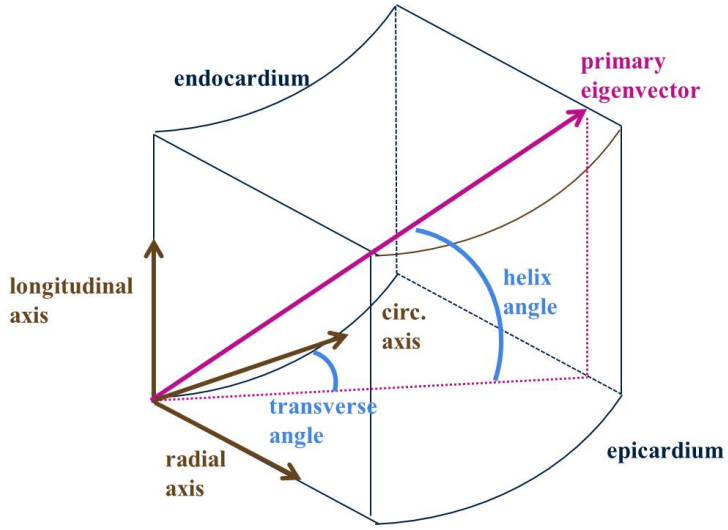

Figure 2.4: Helix and transverse angles in the heart. Axes are in brown, circ. = circumferential. Primary eigenvector marked in pink.

Streeter et al. [6] first analysed myocyte angles in dogs using histological slices cut from a section of the free wall of the heart (Figure 2.5). They found that helix angles ranged from $-60°$ at the epicardium to $60°$ at the endocardium, although they believed that the true range may be closer to $\pm 90°$ but found difficulties in measuring the angles at the epicardium and endocardium. In the healthy human heart, Lombaert et al. [7] used diffusion tensor (DT) MRI to investigate myocyte orientations and found that the helix angle varied linearly from $(-41 \pm 26)°$ at the epicardium to $(66 \pm 15)°$ at the endocardium. The transverse angle was $(7 \pm 31)°$ and varied less with location, although it was highest and more variable at the endocardium than at the midwall. When dividing the LV into the American Heart Association segments [8], there was more variation in the angles at the apex than elsewhere in the LV.

During systole the LV shortens, the cavity narrows and its volume decreases, the wall thickens radially, the LV twists, and myocytes shorten along the long axis and become spaced closer together [2, 9]. Using DT MRI to compare myocyte orientation in systole and diastole in rat hearts, Hales et al. [10] found that the wall thickness increased by $(31 \pm 9)\,\%$. Myocyte density and the distribution of myocyte angles also changed. During contraction, the number of left-handed myocytes

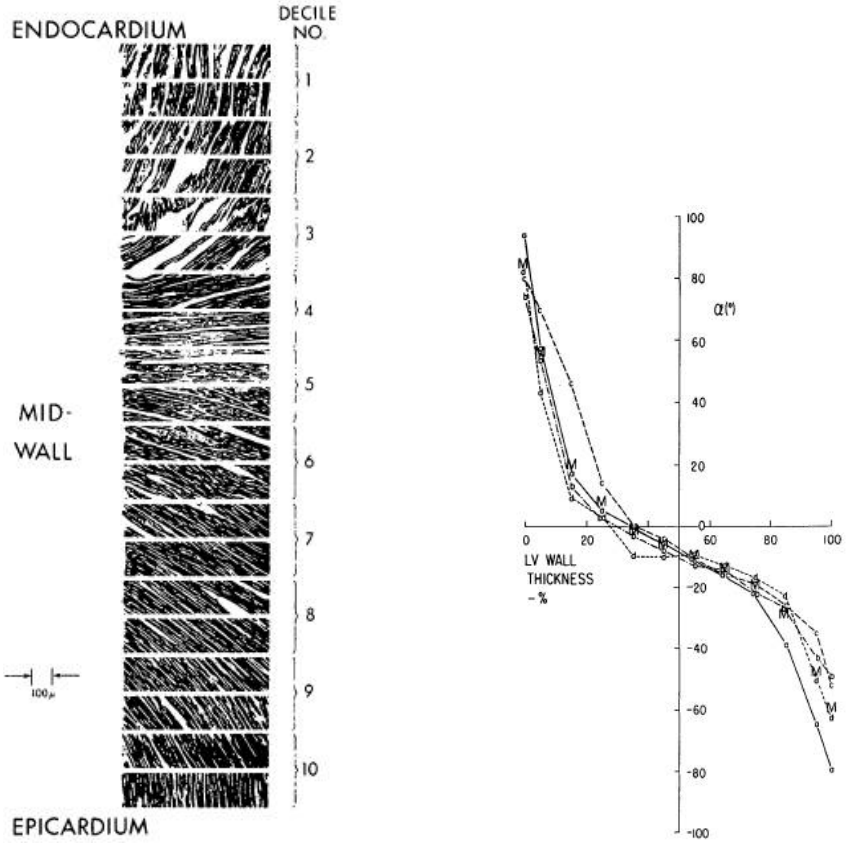

(a) **(b)**

Figure 2.5: Helix angles in the heart. (a) Typical sequence of photomicrographs showing fibre angles in successive sections parallel to the epicardial plane. Fibre angle is 90° at the endocardium, running through 0° at the midwall to −90° at the epicardium. The sequence of numbers refers to deciles of wall thickness. (b) Fibre angles for four sampling sites from a heart in diastole are plotted as a function of percent wall thickness. Zero percent of wall thickness implies the endocardial surface. M represents the mean of the data at these four sites. Reproduced from Streeter et al [6], with permission.

decreased, the number of right-handed myocytes increased, and the intersection angles between sheets increased. Streeter [6] also found that the helix angles increased slightly in systole compared with diastole, and that the largest changes were at the epicardium and endocardium.

Changes in myocyte thickness during contraction cannot fully explain the increase in LV wall thickness without some myocyte rearrangement [9]. It has therefore been suggested that myocytes are arranged in sheets with cleavage planes between the sheets, which allow the myocytes to slide over each other. LeGrice et al. [5] used histology to show the presence of sheets in ex vivo dog hearts, and found that

they were four to six myocytes thick. Takayama et al. [11] investigated the role of sheets in dog hearts in systole and diastole. They found that the sliding and extension of the sheets accounted for approximately 90 % of the wall thickening in the LV free wall. They also found that the changes in sheet architecture were dependent on the location within the LV.

Initially these sheets were shown by histology, which has the problem that they may be caused, or at least enhanced, by the fixation methods carried out for the histology [2]. Gilbert et al. [12] used high spatial resolution contrast enhanced MRI to show the existence of the sheets in rat hearts. They found that the sheets were smoothly continuous through most of the myocardium but there are some regions where the sheets intersect at close to 90°. The advantage of using this method is that it is non-destructive (unlike histology) and direct (unlike dMRI), but it is limited in resolution and cannot be performed in vivo.

2.1.2 Cardiac myocytes

Cardiac myocytes are elongated cells, typically 100 µm to 150 µm long and 20 µm to 35 µm wide [13]. A single myocyte can be seen in Figure 2.6A, and a section of cardiac tissue showing many myocytes in Figure 2.6B. Myocytes have intercalated discs at their ends, made from a thickening of the cell membrane (sarcolemma), which connect longitudinally with neighbouring myocytes; they also branch in a variable manner to connect laterally with adjacent myocytes [14, 15].

Myocytes are formed primarily from myofibrils, which consist of repeating units called sarcomeres, which themselves are made of the contractile myofilaments actin and myosin, and are divided by Z discs [13–15]. Myofibrils are surrounded by the sarcoplasmic reticulum, which stores and releases calcium ions for contraction [14]. The striations seen in Figure 2.6A are due to the alternating actin and myosin filaments [13, 15]. The parts of a myocyte can be seen in Figure 2.7.

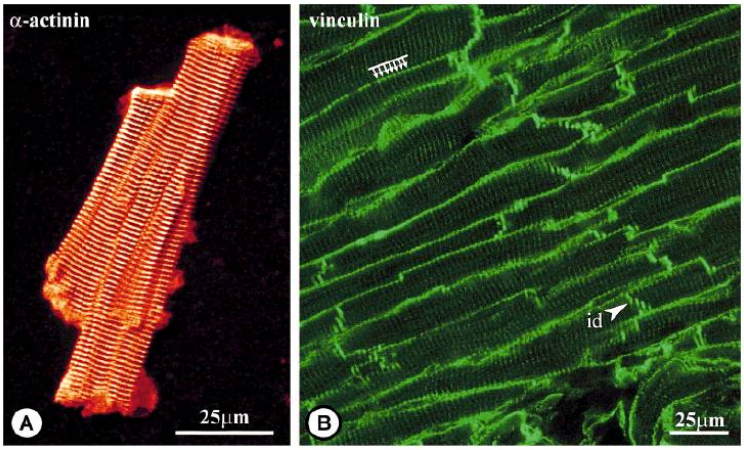

Figure 2.6: Confocal microscopy images of cardiac muscle. (A) shows a single ventricular myocyte, the myofibrils are seen as striations. (B) shows a section of cardiac muscle with numerous cells; id is an intercalated disc. Reproduced from Severs [13], with permission.

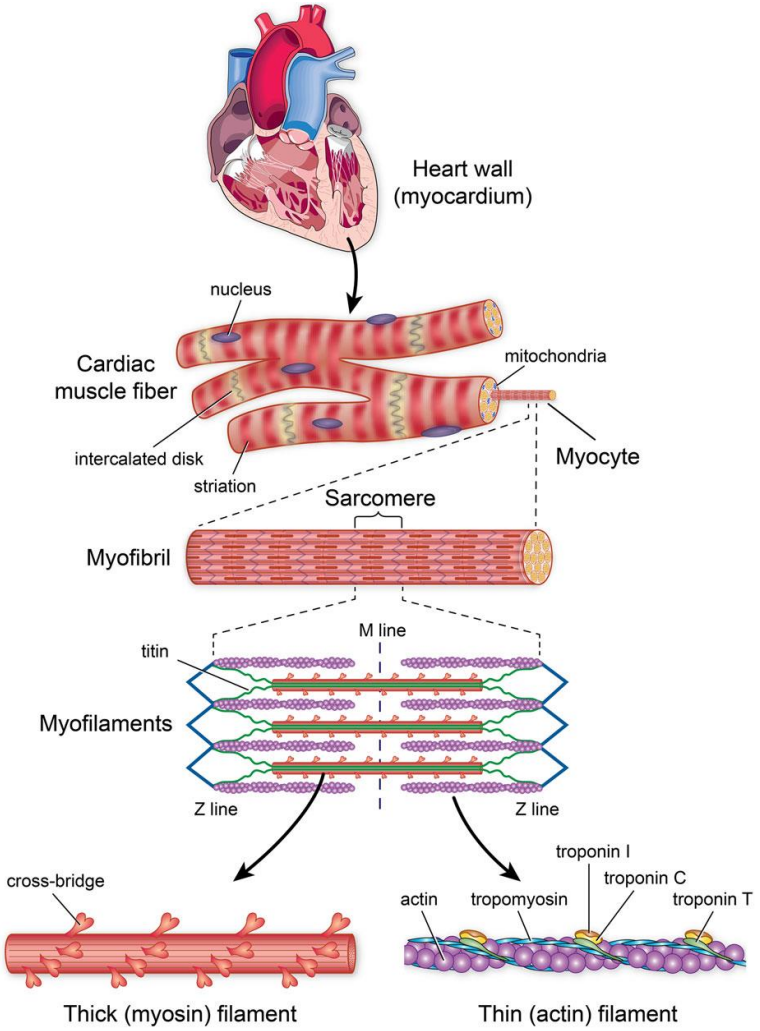

Figure 2.7: Cardiac myocyte structure. Sarcomeres are composed of thin and thick filaments arranged in repeating units. Thin filaments contain actin and thick filaments contains myosin. Reproduced from Golob et al. [16], with permission.

2.2 The pathological heart

Disease may affect the normal structure and function of the heart. Three diseases which are known to cause remodelling of the microstructure are described, followed by a review of the remodelling that is found.

2.2.1 Diseases of the heart

Hypertrophic cardiomyopathy

Hypertrophic Cardiomyopathy (HCM) is hypertrophy of the left ventricle of the heart, which cannot be explained by any other cardiac or systemic disease; it has a prevalence of around 1 in 500 people [17, 18]. HCM is diagnosed based on otherwise unexplained LV hypertrophy, using echocardiography, MRI or both. The most severe effects of HCM are sudden cardiac death (SCD), heart failure, atrial fibrillation and stroke; SCD occurs in up to 1 % of sufferers each year [18, 19]. On the other hand, most people with HCM can expect to live a normal-length life, without invasive treatments or disability [18].

Determining an individual HCM patient's prognosis remains challenging. There are a number of risk factors which indicate that a patient is at high risk of SCD [19], including previous cardiac arrest or ventricular tachycardia, family history of HCM sudden death, very high LV wall thickness and extensive late gadolinium enhancement in the LV myocardium. Those patients deemed at high-risk of SCD are fitted with an implantable defibrillator, which detects and terminates lethal arrhythmias (ventricular tachycardia or ventricular fibrillation). Given that there remain deaths by SCD in patients who have been deemed clinically low-risk, the risk algorithm is incomplete, and additional quantitative risk markers are required [20].

Myocardial infarction

Myocardial infarction (MI) can be defined as myocardial cell death due to prolonged ischaemia [21]. The ischaemia leads to myocardial dysfunction, cell death and then fibrosis. Coronary heart disease, which includes MI and angina, caused 69,000 deaths in the UK in 2014 (12 % of the total), and there were nearly 190,000 cases of MI [22]. Clinical features include pain in the chest and arm, and electrocardiogram (ECG) is used to confirm and classify the MI. Imaging can be useful in diagnosis, classification and prognosis of MI. It can be used to measure perfusion, myocyte viability, myocardial thickening and myocardial motion. [21]

Hypertensive hypertrophy

Hypertensive heart disease causes a pressure overload on the heart which leads to LV hypertrophy. It can be diagnosed by ECG or echocardiography, and is a predictor of cardiovascular mortality and morbidity [23]. The function of the heart is impaired and there is myocardial remodelling [24], which is discussed further in the next section.

2.2.2 Myocardial remodelling

The normal microstructure of the heart is fundamental to its healthy mechanical and electrical function [25, 26]. In disease there can be remodelling of this microstructure which takes many forms.

Myocardial disarray is where the normal arrangement of myocytes becomes disorganised [27]. It is a common finding in HCM [28–30]. Maron and Roberts [28] classified four types of disarray in HCM which are shown in Figure 2.8 alongside normal histology. Maron et al. [29] found type IA to be the most common form of disarray occurring in 66 % of hearts in the LV anterior free wall and 64 % in the LV posterior free wall. Type IB occurred in 34 % and 33 % of the anterior and

posterior LV free wall respectively. Type IIA was only found in one heart, in the posterior LV free wall, and no hearts showed type IIB disarray. Similar results were found in the septum, with type IA disarray in 62 % of the hearts, type IB disarray in 38 % of the hearts and no type II disarray. The mean extent of disarray was 35 % in the septum, 32 % in the anterior free wall and 15 % in the posterior free wall. The total extent per heart ranged from 0 % to 80 %.

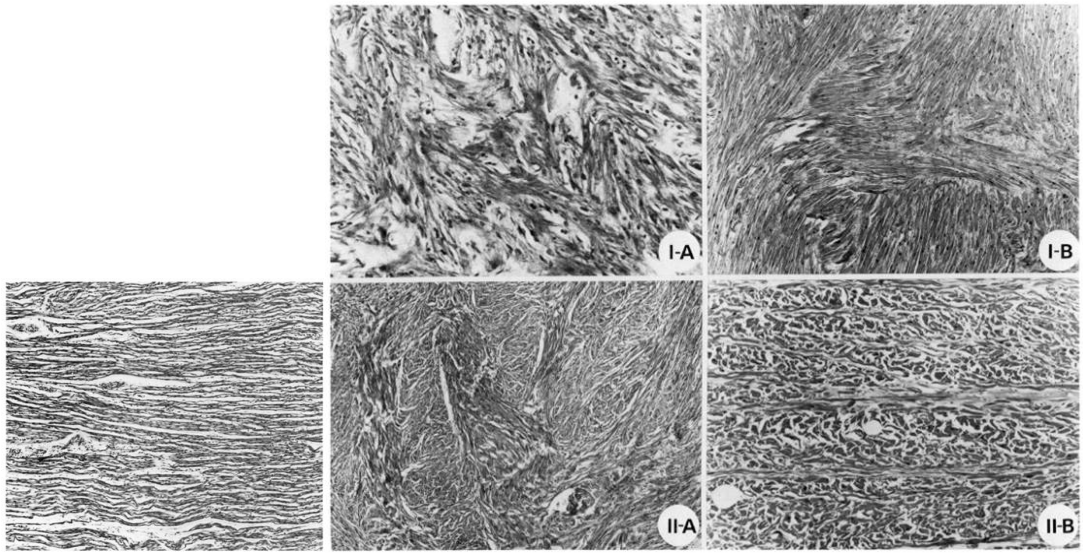

Figure 2.8: Histology of (a) healthy human heart and (b) human hearts with HCM showing the four types of disarray. Reproduced from (a) Maron et al. [31] and (b) Maron and Roberts [28], with permission.

Kuribayashi and Roberts [30] looked at the midwall muscle bundle and found that the usual circular orientation was markedly interrupted in 77 % of HCM hearts at the junction of the RV and LV, and this disarray was present to a lesser extent in the mid-septum, and anterior and posterior LV free wall. Some control hearts showed disarray at the junction but this was less severe. Their findings are seen in Figure 2.9. They concluded that given the amount of disarray it is unlikely that there would be synchronous muscle contraction, and the transmission of electrical signals may also be affected which would further disrupt the contraction of the heart.

Myocardial disarray is not confined to HCM. Inamura [32] found evidence of disarray in hypertensive rats, and Tanaka et al. [33] found disarray in human hypertensive

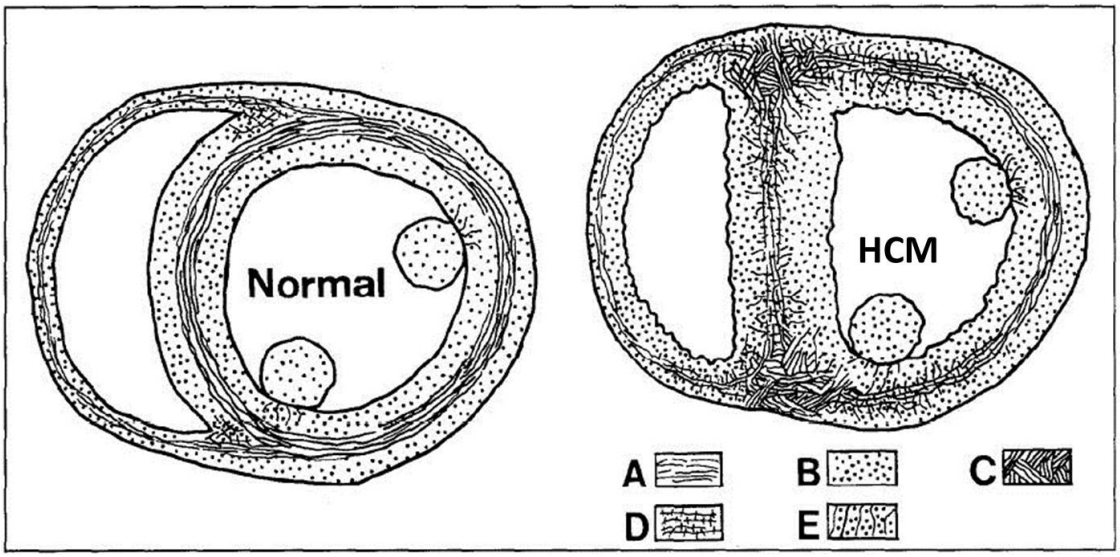

Figure 2.9: Myocardial architecture in midventricular transverse slice of normal and HCM hearts. A: latitudinal fibre layer that is smoothly continuous surrounding LV cavity in normal heart. B: longitudinal fibre layer that is well developed on the left side of ventricular septum in HCM. C: fascicle disarray that is marked in area of junction of 3 ventricular walls in heart with HCM. D: fibre disarray that is marked in portion adjacent to fascicle disarray but relieved as it becomes distant from junctional areas. E: disarray in longitudinal fibre layer which is present in continuity with fascicle or fibre disarray in midwall latitudinal layer. Disarray in normal hearts is restricted to small area of junction between ventricular septum and RV free wall and are adjacent to papillary muscles. Reproduced from Kuribayashi and Roberts [30], with permission.

hearts. Fineschi et al. [34] measured the presence or absence of disarray in eight sites across the LV, RV and septum of hearts with a variety of diseases. No hearts where the cause of death was accidental showed disarray, while disarray was present in at least one of the eight sites in 57 % of transplanted hearts, 56 % of hearts from brain haemorrhage and 45 % of coronary sudden death. In acute MI, Milei et al. [35] found 27 of 29 hearts to have disarray; the posterior septum was the most common site, and types IA and IIA the most prevalent. The extent of disarray was generally small, with 25 of the 41 sites showing disarray having an extent of less than 5 %, and only 3 sites showing more than 10 %. Masuda et al. [36] quantified the degree of disarray by measuring the standard deviation of myocyte orientations. The standard deviation was higher for HCM (38.7 %) than hypertensive heart disease (21.1 %) than controls (15.0 %) .

Fibrosis is the replacement of myocytes with collagen, the main component of cardiac connective tissue [37]. After MI, the damaged tissue is replaced by fibrotic

tissue as part of the healing process to form the scar [21]. Around the scar there is a border zone consisting of a mixture of viable and necrotic myocytes [37]. Fibrosis is also found in HCM [38–40], where Noda [38] found 74 % of RV and 72 % of LV biopsies displayed fibrosis, and hypertensive LV hypertrophy [41, 42].

Other remodelling types that have been found include small vessel disease, where the ratio between the external diameter and the lumen diameter is increased, which has been shown in HCM [40]. Hypertrophy of myocytes was found in 96 % of LV and 56 % of RV biopsies in HCM; it has also been found in hypertensive LV hypertrophy [32, 43]. In most studies, this hypertrophy is measured as an increase in myocyte diameter, but Gerdes et al. [44] found in hypertensive rats that in the LV only the length of cells increased, while in the RV the length and the cross-sectional area (CSA) increased proportionally. Differences in the nuclei, such as changes to size and shape, have been found in HCM [38].

Correlations between the types of remodelling, and with function

The evidence for correlations between different types of remodelling, and between remodelling, imaging measurements and physical symptoms or function remains limited. Studies on post-mortem hearts have investigated the relationship between different types of remodelling, and correlations of remodelling with the cause of death and clinical test results (such as vascular response to exercise) [39, 45, 46]. Some of the types of remodelling can currently be detected in vivo (for example, fibrosis can be detected on gadolinium-enhanced MRI); that they are not routinely used for prognosis indicates that their link with outcome is not yet clear.

The degree of disarray in HCM is not correlated with LV wall thickness [40, 45], heart weight, fibrosis or small vessel disease [40]. Disarray is higher in young deaths and those with an abnormal vascular response to exercise [46]. In HCM, fibrosis is increased in death by heart failure compared with sudden death, while sudden death is associated with smaller hearts [46]. Morimoto et al. [39] found that disarray

is increased in HCM deaths from congestive heart failure compared with deaths not from congestive heart failure; they suggest that this indicates that disarray leads to systolic dysfunction and ventricular dilation. The degree of disarray has been shown to vary in different genotypes of HCM: those with the troponin T genotype have more disarray, less fibrosis, lighter hearts and more sudden death that those without this genotype [47]; the proposed progression of the disease is in Figure 2.10.

In HCM, the disarray has been suggested to disrupt the normal propagation of the electrical signals within the heart, thus leading to the arrhythmias which cause sudden death [19]. Anderson et al. [48] showed that in idiopathic dilated cardiomyopathy there is increased myocardial fibrosis and this correlates with abnormal electrical propagation. The myocardial microstructure, in particular myocyte orientation, has been shown to affect re-entrant arrhythmias [49, 50].

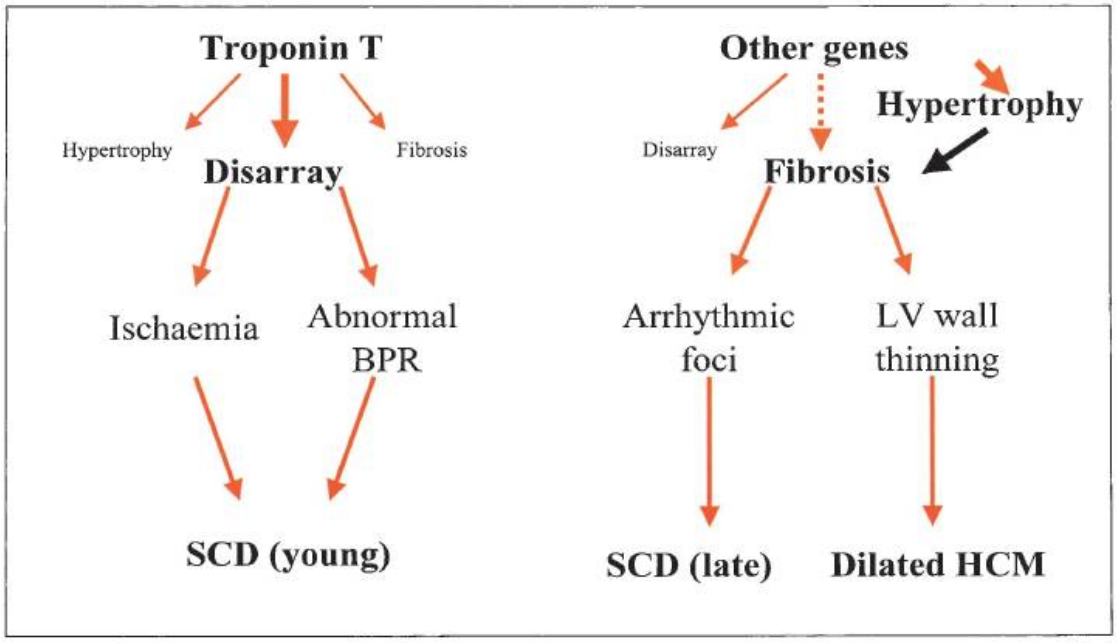

Figure 2.10: Progression of remodelling in HCM. BPR is blood pressure response. SCD is sudden cardiac death. Reproduced from Varnava et al. [47], with permission.

2.3 Diffusion MRI

I firstly introduce diffusion, and then the basics of MRI. I discuss in more detail the principles of diffusion MRI, and summarise how dMRI has been used in the heart.

2.3.1 Diffusion

Movement of particles within a fluid is described by Fick's law [51]: $J = -D\nabla C$, where J is the net flux of the particles, D is the diffusion coefficient, C is the particle concentration and ∇ is the Laplacian operator.

When there is no difference in concentration, the net flux becomes zero, but there is still movement of individual particles. This random movement of particles within a fluid is called diffusion, and was first described by Robert Brown in 1828 [52], hence its alternative name of Brownian motion. For free diffusion, Einstein's equation [53] calculates the mean square distance, $\langle x^2 \rangle$, that the particles move during a certain time, t, as $\langle x^2 \rangle = 2Dt$, where D is the diffusion coefficient.

Figure 2.11 illustrates the difference between free and restricted diffusion in 2D. On the left hand side 1×10^6 molecules all start at the centre of the figure and are free to diffuse within the space. The histograms of the displacement of the molecules shows a Gaussian distribution in both the x and y directions. On the right hand side the same number of molecules are restricted to diffuse from the centre of a rectangle with reflective boundaries. The histogram of the displacements in the y direction, i.e. along the long axis of the rectangle remains approximately Gaussian. In the short axis direction, however, the distribution of displacements is closer to uniform. The time allowed for diffusion, and the geometry determine how different from the Gaussian the distribution becomes. The more restrictive the geometry, the longer the diffusion time and the faster the diffusion, the less Gaussian the distribution of displacements will be.

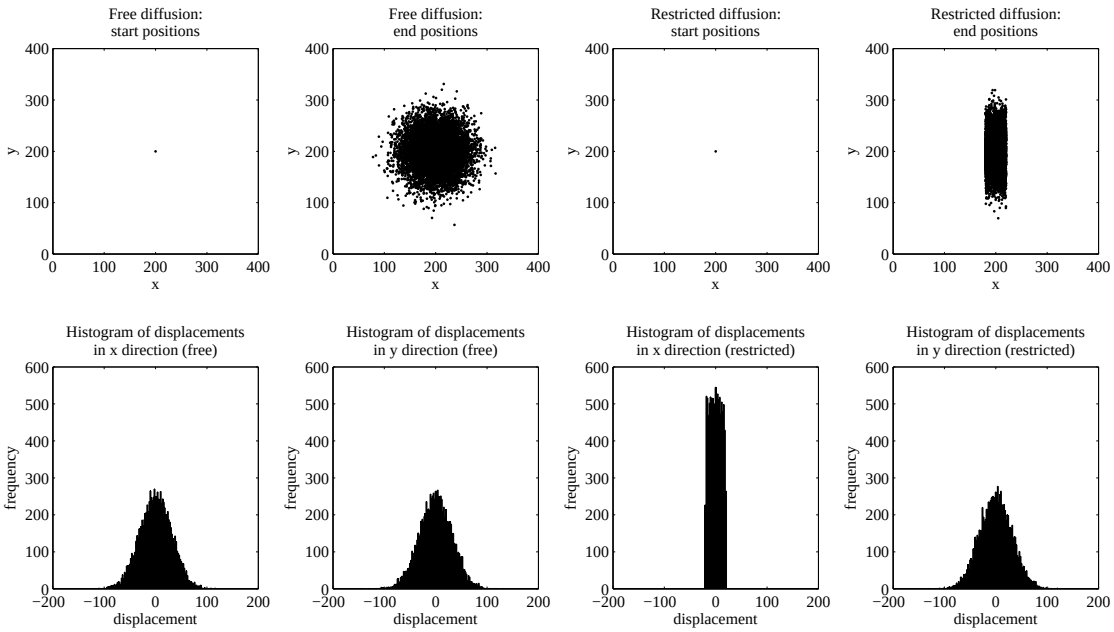

Figure 2.11: 2D diffusion in the free state, and restricted within a rectangle. The top row shows the start and end positions of the molecules. The bottom row shows the histograms of the molecules displacement in the x and y directions.

2.3.2 MRI

Nuclear Magnetic Resonance (NMR) makes use of the spin property of atomic nuclei, usually hydrogen, where the nucleus is a single proton. Usually, the spins are randomly orientated leading to no net magnetisation. In a strong magnetic field, the spins align with the field, either in parallel or anti-parallel, with the parallel alignment more energetically favourable and therefore slightly more common. This leads to an overall net magnetisation in the longitudinal direction, as seen in Figure 2.12

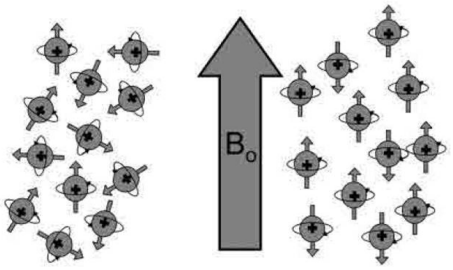

Figure 2.12: Alignment of protons with external magnetic field. (L) With no external magnetic field applied, protons are randomly oriented. (R) With the magnetic field, B_0 applied, protons align in parallel or anti-parallel and there is a net magnetisation parallel to the magnetic field (longitudinal axis). Reproduced from Pooley [54],with permission.

The spins precess with a constant frequency known as the Larmor frequency, ω, which is dependent on the gyromagnetic ratio of the nucleus, γ, and the strength of the applied field B_0:

$$\omega = \gamma B_0 \tag{2.1}$$

A helpful analogy for precession is the rotation of a spinning top, as shown in Figure 2.13.

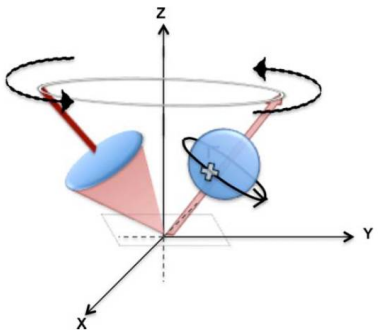

Figure 2.13: Precessing of protons. Precessing of protons (sphere on right) can be compared with a spinning top (cone shape on left). The z-axis is the longitudinal direction along which the magnetic field is applied (or in the case of the spinning top, along which gravity is applied). Reproduced from Currie [55], with permission.

MRI sequences consist of radiofrequency (RF) pulses and gradients designed to measure specific properties of the tissue. An RF pulse is an RF signal at the Larmor frequency applied for a short period of time. The hydrogen protons absorb energy from the RF pulse and this rotates the net magnetisation away from the longitudinal direction, the z-axis in Figure 2.13. A 90° RF pulse rotates the new magnetisation into the transverse plane (perpendicular to the longitudinal direction), leading to no magnetisation in the longitudinal direction, and maximum magnetisation in the transverse plane (Figure 2.14a-b). As protons precess, magnetisation in the longitudinal direction increases: the time taken for this to reach 63 % of its maximum is the T1 time. In the transverse plane, the magnetisation decreases due to dephasing of the protons (Figure 2.14c-d): the time taken for this to decrease to 37 % of its starting value is the T2 time. When a 180° RF pulse is applied some time after a

90° RF pulse, the spins rotate to the opposite axis, and begin to rephase [54]. This is the 'spin echo' sequence which is the basis for dMRI described in the next section.

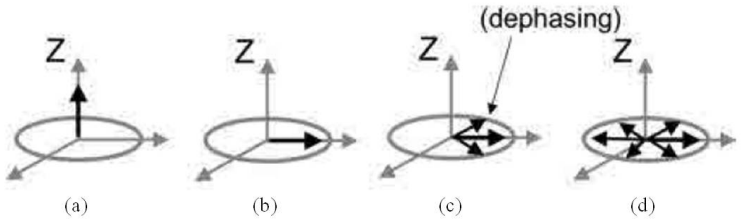

Figure 2.14: Application of 90° RF pulse. (a) prior to application of RF pulse, net magnetisation is along the longitudinal axis (Z). (b) immediately after the RF pulse, net transverse magnetisation is at its maximum. (c) and (d) as protons dephase, the net transverse magnetisation decreases. Reproduced from Pooley [54], with permission.

To convert the NMR signals into an MRI image, three different magnetic field gradients are also applied to provide the spatial information. The slice encoding gradient selects a single slice in the z-direction by applying a field which varies along the z-axis and therefore each slice has a different Larmor frequency. The x and y axis positions are encoded by the frequency and phase encoding gradients respectively. The phase encoding gradient produces a phase offset which is proportional to the duration and intensity of the gradient, which varies linearly along the y-axis. The frequency encoding gradient alters the precessional frequency of the protons along the x-axis.

The resulting data is in the k-space, where each spatial location is encoded by its frequency (x-axis) and phase (y-axis). This is the domain in which the raw data is received by the RF coil. The centre of k-space relates to the low spatial frequencies and contains the contrast information of the image, while the high spatial frequencies at the edge of k-space contain the finer details of the image. To convert this k-space data into an image, a Fourier transform is used, which allows reconstruction of the k-space information into the final image.

2.3.3 Diffusion-weighted MRI

dMRI measures the direction and magnitude of diffusion by assessing the net loss of phase coherence in diffusing molecules (water protons in the heart) in the presence of spatially-varying field gradients. Since diffusion within tissue is affected by factors such as the size and shape of the cells, diffusion MRI can be used to non-invasively infer information about tissue microstructure [56].

The basic in vitro acquisition protocol, the pulse gradient spin echo (PGSE) sequence, was first described by Stejskal and Tanner [57]. A linear spatial magnetic gradient is added to the standard spin-echo sequence of two pulses identical except for a phase difference of 90°, as seen in Figure 2.15.

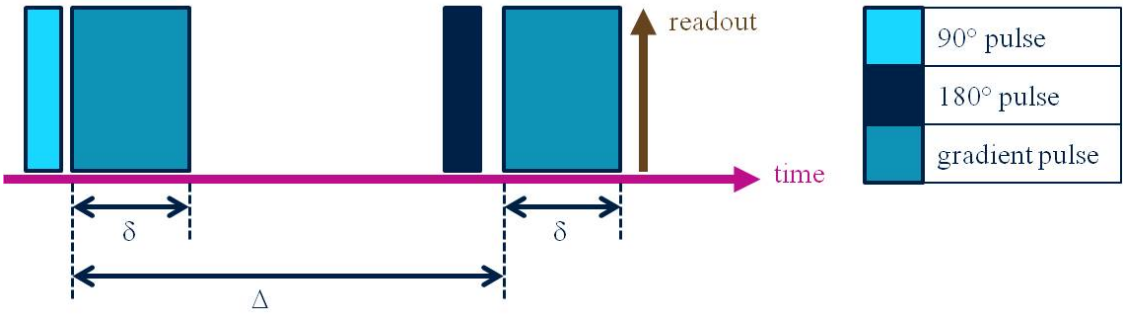

Figure 2.15: Pulse gradient spin echo (PGSE) diffusion MRI sequence.

This allows the diffusion, D, in the direction of the applied gradient to be estimated [58] from:

$$S = S_0 \exp(-Db) \tag{2.2}$$

where S is the signal, S_0 is the reference signal and b is the b-value.

The b-value combines the properties of the applied gradient pulse into a single factor. In the idealised free diffusion state for rectangular pulses, this is given by:

$$b = (G\gamma\delta)^2(\Delta - \frac{\delta}{3}) \tag{2.3}$$

where G is the magnetic field gradient strength, Δ is the separation of the diffusion pulses, δ is the duration of the gradient pulse, and γ is the gyromagnetic ratio (for water this is $267.5\,\mathrm{rad\,\mu s^{-1}\,T^{-1}}$).

A stationary proton will experience the same magnitude (but opposite sign) gradient strength during the two diffusion-encoding pulses, while a proton which moves will experience different gradient strengths leading to a dephasing of the population of protons and a drop in the MRI signal.

This method is referred to as diffusion weighted (DW) imaging and is the simplest diffusion acquisition method available. It gives a single value in each voxel of the diffusion in the direction of the applied magnetic field gradient; the interpretation usually assumes that diffusion is isotropic.

DT MRI

Diffusion within tissue is affected many factors, including the size and shape of cells, cell membrane permeability and the make-up of the intracellular (IC) and extracellular (EC) space. Cell membranes are the key to these effects as they are partially impermeable to water and therefore restrict diffusion through them; since myocytes are much longer than they are wide, restriction is primarily perpendicular to the long axis of these cells. Diffusion tensor imaging (DTI) makes use of this anisotropy of diffusion.

In many applications the assumption of isotropic diffusion is invalid and analysis of the direction of the diffusion is required [59]. Acquiring MRI images with diffusion weighting in at least 6 directions allows the diffusion to be represented by a 3D diffusion tensor (DT) [58]. The methods for fitting the DT to the dMRI data are discussed in Section 3.2.5. Since diffusion is greatest in the direction of

the cell long axis, the primary eigenvector direction is taken to correspond with the cell long axis. The secondary and tertiary eigenvectors indicate the sheetlet structure directions. The eigenvalues quantify the amount of diffusion in each of the eigenvector directions. From the eigenvalues of this DT, quantitative descriptors of the diffusion can be calculated, including the mean apparent diffusion coefficient (ADC, a measure of the magnitude of diffusion) and fractional anisotropy (FA, a measure of the degree of directionality of diffusion). They are calculated from the eigenvalues of the DT as follows:

$$\overline{ADC} = \frac{\lambda_1 + \lambda_2 + \lambda_3}{3} \tag{2.4}$$

$$FA = \sqrt{\frac{3}{2}} \sqrt{\frac{(\lambda_1 - \bar{\lambda})^2 + (\lambda_2 - \bar{\lambda})^2 + (\lambda_3 - \bar{\lambda})^2}{\lambda_1^2 + \lambda_2^2 + \lambda_3^2}} \tag{2.5}$$

where λ_i is the i$^{\text{th}}$ eigenvalue and $\bar{\lambda}$ is the mean of the eigenvalues.

DSI MRI

The interpretation of the DT assumes that all cells are aligned in the same direction, which is given by the primary eigenvector. In some circumstances, this assumption is invalid, for example where there are two or more populations of fibres at difference angles (crossing fibres). Diffusion spectrum imaging (DSI) was designed to overcome this problem [60], as the output is a probability density function (PDF) of diffusion distance.

Many images are acquired, with a range of different b-values, and at different orientations aligned on a Cartesian grid in a domain known as q-space, where the magnitude of q is equal to $\sqrt{b}$. A 3D Fourier transform is applied to the signal attenuation with respect to q-space to produce the PDF of the displacement.

The dephasing of the protons is proportional to the product of the relative spin displacement, $\boldsymbol{r}$, and the gradient wave vector, $\boldsymbol{q}$:

$$\phi = \boldsymbol{q}.\boldsymbol{r} \tag{2.6}$$

where $\boldsymbol{q} = \gamma\delta g$, with γ the gyromagnetic ratio, δ the diffusion-encoding pulse length and g the gradient strength, and $\boldsymbol{r} = \boldsymbol{x}(\Delta) - \boldsymbol{x}(0)$, i.e. the difference in proton position between the times when the second and first diffusion gradient pulses are applied.

$\overline{p}_\Delta(\boldsymbol{r})d^3\boldsymbol{r}$ is a measure of the probability that a proton will move a distance $\boldsymbol{r}$ in the time Δ. It can be shown that there is a Fourier relationship between the MR signal, $S_\Delta(\boldsymbol{q})$, and the density of the average proton displacement in a voxel, $\overline{p}_\Delta(\boldsymbol{r})$:

$$S_\Delta(\boldsymbol{q}) = S_0 \int_{\mathbb{R}^{\not\vdash}} \overline{p}_\Delta(\boldsymbol{r}) e^{iq.r} d^3\boldsymbol{r} \tag{2.7}$$

The diffusion spectrum, $\overline{p}_\Delta(\boldsymbol{r})$, is ultimately given by:

$$\overline{p}_\Delta(\boldsymbol{r}) = S_{)}^{-1}(2\pi)^{-3} \int_{\mathbb{R}^{\not\vdash}} |S_\Delta(\boldsymbol{q})| e^{-iq.r} d^3\boldsymbol{q} \tag{2.8}$$

DSI is sometimes considered to be model-free compared to DTI or multi-compartment models, since the MRI signal and the PDF are related by a Fourier transform rather than a particular model of diffusion. However, it is the interpretation of the data acquired by these methods which is critical to their use: in the case of DSI the interpretation of the PDF is that it relates to cell orientations.

To ensure an accurate reconstruction of the displacements spectrum, the spectrum must be sampled at very high b-values so that the signal hits the noise floor to avoid ringing artefacts from Fourier truncation. This means that the number of images to be acquired in large and thus the scan time is very long. The number of images

was originally 515 although versions with a smaller number of acquisitions have been proposed more recently [59]; the time taken to acquire the images remains too long for in vivo cardiac studies, and a recent review paper concluded of DSI that "it is unlikely that this approach will be useful in the heart" [61].

Non-Gaussian models

Free diffusion has a Gaussian profile, while restriction causes the profile to become non-Gaussian, as shown in Figure 2.11. The DT model assumes Gaussian diffusion, and therefore a variety of models have been developed, which include the non-Gaussian behaviour within the model. The following models each introduce one or more parameters into the basic diffusion equation (Equation 2.2), to allow quantification of the degree of deviation from a Gaussian distribution of diffusion.

The biexponential model fits the dMRI data to two DTs:

$$S = S_0 f_{slow} \exp(-D_{slow} b) + S_0 f_{fast} \exp(-D_{fast} b) \tag{2.9}$$

where f_{slow} and f_{fast} are the volume fractions of the slow and fast components respectively (and sum to 1), D_{slow} and D_{fast} are the diffusion coefficients for the slow and fast components respectively.

The original interpretation of this model was that the fast compartment was the EC space, where it is expected that water would diffuse more quickly than in the more viscous IC compartment. However, the volume fractions produced by the model do not correlate with the known volume fractions of the two compartments in either the heart or the brain. The parameters calculated by the model for the brain are very consistent across studies in the literature which suggests that it represents a true phenomenon [62]. In addition, there are studies that show the biexponential model fits well to data from the IC space only [63, 64]. This has led to the theory that the fast compartment represents the bulk water in the tissue,

while the slow compartment is due to highly structured water trapped in a layer next to the membranes or next to proteins [65].

The stretched exponential [66] introduces a factor, α, which is effectively a measure of the deviation from a Gaussian distribution (a lower α indicates more deviation), and uses a stretch-adjusted diffusion coefficient, D_s:

$$S = S_0 \exp(-b^\alpha D_s) \tag{2.10}$$

Anomalous diffusion [67] uses the same factor, α, as the stretched exponential model, but introduces a second factor, β:

$$S = S_0 E_\beta(-(bD)^\alpha) \tag{2.11}$$

where E_β is the Mittag-Leffler function:

$$E_\beta(z) = \sum_{k=0}^{\infty} \frac{z^k}{\Gamma(1+\beta k)} \tag{2.12}$$

and Γ is the gamma function.

Diffusion kurtosis [68] introduces a kurtosis factor, K, in a truncated Taylor expansion:

$$S = S_0 \exp(-bD_k + \frac{1}{6} b^2 D_k^2 K) \tag{2.13}$$

Multi-compartment models

There are many factors which affect diffusion within tissue: several models take these into account and attempt to give parameters beyond the ADC, FA and cell direction. Multi-compartment models, which model the cells, the EC space and,

in some of the models, a third compartment representing other cellular structures, attempt to fit the dMRI data to this. Panagiotaki et al. [69] compared a large selection of these models with white matter brain images and found that the three compartment models outperformed the two compartment ones. There remain some concerns with these models as some of the parameters which they calculate (e.g. cell radius) do not match physiological values. To my knowledge, no similar models have been suggested for the heart.

2.3.4 Diffusion MRI of the heart

Validation

Various studies have compared cardiac diffusion MRI results with histological data, the current gold standard for analysing microstructure. Hsu et al. [70] compared dMRI and histological data in canine myocardium and found that the primary eigenvector of the DT correlates well with the direction of the local myocardial cells as found in the histology, with a mean error of $(-2.3 \pm 1.0)^\circ$. Chen et al. [71] found that the increased fibre disarray found in histology images correlated with higher angle deviations and inversely correlated with the FA in DTI. Holmes et al. [72] measured fibre orientations in DT MRI and histology from a rabbit heart and found that the difference between the two measurements was $(3.7 \pm 6.4)^\circ$. Scollan et al. [73] measured the correlation between fibre orientations measured by DTI and histology in rabbit hearts, and found a mean difference of 12°.

Pop et al. [37] measured fibrosis using DT MRI, late gadolinium MRI and histology in pig hearts with MI. They found that the ADC from DTI was able to identify fibrosis in dense scar tissue and the border zones, and to differentiate these areas and the remote zone. Li et al [74] showed in a study of hamster hearts with cardiomyopathy that the pixels of the heart with reduced diffusivity and increased FA correlated with those which showed calcium deposits in computed tomography (CT) imaging.

Quantifying the microstructure of the normal heart with dMRI

Its ability to measure the information about cardiac microstructure, including cell orientations, makes dMRI a useful tool for increasing understanding of the normal heart.

Chen et al. [75] measured DT MRI in rat hearts in three states: end diastole, early systole and end systole. The transmural distribution of the helix angles did not change between end diastole and early systole, but in end systole the cells at the epi- and endocardium became more longitudinal in orientation. The sheet angle decreased by 23 % in early systole and 44 % in late systole, supporting the view that the sheet structure allows the macrostructural changes seen during the heart cycle. Hales et al. [10] also investigated differences between contraction states in rat hearts. They found that there was a decrease in the number of left-handed helical fibres and an increase in the number of right-handed helical fibres in contracted state compared with the slack state. The intersection angle between sheets increased from the slack to contracted state, suggesting that in contracted state, the layers of tissue are aligned closer to the short-axis of the heart.

Two studies [7, 76] used DTI on ex vivo human hearts to map the myocyte orientations in the normal heart. Jiang et al. [77] carried out a similar study in mice hearts. Peyrat et al. [78, 79] used dog hearts to create an atlas of myocyte orientations which they used to confirm that fibre orientation is more consistent between subjects than the laminar/sheetlet structure. They also compared the results to a human heart and found that the fibre orientations are more consistent between the two species than the laminar structure. They propose that the technique could be applied to larger sets of data, and different species to better understand the differences within and between species.

Measuring changes in disease

dMRI has been used to measure changes due to disease in ex vivo hearts. Schmitt et al. [80] used DT MRI in normal rat hearts and those with LV hypertrophy induced by hypertension. The hypertrophic hearts showed increased transverse angles, especially at the base and apex, and decreased helix angles in the mid-ventricular section. Li et al. [74] compared DT MRI in normal hamster hearts and those with dilated cardiomyopathy (DCM), at both six and nine months old. Comparing age-matched DCM with controls, older DCM with younger DCM, and older controls with younger controls, the diffusivity (axial, radial and mean) increased and the FA decreased.

Several studies have investigated the effect of MI. In most studies, the infarcted area showed an increased mean ADC and decreased anisotropy [71, 81], although Strijkers et al. [82] found the opposite changes. Wu et al. [81] found that the ADC was similar in the remote and border zones, and the FA was higher in the remote area than the border zone. Pop et al. [37] used DT MRI to measure fibrosis in pigs with MI. The ADC in the dense scar area was higher than that in the border zone which was higher than that in the healthy area. Sosnovik et al. [83] used DSI tractography to analyse the fibre architecture in MI rats and found the architecture was severely perturbed.

In vivo

In vivo dMRI presents challenges due to cardiac and respiratory motion, the short T2 time of the myocardium, and signal inhomogeneity in the thorax [61]. Nonetheless, these problems can be overcome to a certain extent to allow in vivo imaging, albeit with a reduced resolution and SNR.

Edelman et al. [84] were the first to describe dMRI in the heart; they measured ADC in three directions in vivo in the ventricular septum in healthy subjects and those with a variety of cardiac pathologies. In vivo DT MRI has been shown to be reproducible on different days in healthy subjects [85, 86] and those with HCM [87],

and between centres in healthy subjects [88]. These studies all assessed the mean ADC, most also measured the FA [86–88] and some also looked at helix angles [86, 87].

The first reconstruction of in vivo human 3D heart fibre structure was performed by Toussaint et al. in 2010 [89]. They took sparse in vivo DTI slices from a single healthy volunteer. They first mapped the LV geometry onto a truncated ellipsoid and then defined the DT components and the spatial locations of these in terms of a prolate spheroidal system, which they showed gave better results than Cartesian co-ordinates due to the inherent shape of the LV. The fibre orientations found matched known ex vivo results well, especially the helix angle.

To overcome the inherent difficulties with in vivo imaging, a variety of sequences and compensatory strategies have been developed [90]. Spin-echo techniques give good SNR and short acquisition time [91] but can be very sensitive to cardiac motion: several studies have produced motion compensation to overcome this [92, 93]. Strain of cardiac tissue can also have a strong influence of DTI results, especially in the transverse and sheet angles, and must usually therefore be corrected for for in vivo studies [94].

Several studies have used in vivo dMRI to measure the effects of disease in humans. In HCM, Tseng et al. [95] found reduced FA and lower helix angles in five subjects with HCM compared with healthy subjects. Ferreira et al. [96] used DTI to compare HCM and healthy subjects and found changes in the secondary eigenvector in diastole. Wu et al. [97] used DT MRI to measure the effects of MI at two time-points: recent (22 ± 14 days after infarct) and chronic (213 ± 59 days after infarct). The border zone showed increased mean ADC, decreased FA and decreased helix angle compared with the remote zone. In comparison with the recent measurements, the chronic results showed decreased mean ADC in both the border and remote zones; the wall thickness increased in the remote zone and decreased in the border zone.

2.4 Computational Modelling

Computational models can be used to further understanding of dMRI. One of their uses is to determine the accuracy of the results of the models which are used to analyse dMRI data, since it is often hard to acquire a gold standard from living tissue [98]. Analytical models obtain exact solutions to the diffusion equations, while numerical models either obtain a numerical solution to the diffusion equations using the Finite Element Method (FEM) or use a Monte Carlo (MC) approach. Analytical models can only be found for simple geometries such as cylinder and spheres and their use in modelling biological tissue therefore requires marked simplification of the true structure [98]. The MC method allows more complexity and the investigation of more subtle questions [98], for example how the interaction of molecules with boundaries affects the results [62]. The validity of the MC approach has been proven by comparing to analytical data for diffusion between planes [99–102], in spheres [99, 100] and in cylinders [100, 103]. The models must be representative of the tissue which they are simulating [98] and therefore the choice of parameters is very important.

MC models have been used to assess changes due to disease in the spinal cord [104], the brain [98, 103, 105], the lungs [106, 107] and the heart [108, 109]. In one of the first MC models, Lipinski [105] modelled 2D swelling of cells in the brain. The input to their model was histological images which they thresholded to give IC and EC space; they then dilated or eroded the images to simulate swelling or shrinkage. They used their model to assess the tortuosity of the EC diffusion, where the square of the tortuosity is the ratio of the mean square diffusion distance in free diffusion to the mean square distance in the restricted diffusion. They found that as the swelling increased, the tortuosity increased, and that the model matched experimental data from intact brain tissue for a volume fraction of 20 %, and for free diffusion.

Hall and Alexander [98] created an MC simulation of brain white matter. Immediately following a stroke, the ADC is decreased, and they used their model

to test whether cell swelling could account for this. The cells were modelled as parallel cylinders, and as the swelling is increased, cylinders which would overlap are deformed. As the swelling increases, the ADC decreased due to the increased restriction in the extracellular space. The simulated decrease in ADC is faster than the analytical model which used a tortuosity approximation for the EC space and could not take the abutting of the cylinders into account. They also looked at the optimal parameter choice to balance accuracy against computational time, which is discussed further in Section 3.5.

Yeh et al. [110] developed an MC model of the brain with the aim of using it to link dMRI results to the underlying biological tissue structure. Surfaces were created in 3D from a triangular mesh which allowed any geometry to be created. They demonstrated that their model was able to reproduce simulated results from the literature regarding cylinder diameter estimation in parallel impermeable cylinders. They also modelled swelling in spherical cells to confirm that cell swelling leads to a decrease in mean ADC as found in acute ischaemic stroke.

Lin at al. [103] also modelled white matter as parallel cylinders, in this case in a three compartment model consisting of an axon, glial cells and EC space. They modelled the effects of traumatic brain injury (TBI). The four effects of TBI which they simulated were: axonal injury (which decreases the diffusivity in axons), vasogenic oedema (which decreases axon separation), cytotoxic oedema (swelling of glial cells, which increases the volume fraction of glial cells) and demyellination (which increases the permeability of the myelin sheath). The DT MRI outcomes which they assessed were mean diffusivity (MD, also known as mean ADC), FA, radial diffusivity and axial diffusivity. Each of the four TBI effects had a different set of effects on the four outcomes, suggesting that the overall effect when more than one of the TBI effects is present could be small or even negligible as they cancel each other out. They also looked at the optimal number of molecules and number of timesteps, which is discussed further in Section 3.5.

Ford and Hackney [104] modelled the spinal cord as permeable cylinders. They simulated two effects of spinal cord injury: axonal swelling which increases the size and volume fraction of axons, and decreased membrane permeability. Their previous experimental data showed that in spinal cord injury in rats, diffusion parallel to the long axis of the neurons is decreased, and diffusion perpendicular to the long axis is increased. Their MC simulations showed the same results.

Plotkowiak et al. [106] modelled the diffusion of hyperpolarised helium in the lung to understand the effect of chronic obstructive pulmonary disease on the dMRI measured. They showed that it was possible to simulate data which matched clinical findings and therefore that computational models could be useful in further increasing understanding of differences between healthy and diseased tissue. Also in the lung, Sukstanskii and Yablonskiy [107] modelled diffusion in the lungs with and without mild emphysema and found higher signal attenuation in the diseased state, indicating more diffusion due to less restriction.

In the only MC model of cardiac dMRI that, to my knowledge, has been published, Wang et al. [108] firstly created an MC model of parallel myocytes using hexagonal cross-sections. They investigated the effect of the ratio of water content in the IC and EC space. As the ratio of IC to EC water increased, the FA increased. They also used their model to investigate the effect of permeable cell membranes and found that as the permeability increased, the FA decreased. In their follow-up paper [109], they modelled myocytes as cylinders. They distributed 8000 myocytes in different orientations in a cube with sides 2 mm and only placed molecules in the IC space, since the volume fraction of cells was considerably lower than the physiological value (c. 3 %). For equal sized cylinders arranged in a regular pattern to mimic the sheet arrangements, they investigated the accuracy of the fibre direction measured using different numbers of myocytes per voxel. For a single myocyte in a voxel, the error in the fibre angle measurement was never more than 25°, but when the number of myocytes per voxel was increased to eight or 64, the error could be up to 90°. They also found that the number of myocytes per voxel influenced the

effect of the signal-to-noise ratio (SNR). For a poor SNR, eight myocytes gave more accurate results, while for a better SNR, one myocyte was more accurate. They then expanded this model to the whole heart for different stages of the cardiac cycle [111].

The alternative numerical modelling approach to MC is FEM. This is a deterministic approach where the model volume is divided up into a spatial grid and the magnetisation at each node updated at each time step by calculating the probability that protons will move to adjacent nodes. The computational time is dependent on the timestep and spatial resolution, and these must be carefully chosen to ensure model stability [112]. The FEM model does not allow the path of individual protons to be analysed [113]. Chin et al. [114] used FEM modelling to investigate the biexponential model in rat spinal cord, and confirmed that the volume fractions for IC and EC compartments are not correct, but that the multi-compartment behaviour is due to restriction and exchange between the compartments. Recently, Nguyen et al. [85] and Beltrachini et al. [115] have furthered FEM modelling by producing frameworks for solving the Bloch-Torrey equation of diffusion.

2.5 Summary

The normal structure of the heart is essential for its healthy function; remodelling of the microstructure in disease can affect this function. dMRI offers the potential to detect and quantify pathological remodelling. However, for this to be a useful tool, the relationship between microstructural changes and the dMRI signal needs to be better understood. Computational modelling offers an efficient, controlled way to do this.

3

The model: development and sensitivity analysis

In this chapter, I present a new Monte Carlo (MC) model of diffusion MRI (dMRI) in cardiac microstructure. I explain the rationale behind the chosen modelling method and the justification of the model parameters. I carry out a sensitivity analysis of the relative importance of the model parameters which shows that the diffusivity has the greatest effect on the model outcomes.

I presented the model and an earlier version of the sensitivity analysis at the Functional Imaging and Modelling of the Heart (FIMH) conference in Maastricht in June 2015 and this was published in Lecture Notes in Computer Science [116]. This sensitivity analysis forms part of a journal article which I submitted to the IEEE Transactions in Medical Imaging, where it is currently under review.

3.1 Background

Given the relatively limited understanding of the relationship between cardiac tissue microstructure and dMRI measurements, a model of cardiac tissue to simulate

dMRI measurements would be a useful tool. It will allow the investigation of the relationship between changes in the microstructure and the dMRI measurements these produce. It will ultimately facilitate investigation of the effect of pathological changes in cardiac microstructure on the dMRI signal. As Lin at al. [103] found in their study of traumatic brain injury, the different microstructural changes due to disease can have opposing effects on the dMRI outputs. The understanding of these changes could inform the choice of measurements and sequence parameters in clinical imaging to optimise the detection of changes due to disease.

3.2 Overview of the model

The model consists of five steps as shown in Figure 3.1. The details of each step are described below.

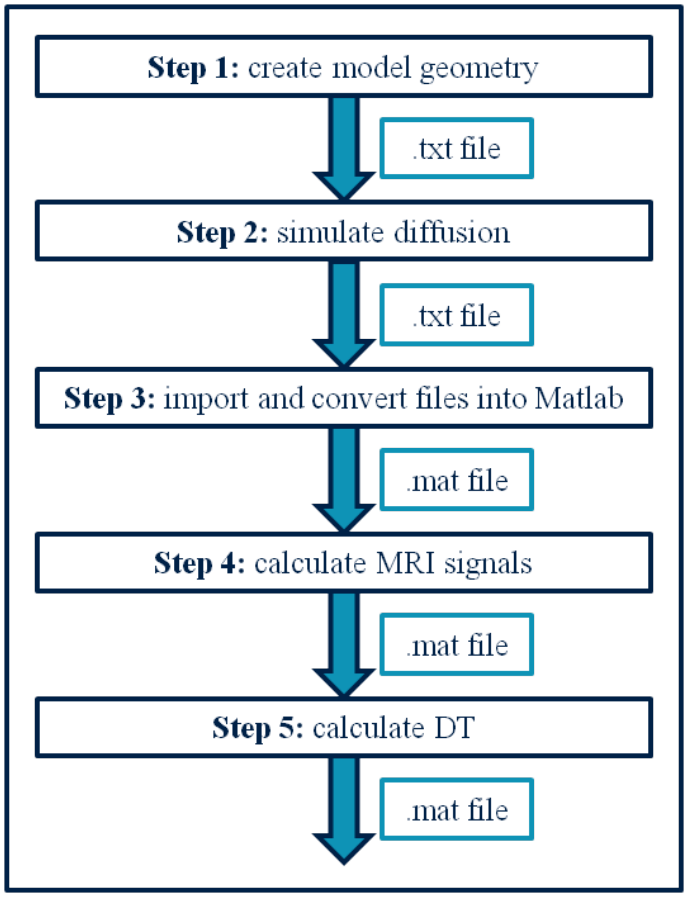

Figure 3.1: Overview of the model.

3.2.1 Step 1: creating the model geometry

Custom-written Matlab (MathWorks, USA) code is used to create the model geometry. The corners of each cell are calculated, according to cell size, orientation and volume fraction, and this used to generate the input text file for Smoldyn. Each cell is created from 12 triangles (two for each surface). The model is described in more detail in Section 3.4.

3.2.2 Step 2: simulating the diffusion

Analytical models obtain exact solutions to the diffusion equations, while numerical models either obtain a numerical solution to the diffusion equations or use an MC approach. MC modelling allows the simulation of set-ups for which there are no analytical solutions and therefore allows more complexity and the investigation of more subtle questions [98], for example how the interaction of molecules with boundaries affects the results [62]. Analytical solutions to the diffusion equations have only been found for relatively simple structures such as for diffusion between parallel plates [99, 117, 118], in a cylinder [117–119] and in a sphere [99, 117, 118].

To simulate diffusion in heart tissue, I needed a software tool which would be able to accurately model the 3D diffusion of large numbers of molecules within potentially complex geometries. Although the initial model was likely to be fairly simple, the method needed to be able to accommodate the intended extensions to the work, including more complex geometries, permeable membranes and advanced diffusivity (compartment-dependent or non-isotropic, for example).

I found three programs which met some or all of these criteria.

- **Smoldyn** [120] is a program developed by Dr Stephen Andrews at the Fred Hutchinson Cancer Research Centre (Seattle) that models stochastic chemical reactions within a defined geometry; diffusion is a large part of this. The

geometry can be defined from built-in shapes or a mesh, allowing very complex geometries to be used. Boundaries can be reflective or semi-permeable. The diffusivity of molecules can be anisotropic and can be dependent on their location.

- **Camino** [121] was developed by Professor Daniel Alexander's group at University College London, primarily for neurological applications. It has several sections, most of which allow different analyses of experimental dMRI data, but there is also a section which allows MC simulation of dMRI for different substrates (geometries of cell arrangements) [98]. There are some inbuilt geometries focussed on the brain, such as parallel cylinders, while complex geometries can be imported using meshes. As well as modelling the diffusion, it calculates the MRI signal and the diffusion tensor (DT) or other models. Surfaces can be permeable, but diffusivity can only be a single value.

- **Diffusion Microscopist Simulator** [110] is an MC model of dMRI in the brain developed by Professor Cyril Poupon's group at NeuroSpin, France. Surfaces are created in 3D from a triangular mesh which allows any geometry to be created. It also allows permeable membranes, polar membranes and a variety of MRI sequences, but has not yet been released for public use.

The alternative to using an existing program was to write a program myself. However, since Smoldyn met all my criteria (arbitrary geometries, ability to alter all parameters including permeability and diffusivity), I chose to use this to model the diffusion. Smoldyn does not calculate the MRI signal and DT, but writing my own code for this part enabled me to have complete freedom to specify the sequence and is not therefore a limitation. The drawback of Smoldyn is its speed when modelling large geometries and many molecules. This is discussed further in Section 3.3.

The basics of Smoldyn

Surfaces can be defined using built-in shapes (triangles, rectangles, cylinders, spheres, discs and hemispheres), or by using a mesh. Compartments can be defined, if required, from one or more surfaces, and can be useful when molecules are only required in certain parts of the simulation volume, or where the molecular properties differ between volumes.

Molecules can be placed randomly and uniformly across the whole volume or within certain compartments, or be placed at a defined point. Molecules have a diffusivity which determines the distance moved in each timestep. The x, y and z components of each molecule's displacement are drawn from a Gaussian distribution with a mean of zero and a standard deviation equal to the 1D diffusion distance, $\sqrt{(2D\Delta t)}$ where D is the diffusivity and Δt is the timestep. This gives a random direction for each molecule's displacement and a mean displacement equal to the 3D diffusion distance, $\sqrt{(6D\Delta t)}$. Anisotropic diffusivity can also be defined using a tensor.

Molecules can reflect off, transmit through or stick to surfaces when they collide with them, and the rate of these can be defined. If a molecule collides with more than one surface during a timestep, it will interact with each of them.

If the surfaces are set to have non-zero permeability there is a possibility, depending on the parameters chosen, that the system could become unstable. It is possible that there will be a flow of molecules from one compartment to another and the resultant density of molecules will become uneven. If such a set-up is chosen the output in terms of the molecules' position and density would need to be carefully monitored to ensure that the system is stable.

If different properties, for example diffusivity, are required in different compartments of the model and the boundaries between these compartments are permeable, the molecule will need to change 'species' as it passes through the boundary to acquire the different properties.

There are different options regarding the outer edges of the model volume. Although one of the first things to set in Smoldyn are the simulation boundaries, it will actually allow molecules to diffuse beyond these boundaries and continue to record their position, although this will slow down the simulations. The boundaries exist for efficient simulation and to scale the graphical output. In theory, the boundaries can be of different types, but the Smoldyn developers advise that if any other surfaces exist in the model then the boundaries become transparent and it is therefore a good idea to create surfaces coincident with the boundary to contain the molecules. There are then two options: the molecules can be absorbed by the surface and therefore exit the simulation or they can reflect off the surface and thus remain in the simulation. I chose to have reflecting surfaces so that the number of molecules in the system remained constant as I felt that this would allow me a better ability to check that the system was behaving as required.

There is no pre-defined system of units in Smoldyn, it is up to the user to choose a unit system and keep to it. I chose micrometres (µm) and milliseconds (ms), since these are the distances and total time scales that the model works in.

The input into Smoldyn is a text file defining the surfaces, compartments and molecules, and their properties. The chosen output is a text file containing the position at each time step of every molecule. An example of an input text file is shown on the next page.

```
dim 3                          #3 dimensional#
#set the 3 boundaries of the simulation volume#
        boundaries 0 0 600
        boundaries 1 0 600
        boundaries 2 0 600
        species species_one         #names of molecule species#
        max_mol 100000              #max no of molecules in sim#
        difc all 1.3                #diffusivity of molecules#
        color all 1 0 0             #colour of molecules#
        display_size all 1          #display size of molecules#
#define start, stop and step times#
        time_start 0
        time_stop 16
        time_step 0.002
#create reflective surfaces coincident with the boundaries#
#to stop molecules escaping the system#
        start_surface walls
        action both all reflect
        color both 0 0 0
        polygon both edge
        panel rect +0 0 0 0 600 600
        panel rect -0 600 0 0 600 600
        panel rect +1 0 0 0 600 600
        panel rect -1 0 600 0 600 600
        panel rect +2 0 0 0 600 600
        panel rect -2 0 0 600 600 600
        end_surface
#create a closed cylinder surface from a cylinder and 2 discs#
        start_surface surface_one
        action all both reflect
        color both purple 0.5
#cylinder defined by ends of long axis and radius#
        panel cyl 300 300 50 300 300 550 5.000000e-01 20 20
#disk defined by centre, radius and normal to surface#
        panel disk 300 300 50 5.000000e-01 0 0 1 20
        panel disk 300 300 550 5.000000e-01 0 0 -1 20
        end_surface
#create a compartment from the surface defined above#
        start_compartment compartment_one
        surface surface_one
        point 300 300 300               #a point within the cylinder#
        end_compartment
#put some molecules of species_one in the compartment#
        compartment_mol 100000 species_one compartment_one
#output the molecules positions to file trajs1.txt#
        output_files trajs1.txt
        cmd n 1 listmols3 one trajs1.txt
```

Diffusion simulation approaches

In the dMRI modelling literature, there are different approaches to simulating diffusion, relating to the collision of molecules with surfaces, and the direction and distance that the molecules move in each timestep.

If a molecule is calculated to collide with a surface during a timestep, then rather than calculating its position according to an elastic collision with the boundary [98, 103, 108], some authors choose to keep the molecule in its original position [104, 106, 107] as this saves computational time and has been claimed not to significantly affect the results [107]. Smoldyn assumes elastic collisions with any boundaries with which a molecule collides.

Most studies, including Smoldyn, move the molecules in a random direction at each timestep [98, 103, 106, 108], but some studies use the simplification of only allowing the molecules to move in certain directions, Lipinski [105] models 2D diffusion and only allows molecules to move in four orthogonal directions and Sukstanskii and Yablonskiy [107] allow eight possible directions in 3D ($[\pm 1 \pm 1 \pm 1]$). The reduced possible number of directions will increase the speed of simulations but decrease the accuracy of the results.

Almost all studies use a fixed step length, although Liu et al. [122] used Gaussian step lengths, and Wang et al. [108] also investigated using a Gaussian distribution of step lengths, but found the fixed step length gave better results for diffusion between two parallel plates. In Smoldyn, a Gaussian distribution of step lengths is used. For isotropic free diffusion they showed that the mean position was close to zero, with the fluctuations within theoretical predictions.

Modelling diffusion is only a part of Smoldyn's purpose, and it therefore tends to use the more complex assumptions than some studies which are purely simulating diffusion, which may require increased computational time.

3.2.3 Step 3: converting the diffusion files

Once the Smoldyn simulation has run, the text file is imported into Matlab and converted into a Matlab matrix of size $M \times T \times 3$ where M is the number of molecules, T is the number of timesteps and the 3 is for the x, y and z components of the positions. Only those molecules which finish inside the voxel are kept as these are the ones used in the next step.

3.2.4 Step 4: calculating the diffusion MRI signal

As originally described by Balinov et al. [99] for molecules diffusing in a gradient field, the total phase shift, Ψ, for each molecule is a function of the sum of the gradient strength that it experiences over every time step, j, and can be calculated as:

$$\Psi = \sum_{j=0}^{T} \Psi_j = \sum_{j=0}^{T} \gamma \langle G(t_j), r(t_j) \rangle \delta t \tag{3.1}$$

where T is the total number of timesteps, $G(t_j)$ is the magnetic field gradient at timestep j, $r(t_j)$ is the molecule position at timestep j and γ is the gyromagnetic ratio ($267.5\,\mathrm{rad\,\mu s^{-1}\,T^{-1}}$ for protons). The MRI sequence modelled was the standard Stejskal-Tanner sequence [57], with rectangular diffusion gradient pulses assumed. For experimental data cross terms between the diffusion and imaging gradients, and non-zero ramp times also contribute to the phase shift, but I did not include these in the simulated sequence.

The MRI signal, S/S_0, for all M molecules is then:

$$\frac{S}{S_0} = \frac{1}{M} \sum_{i=1}^{M} \cos(\Psi) \tag{3.2}$$

This method assumes that the distribution of the phases is symmetrical about zero, which eliminates the sine of the phase shift in the calculation of the MRI signal, since this will be symmetrical around zero and hence sum to zero.

This method is widely used for dMRI simulation including in the brain [98, 103], the lungs [106] and the heart [108, 109].

I implemented this method by calculating the position of each molecule in the direction of each gradient. The total phase shift is the difference between the total gradient strength experienced by each molecule in the first pulse less the total experienced in the second pulse.

The gradient directions for all the simulation studies in this thesis are from Dr Emmanuel Caruyer's website [123], with a single shell and the points per shell distributed by a q^0 rule.

3.2.5 Step 5: calculating the diffusion tensor

The total phase shift and the MRI signal are calculated for each gradient direction and then the diffusion tensor is calculated as it would be for experimental data, from the equations below. There are two main ways of fitting the MRI data to a diffusion tensor [124].

The first method, the $\boldsymbol{H}$-matrix method, puts the tensor elements in a six-element vector as follows:

$$\boldsymbol{Y} = \boldsymbol{H}\boldsymbol{d} \tag{3.3}$$

where $\boldsymbol{Y}$ (size M×1, where M is the number of DW images) contains the image and acquisition data, $\boldsymbol{H}$ (size M×6) the gradient direction data, and $\boldsymbol{d}$ (size 6×1) is the calculated diffusion data which leads to the DT. The components

of $\boldsymbol{Y}$ are calculated from:

$$Y_i = \frac{\ln\left(S_0/S_i\right)}{b_i} \tag{3.4}$$

where S_0 = reference image, S_i = i$^{\text{th}}$ image, b_i = i$^{\text{th}}$ b-value. The b-value is calculated from:

$$b = (G\gamma\delta)^2(\Delta - \frac{\delta}{3}) \tag{3.5}$$

where G is the magnetic field gradient strength and γ is the gyromagnetic ratio (for water this is $267.5\,\text{rad}\,\mu\text{s}^{-1}\,\text{T}^{-1}$). The components of $\boldsymbol{H}$ are calculated from:

$$\boldsymbol{H} = \begin{bmatrix} \boldsymbol{H_1^T} & \boldsymbol{H_2^T} & \dots & \boldsymbol{H_M^T} \end{bmatrix} \tag{3.6}$$

$$\boldsymbol{H_i} = \begin{bmatrix} g_{xi}^2 & g_{yi}^2 & g_{zi}^2 & 2g_{xi}g_{yi} & 2g_{xi}g_{zi} & 2g_{yi}g_{zi} \end{bmatrix} \tag{3.7}$$

where g_{xi}, g_{yi} and g_{zi} are respectively the x, y and z direction components of the gradient direction for the i$^{\text{th}}$ image. The resultant $\boldsymbol{d}$ matrix is:

$$\boldsymbol{d} = \begin{bmatrix} D_{xx} & D_{yy} & D_{zz} & D_{xy} & D_{xz} & D_{yz} \end{bmatrix}^T \tag{3.8}$$

where D_{xx} etc. are the elements of the symmetric diffusion tensor.

The second method, the $\boldsymbol{B}$-matrix method, includes the logarithm of the reference signal intensity along with the six diffusion tensor elements in a seven-element vector as follows:

$$\boldsymbol{x} = \boldsymbol{B\alpha} \tag{3.9}$$

where $\boldsymbol{x}$ (size N×1, where N is the number of images, including the b0 ones) contains the image data, $\boldsymbol{B}$ (size N×7) the diffusion weighting and gradient direction data and $\boldsymbol{\alpha}$ (size 7×1) is the calculated diffusion data which leads to the DT, and are formed as follows:

$$\mathbf{x} = \begin{bmatrix} \ln S_1 & \ln S_2 & ... & \ln S_N \end{bmatrix}^T \tag{3.10}$$

$$\boldsymbol{\alpha} = \begin{bmatrix} D_{xx} & D_{yy} & D_{zz} & D_{xy} & D_{xz} & D_{yz} & \ln S_0 \end{bmatrix}^T \tag{3.11}$$

$$\boldsymbol{B_i} = \begin{bmatrix} -b_{xxi} & -b_{yyi} & -b_{zzi} & -b_{xyi} & -b_{xzi} & -b_{yzi} & 1 \end{bmatrix} \tag{3.12}$$

where b_{xxi} is the xx element of the diffusion weighting b-matrix for the i$^{\text{th}}$ image. These are combined to give the full $\boldsymbol{B}$ matrix:

$$\boldsymbol{B} = \begin{bmatrix} \boldsymbol{B_1} & \boldsymbol{B_2} & ... & \boldsymbol{B_N} \end{bmatrix}^T \tag{3.13}$$

In experimental data, the b-matrix includes cross-terms from the imaging gradients, while in simulated data the b-matrix can be calculated from the b-values and the gradient directions.

When there are only six gradient directions, there is an exact solution and therefore the two methods will give identical results. With more than six directions, there can be small differences between the two methods. The $\boldsymbol{B}$-matrix method allows multiple unweighted "b0" images to be used in the calculations without needing to average them [124]. In addition to the two methods, there are different ways to fit the data: linear fitting fits the tensor in the log domain, while nonlinear fitting fits the tensor in the signal domain. The nonlinear method can be better when there are high b-values or when the signal-to-noise ratio (SNR) is low. The SNR was very good for all my data so this was not required. I found that for the simulated data the nonlinear method caused discontinuities in the results at high b-values, due to it tending to fit the many very small signals to zero. For all analyses of both experimental and simulated data, I therefore used the $\boldsymbol{B}$-matrix with linear fitting.

From the DT, there are two common measures of diffusivity that can be calculated. The mean apparent diffusion coefficient (ADC) is a measure of the overall amount of diffusivity, while the fractional anisotropy (FA) is a measure of the directionality of the diffusion [56]. These are calculated from Equations 2.4 and 2.5.

3.3 Computational time and practicalities

Smoldyn becomes very slow or fails if the number of molecules is too large, and so I ran the model multiple times and combined the molecules to give the overall results. The molecules do not interact with each other so this does not affect the results. There is a maximum text file size which can be imported into Matlab of around 6GB, and therefore the molecules within each Smoldyn simulation were divided into several files. The number of molecules per file, and files per simulation depend on the volume and total length of time to be modelled.

All stages of the model simulation could be run on my desktop PC. To allow many simulations to be run simultaneously, I ran most of the simulations through the Advanced Research Computing centre at the University of Oxford. This did not speed up individual simulations but did allow many to be run simultaneously and provided a large storage space for the text files which are the output from Smoldyn.

Example computational times for a simulation volume of $400 \times 400 \times 400$µm for a total simulation time of 44 ms are shown in Table 3.1.

Table 3.1: Computational time for a 400 µm simulation volume with 6.4×10^6 molecules and 2.2×10^4 timesteps.

stage	program	time per file	total time	notes
1: create model	Matlab	5 s	5 s	once only
2: simulate diffusion	Smoldyn	3.5 h	180 h	50 simulations
3: import/convert files	Matlab	7 min	100 h	16x50 files
4: calculate MRI signal	Matlab	1.7 min	22 h	16x50 files
5: calculate DT	Matlab	5 s	5 s	for every b-value

Suggested methods to improve the computational time are discussed in Chapter 8.

3.4 The model and its parameters

The model is of a simplified volume of left ventricular (LV) myocardium as shown in Figure 3.2.

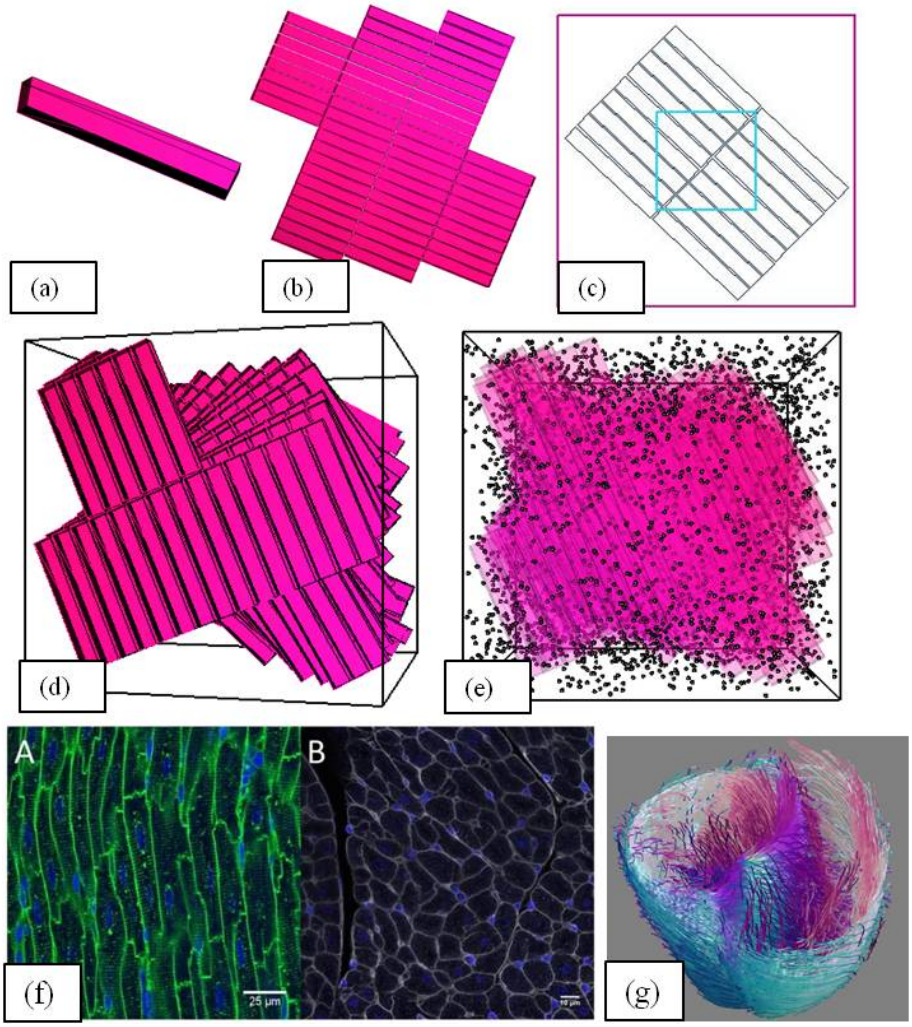

Figure 3.2: Model geometry. (a) Cells are cuboids. (b) Cells are arranged in layers. (c) The central volume (marked in turquoise) is analysed. (d) Each layer is angled to the next layer. (e) Molecules (black) are randomly distributed across the whole model volume. (f) Confocal image of cardiomyocytes in long and cross section from Bensley et al. [125] (CC BY 4.0) (g) Fibre angles from Zhukov et al. [4] © IEEE

Figure 3.2a: Cells are modelled as cuboids with a defined length (L), cross-sectional area (CSA) and aspect ratio of the cross-section (AR, thickness/width). Figure 3.2f shows confocal images of myocytes along the long and short axes. The long axis view shows that cells are approximately rectangular in shape, while the short axis views

show variable cross-sections. The literature on myocyte cross-section reports that there is a difference in the thickness and width [44, 126] but there is little discussion on shape. Myocytes are sometimes modelled as cylinders [108], but given the known difference in width and thickness of the cross-section, an ellipsoid or rectangle allows this difference to be incorporated into the model. I chose a rectangle over an ellipsoid from histology images it appears to be a better approximation, it is a simpler shape to model in Smoldyn, and allows the reported volume fraction of cells to be achieved.

Figure 3.2b: The model consists of layers of cells. A large layer of cells is firstly created and then only cells which are completely within the model boundary are kept to avoid modelling parts of cells, leading to the shape seen here. Cells within each layer are parallel to each other, as this corresponds with histology or confocal images such as that seen in Figure 3.2f and also allows a high volume fraction of cells to be achieved. The gaps between cells within and between layers is equal and is chosen to give the desired volume fraction (VF) of cells, that is, the proportion of the tissue made up of myocytes. It is possible that the gaps between layers or between sheetlets are larger than those between adjacent cells, however, I found no quantitative evidence for this in the literature and therefore kept the gaps equal.

Figure 3.2c: A single cubic voxel is analysed, shown in turquoise. To avoid boundary effects a cube with sides 200 µm larger than the required voxel is modelled, shown in pink. The boundary size was chosen to ensure that any molecule which reaches the outer boundary and is reflected back does not finish in the voxel and therefore does not contribute to the MRI signal.

Figure 3.2d: Each layer of cells is rotated compared to its adjacent layers to mimic the helix angle. The helix angle (that between the cell long-axis projected onto a plane parallel to the epicardium, and the radial-circumferential plane [10], as discussed in Section 2.1.1) varies linearly across the voxel at a rate (ANG) based on the ratio between the range of helix angles found across the myocardium and typical LV wall thickness (see Table 3.2). The LV wall thickness in the literature

ranged from 1.73 mm to 2.67 mm [75, 127, 128], and the total helix angle range varied from 130° to 180° [10, 71, 129]. Each layer is parallel to the epicardium and endocardium, that is, transverse angles (those between the circumferential axis and the projection of the cell long-axis onto the radial-circumferential plane [10]) were set to 0°. Transverse angles have a much smaller variation across the myocardium than helix angles [71] and therefore the change within a single voxel will only be small. By eliminating transverse angles, the model is effectively reduced to a 2D problem since each layer is parallel to the next which makes achieving the desired set-up and volume fraction of myocytes much simpler. This is something which I may want to introduce at a later stage, this is discussed further in Sections 8.1.

Figure 3.2e: Molecules are randomly distributed across the simulation volume; at each time step each molecule moves in a random direction with a step length normally distributed about a mean which is proportional to the diffusivity. If a molecule reaches any boundaries, it reflects elastically off those boundaries. Collisions between molecules are not modelled. Only molecules which finished in the voxel were used to calculate the MRI signal. The diffusivity is assumed to be isotropic, and to be the same in the intra- and extra-cellular space. The restrictions to diffusion from surfaces other than the cell membranes were not modelled explicitly, but assumed to be incorporated in the diffusivity, which is lower than the self-diffusivity of water. Further investigation about the diffusivity in the extracellular space was performed at a later stage in the project and is detailed in Section 5.2.

I carried out an extensive literature review, aiming at finding the range of published values for each of the model parameters. The results are shown in Table 3.2, and reveal a wide range of parameter values. Table 3.5 shows the minimum and maximum values for the sensitivity analysis in Section 3.6.

The wide range of values is due to both inherent variability, and differences in sample preparation and measurement technique. Studies have shown myocyte length and

CSA are dependent on gender [130, 131] and location [132, 133]; LV wall thickness depends on rat strain [128], location [127] and contraction state [75].

Table 3.2: Summary of rat heart parameters found in the literature.

parameter	value	reference	notes
myocyte length (µm)	94.0 ± 4.8	Bishop[134]	
	141.9 ± 14.9	Satoh[126]	
	100–131	Gerdes[132]	location dependent
	113/127	Campbell[130]	female/male
	135 ± 5	Chen[131]	
myocyte cross-sectional area (μm^2)	100.0 ± 3.2	Yeves[135]	
	220 ± 25 283 ± 31	Chen[131]	female male
	140–244	Gerdes[132]	
	$214–257 \pm 25$	Campbell[133]	
	161-327	Campbell[130]	
myocyte aspect ratio (depth:width)	0.41	Satoh[126]	
	0.40–0.67	Kohl[136]	
	0.79	Gerdes[44]	
diffusion coefficient of water in myocardium ($10^{-3}\,mm^2\,s^{-1}$)	0.83 ± 0.05	Cooper[137]	25 °C
	1.8 ± 0.4 2.5 ± 0.5	Garrido[138]	parallel to surface, 37 °C perp. to surface
	0.55	Safford[139]	cat, 37 °C
	1.0/2.5 1.2/3.0	Seland[140] Seland[141]	intra/extra cellular, 37 °C intra/extra cellular, 37 °C
volume fraction myocytes (%)	85.17 ± 1.02	Anversa[142]	LV
	78.3 ± 0.6	Rossi[143]	
LV wall thickness (mm)	1.85 ± 0.33 1.73 ± 0.25	Kromen[127]	anterior LV segment lateral LV segment
	2.3 ± 0.2 3.5 ± 0.1	Chen[75]	diastole systole
	2.67 ± 0.05 2.38 ± 0.04	McAdams[128]	Sprague-Dewley rats Lewis rats
helix angles (°)	c.70 to −60	Chen[71]	
	c.80 to −80	Benoist[129]	
	c.90 to −90	Hales[10]	

3.4.1 Diffusivity

The diffusivity value which is needed for the model is the 'hindered' diffusivity, which takes into account the effect of intracellular barriers, rather than the 'restricted' diffusivity, which also takes the effect of cell membranes into account. The self-diffusivity of water is $2.0 \times 10^{-3}\,\mathrm{mm^2\,s^{-1}}$ at 20 °C, $2.3 \times 10^{-3}\,\mathrm{mm^2\,s^{-1}}$ at 25 °C and $3.0 \times 10^{-3}\,\mathrm{mm^2\,s^{-1}}$ at 37 °C [144]. Both the hindered and restricted diffusivity are lower than the self-diffusivity, with the restricted diffusivity lower than the hindered diffusivity due to the added effect of the cell membranes. The model is of ex vivo cardiac tissue and therefore to correspond with experimental data, which is typically carried out at room temperature, room temperature diffusivity should be used.

Most measurements of diffusivity in the literature are of the ADC from diffusion MRI and are therefore measures of restricted diffusivity. However, diffusion time will affect the amount of restriction measured and therefore ADC measured at a very short diffusion time will approximate the hindered diffusivity [145]. To allow comparison of diffusivity values made at different temperatures, it is useful to normalise the values to the self-diffusivity of water at that temperature (D_{norm}). Garrido et al. [138] measured ADC in rat hearts using diffusion-weighted (DW) imaging at 37 °C for a diffusion time of 7 ms, which is quite short and so will approximate hindered diffusion (D_{norm} 0.6 to 0.8). Safford at al.'s [139] measurements of cat myocardium used an Ussing diffusion cell and gave a D_{norm} of 0.25. Cooper et al. [137] used pulse gradient spin echo (PGSE) nuclear magnetic resonance (NMR) with a range of diffusion times to measure rat myocardium and found D_{norm} of 0.36. Seland et al. [140, 141] measured ADC in rat hearts at 37 °C to give D_{norm} of 0.3 to 1.0. The overall range of D_{norm} is from 0.25 to 1.0, which for a room temperature of 25 °C gives a diffusivity of 0.6×10^{-3} to $2.3 \times 10^{-3}\,\mathrm{mm^2\,s^{-1}}$. Diffusivity is discussed in more detail in Chapter 5.

3.5 Optimising the simulation parameters

There are two parameters which affect the accuracy, repeatability and speed of the simulations: the number of molecules and the length of the timestep. Increasing the number of molecules or decreasing the timestep increases the time taken to simulate the diffusion, as well as increasing the time for the files to be converted and the simulated MRI signal to be calculated. It is therefore desirable to minimise the number of molecules and number of timesteps. However, this must not compromise the accuracy and repeatability of the simulated data. If the number of molecules is too small, then the Gaussian approximation of the phase distribution will not hold in equation 3.2 which will affect the MRI signal simulated. In addition, if there are too few molecules then the stochastic effects will produce results which are too variable. If the timestep is too long then the stochastic effect of the step length will produce variable results. In the extreme case of a single timestep, each molecule will travel only in a single direction, except for where it collides with boundaries which effectively eliminates the modelling of Brownian motion.

Previous work has investigated the optimum number of molecules and timesteps. Hall and Alexander [98] modelled neuronal axons as cylinders of diameter 2 µm and investigated the effect of changing the number of molecules and the number of timesteps in their model. Increasing the number of molecules decreased the variability in the results, and for a fixed 'complexity' (number of molecules × number of timesteps), the error was minimised at 1×10^5 molecules and 1×10^3 timesteps. This corresponds to a timestep of 100 µs and a molecular density of 2×10^9 molecules/mm^3.

Lin et al. [103] also modelled an axon as a cylinder of diameter 2 µm and investigated the effect of changing the number of molecules and the number of timesteps, comparing the results to the analytical solution. They used a relative step length of 2 % to 14 % of the cylinder diameter, and numbers of molecules from 1×10^2 to 1×10^5. The deviation from the analytical solution decreased as the number

of molecules increased, but the step length had little effect. In their analysis of a more complex geometry, they used 1×10^6 molecules and a relative step length of 10 %, which equates to a timestep of 3.3 µs. They do not state the volume which they analyse and therefore the density of molecules is unknown.

It is interesting to note that although they are modelling very similar geometries, the optimal timestep chosen differs greatly between these two studies. Lin et al. [103] found the timestep has no effect on the results but they used short timesteps in comparison to the Hall and Alexander study [98]. The density of molecules is likely to be similar as Hall uses 100 cylinders and 1×10^8 molecules and Lin uses one cylinder and 1×10^6 molecules, although the length of the cylinder in the second one is unknown and there are some differences in their modelling methods. Both studies assume that there is no restriction to diffusion along the long axis of the cylinders.

The size of the step length varies considerably between studies, from 2 % of the diameter of the cylinder modelled [104], to 55 % of the diameter [98], other values used were 3 % [105], 9 % [106], 10 % [103], and 17 % [107], .

To assess the number of molecules and step length required to give accurate and repeatable results, I varied these parameters first for free diffusion, and then for a long thin cylinder.

3.5.1 Free diffusion

For free diffusion, the diffusion, and therefore the MRI signal, should be the same in all directions, within the limits of stochasticity. The expected MRI signal is calculated from:

$$S = S_0 \exp(-Db) \tag{3.14}$$

where S is the signal, S_0 is the reference signal, D is the diffusivity, and b is the b-value.

The accuracy of the simulation can therefore be assessed by comparing the simulated MRI signals to this value. The repeatability can be assessed from the variability of the MRI signal in the different directions.

In a volume of $300 \times 300 \times 300\,\mu m$, molecules were randomly and uniformly distributed across the model volume, and Smoldyn was used to simulate the diffusion of these molecules. Firstly, I changed the number of molecules while keeping the timestep constant at $100\,\mu s$. Secondly, for a constant number of molecules of 1×10^6, I simulated diffusion for different timesteps. I calculated the MRI signal from the central $100 \times 100 \times 100\,\mu m$ for the parameters shown in Table 3.3.

Table 3.3: Free diffusion optimisation parameters

parameter	value
b-value ($s\,mm^{-2}$)	1127 and 3985
diffusion interval, Δ (ms)	8 and 12
diffusion pulse duration, δ (ms)	3
gradient strength ($T\,m^{-1}$)	0.5 and 1.0
diffusivity ($mm^2\,s^{-1}$)	1.3×10^{-3}
number of molecules in 100 µm voxel	1×10^3, 1×10^4, 1×10^5 and 1×10^6
density of molecules (mm^{-3})	1×10^6, 1×10^7, 1×10^8 and 1×10^9
timestep (µs)	100, 50, 20, 10 and 5
number of gradient directions	30

The results of the effect of the number of molecules can be seen in Figure 3.3 and the effect of the timestep can be seen in Figure 3.4.

When the number of molecules is low the MRI signals have a high variability, even taking negative values when the b-value is high ($3985\,s\,mm^{-2}$). As the number of molecules increases, the MRI signals become less variable and all the signals are positive. The mean MRI signal is smaller than the analytical answer for all numbers of molecules for a b-value of $1127\,s\,mm^{-2}$, but close to the analytical answer for

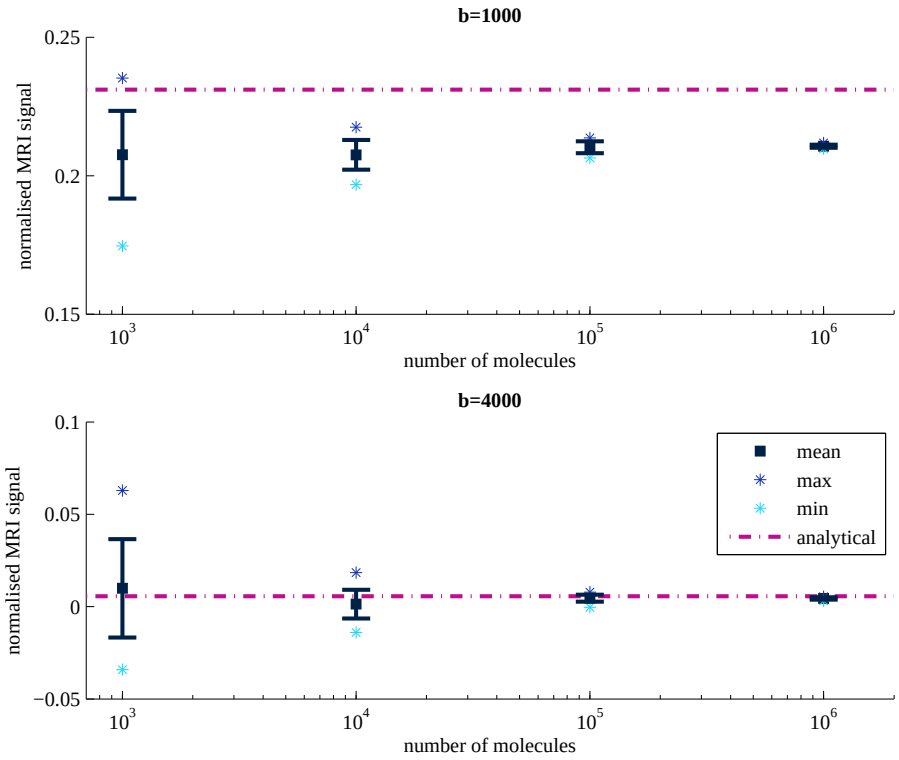

Figure 3.3: Effect of number of molecules on free diffusion MRI signals for b-value of $1127\,\mathrm{s\,mm^{-2}}$ (top) and $3985\,\mathrm{s\,mm^{-2}}$ (bottom).

a b-value of $3985\,\mathrm{s\,mm^{-2}}$. The MRI signal for a b-value of $1127\,\mathrm{s\,mm^{-2}}$ does not match the analytical answer well, however this is due to the long time step used in this analysis (100 µs). In Figure 3.4, the results for a timestep of 100 µs are poor, but the comparison with the analytical answer improves as the timestep is reduced.

Changing the timestep makes little difference to the MRI signal variability. For a b-value of $1127\,\mathrm{s\,mm^{-2}}$ the MRI signal is lower than the analytical answer at the longer timesteps of 50 µs and 100 µs. The simulated signal is close to the analytical signal for the timesteps of 5 µs, 10 µs and 20 µs. For a b-value of $3985\,\mathrm{s\,mm^{-2}}$, the simulated MRI signal is close to the analytical answer for all timesteps analysed her, and the variability does not change substantially.

Negative MRI signals are physically impossible and occur in the simulated data when the phase distribution does not approximate well to a Gaussian, which happens when the number of molecules is low and the signal is close to zero. The

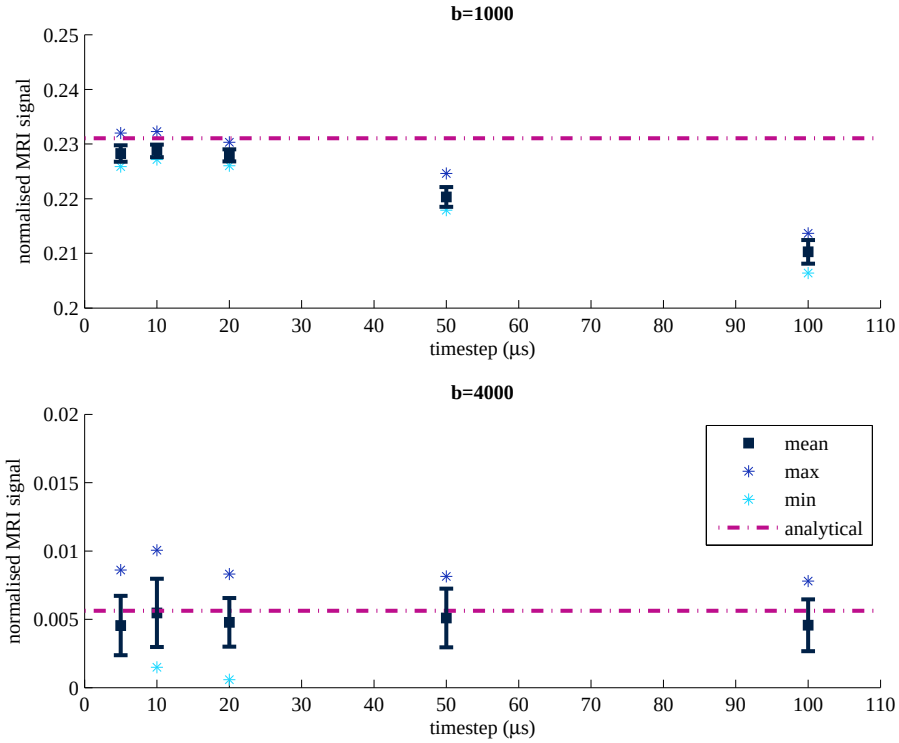

Figure 3.4: Effect of length of timestep on free diffusion MRI signals for b-value of $1127\,\mathrm{s\,mm^{-2}}$ (top) and $3985\,\mathrm{s\,mm^{-2}}$ (bottom).

number of molecules affects mainly the variability of the MRI signals, while the timestep affects the accuracy of the MRI signal. For free diffusion, a timestep of 20 µs and 1×10^5 molecules ($1 \times 10^8\,\mathrm{mm^{-3}}$) give a good compromise between accuracy and computational cost.

3.5.2 Narrow cylinder

As the size of the geometry decreases, the required timestep is likely to decrease as the probability of interactions between the molecules and surfaces increases. To test this, I simulated diffusion in a long thin cylinder. The cylinder has a diameter of 1 µm, which should be the narrowest size and therefore most extreme restriction likely to be encountered in any modelling of cardiac tissue. This cylinder is much smaller than the size of a myocyte but the spaces between myocytes and the pores in the phantom could be as small as this, so this is representative of the most restrictive geometry likely to be encountered. The cylinder is 500 µm long and I analyse the

central 400 µm so that there should be no restriction to diffusion along the long axis. The MRI signal in this direction should therefore be the same as for free diffusion. The MRI signal in the radial direction can be calculated from the following [119]:

$$\ln \frac{S}{S_0} = -2\gamma^2 G^2 \sum_{m=1}^{\infty} \frac{2D\alpha_m^2\delta - 2 + 2e^{-D\alpha_m^2\delta} + 2e^{-D\alpha_m^2\Delta} - e^{-D\alpha_m^2(\Delta-\delta)} - e^{-D\alpha_m^2(\Delta+\delta)}}{D^2\alpha_m^6(R^2\alpha_m^2 - 1)} \tag{3.15}$$

where R is the radius of the cylinder and α_m is the mth root of the Bessel function $J_1'(\alpha_m R)$.

I calculated the MRI signals for the parameters shown in Table 3.4.

Table 3.4: Narrow cylinder optimisation parameters

parameter	value
b-value ($\mathrm{s\,mm^{-2}}$)	1127
diffusion interval, Δ (ms)	8
diffusion pulse duration, δ (ms)	3
gradient strength ($\mathrm{T\,m^{-1}}$)	0.5
diffusivity ($\mathrm{mm^2\,s^{-1}}$)	1.3×10^{-3}
number of molecules	2×10^4, 5×10^4, 1×10^5 and 2×10^5
timestep (µs)	20, 10, 5, 2 and 1
number of radial gradient directions	8
number of axial gradient directions	1
number of repetitions	10

The results are shown in Figure 3.5. In both the axial and radial directions, the trend is for the variability of the MRI signals to decrease as the number of molecules increases. In the axial direction, the MRI signal is close to the analytical answer for timesteps of 1 µs and 2 µs, especially for 1×10^5 and 2×10^5 molecules. In the radial direction, the simulated MRI signal is higher than the analytical solution for the longer timesteps and becomes closer to the analytical answer as the timestep decreases. Timesteps of 1 µs or 2 µs for 1×10^5 or 2×10^5 molecules provide accurate results.

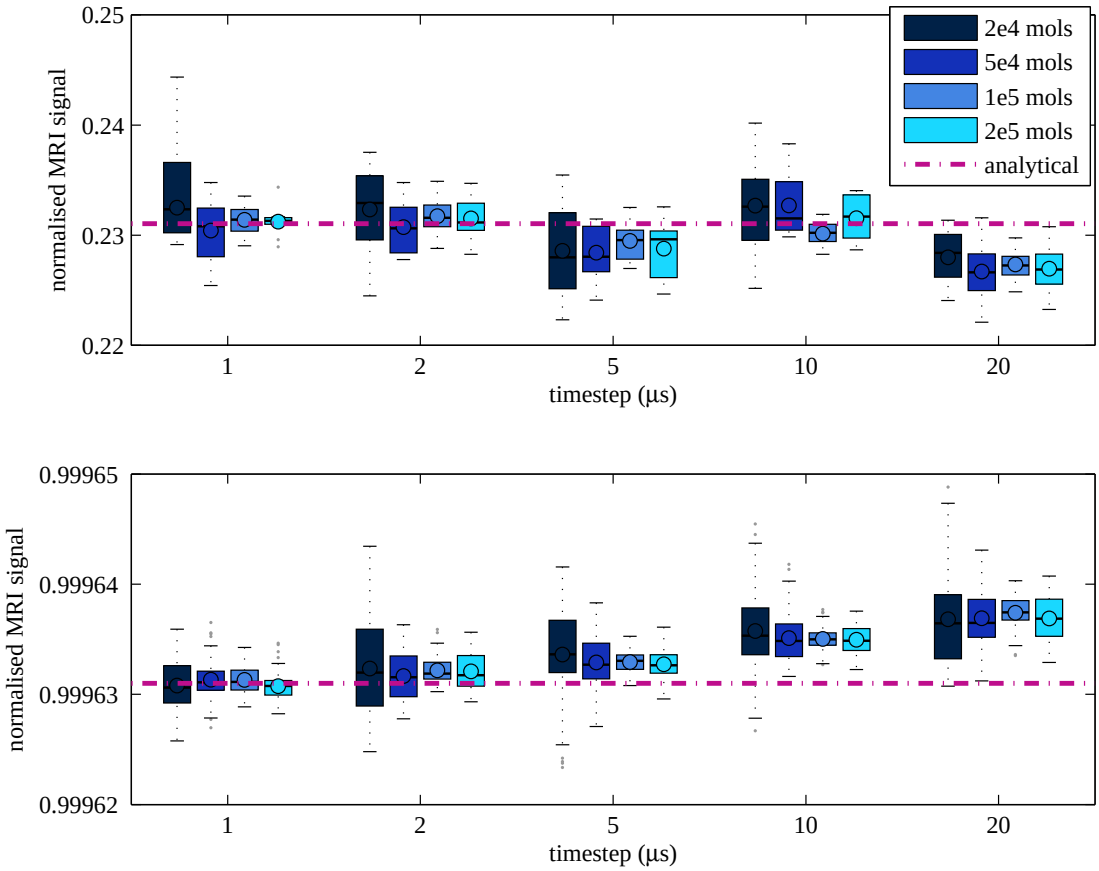

Figure 3.5: Effect of length of timestep and number of molecules on MRI signal in axial (top) and radial (bottom) directions in a cylinder.

3.5.3 Chosen parameters

For both free diffusion and diffusion in a narrow cylinder, the number of molecules affects the repeatability while the timestep affects the accuracy of the MRI signal. From the cylinder results, a timestep of 2 µs is sufficiently small to give accurate results and so this will be used. 1×10^5 molecules gives good repeatability for both the cylinder and free diffusion. Although the accuracy is likely to depend primarily on the number rather than the density of molecules in a simple geometry, in more complex geometry the density may be important and so a density of 1×10^8 molecules/mm^3 (the equivalent of 1×10^5 molecules in the free diffusion study) will be used for all the studies in this thesis.

3.6 Sensitivity analysis

3.6.1 Background

A sensitivity analysis measures the effect of changes in the input parameters on the output of a model. It enhances understanding of the model by revealing the parameters which have the greatest effect on the output.

The simplest type of sensitivity analysis is the one-at-a-time method where all but one of the input factors is kept at a baseline value. That input factor is then changed and its effect on the outcome analysed using linear regression or partial derivatives. The major disadvantage of this method is that it doesn't model interactions between input variables.

Variance methods are the most thorough type of sensitivity analysis. They allow for non-uniform distribution of input factors, are model independent (i.e. there is no assumption of linearity) and consider interactions between factors. However, the number of simulations required to achieve this is at least a few hundred times the number of input factors [146]. The input space is densely sampled, and the model run for each of these sets of input parameters. The variance of the output is decomposed to give the variance related to each input factor. The result is a percentage assigned to each individual input factor, as well as each combination of input factors, which quantifies how much of the output variance of the model is dependent of that input or group of input. It is also possible to calculate a total effect for each input factor, which includes its interactions with other inputs. This allows a very thorough, and quantitative, understanding of the model, but requires considerable computational time.

The Morris method [147] is a simple and economic type of sensitivity analysis, which screens the input factors to determine which are the most important, and was therefore chosen for this study. It takes interactions of factors into account and is model independent. It assumes no stochasticity in the model, which is not true

for this model. However, the variation due to stochasticity is much smaller than that due to the changes in the input factors and so this is not a significant problem. It produces two sensitivity measures for each input factor: μ is the estimated mean of the elementary effects and estimates the overall effect of the factor on the output, and σ is the standard deviation of the elementary effects and estimates non-linear effects and interactions with other factors. Campolongo et al. [148] introduced a modified version, μ^*, which uses absolute values and avoids effects of opposite signs.

3.6.2 Methods

I generated and analysed Modified Morris method [148] parameters using the Matlab (Mathworks, USA) code of [149]. The modified Morris method takes a model with an output y and k inputs $x_1, x_2, ...x_k$ which are collectively in the k-element vector $\mathbf{x}$. Each input is allowed to take one of p levels within its range of possible values, where the levels are $\{0, 1/(p-1), 2/(p-1), ...1\}$. The inputs are assumed to be uniformly distributed between 0 and 1, and these values are later transformed to their actual values.

A number of individual randomised one-at-a-time experiments are carried out. At each of these, one input is changed to another level, while the others are kept constant. The elementary effect from one of these experiments is:

$$d_i(\mathbf{x}) = \left(\frac{y(x_1, ...x_{i-1}, x_i + \Delta, x_{i+1}, ...x_k) - y(\mathbf{x})}{\Delta} \right) \tag{3.16}$$

where Δ is a multiple of $1/(p-1)$

The number of simulations required for the original Morris method is $2kr$, where r is the number of times each input parameter is changed to another level. The Campolongo method improves the Morris method by selecting from many possible experiments those which mean each input has the most even spread across the

levels. This allows fewer simulations to be done compared with the original Morris version ($r(k+1)$), and has a better scan of the input space.

Once the input values for each experiment are determined, the model simulations are run with those parameters. The elementary effects for each simulation are then combined to give the two parameters, μ^* and σ. For each parameter, k,

$$\mu^* = \sum_{i=1}^{r} \frac{|d_i|}{r} \tag{3.17}$$

$$\sigma = \sqrt{\sum_{i=1}^{r} \frac{(d_i - u)^2}{r}} \tag{3.18}$$

I used the model as described in Section 3.4. I analysed a single cubic voxel with sides of 100 µm; the total modelled volume is a cube with sides of 300 µm. The density of molecules is $1 \times 10^8\,\mathrm{mm}^{-3}$. The six model inputs are cross-sectional area, length, aspect ratio, volume fraction, rate of angle change and diffusivity; the minimum and maximum values for the sensitivity analysis are in Table 3.5 and are chosen to reflect the wide range of values available in the literature. I carried out the sensitivity analysis for five model outputs: the three eigenvalues (λs), mean ADC and FA.

Table 3.5: Sensitivity analysis input parameters

parameter (units)	abbreviation	min. value	max. value
cross-sectional area ($\mu\mathrm{m}^2$)	CSA	100	300
length (µm)	L	90	150
aspect ratio [depth/width]	AR	0.33	1.00
volume fraction of myocytes	VF	0.75	0.90
helix angle range ($^\circ\,\mathrm{mm}^{-1}$)	ANG	50	100
diffusivity ($10^{-3}\,\mathrm{mm}^2\,\mathrm{s}^{-1}$)	DIF	0.5	2.5

Table 3.6: Sensitivity analysis MRI sequence parameters and results

simulation						
study no.	δ ms	Δ ms	G $\mathrm{T\,m^{-1}}$	b-value $\mathrm{s\,mm^{-2}}$	mean ADC range (mean) $1 \times 10^{-3}\,\mathrm{s\,mm^{-2}}$	FA range (mean)
1	2.0	7.0	0.9	1474	0.37 to 1.62 (0.83)	0.13 to 0.60 (0.30)
2	2.0	7.0	0.7	888	0.37 to 1.69 (0.85)	0.13 to 0.62 (0.30)
3	2.0	7.0	0.5	453	0.37 to 1.74 (0.86)	0.12 to 0.62 (0.30)

I used the MRI sequence parameters shown in Table 3.6. I used a b-value of $1474\,\mathrm{s\,mm^{-2}}$ (experiment 1 in Table 3.6), which is in the typical range used in ex vivo DT experimental data. To determine whether the b-value affects the sensitivity analysis, I reassessed the Morris method with 2 further b-values (453 and $888\,\mathrm{s\,mm^{-2}}$) (experiments 2 and 3 in Table 3.6).

I chose the Morris Method settings of $r = 8$, $p = 4$ as these are similar to the values shown in the literature to give good results [146]. This meant that 56 simulations were required.

3.6.3 Results

Figure 3.6 shows the sensitivity analysis results for the b-value of $1474\,\mathrm{s\,mm^{-2}}$. Parameters with a large μ^* (along the x-axis) have a large effect on the output of the model, those with a large σ have non-linear effects or interactions with other parameters. For all three λs, mean ADC and FA, the diffusivity is the most important factor as reflected by its large μ^* value. The σ is small so there is primarily a linear effect with little interaction with the other factors. For λ_2, λ_3, FA and mean ADC, the cross-sectional area is the next most important factor. The aspect ratio is important for λ_2, λ_3 and FA. The length, angle rate and volume fraction have only very small effects on all the outcomes.

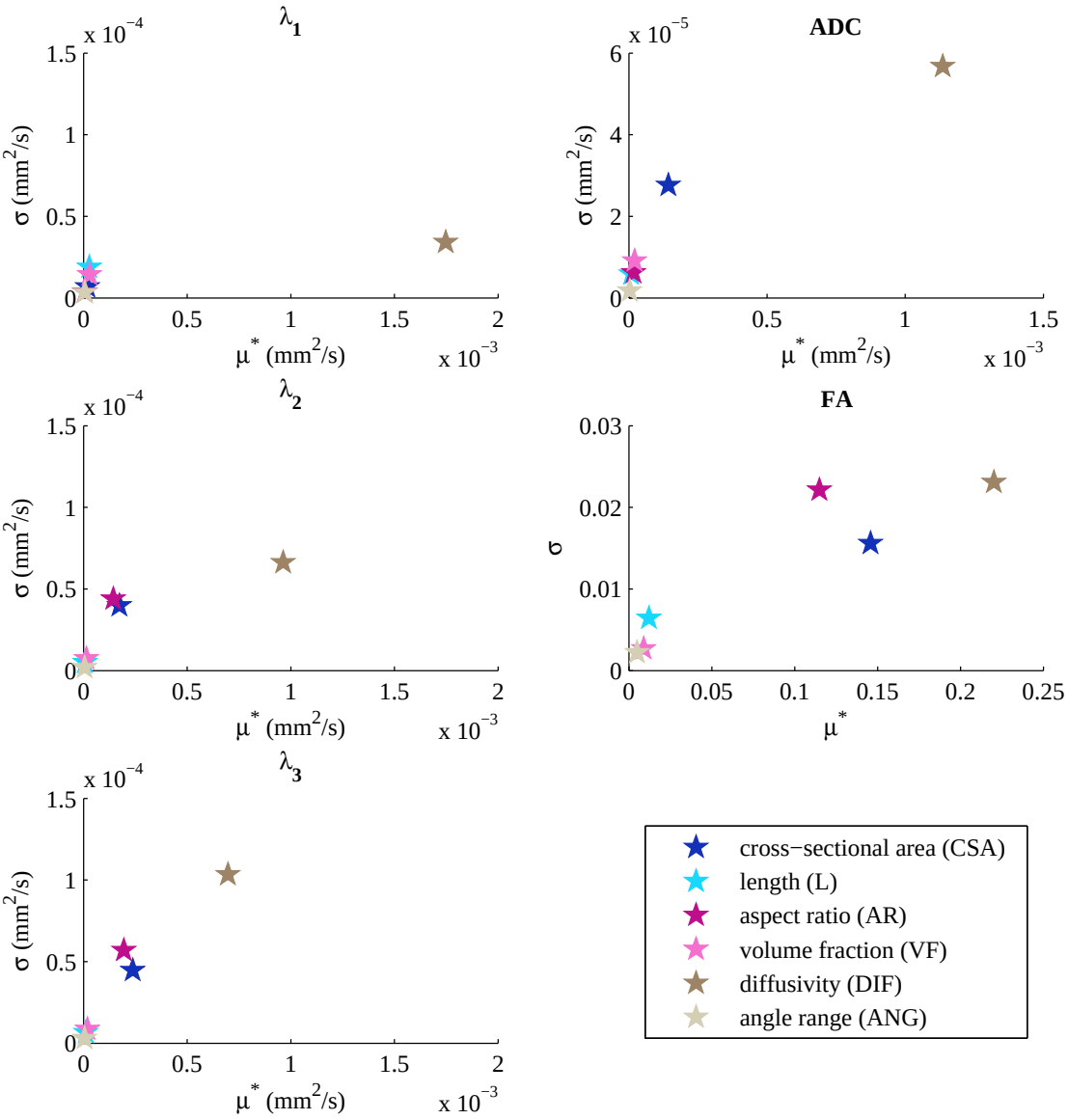

Figure 3.6: Sensitivity analysis results for λ_1, λ_2, λ_3 (left, top to bottom), mean ADC (right, top) and FA (right, middle). μ^* estimates the overall effect of the factor; σ estimates non-linear effects and interactions with other factors

The sensitivity analysis results for different b-values are in Figure 3.7 and are all very similar. For the mean ADC, DIF is always the most important factor by a large amount, followed by CSA. For the FA, the order of DIF, CSA, and AR is constant across all b-values. The range of mean ADC and FA values generated are in Table 3.6 and are similar for all three analyses.

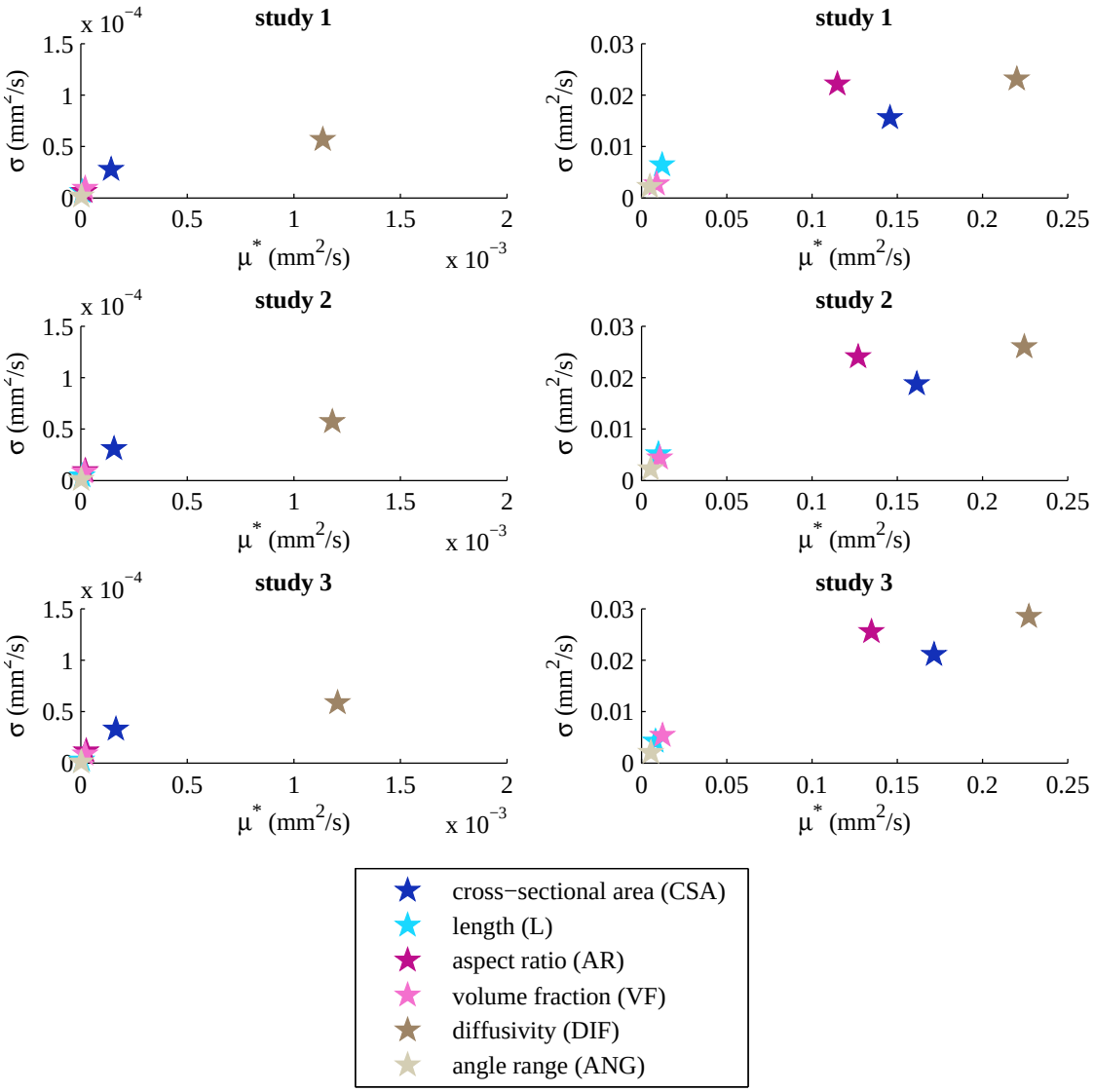

Figure 3.7: Sensitivity analysis results for mean ADC (left) and FA (right) for the different acquisition parameter sets from Table 3.6. Study numbers 1 to 3 from top to bottom . μ^* estimates the overall effect of the factor; σ estimates non-linear effects and interactions with other factors

3.6.4 Discussion

The aim of this sensitivity analysis was to determine which of six factors concerning simplified cell shape and tissue structure have the greatest influence on cardiac DTI results. This is important for two reasons: firstly, as there is a large range of values in the literature for each parameter, it allows us to understand for which parameters the choice of value is critical to the model output. Secondly, as these parameters may change with pathology, it helps understand the effect of pathological

changes in microstructure in dMRI signals, and design MRI sequences that respond to changes in particular parameters.

The diffusivity was by far the most important factor, especially for the λ_1 and the mean ADC. As the diffusivity increases, the mean squared displacement of water in a given time increases thus increasing the λs. In free space, this would be a linear relationship, but in the restricted case, as the step distance increases, the likelihood of interaction with a surface (cell membrane) increases, resulting in reduced phase dispersion and apparent diffusivity. As cardiac myocytes are long narrow structures, these interactions tend to preferentially decrease λ_2 and λ_3, compared to λ_1, in a non-linear manner.

The cross-sectional area has an effect on λ_2 and λ_3, the mean ADC and the FA, although its effect is much smaller than the diffusivity. A smaller cross-sectional area leads to an increase in molecule-surface interactions which will decrease the mean squared displacement within the cross-sectional plane and therefore λ_2 and λ_3. The aspect ratio has a similar importance as the CSA for the λ_2 and λ_3, and the FA. A smaller aspect ratio (greater difference between thickness and width) will cause a greater difference in the diffusion in the direction of the thickness compared with the width and hence a larger λ_2 and smaller λ_3 for the same CSA, and a higher FA.

The length, volume fraction and rate of helix angle change have negligible effects on all three λs. The VF changes the size of the gaps between cells in the simulation but even though this makes the extra-cellular space more restrictive than the intra-cellular space, since the proportion of extra-cellular space is small, changes in the VF do not significantly affect the DT. Since the cells are much longer than they are wide or thick, molecule-surface interactions with the ends of the cells are infrequent compared with those with the sides and hence the length does not have a large effect on the results. The angular differences within a single voxel are small, and therefore the ANG has little effect.

There is very little difference in the ranking order of importance of the factors as the b-value changes, and the values of μ^* and σ remain similar.

There are a wide range of values available for the diffusivity in the literature since the diffusivity is dependent on the measurement technique and the temperature, so different diffusivity values would be needed for ex vivo and in vivo simulations. Since the diffusivity has such a dominant effect on measurements, this uncertainty is a significant limitation to the model. However, since the σ is low, there is little non-linearity or interaction with other factors and therefore the relative results of simulations should not be affected significantly by the diffusivity. Diffusivity is assumed to be a single value, which is the same in all directions within the cell and outside it. Intracellular structures and the extracellular matrix will affect the rate of diffusion. This may not be the same intra and extra cellularly, as suggested by Seland et al. [140], nor the same in each direction in the cell. Disease may affect the intra and extra cellular environments and thus the diffusivity. Experimental investigation of these effects, especially in pathology, would enhance the model and the understanding of DTI in disease. The importance of diffusivity revealed in this Chapter motivated a further analysis of this parameter, and in particular of the differences between intra- and extracellular values. This work is presented in Chapter 5.

3.7 Summary of chapter

In this chapter I present a simplified model of heart microstructure which is used to simulate dMRI signals. The intended purpose of this model is to explore the relationship between changes in cardiac microstructure and the dMRI signal.

Assessment of the optimal simulation parameters for free and highly restricted diffusion shows that the timestep is more important for accuracy than the number of molecules, but the number of molecules is more important for variability.

The chosen parameters for the rest of the studies were a timestep of 2 µs and 1×10^8 molecules/mm^3.

A sensitivity analysis of the model showed that the diffusivity was by far the most important factor affecting the FA and the mean ADC. The cross-sectional area of the cells was the next most important factor, with the aspect ratio of the cross-section also affecting the FA.

4

The model: validation against ex vivo heart and phantom data

In Chapter 3 the model was presented and its sensitivity to the input parameters explored. In this chapter, the model outputs are compared with experimental data from five ex vivo rat hearts. MRI sequence parameters are systematically explored to analyse the effect of changes in the b-value and its components on the results. As described in Chapter 2, the diffusion weighting (b-value) is dependent on both the gradient strength and the diffusion time. In the analyses here I vary both factors to assess the response of the model compared with the experimental data. I then model a phantom and compare the simulated results to the experimental phantom results to further test the modelling method.

A brief comparison of the model to ex vivo heart data formed part of my presentation at the Functional Imaging and Modelling of the Heart (FIMH) conference in Maastricht in June 2015 and this was published in Lecture Notes in Computer Science [116]. This comparison to the ex vivo heart data forms part of a journal article which I submitted to the IEEE Transactions in Medical Imaging, where it is currently under review.

4.1 Validation against ex vivo hearts

4.1.1 Methods

Experimental data acquisition

Colleagues in the Radcliffe Department of Medicine at the University of Oxford provided me with the experimental data which I then analysed.

Hearts from five healthy Sprague-Dawley rats were isolated, fixed with isosmotic Karnovsky's fixative with 2mM gadolinium (Gd) (Prohance, Bracco, MN, USA), rinsed and embedded in 1 % agarose gel comprising phosphate buffered saline (PBS) and 2mM Gd [150]. Experimental investigations conformed to the UK Home Office guidance on the Operations of Animals (Scientific Procedures) Act 1986 and were approved by the University of Oxford's ethical review board.

Two datasets were acquired. For the first, which I used to investigate the effect of gradient strength, diffusion spectrum imaging (DSI) data were acquired using a 3D fast spin echo sequence, on a 9.4T horizontal bore MRI scanner (Agilent, CA, USA) with shielded gradients, using a transmit/receive quadrature-driven birdcage coil (inner diameter = 20 mm; Rapid Biomedical, Rimpar, Germany) with the parameters in Table 4.1. The total number of gradient directions was 257 over 22 different b-values, with between 3 and 24 gradient directions per b-value. The MRI sequence timings were kept constant for all b-values, so the b-value was altered only by the gradient strength.

A second 3D echo planar diffusion tensor imaging (DTI) dataset was acquired, which I used to assess the effect of diffusion time. For this dataset, there were four different diffusion intervals (Δ) at each of five different b-values. For simplicity, I will refer to Δ as the diffusion time from now on. Since the b-value is dependent on diffusion time, when the diffusion time was increased for a fixed b-value, the

gradient strength was decreased. These parameters are all shown in Table 4.2. The full parameters are shown in Table 4.1.

Table 4.1: DTI sequence parameters for simulated and experimental rat heart tissue. Differences between simulation and experimental parameters are explained in the text.

	Dataset 1 effect of gradient strength		Dataset 2 effect of diffusion time	
	expt	sim	expt	sim
diffusion pulse duration, δ (ms)	5		2.5	
diffusion interval, Δ (ms)	9		10 to 40	
b-value ($\mathrm{s\,mm^{-2}}$)	400 to 10 000		400 to 6400	
gradient strength ($\mathrm{T\,m^{-1}}$)	0.17 to 0.87		0.15 to 0.88	
voxel size ($\mu\mathrm{m}^3$)	200×200×200		500×500×500	
timestep (µs)		2		2
number of molecules in voxel		8×10^5		1.25×10^7
directions per b-value	3 to 24	100	6	100
SNR	91	127	52 to 69	60
TR/TE (ms)	250/15		250/10	
echo train length	8		16	
field of view (mm)	20×16×16		20×16×16	
matrix	100×80×80		40×32×32	
non-DW images	4		5	
acquisition time (hours)	14:30		1:20	

Table 4.2: Experimental dataset 2: gradient strength ($\mathrm{T\,\mu m^{-1}}$) for each diffusion time and b-value. The combination of $\Delta = 10\,\mathrm{ms}$ and b-value $= 6400\,\mathrm{s\,mm^{-2}}$ is not carried out as it requires a gradient strength beyond the capabilities of the MRI scanner.

	b-value ($\mathrm{s\,mm^{-2}}$)				
Δ (ms)	400	800	1600	3200	6400
10	0.31	0.44	0.62	0.88	n/a
20	0.22	0.31	0.43	0.61	0.86
30	0.18	0.25	0.35	0.50	0.70
40	0.15	0.21	0.30	0.43	0.60

Experimental data analysis: segmentation

For the first dataset, a colleague in the Radcliffe Department of Medicine, Dr Darryl McClymont, manually defined a 3D region of interest (ROI) within the left ventricle, with reference to high-resolution anatomical images. When defining the region, Dr McClymont took particular care to avoid regions containing buffer, gel or residual blood, thus avoiding the unwanted influence of these non-representative areas. The ROIs had a volume of at least 1.6 mm^3 (200 voxels) and I used them for the analyses of both the MRI signals and the diffusion tensors (DT).

Due to the poorer spatial resolution of the second dataset, I segmented the heart from the background by thresholding on the non-diffusion weighted (b0) image and analysed the whole heart for all the analyses.

Experimental data analysis: MRI signals

For both datasets, I normalised the diffusion-weighted MRI signal for each voxel by dividing by the reference S_0 signal in that voxel.

For the first dataset, I analysed the MRI signals in two ways. Firstly, I calculated the mean, median and interquartile range of the normalised MRI signals across all the voxels and gradient directions for individual b-values. The b-values were 800, 2000, 3200, 4400, 5600 and 8000 $\mathrm{s\,mm}^{-2}$, as they were evenly spaced and there were at least 6 gradient directions at each of these b-values.

Secondly, to give a more detailed analysis, I analysed the MRI signals in the directions of the DT's eigenvectors. Since the DSI gradients are in a grid layout aligned with the co-ordinate system axes, there are five b-values acquisitions along each of the co-ordinate axes (400, 1600, 3600, 6400 and 10 000 $\mathrm{s\,mm}^{-2}$). Since these are the directions in which the largest number of aligned acquisitions are available, I wanted to find voxels where the DT aligned with the co-ordinate axes and hence these gradient directions. I calculated the DT for all voxels for all

b-values up to 3000 s mm^{-2}. I then identified all voxels where the eigenvectors of the DT aligned to within 8° of the co-ordinate system axes, and took the largest connected volume of voxels with this alignment, to avoid isolated coincidences that might be caused by noise or imaging artefacts. I averaged the MRI signals for the gradient directions along the co-ordinate system axes over all those voxels for each b-value. I chose the value of 8° to give sufficient number of voxels per direction for the analysis (24-90 voxels per b-value per heart), while keeping the alignment of the eigenvectors to the gradient directions fairly close.

For the second dataset, for each combination of diffusion time and b-value, I analysed the normalised MRI signals over all voxels and gradient directions.

Experimental data analysis: DT

For the first dataset, I divided the data up into sets of similar b-values with at least 20 directions in total, and carried out DT analysis using the linear fitting method.

For the second dataset, for each combination of diffusion time and b-value, I carried out the DT analysis, again using the linear fitting method.

From the DT, I calculated the mean apparent diffusion coefficient (ADC) and fractional anisotropy (FA).

Simulated data generation

I used the model as described in Chapter 3, with the model parameters in the mid-range of published values, as listed in Table 4.3. The total simulation size was 700 µm to match the isotropic voxel size for the 2nd dataset of 500 µm plus a boundary of 100 µm along each edge. For both datasets, I chose the settings for the simulations to match the settings for the experimental data: these are listed in Table 4.1.

Table 4.3: Model parameters used for comparison with experimental data. The angle rate is calculated as the ratio of the helix angles to the LV wall thickness.

parameter	abbreviation	units	mid value
cross-sectional area	CSA	μm^3	200
length	L	μm	120
aspect ratio (thickness/width)	AR		0.67
volume fraction of myocytes	VF		0.825
diffusivity	DIF	$mm^2\,s^{-1}$	1.5×10^{-3}
helix angle rate	ANG	$^\circ\,mm^{-1}$	75

For the comparison with the first experimental dataset, for the analysis of the MRI signals in the directions of the eigenvectors of the diffusion tensor, I calculated the DT of the simulated data using all of the gradient directions. I then calculated the MRI signals in the directions of the eigenvectors of this DT.

For the comparison with both experimental datasets, for the analysis of the MRI signals over all voxels and directions, I increased the number of gradient directions compared with the experimental data. This is to mimic the experimental variation of gradient directions in relation to the microstructure. For the experimental data I analysed the MRI signals over all of the gradient directions and all of the voxels, each of which will have had a different microstructure and orientation of that microstructure compared with the gradient directions. In the simulation, there was only a single voxel, so only one microstructure. I used 100 directions, which I found gave stable results.

For the comparison with the first dataset, I used the same b-values for the analysis of the MRI signals. For the analysis of the DT, I used evenly-spaced b-values within the same range to the experimental data. The b-values for the experimental data are not evenly spaced, especially once combined into datasets with similar values and so I chose to simplify the analysis by not mimicking this exactly.

For the comparison with the second dataset, I used exactly the same parameter

values as the experimental data, apart from the number of gradient directions as discussed above.

Simulation of noise

I added noise to the simulated data using a Rician noise model [151]:

$$S = |S^* + N_1 + iN_2| \tag{4.1}$$

where S is the noisy MRI signal and S^* is the noise-free MRI signal. N_1 and N_2 are random numbers taken from a normal distribution with a mean of 0 and a standard deviation of 1/SNR (signal to noise ratio). For noisy simulations, I added noise to the noise-free signal to give noisy MRI signals for 100 repetitions, which was shown in initial experiments to give stable results. For each repetition, I then calculated the DT; the mean and standard deviation over all the repetitions is reported.

I matched the SNR for the simulations to that measured in the b0 experimental data. For the effect of gradient strength data, the absolute noise level in the b0 scan was higher than in the diffusion-weighted scans: 350 compared with 250 (units = MRI signal intensity). I therefore increased the SNR in the simulated data from 91 to 127 to give appropriate absolute noise levels ($91 \times 350/250 = 127$).

4.1.2 Results

The experimental results from the five hearts were very similar, as seen in Figure 4.1, and I therefore averaged them for clarity when assessing the results.

MRI signals

Figure 4.2 shows the effect of changing the b-value by gradient strength on the MRI signals for the simulated and experimental data. The mean, median and inter-quartile range are similar for the simulated and experimental data across the

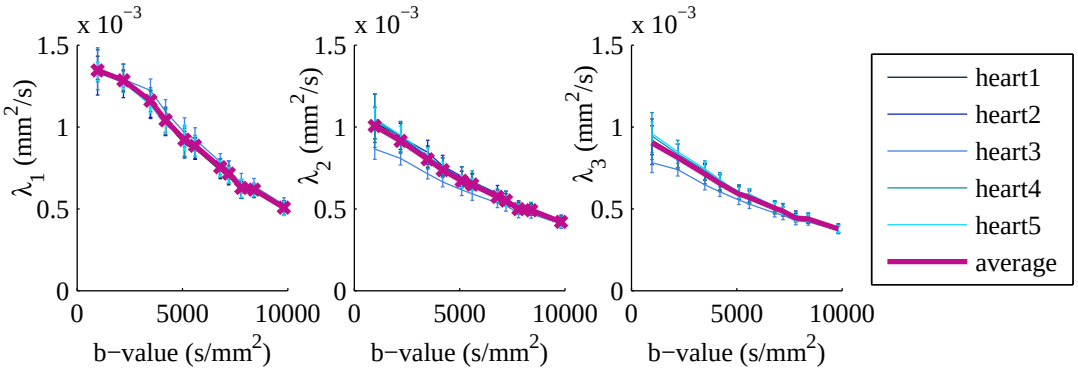

Figure 4.1: Experimental data consistency. Eigenvalues from each of the five hearts analysed for the effect of gradient strength. Each heart's data is the average of all voxels within the ROI, errorbars are the standard deviation. The average of all 5 hearts is shown in pink.

whole range of b-values, and show a similar decrease as the b-value increases. The simulated data has fewer very small values than the experimental data. In the simulations the mean is larger than the median; the experimental mean and median are more similar and the experimental median is higher than the simulated data at higher b-values. Adding noise to the simulated data has little effect at the lower b-values, but at the higher b-values it increases the mean and median, improving the match with the experiments, and leads to more outliers.

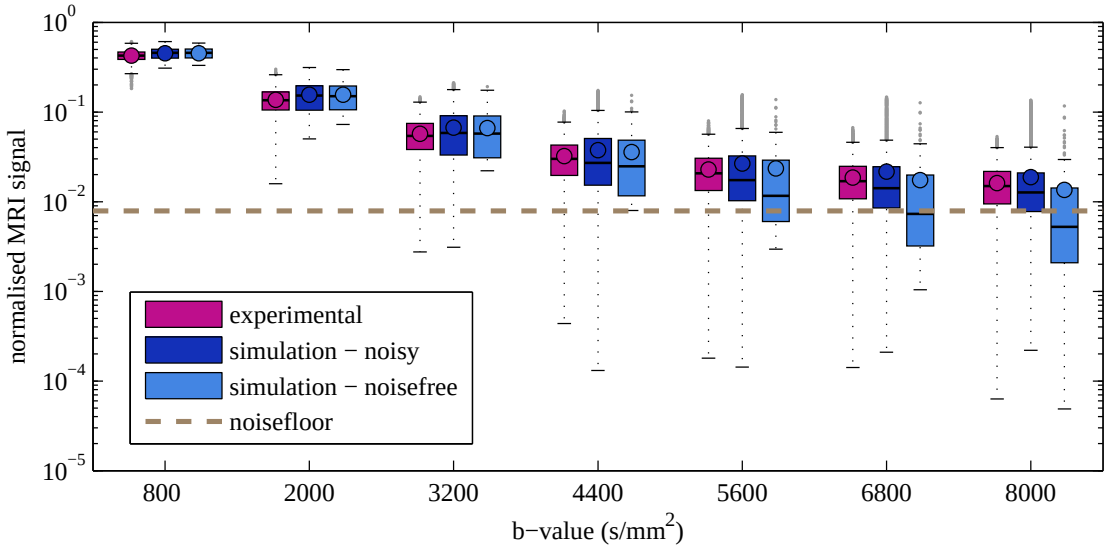

Figure 4.2: Effect of gradient strength on MRI signals. b-value changed by gradient strength. Boxes are inter-quartile ranges with the median as a horizontal line and the circle indicating the mean; whiskers are 1.5 times the interquartile range, and outliers are beyond that. Dashed line indicates the approximate noise floor.

Figure 4.3 shows the effect of changing the diffusion time on the MRI signals for the simulated and experimental data for a fixed b-value. As the diffusion time increases the MRI signal increases for the same b-value. The simulated signal intensities are higher than the experimental data and appear to increase more quickly as the diffusion time increases. Figure 4.4 shows the effects in more detail for the middle b-value of $1600\,\mathrm{s\,mm^{-2}}$. For the shortest diffusion time, the mean, median and inter-quartile range of the MRI signals are very close to the experimental data. The mean, median and inter-quartile range increases slightly for the experimental data as the diffusion time increases; the simulated data also increase but more quickly. The addition of noise leads to more extreme outliers, but has no other marked effect.

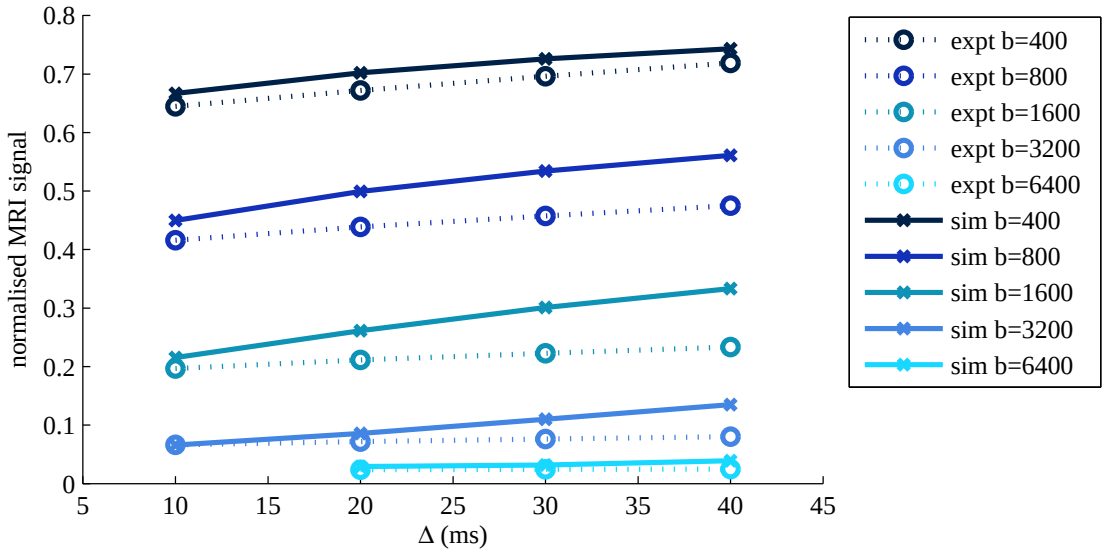

Figure 4.3: Effect of diffusion time on MRI signals for simulated (solid lines) and experimental (dotted lines) data.

Figure 4.5 shows the effect of changing the b-value by gradient strength on the MRI signals in the directions of the eigenvectors of the DT for the simulated and experimental data. The noisy simulated signals in the direction of the primary eigenvector are very similar to the experimental data. The simulated signals in the directions of the secondary and tertiary eigenvectors are higher than the experimental data, but decrease in a similar manner with b-value. The addition of noise has little effect on the simulated signals in the secondary and tertiary direction, but increases the signal at higher b-values in the primary direction.

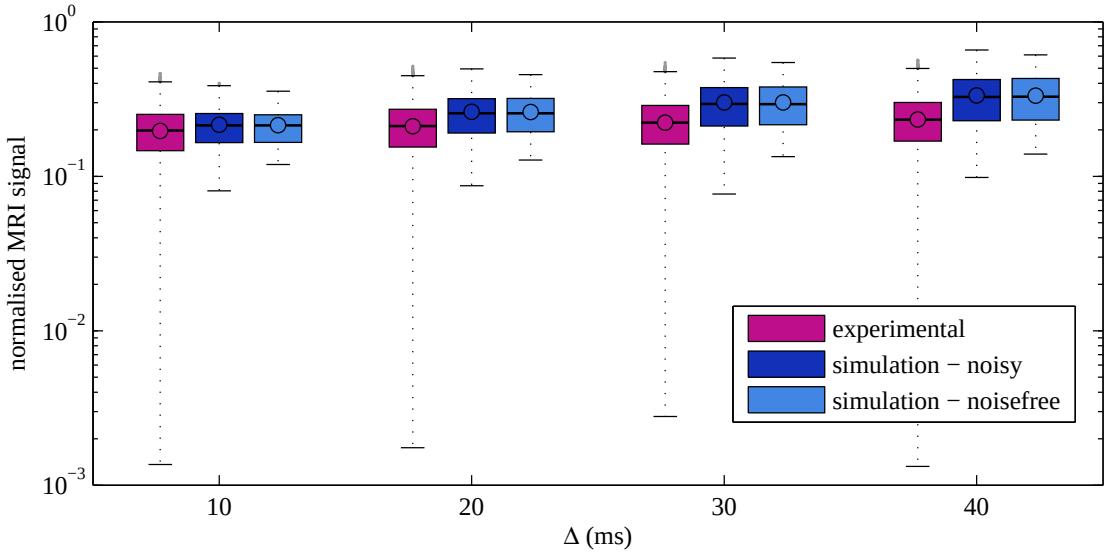

Figure 4.4: Effect of diffusion time on MRI signals for experimental and simulated data for a b-value of 1600 s mm^{-2}. Boxes are inter-quartile ranges with the median as a horizontal line and the circle indicating the mean; whiskers are 1.5 times the interquartile range, and outliers are beyond that.

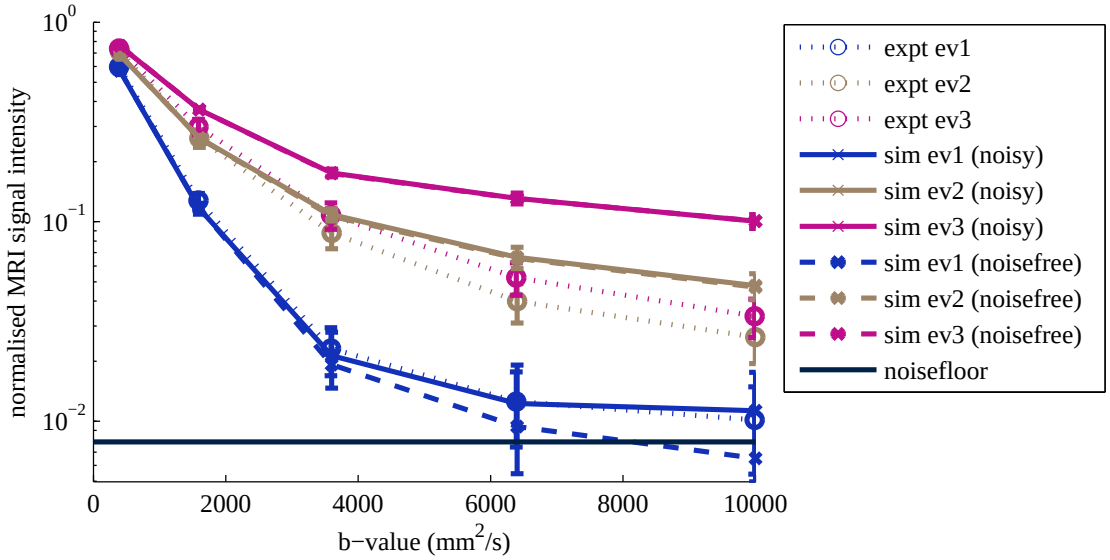

Figure 4.5: Effect of gradient strength on MRI signals in eigenvector directions. B-value changed by gradient strength. MRI signals in the directions of the eigenvectors (ev) of the DT for experimental (dotted line), noisy simulated (solid line) and noisefree simulated (dashed line) data. Solid pink line indicates the approximate noise floor. Colours are used to differentiate primary (ev1, blue), secondary (ev2, beige) and tertiary (ev3, pink) eigenvector directions.

Diffusion tensor and derivatives

Figure 4.6 shows the experimental and simulated results for the effect of b-value by gradient strength on the eigenvalues (λs), the mean ADC and the FA. The experimental and simulated λs have similar values, and decrease in a similar pattern with increasing b-value. λ_1 is higher, and λ_2 and λ_3 are lower, for the noisy simulated data than the experimental data, leading to a good estimation of the mean ADC in the simulated data, and an overestimation of the FA. The noisy simulated FA decreases more rapidly than the experimental FA at the higher b-values.

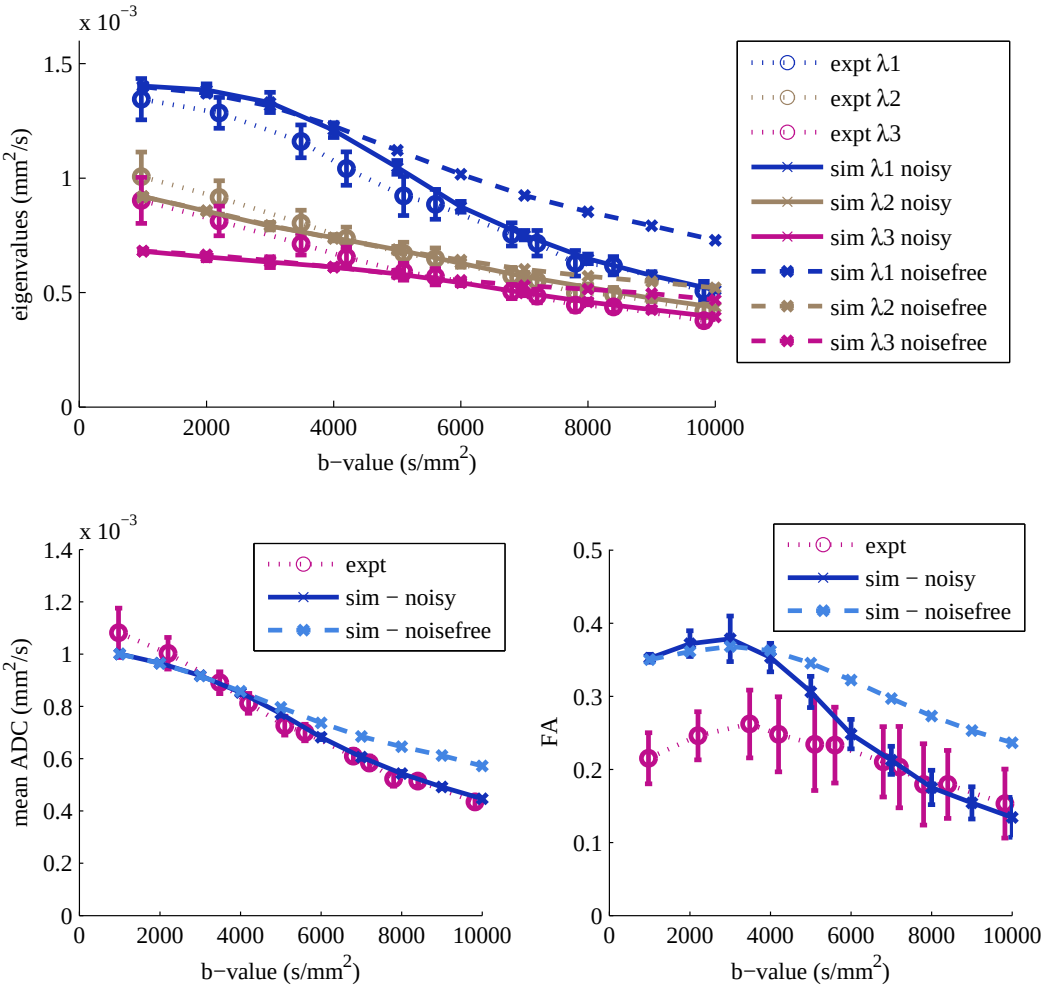

Figure 4.6: Effect of gradient strength on DT. b-value changed by gradient strength. λs (top), mean ADC (bottom left) and FA (bottom right). Noisy/noisefree simulated (solid/dashed lines) and experimental (dotted lines) data. Data points are mean values over all voxels and all hearts (expt), and all repetitions (sim). Colours are used to differentiate λ_1 (blue), λ_2 (beige) and λ_3 (pink). Error bars are ± 1 sd

Figure 4.7 shows the effect of the diffusion time on the λs of the diffusion tensor, the mean ADC and the FA for the simulated and experimental data for a b-value of 1600 s mm^{-2}. All of the experimental and simulated λs decrease as the diffusion time increases. λ_1 is very similar between the experimental and simulated data; the simulated λ_2 and λ_3 are lower than the experimental ones and decrease more rapidly. The mean ADC is lower for the simulation than the experiments and decreases more quickly. The FA is higher for the simulation than the experiments and increases more quickly. Similar results were seen for the other b-values.

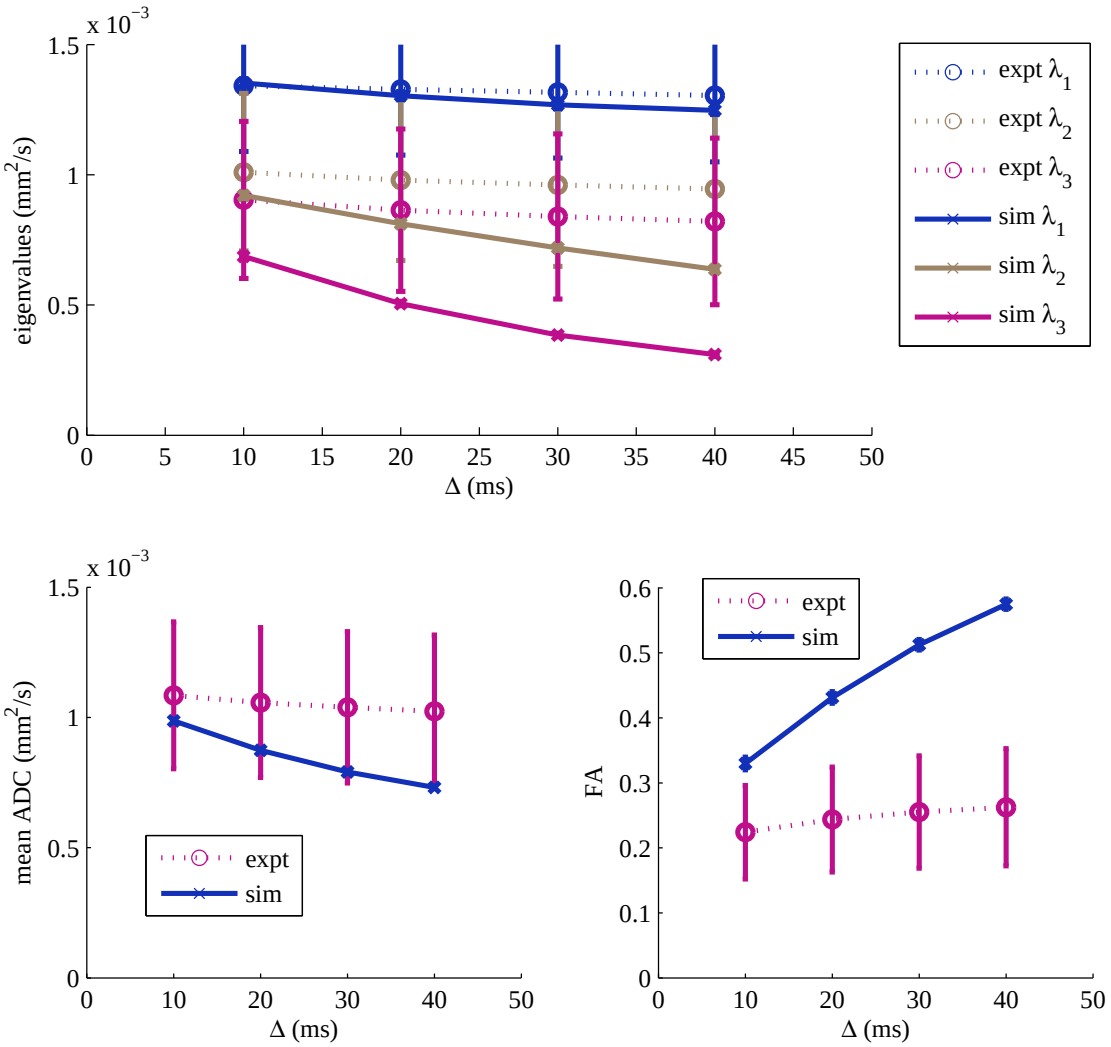

Figure 4.7: Effect of diffusion time on DT. λs (top), mean ADC (bottom left) and FA (bottom right) for simulated (solid lines) and experimental (dotted lines) data for b=1600 s mm^{-2}. Data points are mean values over all voxels and all hearts (expt), and all repetitions (sim); error bars are $\pm$1 sd.

4.1.3 Discussion

The model reproduces the MRI signals very well compared with the experimental data. The DT and its derivatives also correspond well with the experimental data.

The noisy simulated MRI signal in the direction of the primary eigenvector is very close to the experimental data, while for the secondary and tertiary directions the simulated signal is higher than the experimental data. The addition of noise has little effect on the simulated signals in the secondary and tertiary directions, but causes the signal in the primary direction to decrease less sharply at higher b-values.

The λs of the DT show similar results to the MRI signals. The noisy λ_1 is similar to the data, while the simulated λ_2 and λ_3 are lower than the experimental ones. The addition of noise has little effect on λ_2 and λ_3, but causes λ_1 to decrease more rapidly than without noise and the experimental data.

These λs lead to a similar mean ADC in the noisy simulated and experimental data, while the FA is higher in the simulations than the experiments at lower b-values and then decreases more rapidly than the experimental FA. The addition of noise causes the simulated mean ADC and FA to decrease more rapidly than the experimental or noisefree data at higher b-values.

The differences between the experimental and simulated data can probably be attributed to the structural homogeneity of the model.

The model geometry is simplified compared with biological tissue, with only helix angles modelled, uniformly sized cells, all layers parallel to each other, cell membranes as the only restriction to diffusion, and intra- and extra-cellular compartments with identical diffusivities. This is to allow the understanding of the separate effects of changing these parameters. The regular geometry of the model enhances the restriction of diffusion perpendicular to the cell long-axis compared with the diffusion along the cell long-axis. There is therefore a greater difference in

the MRI signals in the three eigenvector directions in the simulated data compared with the experimental data, and the MRI signals in the secondary and tertiary directions are larger in the simulation than the experiment. This leads to greater differences in the λs of the DT, and therefore a higher FA in the simulated data.

The addition of noise to the simulations has a marked effect, particularly on the FA. At higher b-values, λ_1 is preferentially affected by the noise floor leading to its underestimation and a decrease in FA. As the b-value increases, the MRI signals decrease and therefore the SNR decreases, and more of the MRI signals reach the noise floor. As this affects the smaller signals first, the range of MRI signals is reduced with the addition of noise (Figure 4.2), and the difference between MRI signals in the directions of the eigenvectors in decreased (Figure 4.5). In the simulated data there is a larger difference between the signals in the direction of the primary eigenvector and the other two eigenvectors than for the experimental data. Therefore, once this signal reaches the noise floor and levels off, the effect on the FA is sharper for the simulated data than for the experimental data, where the signals are already closer.

As the diffusion time increases, the likelihood of molecules interacting with a boundary increases and so there are greater effects of restriction which should lead to a lower mean ADC and a higher FA since the restrictions across the cells have more effect than along the length of the cell. This is what is found in the results from the second dataset: the mean ADC decreases with diffusion time and the FA increase with diffusion time, and in both cases the simulated data changes more quickly than the experimental data. The fact that only small changes are seen in the experimental results are likely to be due to the confounding effects of keeping the b-value constant, which means that as Δ is increased, the gradient strength must decrease. As seen from the first dataset, a decrease in gradient strength leads to a higher ADC, which may partly cancel out the expected decrease in ADC with diffusion time. Again, the increased structural homogeneity of the model is likely to be the cause of the differences seen between the simulated and experimental results.

4.2 Validation against a phantom

4.2.1 Background

Phantoms are commonly used in medical imaging as they can be manufactured to match certain properties such as geometry or chemical composition, so can be used to test whether imaging equipment is measuring correctly [152] or to test modelling methods [153]. Physical phantoms for diffusion MRI take two forms: hollow capillaries or synthetic fibres [110]. Fieremans et al. [154] used an MC model and analytical analysis to show that a fibre phantom could be useful for the validation of dMRI on clinical MRI scanners for neural imaging.

A cardiac dMRI phantom of the hollow capillaries type has recently been presented by colleagues from the Radcliffe Department of Medicine and their collaborators at the University of Manchester [155]. I used this as the basis of my phantom model comparison. The main reason for using a phantom model as validation was that the diffusivity within the model is known (cyclohexane has a diffusivity of $1.32\,\mathrm{mm^2\,s^{-1}}$ at 21° [144]). Since the diffusivity was shown in the sensitivity analysis in Chapter 3 to be the most important input factor in the model, eliminating the uncertainty which comes from this parameter in the cardiac tissue model is particularly important.

The phantom is made from 0.5 mm thick fibre strips, which are made of polymer with hollow pores filled with cyclohexane. Three layers of these fibre strips are wound around a spindle at different angles to simulate helical cardiac fibre angles, as shown in Figure 4.8. The helix angles of the layers are 52°, 2° and −58°. Each layer is held in place by a filament wound helically around the spindle. A section of the fibre strip not used in making the phantom was imaged using scanning electron microscopy (SEM) to characterise the pores. The area weighted pore diameter was calculated from this using the Binary and Analyze Particles functions in ImageJ (NIH, Bethseda, MD,USA). The SEM image and fractional area histogram of the fibre diameters are show in Figure 4.9.

In Teh et al. [155], the authors show that the mean ADC and FA are stable over a four month measuring period, and the values are similar to typical values for ex vivo hearts. They also found that the mean ADC was 11 % lower and the FA 18 % higher in the middle layer compared with the inner and outer layer; and that the middle layer was thinner with a lower b0 signal intensity. They hypothesise that this is due to the higher radius of curvature in the middle layer (inner = 273, middle = 4.88 and outer = 526mm) leading to a greater force needed to wind it around the spindle and hence greater compression of this layer compared with the other two. It is also possible that the pores in this section become more ellipsoidal in cross-section which could contribute to the higher FA; the increased bending in this middle layer is another possible factor contributing to the higher FA. Although not obvious from the SEM image, the authors suggest that the manufacturing method leads to slightly elliptical pore cross-sections which have the short axis aligned with the fibre strip depth, and therefore a sheet-like structure which allows the secondary and tertiary eigenvectors to be separated.

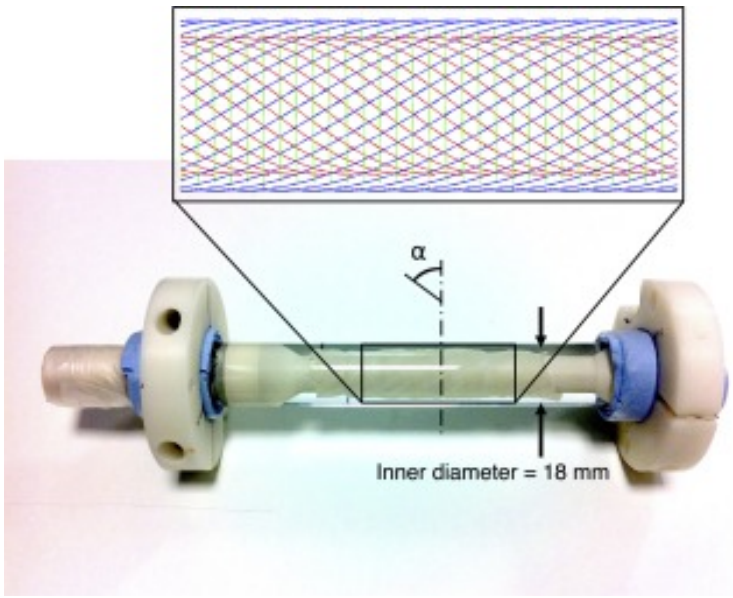

Figure 4.8: Photograph of the phantom. Three layers of fibre strips wound at different helix angles (α). The inset shows a schematic of the fibre orientation in the inner (red), middle (green) and outer (blue) fibre strips. Image reproduced from Teh et al. [155] with permission.

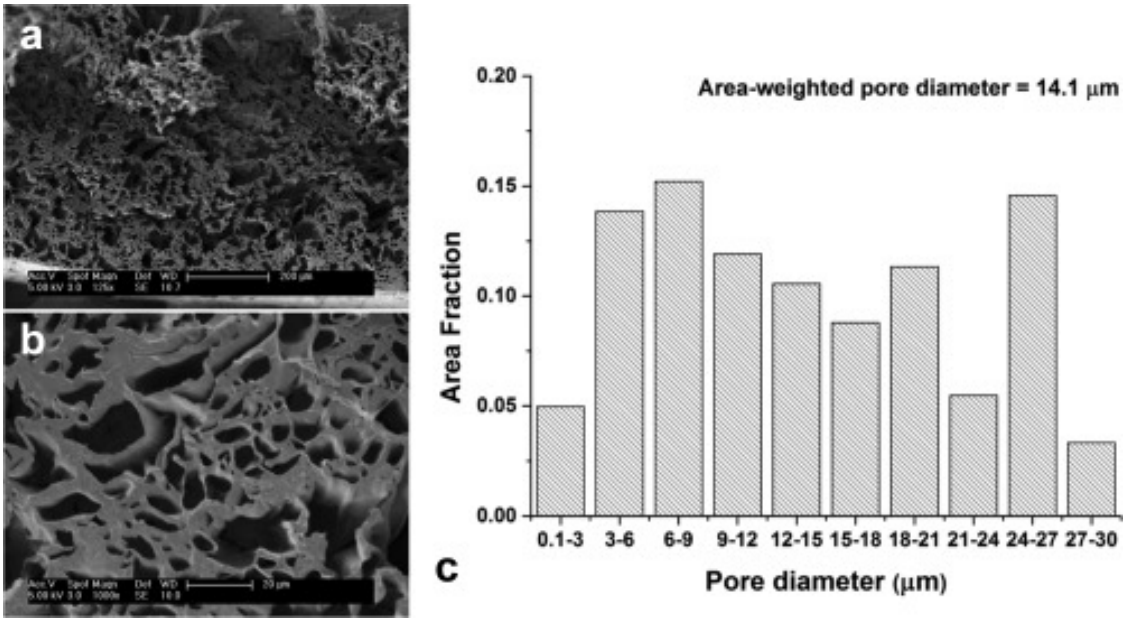

Figure 4.9: SEM images of cross-section of the fibre strip at (a) 125x and (b)1000x magnification. (c) Histogram of the measured pore size distribution across 10 SEM images (1000x magnification) in the fibre strip. Image reproduced from Teh et al. [155] with permission.

4.2.2 Methods

Phantom model

I modelled a section through the phantom described by Teh et al. [155] and in Section 4.1 of this chapter, as shown in Figure 4.10.

An SEM image of a section of the material used to make the phantom is seen in Figure 4.9. It can be seen that the cross-sections of the pores vary in shape. The distribution of the area-weighted pore diameters is also shown in Figure 4.9. I chose to model the pores as long cylinders, as a suitable approximation; possible modelling options are discussed in Section 4.2.4.

The fibres are wound around the spindle leading to effective radii of curvature of 273, 4.88 and 526mm respectively [155]. Within a voxel of 100 µm, the curve of a fibre within a voxel is very small, even in the middle layer, and so this was ignored in the simulations. A comparison of the image of the phantom's cross-section and the simulated cross-section is shown in Figure 4.11.

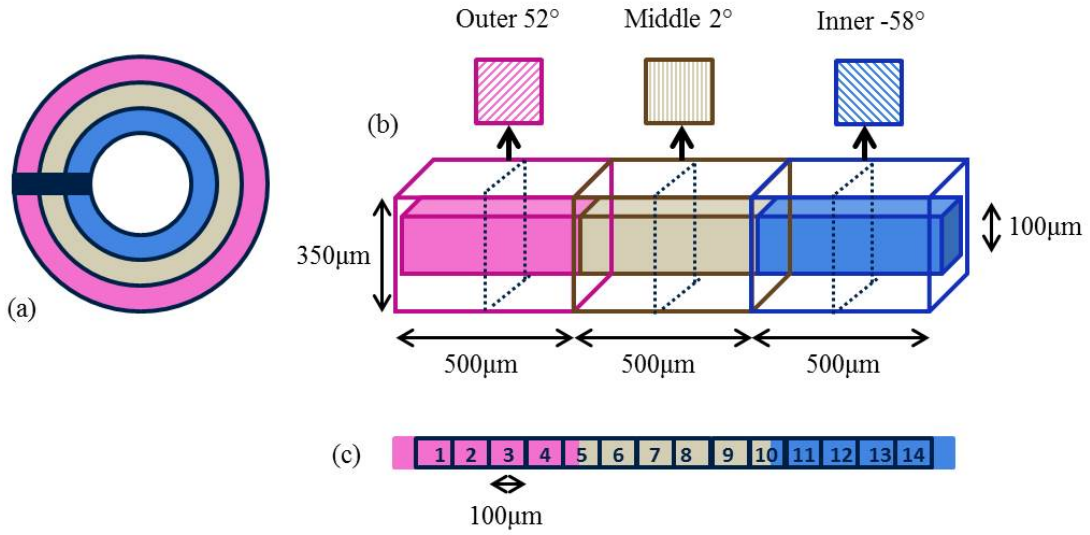

Figure 4.10: Model of the phantom. (a) End on view of phantom showing the three layers, dark blue rectangle is the section of the phantom created in the model. (b) Three layers with different fibre orientations. The total volume modelled is larger than the voxels to avoid boundary effects. (c) Three layers and the 14 voxels which are offset to avoid every voxel containing only one fibre angle.

From the higher resolution SEM, I used a basic thresholding method to calculate the volume fraction of pores as 38.4 %. The distribution of pore diameters is shown in the histogram in Figure 4.9: there is no clear pattern, so for the model I took the distribution to be uniform between diameters of 1 and 30 µm. For each of the three layers in the model, I created the cross-section as a random distribution of circles (as seen in Figure 4.11) using the following algorithm, adapted from the method used by Hall and Alexander [98] to distribute circles in an area:

- Calculate the number of pores (N_p) required based on the area-weighted mean diameter, the area to be filled and the volume fraction of pores.
- From a list of possible pore diameters (integers from 1 to 30 µm, with frequency selected to give equal area-weighting), randomly select N_p diameters from the list of diameters. Check that these give the required volume fraction (± 0.001), if not, then redo this step until required volume fraction is achieved.
- Order the pore diameters from largest to smallest.

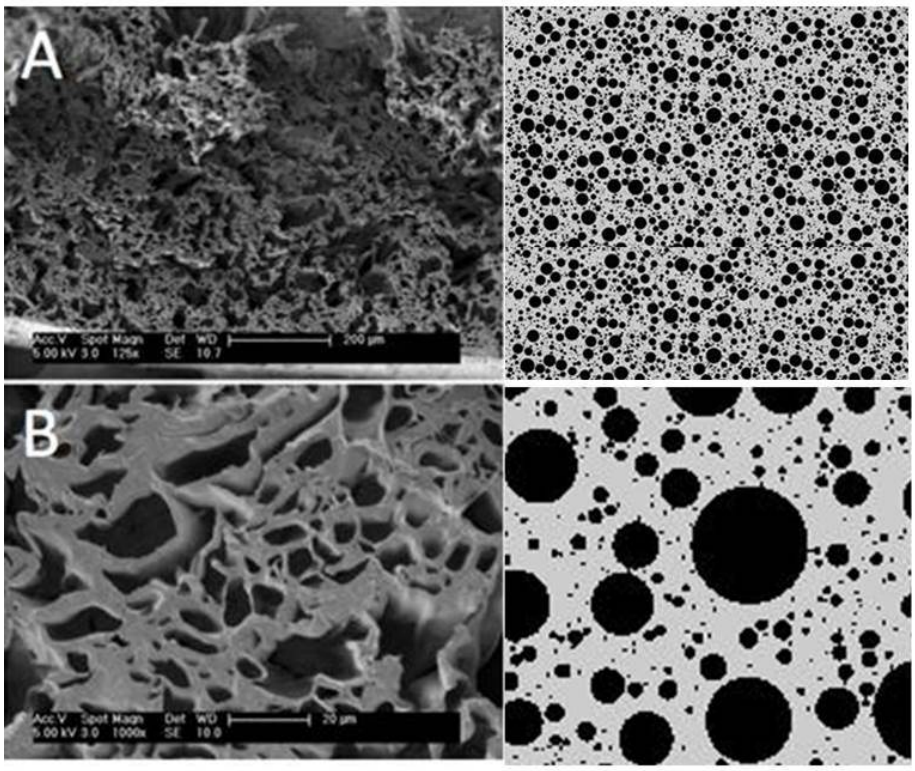

Figure 4.11: Phantom cross-section in experiment and simulation. (L) SEM images of cross-section of the fibre strip at (a) 125x and (b)1000x magnification. Image reproduced from Teh et al. [155] with permission. (R) Example cross-section of the simulated phantom at the same scale as the SEM.

- Randomly position the largest pore, then check that it does not overlap the edge of the area. If it does overlap, select a new random position until it is within the area.

- For each subsequent pore, randomly position it, then check that it does not overlap existing pores or the edge of the area. If it does overlap, select a new random position until it is within the area.

As for the cardiac tissue model, the total volume that I modelled was larger than the voxels required to avoid boundary effects (Figure 4.10). The total length of the simulated volume was 1500 µm and the size of each voxel 100 µm, which gives 15 simulated voxels, each only containing one pore orientation. As the experimental results will contain some voxels which span two pore orientations, I only analysed 14 voxels, where the 5th and 9th voxels contain two pore orientations (see Figure 4.10c).

Experimental data

The experimental data was provided by colleagues in the Radcliffe Department of Medicine at the University of Oxford which I then analysed. Six direction DTI was acquired for six diffusion times and five b-values. The acquisition parameters are in Table 4.4.

Table 4.4: DTI sequence parameters for the phantom

parameter	value
diffusion pulse duration, δ (ms)	4
diffusion interval, Δ (ms)	6.5, 10, 15, 20, 27 and 32
gradient strength ($\mathrm{T\,m^{-1}}$)	0.16 to 0.91
b-value ($\mathrm{s\,mm^{-2}}$)	1000, 2000, 3000, 4000 and 5000
voxel size ($\mu\mathrm{m}^3$)	100×100×100
directions per b-value	6 (expt), 100 (sim)
SNR	50

Data analysis

For the simulations and experiments, for each diffusion time and b-value I calculated the mean, median and interquartile range of the normalised MRI signals over all the voxels. I calculated the DT for each voxel for each diffusion time and b-value. For the simulation, I added noise to the MRI signals with an SNR of 50, as this was the value measured in the experimental data.

4.2.3 Results

Figures 4.12 and 4.13 show the normalised MRI signal intensities for the simulated and experimental phantom data for a diffusion time of 15 ms and for a b-value of $3000\,\mathrm{mm^2\,s^{-1}}$ respectively. For both the simulated and experimental data, the

MRI signals decrease as the b-value increases, and increase as the diffusion time increases. The simulated signals are smaller than the experimental ones, with a larger inter-quartile range, but a smaller overall range.

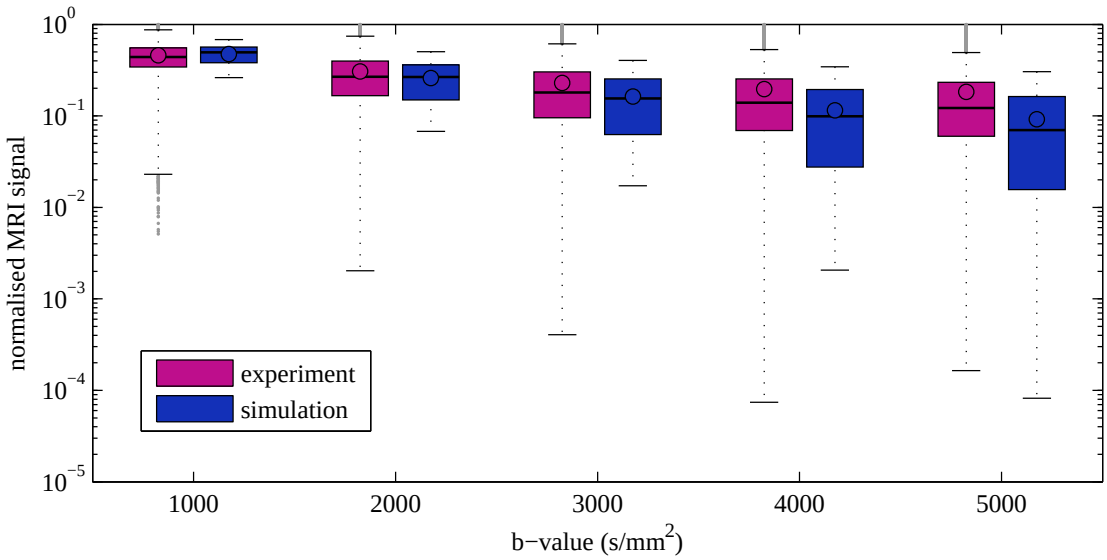

Figure 4.12: Phantom MRI signals by b-value. For a diffusion time (Δ) of 15 ms. Boxes are inter-quartile ranges with the median as a horizontal line and the circle indicating the mean; whiskers are 1.5 times the interquartile range, and outliers are beyond that.

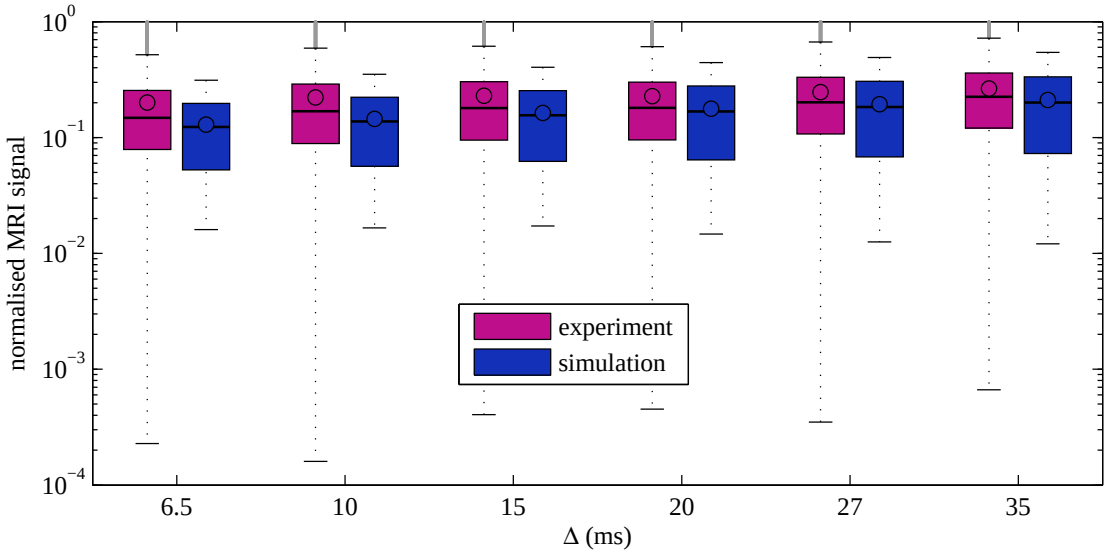

Figure 4.13: Phantom MRI signals by diffusion time. For a b-value of 3000 s mm^{-2}. Boxes are inter-quartile ranges with the median as a horizontal line and the circle indicating the mean; whiskers are 1.5 times the interquartile range, and outliers are beyond that.

Figure 4.14 shows the λs, mean ADC and FA for the experimental and simulated phantom data for a diffusion time of 15 ms. λ_1 is higher for the simulated data than the experimental data; and decreases more slowly with b-value than the experimental data. λ_2 and λ_3 are very similar for the simulated data, with λ_3 larger than the experimental data and λ_2 higher than the experimental data; both decrease at a similar rate for the simulations and experiments. The mean ADC decreases with b-value for the simulations and experiments, but at a faster rate for the experiments. The FA is higher for the simulations than for the experiments, and increases at a faster rate with increasing b-value.

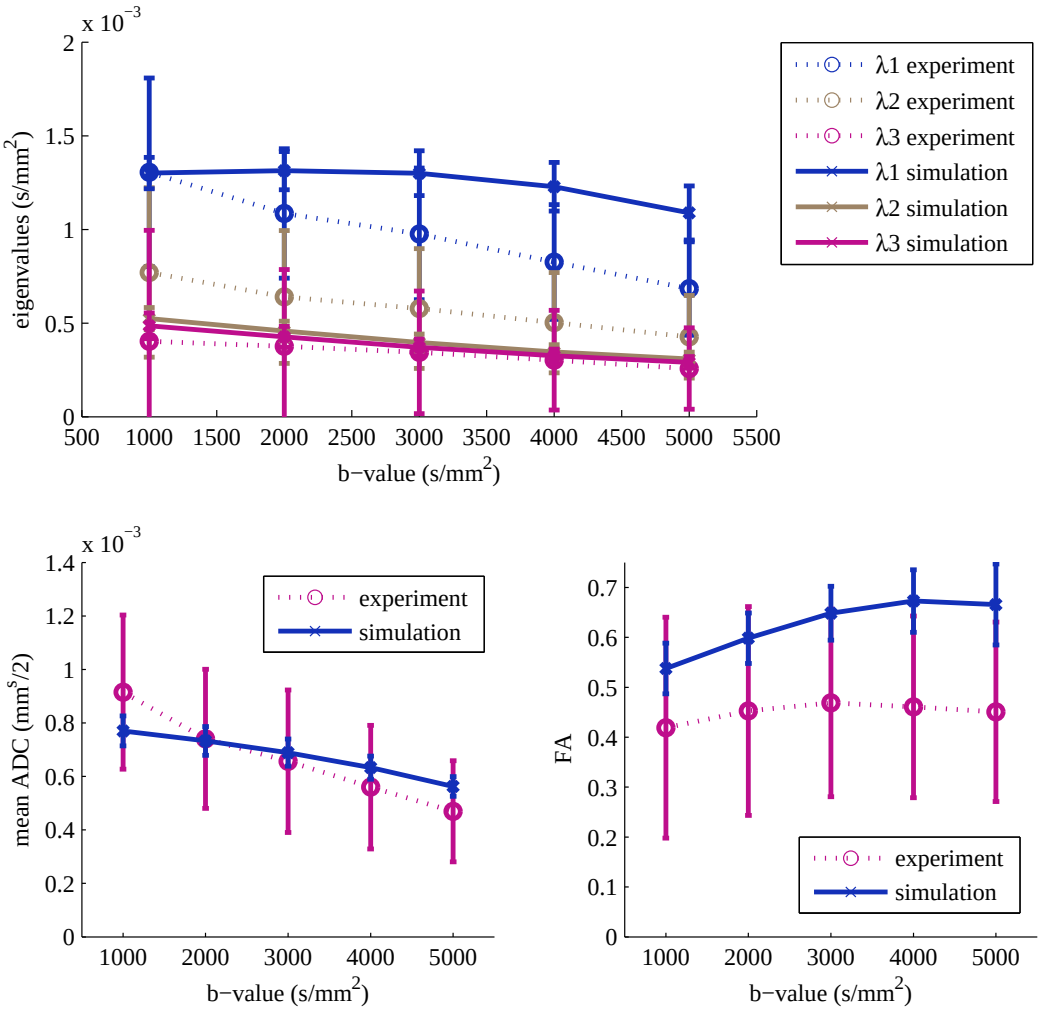

Figure 4.14: Phantom DT results by b-value. Effect of b-value changed by gradient strength on DT. (Top) λs, (bottom left) mean ADC and (bottom right) FA for the simulated (solid lines) and experimental (dotted lines) phantom data. Data points are mean values over all voxels and all repetitions; error bars are ± 1 sd. Colours are used to differentiate λ_1 (blue), λ_2 (beige) and λ_3 (pink). Diffusion time (Δ) is 15 ms

Figure 4.15 shows the λs, mean ADC and FA for the experimental and simulated phantom data for a b-value of $3000\,\mathrm{s\,mm^{-2}}$. λ_1 is higher for the simulated data than for the experimental data. λ_2 and λ_3 are very similar for the simulated data, with λ_3 about the same value as the experimental data and λ_2 higher than the experimental data. All three λs decrease slowly with increasing diffusion time, with similar rates for the experiments and simulations. The ADC is slightly higher for the simulations than the experiments, and decreases at a similar rate with increasing diffusion time. The simulated FA is higher than the experimental one, and increases more sharply with increasing diffusion time.

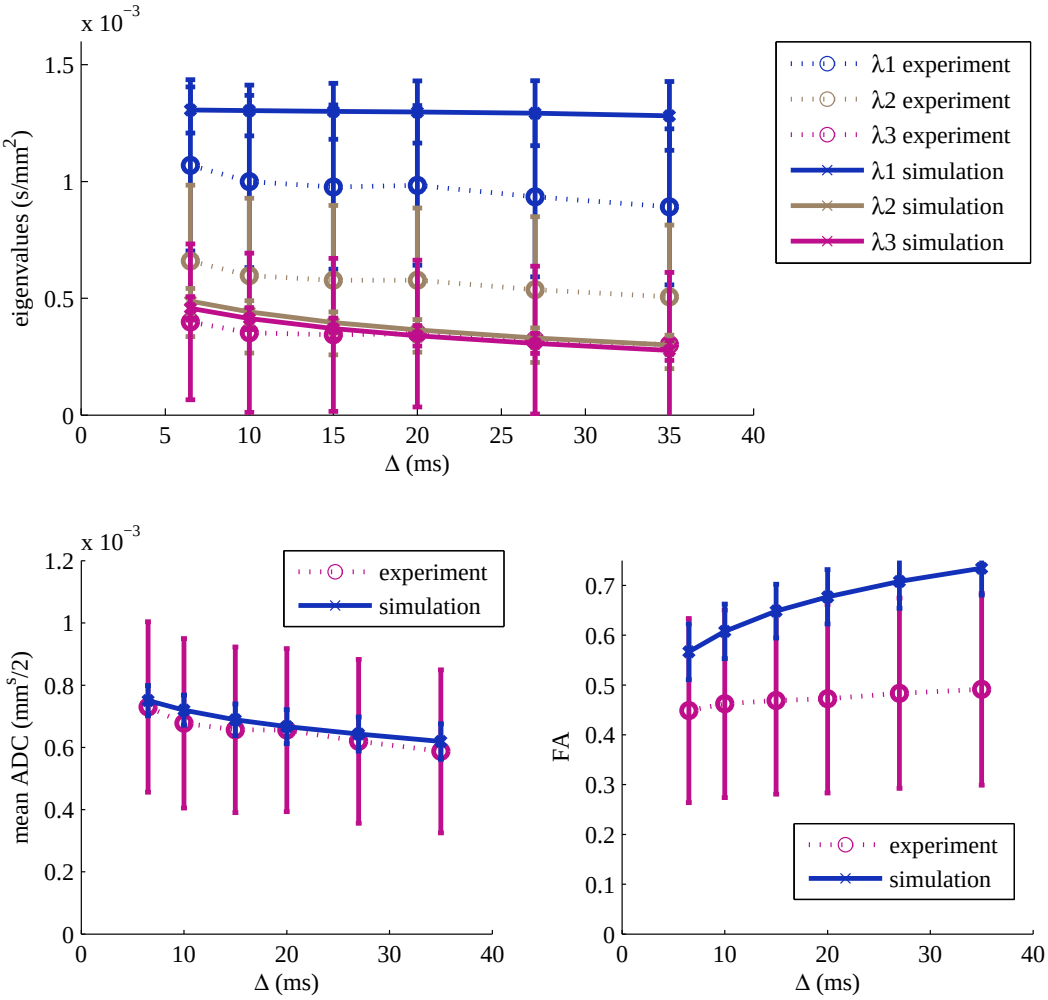

Figure 4.15: Phantom DT results by diffusion time. Effect of diffusion time (Δ) on DT. (Top) λs, (bottom left) mean ADC and (bottom right) FA for the simulated (solid lines) and experimental (dotted lines) phantom data. Data points are mean values over all voxels and all repetitions; error bars are ± 1 sd. Colours are used to differentiate λ_1 (blue), λ_2 (beige) and λ_3 (pink). B-value is $3000\,\mathrm{s\,mm^{-2}}$.

4.2.4 Discussion

The main reason for modelling the phantom and trying to use it for validating the model was that the diffusivity of the fluid (cyclohexane) was known so the uncertainty as to the correct diffusivity value, which is a limitation of the cardiac model, is removed. Although modelling the phantom does not validate the cardiac model in terms of its geometry, it does help validate the modelling method. At first, parallel pores wrapped around a spindle appeared to be a relatively straightforward geometry to model. However, there is considerable uncertainty as to the geometry of the pores in the phantom for two main reasons. Firstly, only 2D SEM images of the pores cross-section are available and so the changes in cross-section along the length, and the length of the pores are unknown. Secondly, the cross-section is of the fibre strip prior to winding around the phantom spindle, when it is bent and compressed to create the phantom geometry. The assumptions and simplifications made can explain the differences found between the simulated and experimental results.

I modelled the pores as straight parallel cylinders since the 3D structure of the pores, especially once wrapped around the spindle, is unknown. The circular cross-section leads to equal diffusion perpendicular to the cylinders' long axes and hence equal λ_2 and λ_3, unlike in the experimental results where there are differences between these λs due to the slightly ellipsoidal cross-sections. I considered creating a mesh from the SEM image and using this to create the model of the phantom in Smoldyn. However, I decided to model the pores as cylinders for three reasons. Firstly, the image is 2D and gives only a snapshot of one part of the fibre strips. Secondly, the fibre cross-sections are very variable and so there is considerable uncertainty as to the pore cross-sections in any particular voxel. Thirdly, as the fibre strips are wound around the spindle and held in position there is some bending and compression of the material and the pores compared with the SEM image. Given these three limitations, I chose to simplify the model by modelling the pores as long cylinders. I also considered creating oval cross-sections rather than circular to take the compression of the fibres into account, but since we

have no measurement of the extent of this effect, I considered cylinders as a good approximation, given the available information.

Although 3D images of the pores are not currently available, it is very likely that the cross-section of each pore changes along its length, and that the pores do not extend along the full length of the fibre strip. This means that there is more restriction to diffusion in this direction than in the straight parallel pores of the model. This leads to greater diffusion in this direction in the model and therefore a higher λ_1.

Despite these differences in the absolute values of the MRI signals and λs, the pattern of these as the diffusion time is changed is very similar and therefore shows that the modelling method works well, within the limits of the geometrical simplifications. λ_1 remains approximately constant rather than decreasing with b-value in the simulated data, which leads to differences in the ADC and FA between the simulated and experimental data. This is due to the lack of restriction in this direction: in free diffusion there is no change in λ as the b-value changes. These phantom tests, although not perfect, still serve their main purpose. In the experimental data, the big limitation is the value of the diffusivity. For the phantom we know the diffusivity and the simulations produce a mean ADC which matches the experimental data well, showing that the modelling method is valid.

4.3 Summary of chapter

The comparison of simulation results to data from five ex vivo rat hearts shows good correspondence of MRI signals and well-matched DT derivatives. There are small differences remaining, which can mainly be attributed to the increased regularity of the model's geometry compared with cardiac tissue.

Comparison with a phantom proved to be more challenging than originally thought, but the results support the modelling method, within the limits of the geometrical simplifications.

Overall, I have shown that the model is a good approximation of cardiac tissue and it can therefore be considered a useful tool in investigating cardiac diffusion MRI.

5

Model enhancements: permeability and diffusivity

In this chapter I investigate the effect of two of the model parameters, membrane permeability and extra-cellular diffusivity, to determine whether they can explain the deviations of the simulated results from the experimental ones in Chapter 4.

There are small differences between the results from the simulated and the ex vivo heart data in Chapter 4. In addition to the simplification of the geometry, my colleagues and I felt that there were two possible factors that may be limiting the model's performance: permeability and diffusivity. Permeability has been shown by Wang et al. [108] to affect the fractional anisotropy (FA) in a cardiac model. Diffusivity was shown in the sensitivity analysis in Chapter 3 to be very important. One of the simplifications made in the model is to assume that the intra- and extra-cellular diffusivity are equal, but given the importance of diffusivity as an input parameter, this may be an oversimplification which affects the model results. I therefore investigated the effect of introducing permeable cell membranes and increasing the extra-cellular diffusivity.

5.1 Permeable membranes

5.1.1 Background

In the model so far I have assumed that the membranes are impermeable. However, cell membranes are not completely impermeable to water molecules. Values of the permeability of cardiac myocytes found in the literature are shown in Table 5.1. There are some small differences between species, and it can be seen that the permeability is strongly dependent on temperature. Ogura et al. [156] and Suleymanian et al. [157] used a similar method to measure permeability. Individual myocytes were excised and placed in solutions with different, known osmolalities. As the cells swelled or shrank, the changes in cell size were recorded and measured using a video-microscope. Safford et al. [139] used a different approach, as part of their work on estimating diffusivity in cardiac tissue. They placed a strip of tissue in an Ussing diffusion cell and took a variety of measurements, including electrical resistance, water content and the movement of tracers, to allow them to fit a model of diffusion and permeability in cardiac tissue.

Table 5.1: Permeability of cardiac myocytes

value	species	temperature	notes	source
$12\,\mu m\,s^{-1}$	guinea pig	22 °C	isolated ventricular myocytes	[156]
$22\,\mu m\,s^{-1}$		35 °C		
$4\,\mu m\,s^{-1}$	rabbit	6 °C	isolated ventricular myocytes	[157]
$16\,\mu m\,s^{-1}$		22 °C		
$33\,\mu m\,s^{-1}$		35 °C		
$19\,\mu m\,s^{-1}$	cat	23 °C	ventricular muscle	[139]

There is some disagreement in the literature regarding the primary mechanism of water transport across the myocyte membranes: Ogura et al. [156] concluded from their results that aquaporin channels play an important role, while Suleymanian et al. [157] decided that diffusion across the membrane lipid bilayers was the primary

mechanism. These two studies found similar permeability coefficients; the difference in their conclusions is due to a difference in the activation energy that they measured, that is the amount of energy required to transport water across the membrane. For the purposes of this study, the mechanism of permeability is not important. However, the mechanism may lead to differences between in vivo and ex vivo permeability, which could be important when modelling in vivo diffusion MRI (dMRI).

Wang et al. [108] investigated the effect of membrane permeability on the FA using their Monte Carlo (MC) model of cardiac dMRI in parallel myocytes. They used permeability values up to $100\,\mu m\,s^{-1}$, which is much higher than I found in the literature, and higher than in the paper which they cite as their source [156]. Their findings are in Figure 5.1 and show that the FA decreases as the permeability increases. Their conclusions from their results were that when the permeability is less than $50\,\mu m\,s^{-1}$, its influence on the dMRI results can be ignored. From their results in Figure 5.1, the threshold which they have chosen appears to be quite high, and values of permeability smaller than $50\,\mu m\,s^{-1}$ may be important.

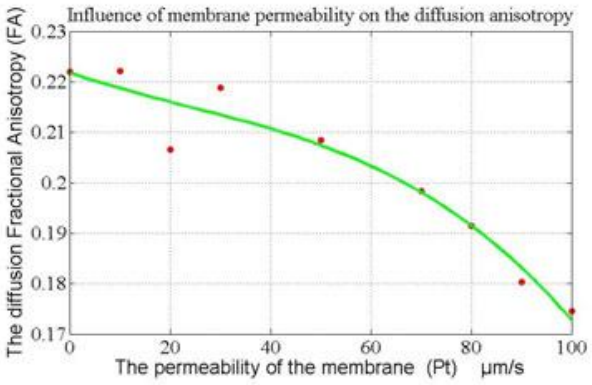

Figure 5.1: Effect of permeability on FA in an MC model of cardiac dMRI. Reproduced from Wang et al. [108] with permission.

In a multi-compartment MC model of brain tissue, Stanisz [158] modelled axons with a permeability of $9\,\mu m\,s^{-1}$ and glial cells with a permeability of $17\,\mu m\,s^{-1}$. He concluded that cell membrane permeability did affect the diffusion measurements in biological tissue, and that the effect increases with diffusion time.

5.1.2 Method

From Table 5.1, permeability at room temperature is in the range $12\,\mu m\,s^{-1}$ to $19\,\mu m\,s^{-1}$, so I took a value in the middle of this range of $15\,\mu m\,s^{-1}$.

I simulated the model with permeable membranes using the parameters in Table 5.2. I compared the results with simulated data of impermeable membranes and the experimental data from ex vivo hearts used in Chapter 4.

As in Chapter 4, the SNR was chosen to match the experimental data and is therefore higher for the effect of gradient strength (127) than for the effect of diffusion time (60).

Table 5.2: DTI sequence parameters for studying the effect of permeable membranes. The important parameter change for this study, the permeability, is in **bold**

parameter	effect of gradient strength	effect of diffusion time
cell cross-sectional area (μm^3)	200	
cell length (μm)	120	
cell aspect ratio (thickness/width)	0.67	
volume fraction of myocytes	0.825	
helix angle rate ($^\circ\,mm^{-1}$)	75	
diffusivity ($mm^2\,s^{-1}$)	1.5×10^{-3}	
permeability ($\mu m\,s^{-1}$)	**0 (impermeable) or 15 (permeable)**	
diffusion pulse duration, δ (ms)	5	2.5
diffusion interval, Δ (ms)	9	10 to 40
gradient strength ($T\,m^{-1}$)	0.24 to 0.78	0.30 to 0.62
b-value ($s\,mm^{-2}$)	800 to 8000	1600
voxel size (μm^3)	200×200×200	200×200×200
SNR	127	60

Voxel size

The voxel size was 200 µm for both the effect of gradient strength and effect of diffusion time analysis. The original analysis of the effect of diffusion time in Chapter 4 used a voxel size of 500 µm since this was the experimental voxel size. I analysed the effect of voxel size on the results, and found only small differences (see Figure 5.2) so, to reduce computational time, I used the smaller voxel size for this study.

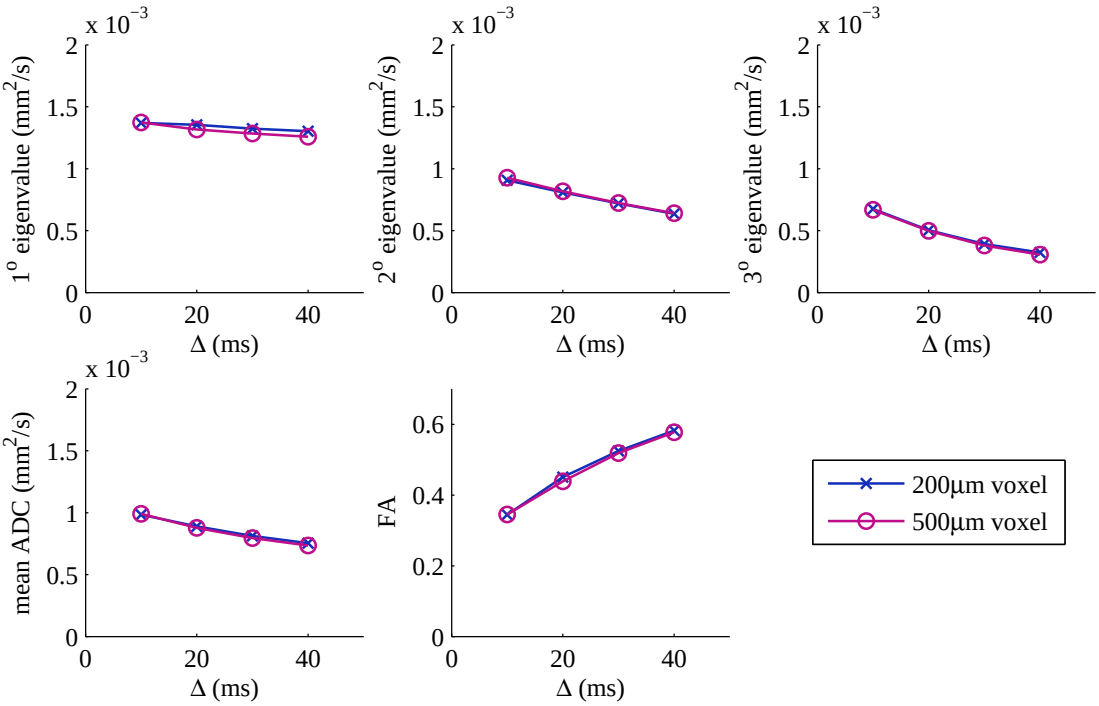

Figure 5.2: Effect of voxel size. Eigenvalues, mean ADC and FA for the effect of diffusion time for isotropic voxel sizes of 200 µm and 500 µm.

5.1.3 Results

Figures 5.3 and 5.4 show the MRI signals for the permeable and impermeable membranes as the gradient strength and diffusion time are increased respectively. For both studies, the permeable MRI signals are slightly lower than the impermeable MRI signals.

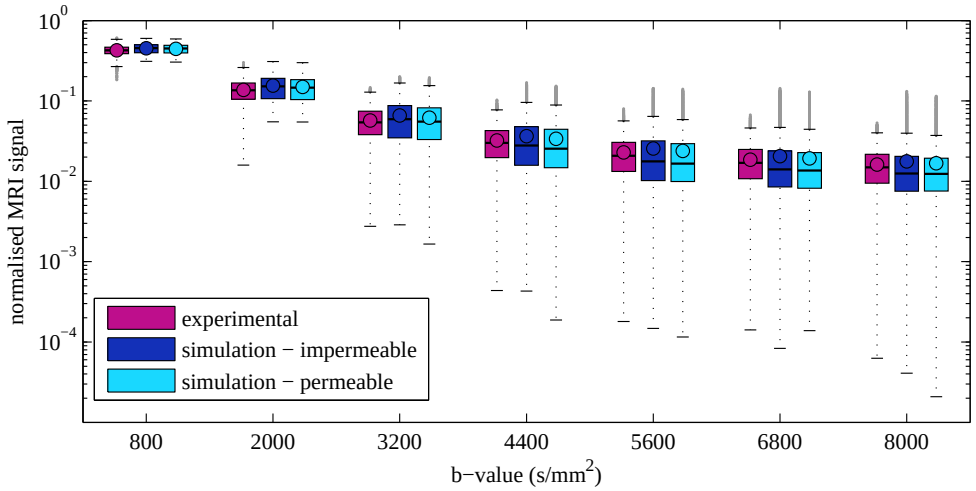

Figure 5.3: MRI signals for permeable and impermeable membranes. The b-value is altered by gradient strength. Boxes are inter-quartile ranges with the median as a horizontal line and the circle indicating the mean; whiskers are 1.5 times the interquartile range, outliers are beyond that. Simulated data are from 100 directions and 100 repetitions for an SNR of 127.

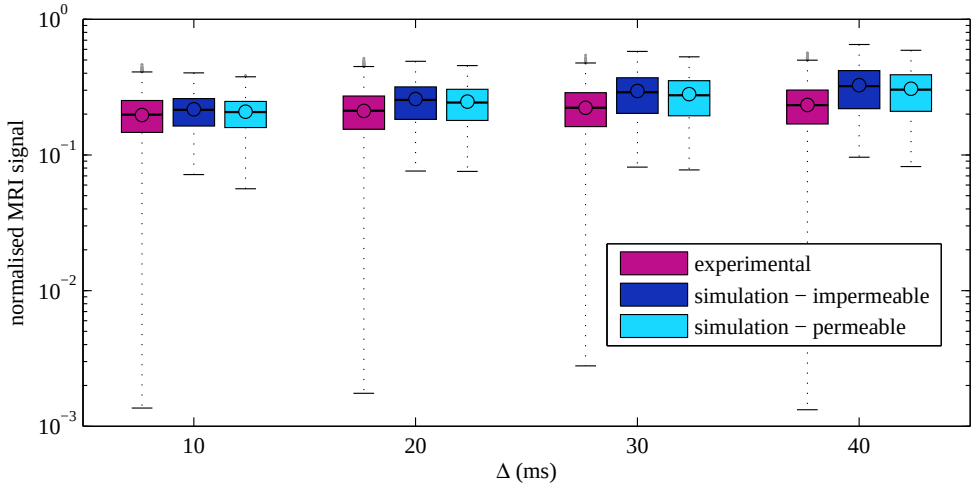

Figure 5.4: MRI signals for permeable and impermeable membranes by diffusion time. Boxes are inter-quartile ranges with the median as a horizontal line and the circle indicating the mean; whiskers are 1.5 times the interquartile range, and outliers are beyond that. Simulated data are from 100 gradient directions and 100 repetitions for an SNR of 60.

Figure 5.5 shows the DT parameters for the permeable and impermeable membranes as the b-value is changed by the gradient strength. The changes are only small. λ_2 and λ_3 are slightly higher for the permeable simulation leading to a lower FA.

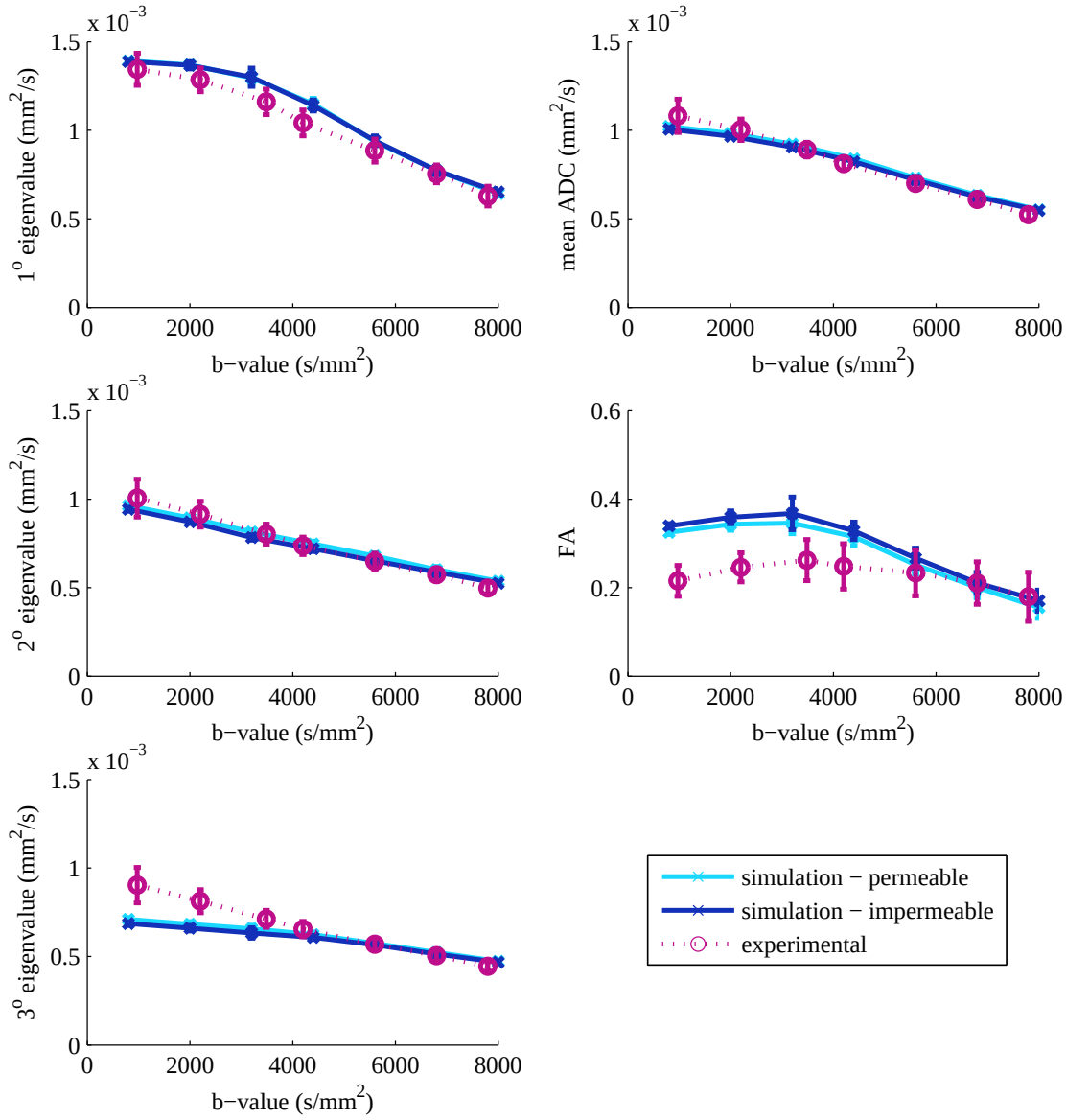

Figure 5.5: DT results for permeable and impermeable membranes. The b-value is altered by gradient strength. Data points are the mean, error bars are ±1 standard deviation. Simulated data are from 100 gradient directions and 100 repetitions for an SNR of 127.

Figure 5.6 shows the DT parameters for the permeable and impermeable membranes for different diffusion times. Again, the changes are only small. λ_2 and λ_3 are slightly higher for the permeable simulation leading to a lower FA. The differences increase as the diffusion time increases.

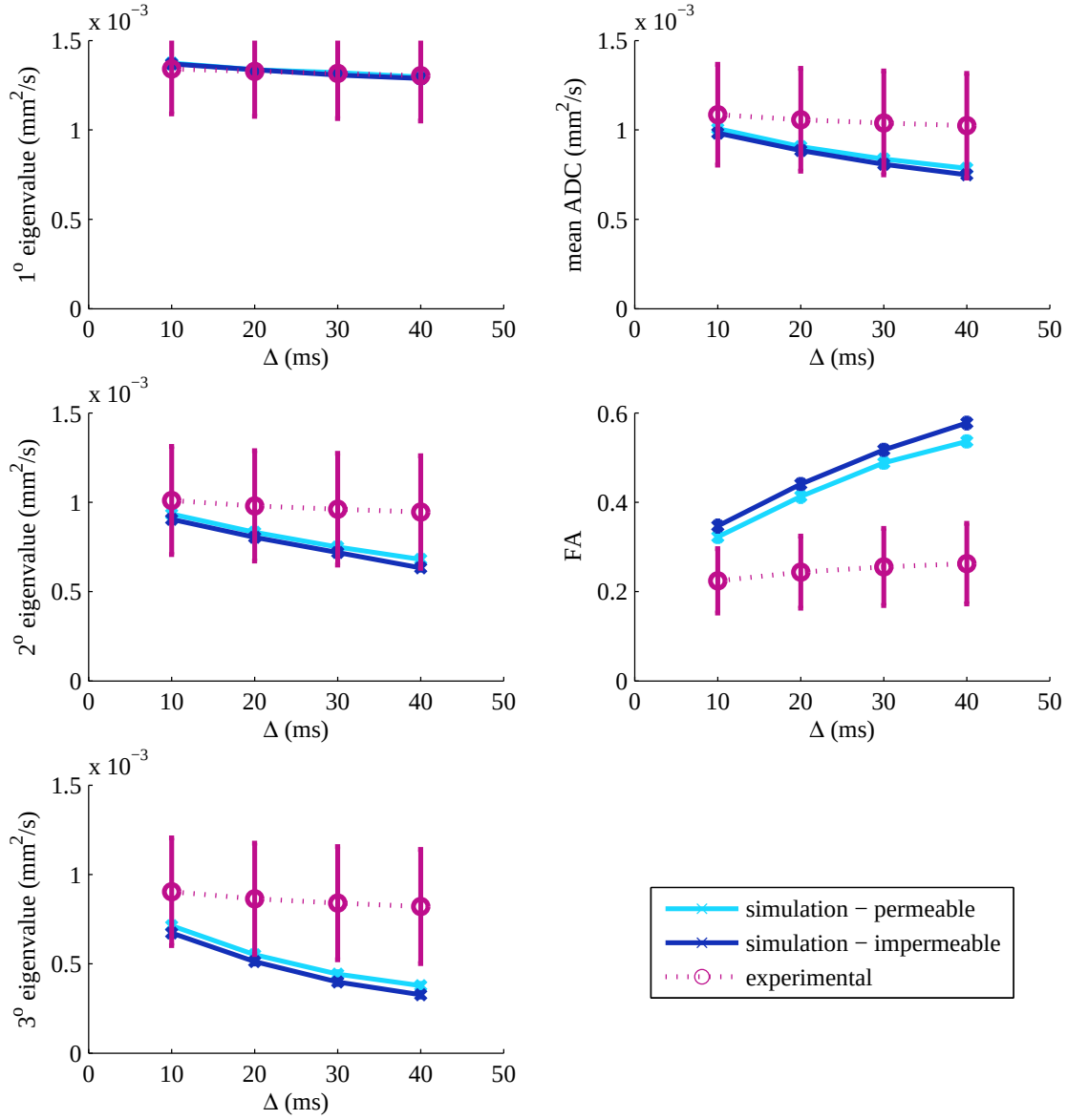

Figure 5.6: DT results for permeable and impermeable membranes by diffusion time. Data points are the mean, error bars are ±1 standard deviation. Simulated data are from 100 gradient directions and 100 repetitions for an SNR of 60.

5.1.4 Discussion

With permeable membranes, λ_2 and λ_3 are slightly increased, which indicates increased diffusion in these directions. This is a result of some of the water molecules passing though the cell membranes rather than reflecting off them. The changes in the λs leads to a lower FA as the diffusion is more isotropic. The changes in the λs and FA are only small and do not markedly improve the comparison with experimental data. The lack of permeability in the model in Chapter 4 is not therefore the reason for the discrepancies between the simulated and experimental data, and therefore other factors, probably geometry, need to be addressed.

As Wang et al. [108] found, physiological permeability values only have a small effect on the FA. They simulated a diffusion time of 50 ms. From Figure 5.1, for a permeability of $15\,\mu m\,s^{-1}$, the FA drops from approximately 0.222 to 0.217, that is a decrease of 3 %. In my study, for a diffusion time of 40 ms, the FA drops from 0.577 to 0.536, which is a decrease of 7 % and is the largest difference found across all the simulations. The difference in FA between the two studies can be attributed to differences in the size of the modelled myocytes: Wang et al. [108] modelled shorter, fatter cells with a CSA nearly double that in my study ($375\,\mu m^2$ versus $200\,\mu m^2$), which will reduce the FA. They also use a very high gradient strength of 2 T/m, which may contribute to the differences between the two studies in the FA and the effect of the permeability. The differences in FA with and without permeability are small, and therefore biological changes in permeability are likely to be much smaller and thus will not have a great effect on dMRI signals.

5.2 Extra-cellular diffusivity

5.2.1 Background

The Sensitivity Analysis in Chapter 3 showed that the diffusivity has the largest effect on the output of the model and, as briefly discussed in Chapter 3, the choice of diffusivity value can be complex. Diffusivity varies according to a number of factors and is likely to differ from inside to outside the cells.

Hindered and restricted diffusion

Diffusion within cardiac tissue depends on interactions of the water molecules with intracellular (IC) and extracellular (EC) structures, and cell membranes. Diffusion can be described as being restricted when boundaries stop molecules from moving freely, or hindered when molecules have to diffuse around obstacles and therefore take a longer path [159]. In the context of the cardiac model, we can define restricted diffusion as when the molecules are stopped by cell membranes, and hindered diffusion as when they are inhibited by IC or EC structures. In the model it is the hindered diffusivity that I want to use as an input parameter, since the effect of the cell membranes is included in the model's geometry, and therefore the restriction is taken into account there. I do not model IC structures explicitly and therefore the effect of these needs to be included in the diffusivity.

Most measurements of diffusivity in the literature are of the apparent diffusion coefficient (ADC) from dMRI. The relative values of the diffusion distance and the size of the cells that are being measured affects how much restriction is measured. At short diffusion times (distances), especially in large cells, there will be little interaction of molecules with cell membranes and therefore the measured ADC will approximate the hindered diffusivity [145].

The self-diffusivity of water is $2.0 \times 10^{-3}\,\mathrm{mm^2\,s^{-1}}$ at 20 °C, $2.3 \times 10^{-3}\,\mathrm{mm^2\,s^{-1}}$ at 25 °C and $3.0 \times 10^{-3}\,\mathrm{mm^2\,s^{-1}}$ at 37 °C [144]. Both the hindered and restricted diffusivity are lower than the self-diffusivity, with the restricted diffusivity lower than the hindered diffusivity due to the added effect of the cell membranes. The model is of ex vivo cardiac tissue and therefore to correspond with experimental data, which is typically carried out at room temperature, room temperature diffusivity should be used.

To allow comparison of diffusivity values made at different temperatures, it is useful to normalise the values to the self-diffusivity of water at that temperature (D_{norm}). Garrido et al. [138] measured ADC in rat hearts using diffusion weighted (DW) imaging at 37 °C for a diffusion time of 7 ms, which is quite short and so will begin to approximate hindered diffusion. They found D_{norm} of 0.6 to 0.8 for diffusion perpendicular or parallel to the endocardium respectively, suggesting that the diffusion time is not sufficiently short to give hindered diffusion only, or that there is anisotropy of diffusion in cells. Cooper et al. [137] used nuclear magnetic resonance (NMR) with a range of diffusion times, from approximately 3 to 60 ms, to measure rat myocardium and found D_{norm} of 0.36, which surprisingly did not change with diffusion time. Seland et al. [140, 141] measured ADC in rat hearts at 37 °C to give D_{norm} of 0.3 to 1.0, with the different values associated with different compartments. In a non-NMR approach, Safford et al. [139] used an Ussing diffusion cell to measure diffusivity in cat myocardium. This takes strips of tissue and measures the rate at which tritiated water diffuses across it. By applying these results to their cell matrix model, they estimated that the D_{norm} was 0.25.

The overall range of D_{norm} is from 0.25 to 1.0, which for a room temperature of 25 °C gives a diffusivity of $0.6 \times 10^{-3}\,\mathrm{mm^2\,s^{-1}}$ to $2.3 \times 10^{-3}\,\mathrm{mm^2\,s^{-1}}$. The differences are probably due to measurement techniques, while within studies such as Garrido et al.'s [138] and Seland et al.'s [141] multiple values depend on direction or compartments.

IC v EC diffusivity

Since EC space is different from IC space, it is possible that there are differences in the diffusivities within these two compartments. For large cells and high resolution MRI imaging, it is possible to have voxels containing only the IC space. Various studies have used large cells and short diffusion times to measure IC diffusivity.

Zhao [160] measured diffusivity of $(2.0 \pm 0.3) \times 10^{-3}\,\mathrm{mm^2\,s^{-1}}$ at 37 °C in HeLa cells which have a diameter of around 20 µm. Beaulieu et al. [161] analysed squid giant axons, which are very large (300 µm in diameter and 3 cm long); they found that at 20 °C, the axial diffusion was greater than the radial diffusion ($1.61 \times 10^{-3}\,\mathrm{mm^2\,s^{-1}}$ vs $1.33 \times 10^{-3}\,\mathrm{mm^2\,s^{-1}}$). Sehy [63] found inhomogeneous ADC in frog oocytes of 0.5 to $1.7 \times 10^{-3}\,\mathrm{mm^2\,s^{-1}}$ at 23 °C; these cells are much bigger (1.2 mm diameter) than myocytes or neurons.

Separating the effects of the IC and EC compartments is difficult experimentally, but some studies have found ways to measure this.

Two studies of rat brains found no difference in diffusivity between the IC and EC space [162, 163]. Silva et al. [162] used NMR with and without IC contrast to measure ADC for the IC compartment only, and for the IC and EC compartments combined for in vivo rat brains. They found the IC ADC to be $(0.69 \pm 0.06)\,\mathrm{mm^2\,s^{-1}}$ and the combined ADC to be $(0.70 \pm 0.05)\,\mathrm{mm^2\,s^{-1}}$. The EC signal does not therefore significantly change the overall ADC. However, the EC has only a small volume fraction (VF), so it may be that any difference is too small to measure. Duong et al. [163] used IC and EC contrast-enhanced NMR of in vivo rat brain to calculate the IC and EC ADCs and found no statistically significant difference. The IC ADC was $(0.157 \pm 0.028)\,\mathrm{mm^2\,s^{-1}}$ and the EC ADC was $(0.144 \pm 0.018)\,\mathrm{mm^2\,s^{-1}}$.

Aslund and Topgaard [164] have developed a method for calculating IC and EC diffusivity from NMR experiments, by making use of the decrease in the apparent mean-square displacement with increasing diffusion-encoding time while keeping

the effective diffusion time constant. They demonstrated this using yeast cells suspended in water to give an IC diffusivity of $0.65\,\mathrm{mm^2\,s^{-1}}$ and an EC diffusivity of $1.27\,\mathrm{mm^2\,s^{-1}}$. Given that the EC space was water, and the measured EC diffusivity is 55 % of free water at 25 °C this is a measure of restricted rather than hindered diffusivity. To my knowledge, it has not been used for determining IC and EC diffusivities in biological tissue.

In two studies on rat hearts, Seland et al. [140, 141] used contrast-enhanced NMR to correlate relaxation times with diffusivity and found that two compartments can be identified: 'slow' and 'fast'. The 'fast' compartment, which they attributed to the EC compartment, had a diffusivity of $3.0\,\mathrm{mm^2\,s^{-1}}$ and the 'slow', IC, compartment had a diffusivity of $1.2\,\mathrm{mm^2\,s^{-1}}$. The EC compartment therefore has a diffusivity close to that of free water. They used the T2 relaxation to measure the VFs, and found the IC and EC compartments to be 54 % and 46 % respectively, which does not match the known VFs. It therefore seems likely that the assumption that the two compartments correspond directly to the EC and IC compartments is an oversimplification.

Using the biexponential model to analyse diffusion MRI data from rat hearts, Hsu et al. [165] found the 'fast' compartment had a diffusivity of $1.52\,\mathrm{mm^2\,s^{-1}}$ and the 'slow' compartment had a diffusivity of $0.40\,\mathrm{mm^2\,s^{-1}}$ at 37 °C. Forder et al. [166] analysed heart tissue slices and found the 'fast' compartment had a diffusivity of $0.72\,\mathrm{mm^2\,s^{-1}}$ and the 'slow' compartment had a diffusivity of $0.06\,\mathrm{mm^2\,s^{-1}}$ at 19 °C. The VF of the 'fast' compartment was measured as 0.76 [165] and 0.82 [166] respectively, which does not correspond to the known VFs and is therefore unlikely to represent IC and EC diffusivity. There is growing evidence for the theory that the 'fast' and 'slow' compartments represent fairly free molecules and those bound to the membrane respectively [65].

Causes of restriction and anisotropy of diffusion

Several studies have investigated which structures affect diffusion in a variety of tissues, and there remains a degree of disagreement in the literature.

Early studies found that the physical barriers to diffusion could not explain the reduction in diffusivity. Cleveland et al. [167] performed NMR on rat tibialis anterior muscle. They found that their results show that decreased diffusivity and anisotropy compared with free water cannot be explained only by IC barriers, but that some of the water molecules are 'associated' with proteins which decreases the diffusivity of the water molecules. Cooper et al. [137] used PGSE NMR on rat hearts with different diffusion times and found little dependence of the diffusivity on the diffusion time. They concluded that this supports the 'trapped water' theory, where some of the water molecules are bound to proteins or organelles. More recent analysis supports these findings, especially when analysing the biexponential model [65].

Later, Kinsey et al. [168] used NMR to measure diffusion of phosphocreatine in fish skeletal muscle to explore which structures cause anisotropy of diffusion. Phosphocreatine is only found in the IC environment so can be used to explore only this compartment. They identified three possible structures at different scales: the myofilament lattice (actin and myosin, nm), subcellular membranes (sarcoplasmic reticulum and mitochondria, µm) and the sarcolema (membrane around each muscle cell, 10^2 µm). They found that the myofilament lattice was at too small a scale to cause the anisotropy, and that the sarcolema could not account for the time-dependence of the results. They therefore concluded that it is the subcellular membranes that cause the anisotropy. Red muscle has a greater decrease in diffusivity with diffusion time than white muscle, especially in the direction parallel to the long axis of the cells, as shown in Figure 5.7. There are more mitochondria in red muscle than in white muscle which accounts for this difference. The sarcoplasmic reticulum and mitochondria restrict the radial diffusion while the axial diffusion is only restricted by the mitochondria. Cardiac muscle has more

mitochondria and less sarcoplasmic reticulum compared with skeletal muscle [14] which suggests that there would be more axial and less radial restriction compared with skeletal muscle, and therefore less anisotropy of diffusion.

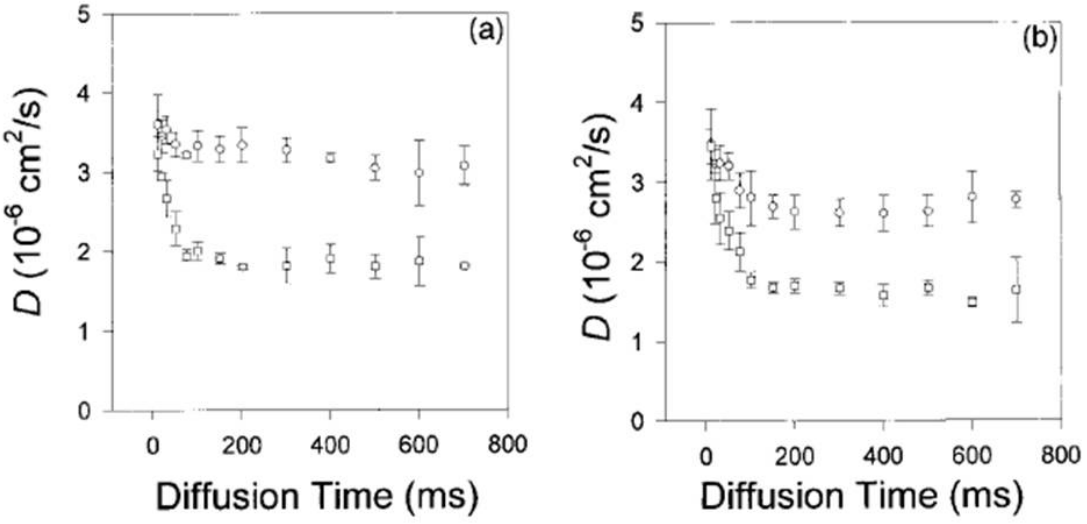

Figure 5.7: Diffusion in skeletal muscle. Time dependence of diffusivity parallel (circles) and perpendicular (squares) to the long axis of cells in (a) white; and (b) red skeletal muscle strips of fish. Measurements are diffusivity ± s.e.m. Reproduced from Kinsey et al. [168] with permission.

Beaulieu [145] reviewed anisotropy in neural tissue. Neural white matter is highly anisotropic, and nerve cells are more anisotropic than muscle. The main reason for the anisotropy is the cell membranes, while myelin further increases the anisotropy and reduces the diffusivity. In their work on squid giant axons [161] they made use of the large size of these cells to look at intracellular hindered diffusivity, and found a much smaller degree of anisotropy compared with white matter which they attributed to neurofilaments.

IC anisotropy of diffusion

As Beaulieu et al. found in neural tissue [161] and Kinsey et al. found in skeletal muscle [168], the complexity and anisotropy of the intracellular structure may lead to anisotropic hindered diffusivity.

In a study of squid giant axons, Beaulieu et al. [161] isolated individual axons and immersed them in paraffin oil to ensure that only the IC signal is measured. The axon is very large ($(300 \pm 80)\,\mu m$ in diameter and around 3 cm long), which means that the diffusion step length is much smaller than the size of the cell and therefore it is hindered diffusion that is measured. They found that the axial diffusion was greater than the radial diffusion ($(1.61 \pm 0.06) \times 10^{-3}\,mm^2\,s^{-1}$ vs $(1.33 \pm 0.09) \times 10^{-3}\,mm^2\,s^{-1}$). The anisotropy is small compared with white matter, and is due to neurofilaments in the cells.

In their study of fish skeletal muscle, Kinsey et al. [168] found axial diffusion of phosphocreatine to be greater than radial diffusion ($0.32 \times 10^{-3}\,mm^2\,s^{-1}$ vs $0.18 \times 10^{-3}\,mm^2\,s^{-1}$ for white muscle; $0.26 \times 10^{-3}\,mm^2\,s^{-1}$ vs $0.16 \times 10^{-3}\,mm^2\,s^{-1}$ for red muscle) at diffusion times of more than 200 ms. Fish skeletal muscle cells are very large (a diameter of 85 µm for red muscle and 112 µm for white muscle), so even at a diffusion time of 200 ms, the diffusion distance is smaller than the cell diameter (1D diffusion distance for a diffusion time of 200 ms is 20 µm for a diffusivity of $1 \times 10^{-3}\,mm^2\,s^{-1}$).

Summary

Diffusivity in biological tissue is complex and may vary between IC and EC compartments [141], have variation in different areas of the IC compartment [63] and be anisotropic in the IC compartment [168]. Given these possible variations, modelling using a single isotropic value for diffusivity in the IC and EC space may be too simplistic. It would therefore be worth investigating whether changes in the diffusivity affect the model.

Cardiac myocytes are too small to measure variations in diffusion within a single cell. The only evidence for heterogeneity of diffusion within them comes from the biexponential model. It is not possible to derive appropriate model parameters

from these results without making many assumptions, and it is therefore hard to justify modelling separate areas with different diffusivities within a myocyte.

Overall, there is some evidence for anisotropy of diffusion within neurons and skeletal muscle, but the evidence in cardiac muscle is less certain. In skeletal myocytes Kinsey et al. [168] found a ratio of axial to radial diffusivity of 1.8 in white muscle and 1.6 in red muscle. The differences between cardiac and skeletal myocytes mean it is likely that this ratio will be smaller in cardiac myocytes. Without stronger evidence for anisotropy, I decided to continue to use an isotropic diffusivity for this study.

Seland et al. [141] is the only source of separate IC and EC diffusivities in the heart, apart from perhaps the biexponential models, although these are unlikely to represent IC and EC compartments. The difference they found was large ($1.2 \times 10^{-3}\,\mathrm{mm^2\,s^{-1}}$ in the IC, and $3.0 \times 10^{-3}\,\mathrm{mm^2\,s^{-1}}$ in the EC at 37 °C), however, the VFs which they associated with each of these (54 % and 46 %) do not correlate with IC and EC VFs. It is therefore uncertain what these two diffusivities are associated with, and they may not correspond to IC and EC space. There is some consensus that the diffusivity in the EC is likely to be higher than in the IC [140, 141, 169], and I therefore decided to model a higher EC diffusivity than IC diffusivity.

Given that the sensitivity analysis in Chapter 3 showed that the diffusivity has a large effect on the model outputs, and that the validation work in Chapter 4 showed that the model outputs match the experimental outputs well, the overall diffusivity value of $1.5 \times 10^{-3}\,\mathrm{mm^2\,s^{-1}}$ is likely to be close to the correct value. The IC space is 82.5 % of the model and will contribute a large amount to the overall diffusivity so I therefore kept the IC diffusivity at $1.5 \times 10^{-3}\,\mathrm{mm^2\,s^{-1}}$ and increased the EC diffusivity.

The aim is to investigate whether changing the EC diffusivity affects the overall results of the dMRI model, and whether this can account for the deviations of the simulated results from the experimental ones in Chapter 4.

5.2.2 Methods

I used the model as presented in Chapter 3. Instead of randomly distributing one type of molecule across the whole of the modelling volume, I distributed two types of molecules: one in the IC space and one in the EC space. The IC molecules had a diffusivity of $1.5 \times 10^{-3}\,\mathrm{mm^2\,s^{-1}}$, as used in the comparison against experimental data in Chapter 4. The EC molecules were analysed with three different diffusivities: 1.5, 1.8 and $2.1 \times 10^{-3}\,\mathrm{mm^2\,s^{-1}}$. The model parameters are shown in Table 5.3.

Table 5.3: DTI sequence parameters for different EC diffusivities. The important parameter change for this study, the EC diffusivity, is in **bold**

parameter	effect of gradient strength	effect of diffusion time
cell cross-sectional area (μm^3)	200	
cell length (μm)	120	
cell aspect ratio (thickness/width)	0.67	
volume fraction of myocytes	0.825	
helix angle rate ($^\circ\,mm^{-1}$)	75	
IC diffusivity ($mm^2\,s^{-1}$)	1.5×10^{-3}	
EC diffusivity ($mm^2\,s^{-1}$)	**1.5, 1.8 and 2.1×10^{-3}**	
permeability ($\mu m\,s^{-1}$)	0	
diffusion pulse duration, δ (ms)	5	2.5
diffusion interval, Δ (ms)	9	10 to 40
gradient strength ($T\,m^{-1}$)	0.25 to 0.78	0.30 to 0.62
b-value ($s\,mm^{-2}$)	800 to 8000	1600
voxel size (μm^3)	200×200×200	200×200×200
SNR	127	60

As for the permeability study, the voxel size was 200 µm for both the effect of gradient strength and effect of diffusion time analysis.

Firstly, I calculated the MRI signals and DT derivatives for the IC and EC space separately. I then combined the signals by weighting them according to their VFs to calculate the overall signal. From this I calculated the overall DT and its derivatives.

5.2.3 Results

Separate IC and EC data

These results are from the separate analyses of the IC and EC space. Diffusivity in the IC space is $1.5 \times 10^{-3}\,\mathrm{mm^2\,s^{-1}}$. Three different diffusivities are modelled in the EC space: EC(low) $= 1.5 \times 10^{-3}\,\mathrm{mm^2\,s^{-1}}$, EC(mid) $= 1.8 \times 10^{-3}\,\mathrm{mm^2\,s^{-1}}$, EC(high) $= 2.1 \times 10^{-3}\,\mathrm{mm^2\,s^{-1}}$.

Figure 5.8 shows the MRI signals for different b-values altered by gradient strength. The IC signals have a narrower inter-quartile range than the EC signals. As the EC diffusivity increases, the MRI signals decrease. The mean is greater than the median, especially for the EC, and the difference increases with b-value. All signals decrease with b-value. The geometry has a marked effect on the MRI signals, as the IC and EC(low) diffusivity are the same, but the IC signal is lower, with a smaller range than the EC(low) MRI signals.

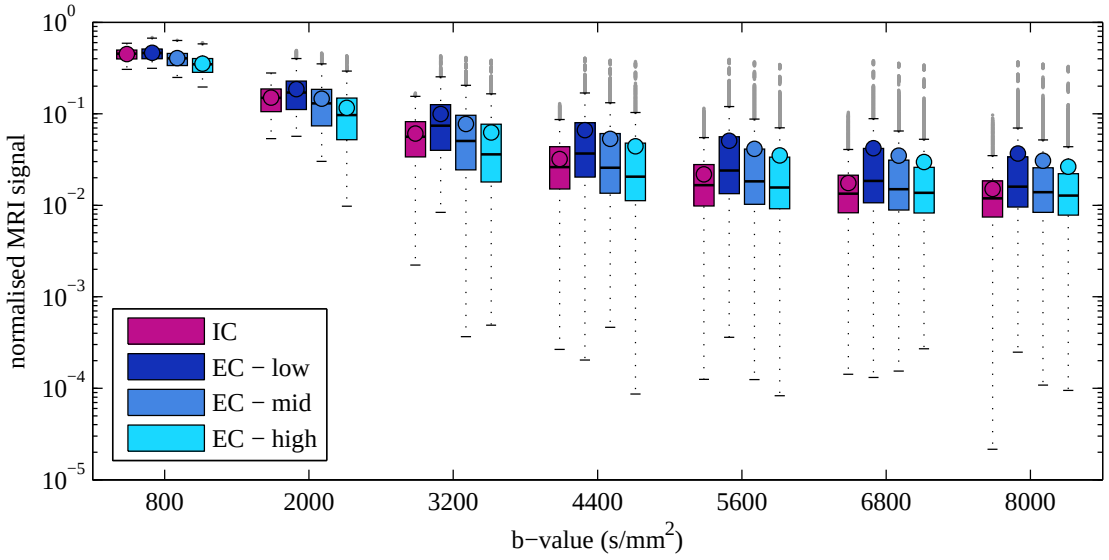

Figure 5.8: MRI signals in EC and IC space. The b-value is altered by gradient strength. Diffusivity in the IC space is $1.5 \times 10^{-3}\,\mathrm{mm^2\,s^{-1}}$; three different diffusivities are modelled in the EC space (low $= 1.5 \times 10^{-3}\,\mathrm{mm^2\,s^{-1}}$, mid $= 1.8 \times 10^{-3}\,\mathrm{mm^2\,s^{-1}}$, high $= 2.1 \times 10^{-3}\,\mathrm{mm^2\,s^{-1}}$). Boxes are inter-quartile ranges with the median as a horizontal line and the circle indicating the mean; whiskers are 1.5 times the interquartile range, and outliers are beyond that. Data are from 100 gradient directions and 100 repetitions for an SNR of 127.

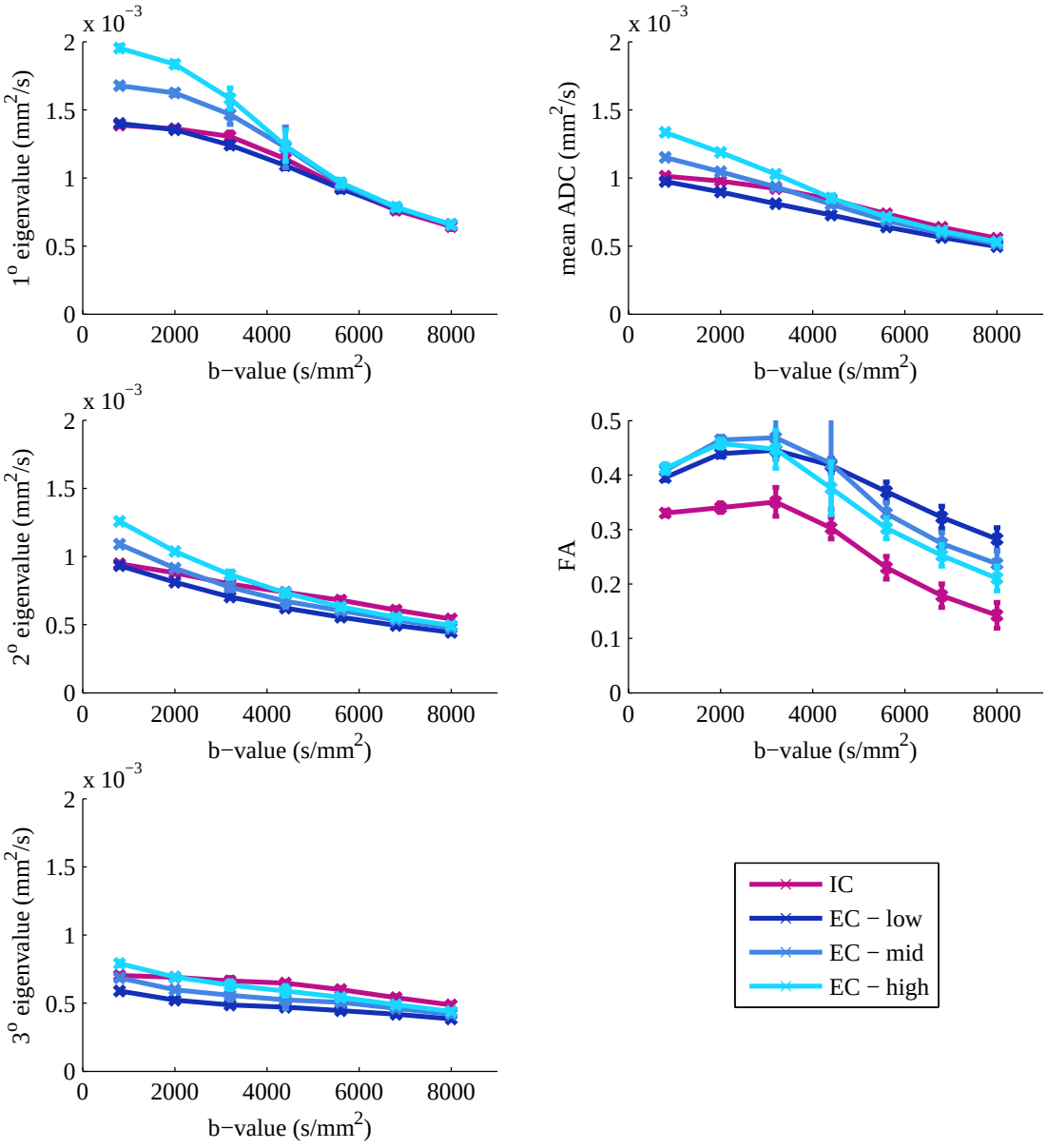

Figure 5.9: DT in EC and IC space. The b-value is altered by gradient strength. Eigenvalues (left, top - λ_1, middle - λ_2, bottom - λ_3), mean ADC (right, top) and FA (right, middle) from the molecules in the IC (pink) and EC space. Diffusivity in the IC space is $1.5 \times 10^{-3}\,\mathrm{mm^2\,s^{-1}}$; three different diffusivities are modelled in the EC space (low = $1.5 \times 10^{-3}\,\mathrm{mm^2\,s^{-1}}$, mid = $1.8 \times 10^{-3}\,\mathrm{mm^2\,s^{-1}}$, high = $2.1 \times 10^{-3}\,\mathrm{mm^2\,s^{-1}}$). Data points are the mean, error bars are ± 1 standard deviation. Data are from 100 gradient directions and 100 repetitions for an SNR of 127.

Figure 5.9 shows the λs, mean ADC and FA from signals for different b-values altered by gradient strength. At the lower b-values, λ_1 and λ_2 are much higher for the EC(high) and EC(mid) than for the IC and EC(low), and they then decrease more rapidly. At the higher b-values, λ_1 is approximately the same for all simulations; the IC and EC(low) have a similar λ_1 for all b-values. λ_2 and λ_3 are higher for the

IC than for all the ECs at higher b-values. All λs are higher for EC(high) than EC(mid), and for EC(mid) than EC(low). The mean ADC starts high for EC(high) then decreases more rapidly. The FA is higher for all ECs than IC. At lower b-values the FA is similar for all ECs, but EC(high) decreases more rapidly at higher b-values. The geometrical effects are again seen as compared with the IC results, the EC(low) has a similar λ_1 and lower λ_2 and λ_3 , leading to a lower ADC and a higher FA.

Figure 5.10 shows the MRI signals for different diffusion times for a constant b-value of $1600\,\mathrm{s\,mm^{-2}}$. The IC signals have a smaller interquartile range than the EC signals, and the mean signal increases with diffusion time. The EC(high) signal is lower than for the EC(mid), and the EC(mid) lower than the EC(low). The mean and median are similar for the IC signals; for the EC, the mean is higher than the median especially for the EC(high). The EC signals are approximately constant with diffusion time; the IC increases with diffusion time.

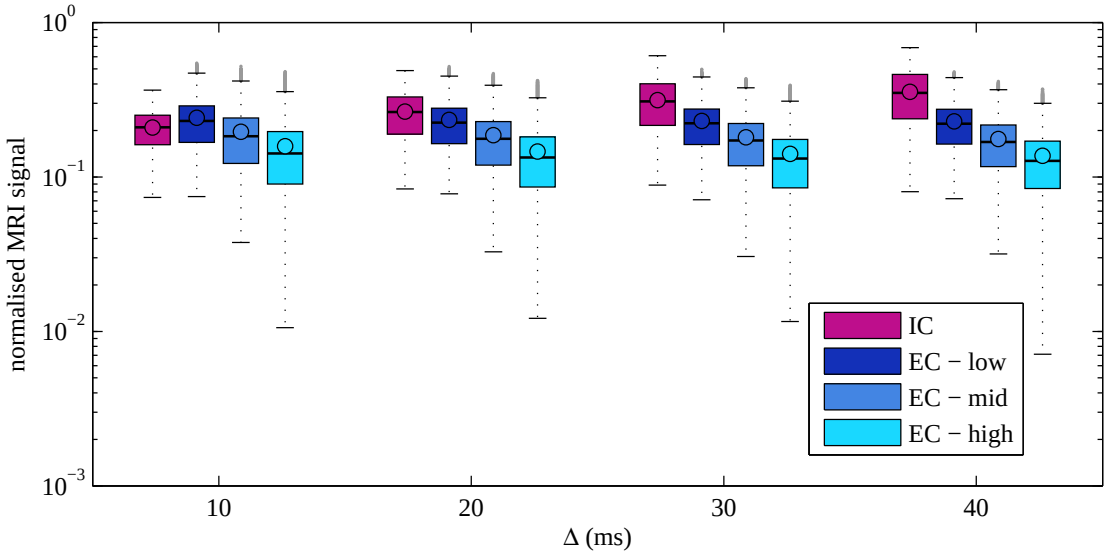

Figure 5.10: MRI signals in EC and IC space by diffusion time. Diffusivity in the IC space is $1.5 \times 10^{-3}\,\mathrm{mm^2\,s^{-1}}$; three different diffusivities are modelled in the EC space (low $= 1.5 \times 10^{-3}\,\mathrm{mm^2\,s^{-1}}$, mid $= 1.8 \times 10^{-3}\,\mathrm{mm^2\,s^{-1}}$, high $= 2.1 \times 10^{-3}\,\mathrm{mm^2\,s^{-1}}$). The b-value is $1600\,\mathrm{s\,mm^{-2}}$. Boxes are inter-quartile ranges with the median as a horizontal line and the circle indicating the mean; whiskers are 1.5 times the interquartile range, and outliers are beyond that. Data are from 100 gradient directions and 100 repetitions for an SNR of 60.

Figure 5.11 shows the λs, mean ADC and FA for different diffusion times for a constant b-value of $1600\,\mathrm{s\,mm^{-2}}$. The λs and mean ADC are higher for the EC(high)

than for the EC(mid), and higher for the EC(mid) than for the IC and EC(low). The λs and mean ADC increase slowly with diffusion time for the EC simulations. For the IC the λs and mean ADC decrease with diffusion time; λ_2 and λ_3 decrease more sharply than λ_1. The FA is approximately the same for all the EC simulations and decreases slowly with diffusion time. The FA for the IC increases with diffusion time.

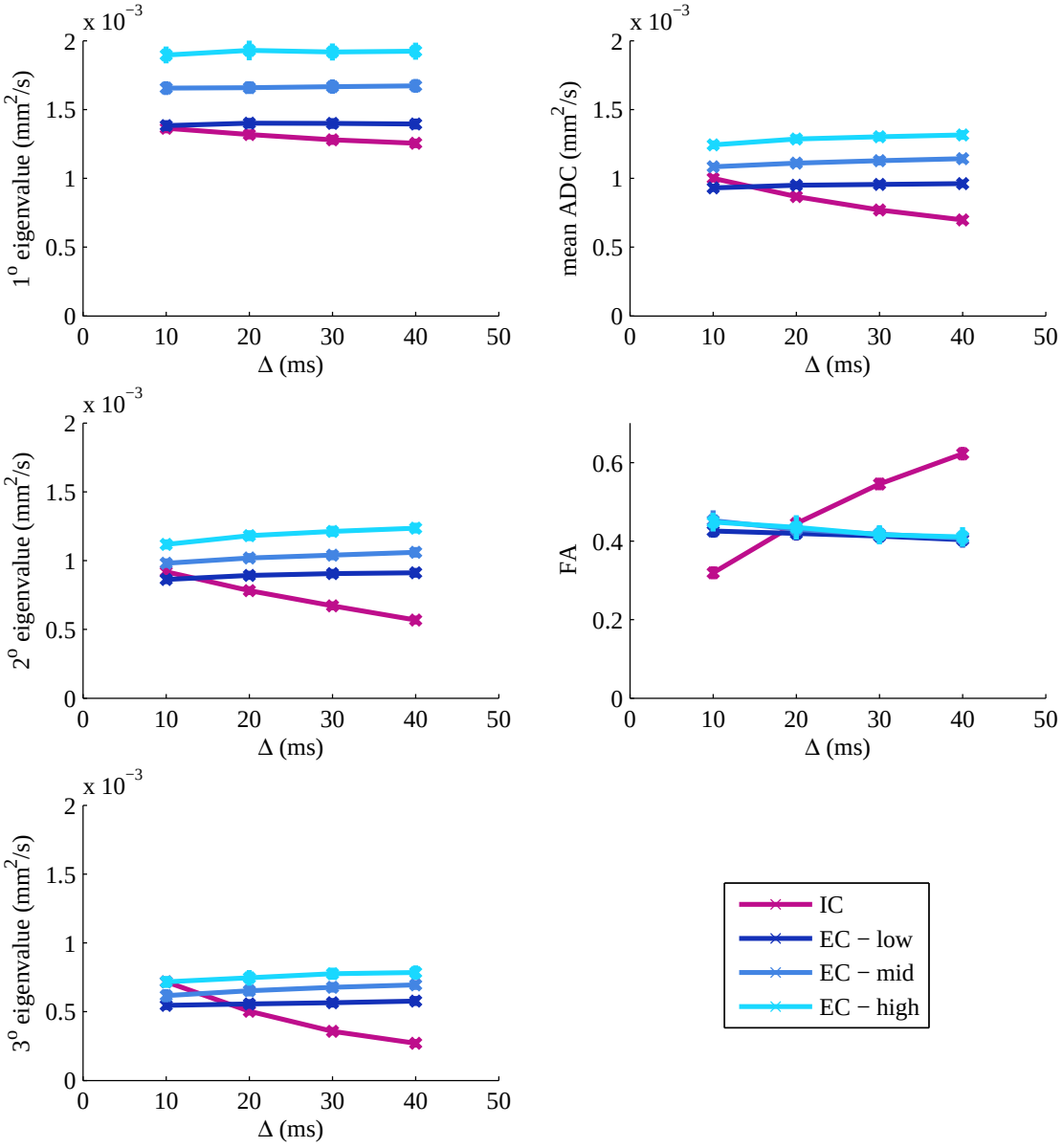

Figure 5.11: DT in EC and IC space by diffusion time. Eigenvalues (left, top - λ_1, middle - λ_2, bottom - λ_3), mean ADC (right, top) and FA (right, middle). Diffusivity in the IC space is $1.5 \times 10^{-3}\,\mathrm{mm^2\,s^{-1}}$; three different diffusivities are modelled in the EC space (low $= 1.5 \times 10^{-3}\,\mathrm{mm^2\,s^{-1}}$, mid $= 1.8 \times 10^{-3}\,\mathrm{mm^2\,s^{-1}}$, high $= 2.1 \times 10^{-3}\,\mathrm{mm^2\,s^{-1}}$). The b-value is $1600\,\mathrm{s\,mm^{-2}}$. Data points are the mean, error bars are ± 1 standard deviation. Data are from 100 gradient directions and 100 repetitions for an SNR of 60.

Effect of different EC diffusivity on overall results

These results are for the combined IC and EC data. Diffusivity in the EC space is 1.5, 1.8 and 2.1 $\times 10^{-3}\,\mathrm{mm^2\,s^{-1}}$ for sim(low), sim(mid) and sim(high) respectively.

Figures 5.12 and 5.13 show the MRI signals for different b-values and diffusion times respectively. There are only very small differences in the simulated data with the different diffusivities. The signals are slightly lower when the EC diffusivity is high. The signals decrease with b-value and increase with diffusion time.

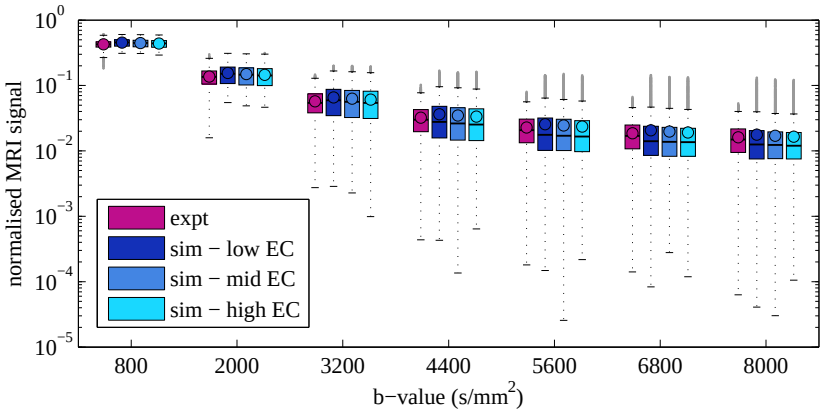

Figure 5.12: MRI signals with different EC diffusivities. The b-value is altered by gradient strength. Boxes are inter-quartile ranges with the median as a horizontal line and the circle indicating the mean; whiskers are 1.5 times the interquartile range, and outliers are beyond that. Data are from 100 gradient directions and 100 repetitions for an SNR of 127.

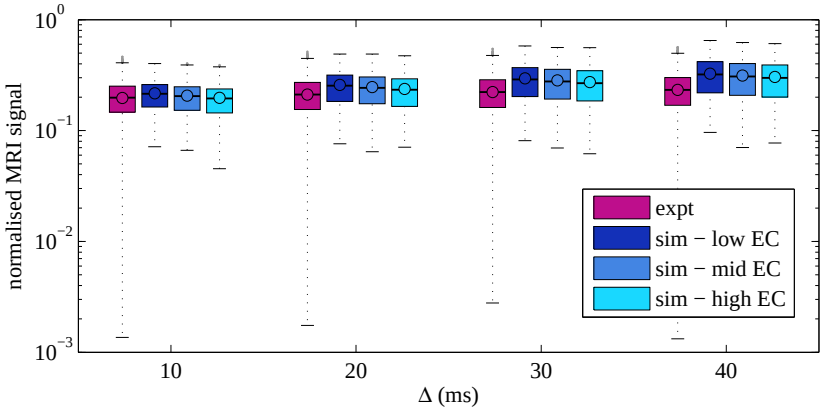

Figure 5.13: MRI signals with different EC diffusivities by diffusion time. The b-value is $1600\,\mathrm{s\,mm^{-2}}$. Boxes are inter-quartile ranges with the median as a horizontal line and the circle indicating the mean; whiskers are 1.5 times the interquartile range, and outliers are beyond that. Data are from 100 gradient directions and 100 repetitions for an SNR of 60.

Figure 5.14 shows the λs, mean ADC and FA for different b-values altered by gradient strength. There are only very small differences with EC diffusivity. At the lowest b-values the λs and therefore the ADC are slightly higher for the sim(high) than for the sim(mid) and the sim(low). At high b-values, the FA is slightly higher for the sim(low) than the sim(mid) and the sim(high).

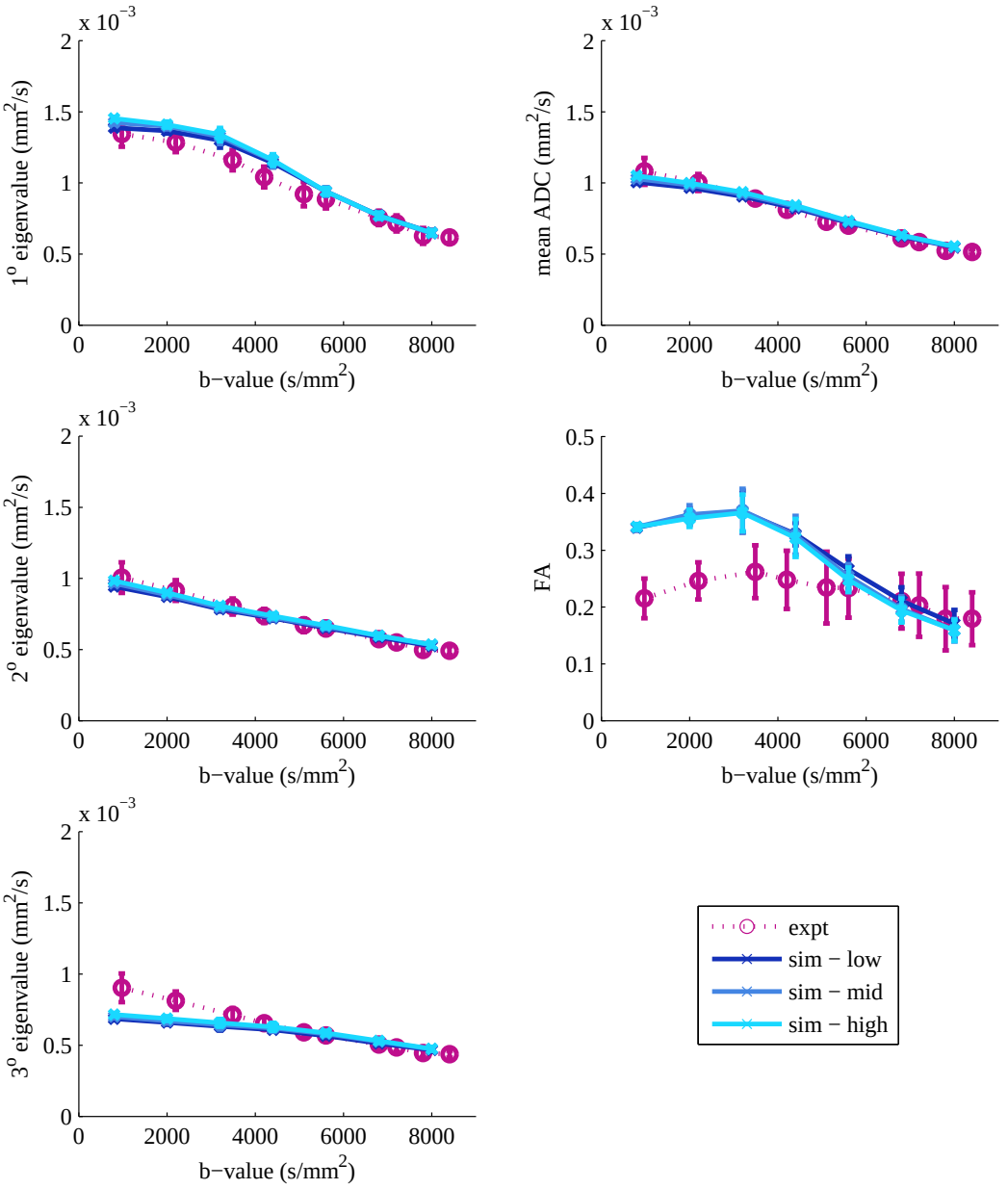

Figure 5.14: DT with different EC diffusivities. The b-value is altered by gradient strength. Eigenvalues (left, top - λ_1, middle - λ_2, bottom - λ_3), mean ADC (right, top) and FA (right, middle). Data points are the mean, error bars are ± 1 standard deviation. Data are from 100 gradient directions and 100 repetitions for an SNR of 127.

Figure 5.15 shows the λs, mean ADC and FA for different diffusion times. The λs and therefore the mean ADC increase very slightly with EC diffusivity. The FAs are the same.

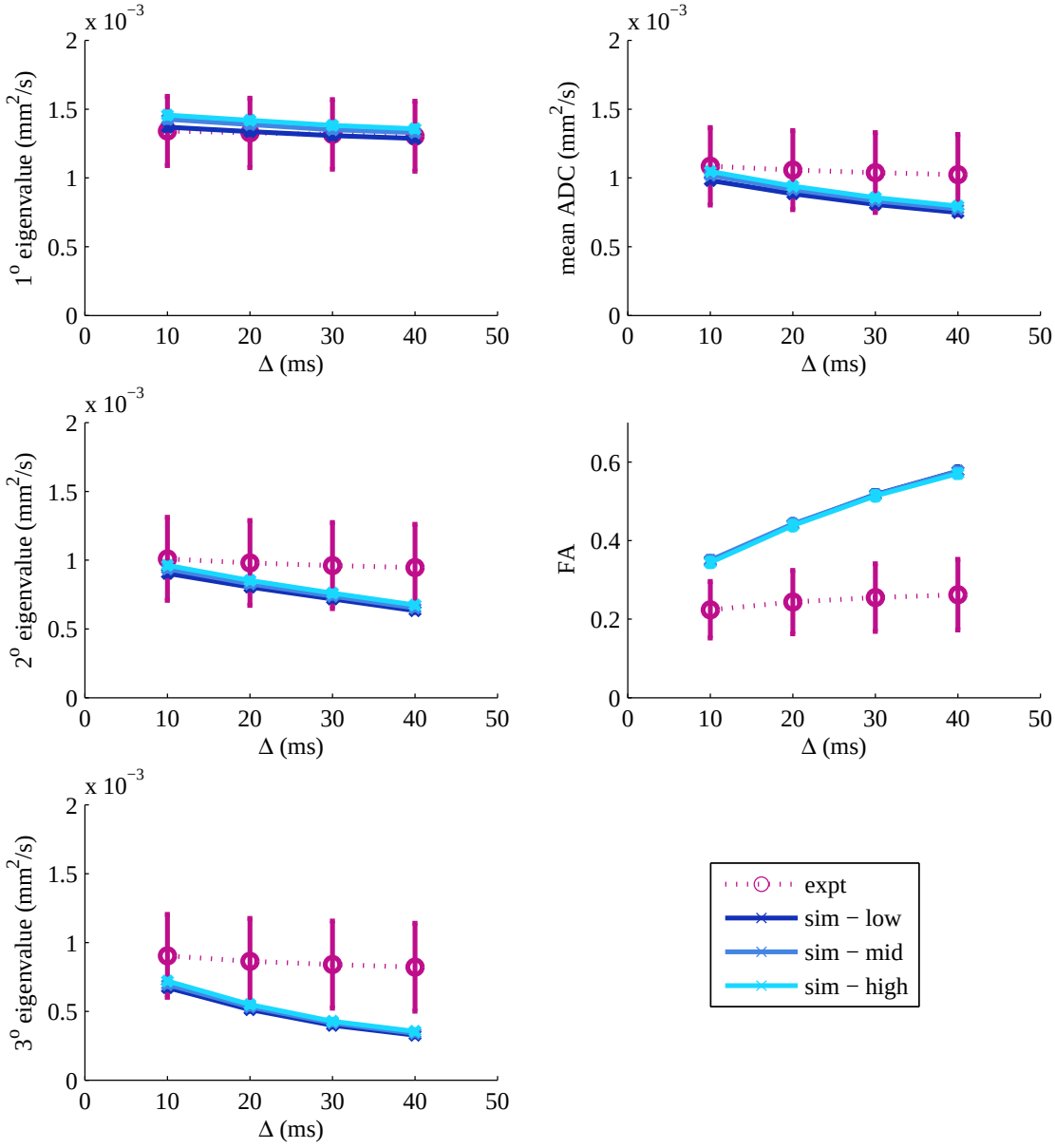

Figure 5.15: DT with different EC diffusivities by diffusion time. Eigenvalues (left, top - λ_1, middle - λ_2, bottom - λ_3), mean ADC (right, top) and FA (right, middle) from the experimental data (pink) and simulated data. The b-value is 1600 s mm^{-2}. Data points are the mean, error bars are ± 1 standard deviation. Data are from 100 gradient directions and 100 repetitions for an SNR of 60.

5.2.4 Discussion

Although when analysed separately, the EC space exhibits different behaviour from the IC space, when the two compartments are combined the effects of changing the EC space are only very small. This is presumably due to the small VF of the EC space (17.5 % in the model).

In the model, the EC space aligns with the cells and therefore both have much smaller restrictions in the direction of the cell long axis than perpendicular to it. Both the cells and EC space have only small restrictions to diffusion in this direction leading to similar λ_1s when the diffusivity is equal. Parallel to the layers, the EC space has two difference sections: the gaps between each cell in a single layer which have the same depth as the cells but are much narrower, and the gap between layers which extend across the width of all the cells but are much narrower than the depth of the cells (see Figure 5.16 for a diagram of the EC space). Overall the EC space is more restrictive both parallel and perpendicular to the layers than the IC space.

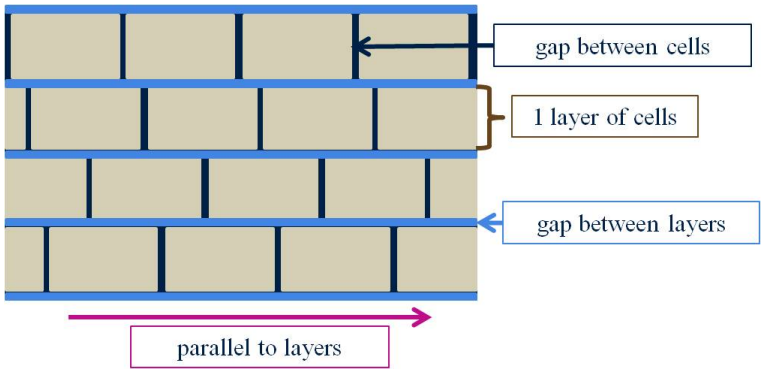

Figure 5.16: Diagram of EC space parallel to layers of cells. The gap between cells within a layer is shown in dark blue, the gap between layers in shown in light blue, cells are beige. The EC space in the direction parallel to the layers consists of the dark and light blue, which have different shapes.

For the separate analysis, λ_1 increases with EC diffusivity at lower b-values, and is approximately the same for the IC and EC(low). λ_2, λ_3 and ADC also increase with EC diffusivity. The higher diffusivity leads to longer diffusion distances, and therefore to higher λs and hence ADC. At the higher b-values, the MRI signals approach the noise floor and therefore no longer display a linear decrease on the

log scale with increasing b-value. This leads to λ_1 becoming equal for the IC and all EC simulations at the higher b-values.

For the effect of diffusion time for the IC space, the λs and therefore the ADC all decrease with diffusion time, and the FA increases. As the diffusion time increases, the probability of reaching the cell membrane in a timestep increases and therefore the apparent diffusion decreases. The effect is more marked along the width and depth of the cells (λ_2 and λ_3) than along the cells (λ_1) and this leads to greater measured anisotropy in a higher FA. For the EC space, the λs and therefore ADC increase with EC diffusivity, and are higher than the IC values, except at the shortest diffusion time. The λs and ADC increase with diffusion time for the EC.

In summary, the effects of the EC diffusivity are very small, due to the small VF. When compared with the experimental data, changing the EC diffusivity does not change the correlation of simulated data to the experimental data, and so does not explain the differences between the simulated and experimental data.

Further work

Increasing the EC diffusivity had little effect on the results, which is perhaps unsurprising given the small VF of the EC space. Diffusivity, however, remains an interesting topic for further investigation.

It would be helpful to have further experimental values for the IC and EC diffusivity in myocardial tissue, and to explore the inherent anisotropy within cells. There are ways this could be done. As Silva et al. [162] did for the brain, IC contrast agent could be used to allow diffusivity for IC only and combined IC and EC compartments to be calculated. To investigate IC anisotropy, very short diffusion times could be used, although myocytes are probably too small for this to be experimentally feasible. An alternative would be to use 'skinned' cells where for a sample of myocytes, the cell membranes are dissolved so that this restriction to diffusion is

removed and any anisotropy measured is therefore due to IC components. The Aslund method [164] could also be used to determine the IC and EC diffusivities.

The biexponential model is commonly used in fitting dMRI data, and the dMRI data fits well to the model. It produces two DTs, one for the 'fast' and one for the 'slow' compartment and a VF for each compartment. It was originally thought that the two compartments relate to the IC and EC space, but the VFs do not correlate with the known VFs of IC and EC. In both the heart and the brain, the VFs are the opposite of that expected [62, 166].

Sehy et al.'s [63] study of IC diffusion in oocytes found that the biexponential model fits well to the IC diffusion data with similar results to those found in the brain (89 % 'fast' and 11 % 'slow'). Galons et al.'s [64] work on glioma cells also found that the IC results fit the biexponential model. These results further support the idea that diffusion may not be able to be divided simply into IC and EC, but that there are more complex variations occurring. The most plausible explanation is that the 'slow' compartment relates to water bound near the membrane and to proteins, and the 'fast' compartment is the bulk IC and EC water. Further biexponential analysis could be carried out to generate appropriate parameters to model the slow diffusing membrane layer.

5.3 Summary of chapter

In this chapter I investigated the effect of two parameters on the dMRI model: the permeability of the cell membranes and the extra-cellular diffusivity to determine whether they had a significant effect and whether they could explain the differences between the simulated and experimental data in Chapter 4.

Cell membranes are permeable to water molecules and have been shown in previous work [108] to have an effect on the FA. Diffusivity was found in the sensitivity analysis in Chapter 3 to be the most important input parameter, and a review of the

literature shows that there may be differences between IC and EC diffusivity [141], anisotropy of IC diffusivity [168] and even variable diffusivity within a cell [63].

Introducing permeable membranes only had a very small effect on the results when using ex vivo values for permeability at room temperature. Permeability is strongly influenced by temperature and therefore the in vivo effect may be more marked.

Increasing the EC diffusivity in the model compared with the IC diffusivity has very little effect on the dMRI results, presumably due to the small VF of the EC space.

There remain many unknowns regarding IC and EC diffusion, including their relative values and the degree of anisotropy. The biexponential model suggests there may be inhomogeneity within the IC space. These would all be of interest to investigate experimentally, especially as diffusivity is important in models of dMRI.

6

The effects of disarray

In this chapter I model type IB disarray as found in hypertrophic cardiomyopathy (HCM) to investigate whether diffusion MRI (dMRI) could be a useful tool in identifying and quantifying disarray in disease. I show that changes in the amount of disarray affect the dMRI results and that the model could therefore help understand the relationship between disarray and dMRI data.

6.1 Background

As discussed in Chapter 2, in pathology there is often remodelling of the cardiac microstructure. This can take many forms, including disarray, fibrosis, cell hypertrophy and intracellular changes [38]. In this chapter, I focus on disarray, where the regular microstructure of the heart tissue becomes disorganised, especially that found in HCM. The disarray found in HCM is thought to cause the disruption to the electrical signals which can lead to sudden cardiac death (SCD) [19]. Implantable defibrillators are used in patients deemed at high risk of SCD, but there are significant risks associated with these which makes identifying these high-risk patients very important. If dMRI could quantify the amount of disarray then this could be used

to assess risk, stratify patients and guide treatment. The first step in using dMRI to quantify disarray is to understand how changes in disarray affect the dMRI signal.

6.1.1 Classification and quantification of disarray

Maron and Roberts [28] used histological sections of post-mortem human hearts with and without HCM to classify and quantify disarray. They defined four types of disarray as shown in Figure 6.1, and in diagrammatic form in Figure 6.2.

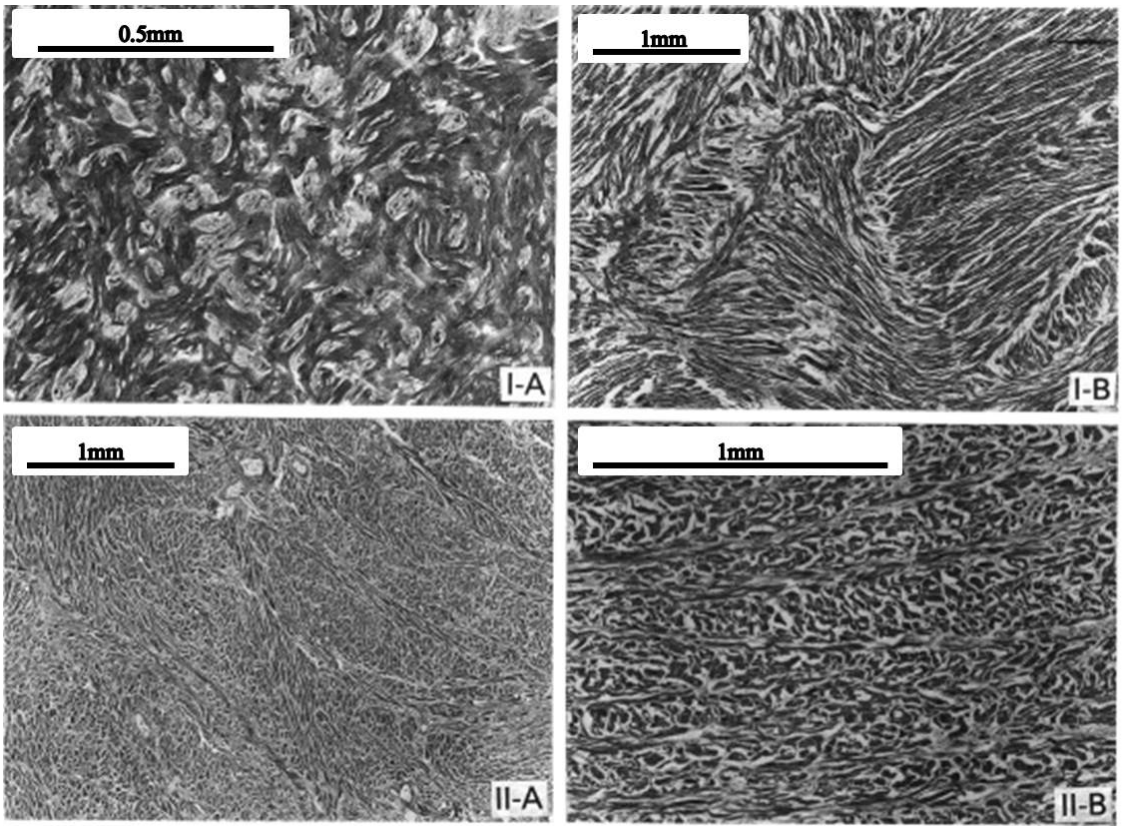

Figure 6.1: The four types of disarray as defined by Maron and Roberts [28]. Reproduced from Maron and Roberts [28] with permission.

Types IA and IB are identified when the cells are cut longitudinally, types IIA and IIB are found when the cells are cut transversely. It is not therefore possible to identify both types in the same area as cells will either be cut longitudinally or transversely. Type IA is the most common type and is described as areas where

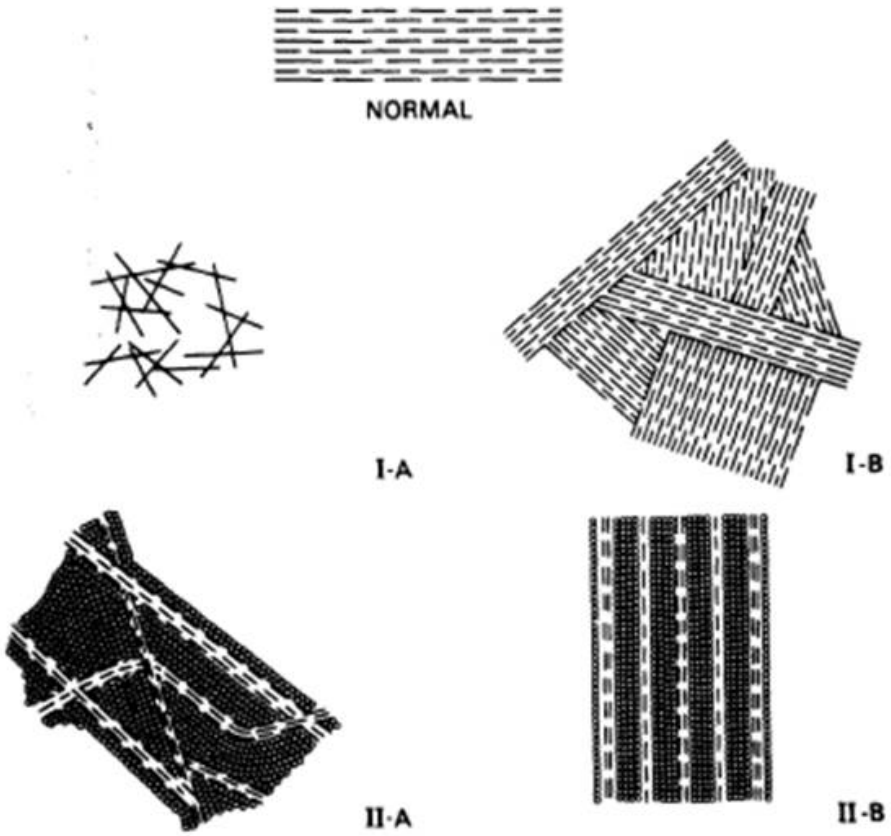

Figure 6.2: Diagram of types of disarray. Diagrammatic representation of the four types of cardiac muscle cell disorganization. Normal arrangement of cardiac muscle cells is shown at the top for comparison. Reproduced from Maron and Roberts [28] with permission.

myocytes are aligned perpendicularly or obliquely to adjacent myocytes leading to tangled masses or a pinwheel configuration. The lesions vary in size, but are mainly small. There are a wide range of varieties of this type of disarray, as shown in Figure 6.3. Type IB has bundles of cells oriented perpendicularly or obliquely to each other. Within each bundle, the cells are arranged normally. Type IIA has narrow bundles of longitudinally-cut cells interspersed within larger groups of transversely-cut cells in various directions. The narrow bundles are usually one or two cells wide, and this gives a swirled pattern. Type IIB is similar to type IIA, but the narrow bundles are straighter.

To quantify the extent of the disarray, Maron and Roberts [28] manually outlined type I and type II disarrayed areas on histology images, as well as defining which areas were transversely or longitudinally cut. They excluded areas with blood

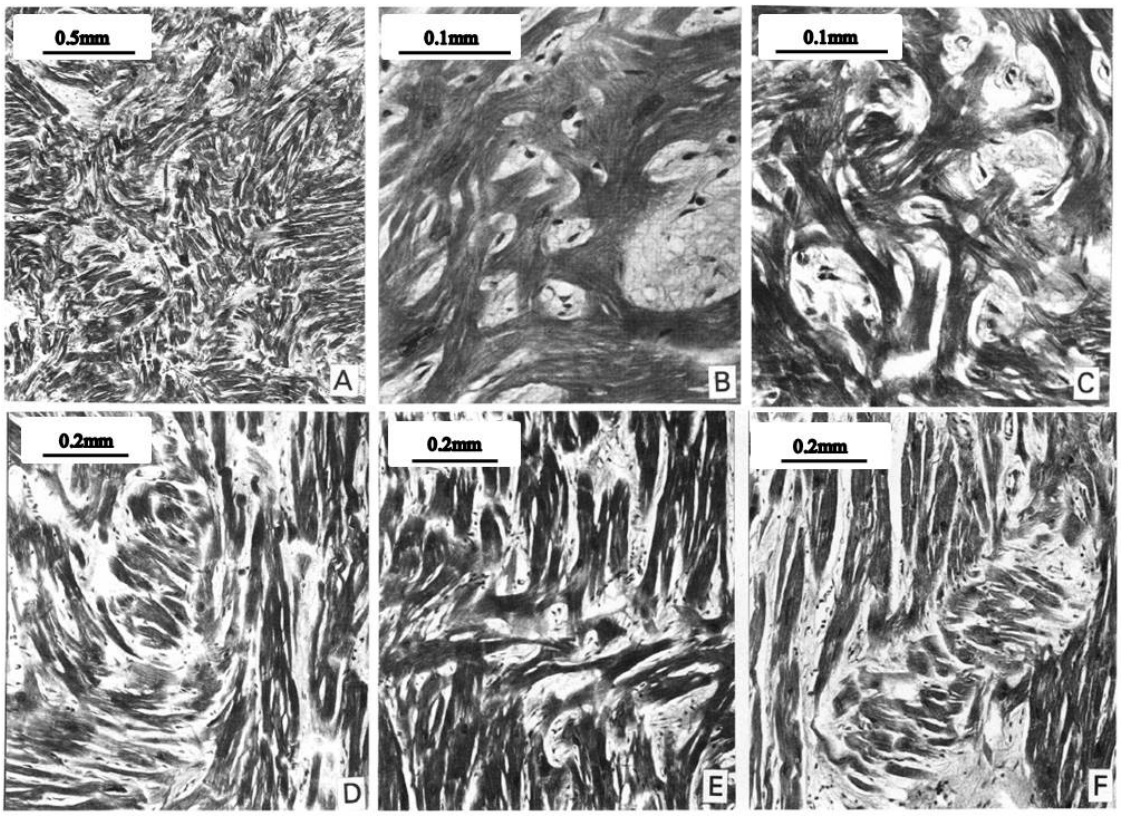

Figure 6.3: Examples of type 1A disarray. A) "Chaotic" pattern in which adjacent cells are arranged at perpendicular and oblique angles to each other; B) "Swiss cheese" appearance that results when adjacent cells are oriented at particularly acute angles; C) Tangled arrangement of cardiac muscle cells in whorled configurations; D) Whorl pattern in which some cells are oriented circumferentially to other cells; E) and F) Patterns in which small groups of cells are oriented at extremely acute angles to larger groups of cells. Reproduced from Maron and Roberts [28] with permission.

vessels, fibrosis or excessive gel. The extent of the disarray was calculated as follows:

$$typeI = \frac{D_I}{L + D_I} \times 100 \tag{6.1}$$

$$typeII = \frac{D_{II}}{L + T + D_{II}} \times 100 \tag{6.2}$$

where D_I and D_{II} are respectively the area on the histology image classified as type I or type II, and T and L are the areas classified as transversely or longitudinally cut on the histology image.

Maron and Roberts [28] studied the ventricular septum of 54 post-mortem HCM hearts, of whom 48% died from SCD. They found type IA disarray was present in 85% of the hearts, type IB disarray in 46% of the hearts, type IIA in 11% of the hearts and type IIB in 9% of the hearts. The mean extent of disarray was 31%. In a later study, Maron et al. [29] analysed the left ventricular (LV) wall of 52 post-mortem hearts with HCM, of whom 52% had died from SCD. They found type IA to be the most common form of disarray occurring in 66% of hearts in the LV anterior free wall and 64% in the LV posterior free wall. Type IB occurred in 34% and 33% of the anterior and posterior LV free walls respectively. Type IIA was only found in one heart, in the posterior LV free wall, and no hearts showed type IIB disarray. The mean extent of disarray was 32% in the anterior free wall and 15% in the posterior free wall. The total extent per heart ranged from 0% to 80%.

Noda [38] analysed one endomyocardial biopsy from each of 62 living HCM patients. They used their own 5-point scale to classify disarray (none, 1+, 2+, 3+ and 4+), where grade 1+ indicates only minimal and focal myofibre disarray and grade 4+ indicates marked disorientation of the myofibres throughout the biopsy. They found that 78% of RV biopsies and 72% of LV biopsies showed disarray, mostly at grade 1+ or 2+.

Kuribayashi and Roberts [30] graded disarray in 47 post-mortem HCM hearts, of whom 62% died from SCD. They used their own 4-point scale (none, 1+, 2+ and 3+) dependent on the level of disorder of the muscle fibres in the midwall layer, where grade 1+ meant fibres were slightly deviated from a parallel alignment, and grade 3+ meant there was no circular unit of muscle bundle. In the LV, disarray was present in 11% of hearts in the lateral free wall, 56% in the posterior free wall and 64% in the anterior free wall. The degree of disarray was mostly graded as 1+ or 2+. Levels of disarray were much higher at the junction of the LV and RV: 93% and 84% in the anterior and posterior junctions respectively, with over 50% of hearts graded at level 3+.

Varnava et al. [40] quantified disarray in 72 hearts with HCM at either death or transplant. They took 19 sections from different locations in the heart and for approximately 60 fields per section scored type IA disarray as either present or absent. They found large variations in the extent of disarray within individual hearts, ranging from less than 10% in one section to over 90% in another section. There was also variation within sections. The mean extent of disarray ranged from 12.9% in the mid-level lateral wall to 30.5% in the mid-level anterior septum.

Morimoto et al. [39] scored type IA disarray as present or absent at approximately 900 sites for each of 16 post-mortem hearts with HCM. They found the mean extent of disarray ranged from 67.4% in the ventricular septum in the transverse plane to 12.4% in the RV free wall in the longitudinal plane. In individual hearts, the extent ranged from 1.2% to 100%.

To my knowledge, the only study that quantifies the angle of disarray was by Masuda et al. [36]. They took microphotographs of the biopsies of the myocardium from living patients, eight with HCM and eight controls, and magnified them 250 times. They drew the long axis of each myocyte and then calculated the standard deviation of the angles, as shown in Figure 6.4. In the control hearts the standard deviation was 15.0 ± 5.2, in the HCM hearts it was 38.8 ± 8.3.

The studies by Noda [38] and Masuda et al. [36] used biopsies of living patients, while all the other studies used post-mortem hearts, approximately half of whom had died from SCD. If the degree or extent of disarray is related to SCD, as proposed by Varnava et al. [47], then there may be an overestimation of the disarray due to the high proportion of SCD subjects within these studies. The two biopsy studies also show large amounts of disarray and may also be an overestimation of the general HCM population. Noda's [38] subjects had the biopsies taken during cardiac procedures and were therefore presumably displaying symptoms of HCM at the more severe end of the spectrum. Masuda et al. [36] do not state when their biopsies were taken and therefore the level of symptoms of the subjects is unknown.

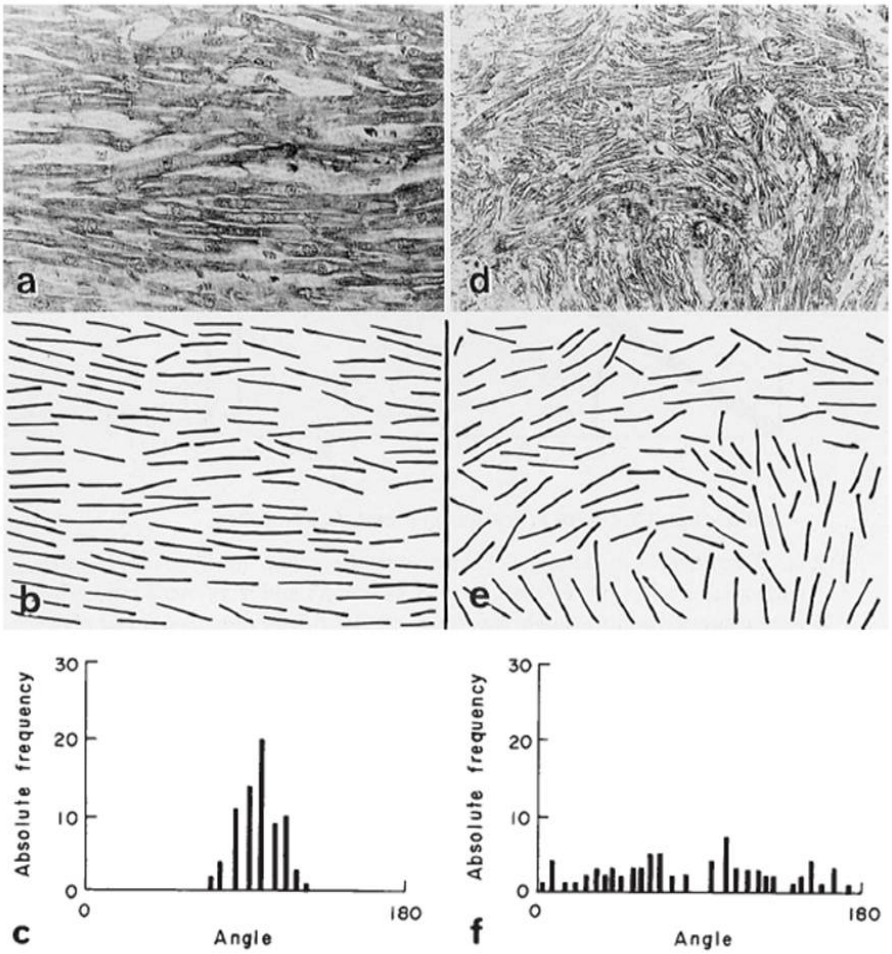

Figure 6.4: Measurement of myocyte orientations. (a and d) Microphotographs of the myocardium (x250). (b and e) Direction of myocytes traced onto transparent sheets. (c and f) Histogram of myofibre angles. Reproduced from Masuda et al. [36] with permission from Tohoku University Medical Press.

Overall, disarray is present in a large proportion of HCM patients. The prevalence depends on the area of the myocardium that is measured, but is approximately 60-80%. The extent of disarray also varies a large amount, from 0 to 100% depending on measurement technique, area of the myocardium and individual subjects.

6.2 Methods

Although it is the most common type of disarray, Type IA disarray has a wide variety of subtypes (Figure 6.3). Type IB is the second most common, is more consistent, and is simpler to model. I therefore decided to start by modelling this type.

Figure 6.5 shows type IB disarray from Maron and Roberts [28] with a voxel of 200 µm superimposed. It shows that it is likely that a single voxel would contain no more than two cell orientations due to the size of the sections of aligned cells compared with the voxel size. I therefore modelled two sections of aligned cells, each taking up half of each layer of cells.

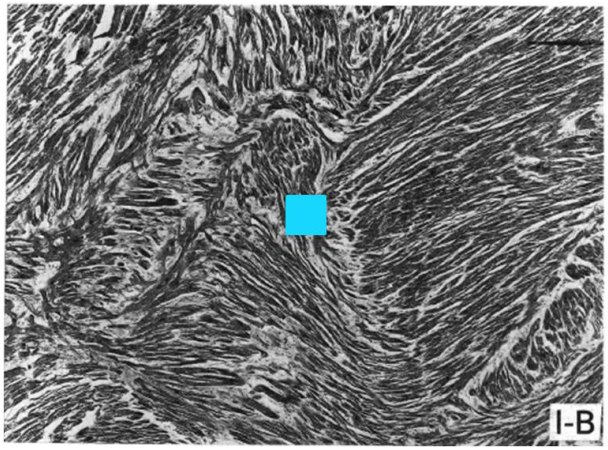

Figure 6.5: Type IB disarray. 200 µm voxel superimposed in turquoise to show scale. Reproduced from Maron and Roberts [28] with permission.

For each layer with disarray, I created cells in the two halves as shown in Figure 6.6. From Maron and Roberts' [28] images and figures as seen in Figures 6.1 and 6.2, the angles between two sections of aligned cells can take any value. I therefore angled the cells in each half so that the total angle between them was 0°, 15°, 30°, 45°, 60° and 75°. I have termed this the 'angle of disarray'.

From the studies which measured the extent of disarray in a sample, this varies considerably and can be up to 100% [39]. I therefore modelled the proportion of the simulated tissue that was disarrayed from 0% to 100%, in steps of 20%. I refer to this as the 'extent of disarray'.

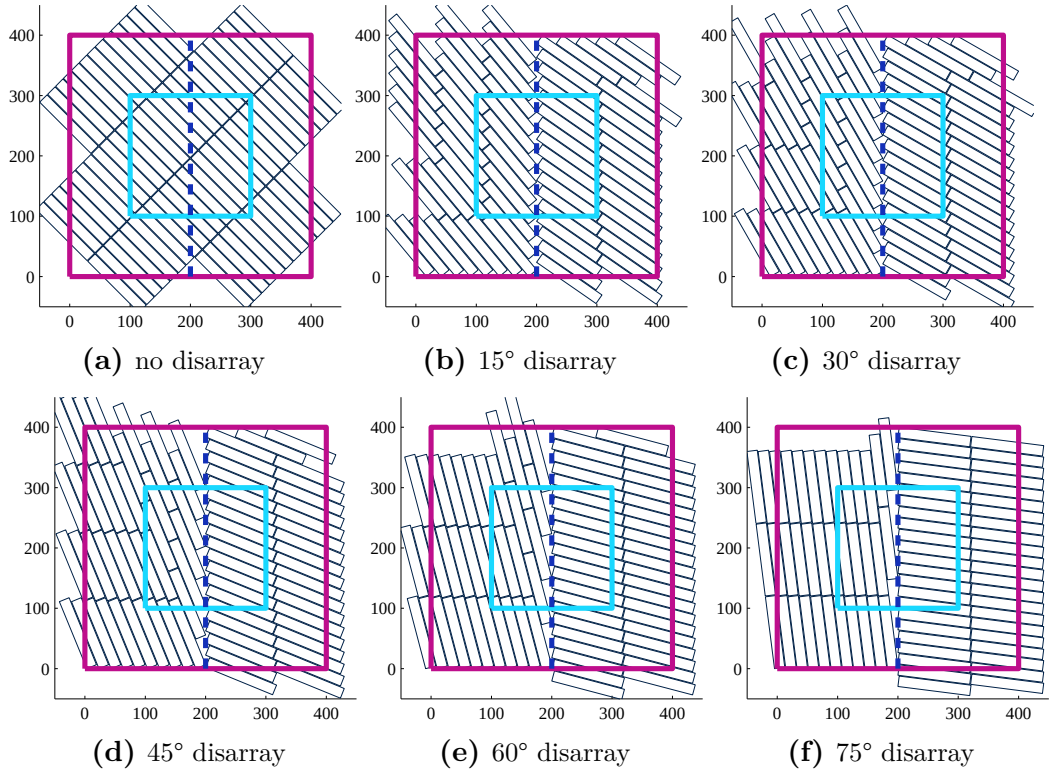

Figure 6.6: Disarray set-ups for comparable slices for different angles of disarray.

There are no 3D histology studies of disarray available in the literature, so the changes through the voxel are hard to ascertain. I therefore kept the parallel layers of cells, each of which was either disarrayed or not disarrayed. To my knowledge, there is no published data on how thick the disarrayed layers are. However, it seems unlikely that there would be alternating layers of disarrayed and non-disarrayed layers. I therefore assumed that there were two populations of cells through the voxel: disarrayed and non-disarrayed. This set-up can be seen in Figure 6.7.

The model and simulation parameters are in Table 6.1. I simulated the data using a single set of MRI sequence parameters. I chose these parameters as the timings are similar to those used in the studies in Chapter 4, and the b-value in the range that is used in both ex vivo and in vivo studies. As for previous studies, I used a timestep of 2 µs and a density of molecules of $1 \times 10^8\,\mathrm{mm}^{-3}$.

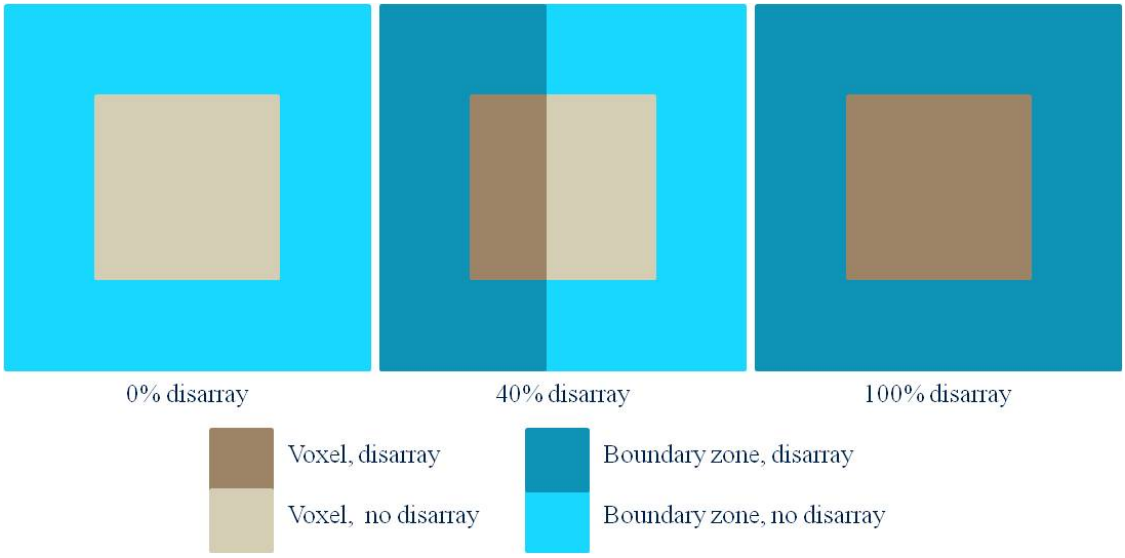

Figure 6.7: Diagram showing different extents of disarray. View is side-on to the layers. Percentage is for central voxel (beige).

Table 6.1: DTI sequence and model parameters for type IB disarray simulations.

parameter	units	value
diffusion pulse duration, δ	ms	4
diffusion interval, Δ	ms	9
b-value	$\mathrm{s\,mm^{-2}}$	1500
gradient strength	$\mathrm{T\,m^{-1}}$	0.41
voxel size	$\mu\mathrm{m}^3$	$200 \times 200 \times 200$
total simulation volume	$\mu\mathrm{m}^3$	$400 \times 400 \times 400$
timestep	μs	2
total number of molecules		6.4×10^6
number of molecules in voxel		8×10^5
no. of gradient directions		100
SNR		127
cross-sectional area	$\mu\mathrm{m}^3$	200
length	μm	120
aspect ratio (thickness/width)		0.67
volume fraction of myocytes		0.825
diffusivity	$\mathrm{mm^2\,s^{-1}}$	1.5×10^{-3}
helix angle rate	$^\circ\,\mathrm{mm^{-1}}$	75
angle of disarray	$^\circ$	0, 15, 30, 45, 60 and 75
extent of disarray	%	0, 20, 40, 60, 80 and 100

6.3 Results

Figure 6.8 shows the effect of type IB disarray on the MRI signal. As either the extent or the angle of disarray increases, the inter-quartile and total range of MRI signals decreases. The mean MRI signal stays constant.

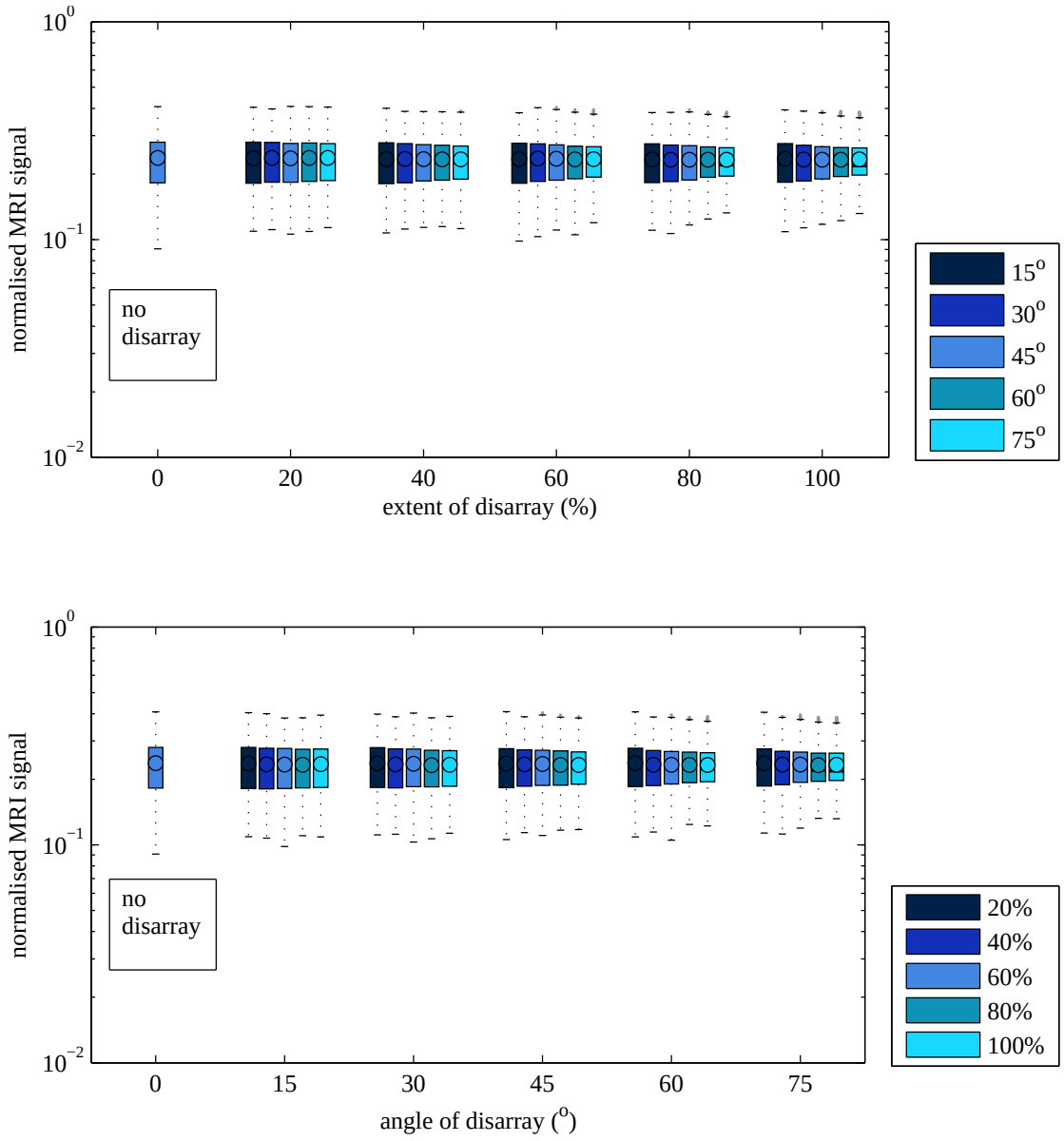

Figure 6.8: Disarray MRI results. Top figure is by extent of disarray, with different angles of disarray in different colours. Bottom figure is by angle of disarray, with different extents of disarray in different colours. Far left box shows no disarray results. Boxes are inter-quartile ranges with the median as a horizontal line and the circle indicating the mean; whiskers are 1.5 times the interquartile range, and outliers are beyond that.

Figures 6.9 and 6.10 show the DT results by angle and extent of disarray. As either the angle or extent of disarray increases, λ_1 decreases, λ_2 increases and the FA decreases. λ_3 and the mean ADC remain approximately constant.

The angle and extent of disarray have similar effects on both the MRI signals and the DT.

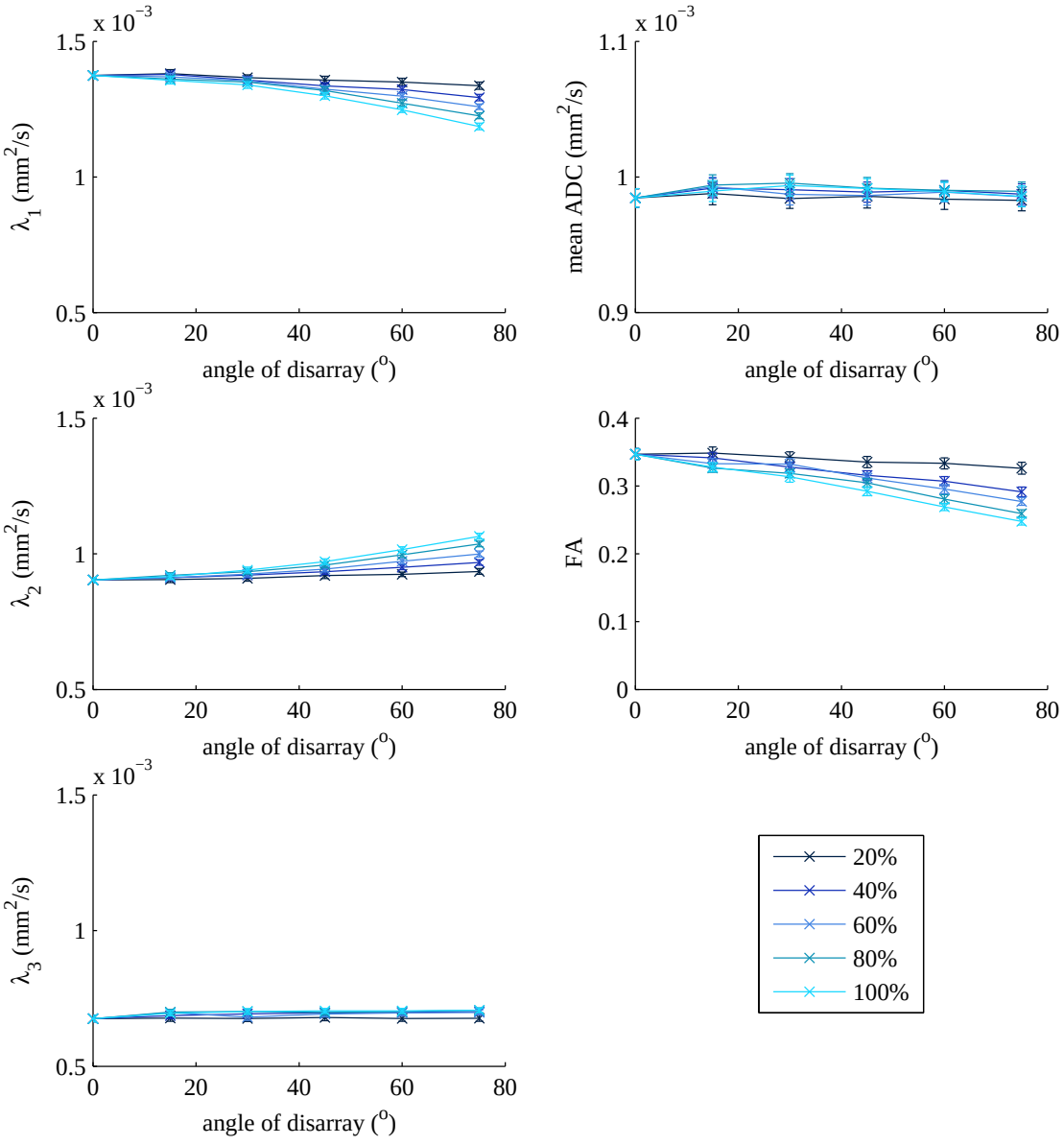

Figure 6.9: Disarray DT results by angle of disarray. λs (left), and mean ADC and FA (right) by angle of disarray. Different extents of disarray are in different colours.

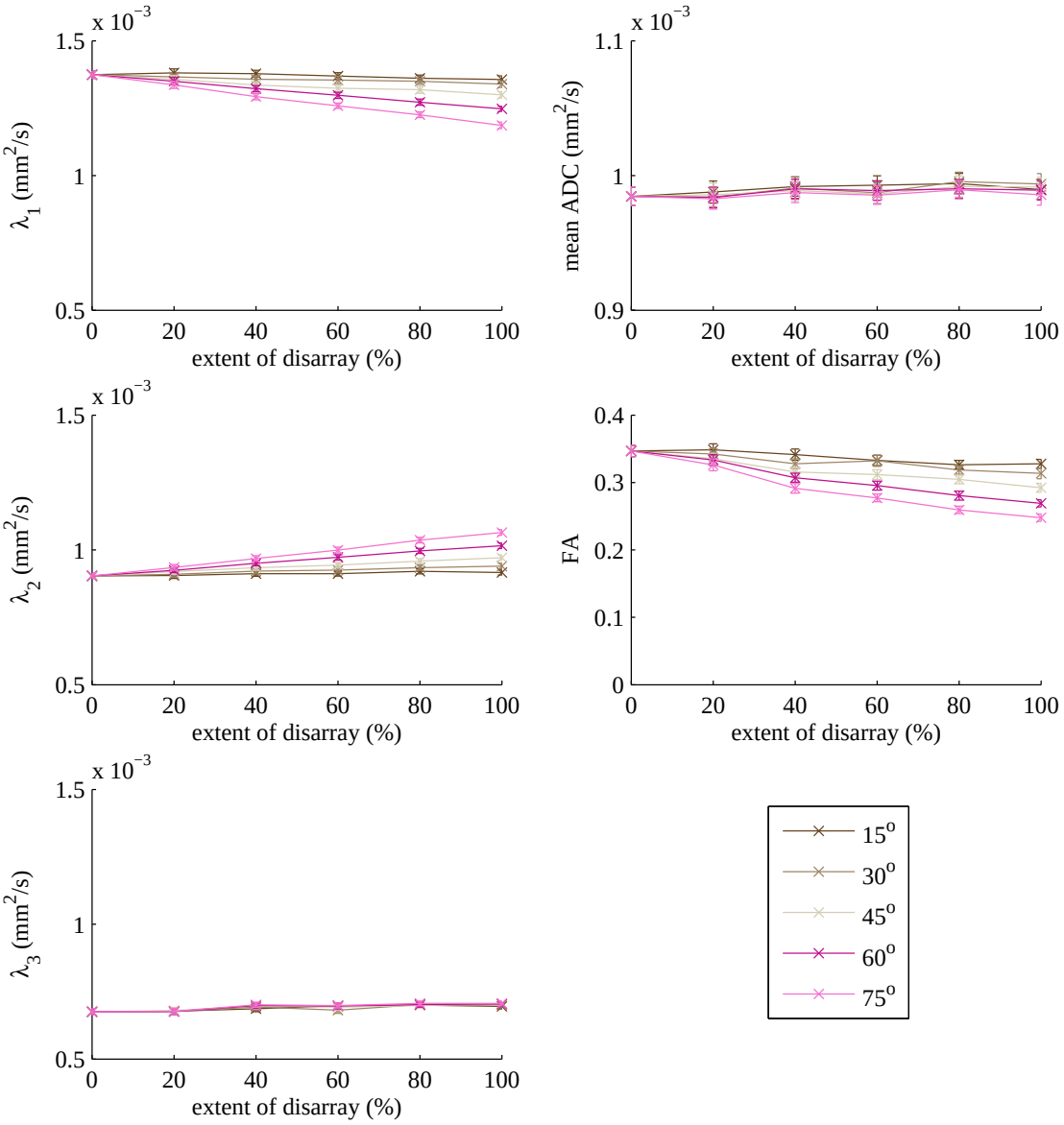

Figure 6.10: Disarray DT results by extent of disarrayed tissue. λs (left), and mean ADC and FA (right) by extent of disarray. Different angles of disarray are in different colours.

6.4 Discussion

To my knowledge, this is the first study which models myocardial disarray and its effect on the dMRI signal. The results show that type IB disarray affects λ_1, λ_2 and the FA and therefore measuring these parameters in hearts with HCM could help detect and quantify the amount of disarray in these hearts. These results show that the model may help uncover the relationship between disarray and dMRI signals.

In this model of type IB disarray in HCM, when the angle or extent of disarray increases, the range of MRI signals, λ_1 and the FA decrease, while λ_2 increases. As the disarray increases, the restrictions to diffusion become more similar in each direction within a layer. This leads to less variation in the MRI signals over the different gradient directions. In this model of disarray the layers remain parallel to each other, therefore the addition of disarray has no effect in the direction perpendicular to the layers, and λ_3 remains approximately constant. There is no change in the mean ADC since the cell sizes and therefore the lengths of restriction are unchanged. At mid-range disarray with an angle of 45° and extent of 60% the changes in the λs are only small: λ_1 decreases by 4% and λ_2 increases by 4%, compared with no disarray. These changes in λ_1 and λ_2 lead to larger changes in the FA (10% decrease at a degree of 45° and extent of 60%). This suggest that FA would be the most likely parameter to show clinical changes.

One in vivo study has shown that FA is decreased in HCM compared with controls, especially in the septum [95], which corresponds with the changes I found in my model. Tseng et al. [95] also found lower helix angles, while Ferreira et al. [96] found changes in the secondary eigenvector in diastole. As my model is currently of a single voxel, I cannot meaningfully analyse the changes in angles and eigenvectors, especially in different contraction states.

6.4.1 Current limitations, difficulties and unknowns

There are many types of disarray, as well as variation within the types. In this work I have only modelled type IB disarray, as this is less variable than type IA disarray and is simpler to model. I have, however, simplified this disarray by assuming that there are still parallel layers of cells. Type IIA and IIB disarray are found when the cells are cut transversely and therefore show changes between the layers of cells. Neither of these types are commonly found in HCM [29] and it is therefore a reasonable first approximation to assume that there are no changes in this direction. However, the assumption that the layers of cells are parallel to each other is already a simplification in normal tissue, and this assumption may be less valid in diseased tissue.

The variation in type IA disarray presents a significant modelling challenge, especially given the lack of quantification of disarray. Masuda et al. [36] is the only work I have found on quantifying the degree of disarray, and is a 2D measurement of the variation of the orientation of the long axis of the cells. There is a lack of detailed knowledge regarding the 3D arrangement of myocytes, especially in disease, which inhibits both the modelling of disarray, and the general understanding of how disarray may affect the heart's function.

Type IA modelling as shown in Figure 6.2 consists of individual cells arranged at random angles relative to each other. Masuda et al. [36] found that the angle of the cells in type IA disarray varies between 0 and 180°. In modelling, introducing variable orientations of the cells while maintaining the required volume fraction of cells is challenging, as found by Yeh et al. [110] in their modelling of the brain.

6.4.2 Future work

So far I have only modelled type IB disarray; modelling the other types of disarray, especially all the variations of type IA will be essential in understanding how to use

dMRI to identify and quantify disarray in diseased hearts. As well as disarray, there are other remodelling changes in disease. In HCM, changes include increased wall thickness [28], hypertrophy of myocytes [38], fibrosis, and small vessel disease [40]. These changes could all be introduced into the model. Cell sizes are already a model parameter and therefore increasing the CSA and length of the cells is straightforward; the sensitivity analysis in Chapter 3 showed that the CSA is an important parameter on both the FA and the mean ADC and this would therefore be expected to show changes in disease. Fibrotic areas in the heart have been shown to have a lower FA and higher mean ADC [37] and could perhaps therefore be modelled as a fairly homogeneous area with small restrictions to diffusion. Vessels are introduced into the model in Chapter 7; it would be straightforward to change their parameters.

As Lin et al. [103] found when modelling the effects of traumatic brain injury, different physiological changes can have opposing effects on the DT and its derivatives. The DT may not therefore be sufficiently sensitive to determine the effects of disarray and more complex models may be needed to analyse dMRI data. Different models were discussed in Section 2.3.3; non-Gaussian or multi-compartment models could prove to be better ways of analysing the data from pathological hearts. Each of them is a different method of analysing the dMRI signals and could therefore easily be used to analyse the dMRI signals simulated by the model.

The limited knowledge of the 3D structure of the heart is a challenge when modelling the cardiac microstructure. Colleagues are working on two studies which may improve this understanding. Initial results from our group, led by Dr Ramon Casero, show the possibility of reconstructing 3D histology images from parallel slices covering a complete murine heart. Dr Irvin Teh [170] has recently acquired synchrotron images of mice hearts, along with DT imaging.

Using a mesh generated from either the histology or synchrotron imaging as the input geometry of the model would be helpful in two ways. Firstly, it could be used to better quantify disarray, particularly in 3D. Secondly, it would allow further

validation of the model. Using the synchrotron images as a mesh input to the model and comparing this with the DT would be a good validation of the modelling method.

Taking a mesh from 3D histology or synchrotron images avoids the need for an algorithm to create the model geometry. However, it does not allow the geometry to be changed in a controlled manner, which is the main advantage of using a parameterised geometry model, as we can change the structure and parameters by a known amount and measure the effects of these on the output. We can also fit the simulated data to many different models to investigate which will best allow us to discern changes in the underlying physiological geometry.

6.5 Summary of chapter

In this chapter I present the first model, to my knowledge, of myocardial disarray and its effect on dMRI results. I show that type IB disarray in HCM can be modelled and changes in the dMRI signal measured. These results show that the model may help uncover the relationship between disarray and dMRI signals.

I modelled type IB disarray as found in HCM hearts. I varied the extent of disarray, that is the proportion of the voxel containing disarrayed cells, and the angle of disarray, that is the relative alignment of the two sections of cells within a layer. As the angle or extent of disarray increases, the range of MRI signals, λ_1 and the FA decrease, while λ_2 increases.

The work in this chapter is preliminary work which demonstrates that it is possible to model disarray within an MC model and to achieve plausible results. There are many unknowns regarding the changes that occur in disarray which make modelling challenging but recent advances in imaging and image reconstruction should improve this.

Future work will be to model different types of disarray in conjunction with other remodelling such as fibrosis and cell hypertrophy. The interactions of these physiological changes may mean that the DT is insufficiently sensitive to quantify and differentiate these changes. Multi-compartment models equivalent to those used in the brain or non-Gaussian models may therefore be needed.

7

Modelling the effect of blood vessels

In this chapter, I extend the model to include blood vessels with the aim of determining what effect they have on the diffusion MRI (dMRI) results, to support experimental work carried out by colleagues in the Radcliffe Department of Medicine. Since capillaries are longer and thinner than myocytes, diffusion in them will be more directional than in myocytes and the capillaries could therefore have a marked effect on the dMRI results. If the effect is large, it could mask changes in the orientation of the myocytes, which would be important in detecting pathological changes. The results show that the effects are small, which corresponds with the experimental results found by my colleagues.

7.1 Background

Capillaries are predominantly parallel to the myocyte orientation [3]. dMRI measures the predominant direction of diffusion within tissue to infer information about the structure of the tissue. Since capillaries are longer and thinner than myocytes, diffusion within them will be more directional than in the myocytes. In live tissue, there will also be blood flow through the capillaries. It is therefore possible that the

diffusion and/or flow within the capillaries have a marked influence on the results of the dMRI studies and could affect the interpretation of dMRI results.

Colleagues in the Radcliffe Department of Medicine have carried out experimental work to analyse the effect of diffusion within vessels. They used ex vivo rat hearts where half of the heart had its blood vessels filled with microfil, and the other half was left unfilled. Initial results have shown only small differences between the filled regions (where blood vessels do not contribute to the MRI signal - 'without vessels') and unfilled regions (where blood vessels do contribute to the overall MRI signal - 'with vessels'). They found that in the areas 'without vessels' the FA is reduced, and the mean ADC is increased compared with the areas 'with vessels'. Since it was hard to determine how successfully the blood vessels were filled, it was not known whether the results were accurate or due to incomplete filling of the blood vessels.

Table 7.1 shows a summary of the size and prevalence of capillaries in rat myocardium. The diameter of capillaries is around 5 µm. The prevalence of capillaries is described in three ways: the volume fraction ranges from 5 % to 22 %, the ratio of capillaries to myocytes is from 0.75 to 1.3, and the capillary density is from 2100 mm^{-2} to 4200 mm^{-2}. Assuming a capillary diameter of 5 µm, these densities give volume fractions of 4.1 % to 8.2 %. Combining the range of diameters found with the range of capillary densities gives a volume fraction of 3 % to 23 %. As for the literature review of myocyte parameters in Chapter 3, there is a wide range of values, which may be due to variability within animals, differences between types of rat or gender, or the preparation and measurement techniques. Smith and Clark [171] found that capillary density decreases with age, but there were no differences by gender. Watanabe et al. [172] found a much higher volume fraction than the other studies: they used 3D confocal imaging with a contrast agent in the vasculature compared with 2D methods in all other studies, which could account for the difference.

The purpose of this study was to firstly analyse the effect of the inclusion of blood vessels in the model on dMRI results. Secondly, to determine whether the MRI

Table 7.1: Size, density and prevalence of capillaries in rat myocardium

parameter	value	reference
capillary diameter (µm)	4.38–5.29	Poole [173]
	4.6	Chen [174]
	5.4	Anversa [175]
	5.63 ± 0.28	Kano [176]
	8.2 ± 0.1	Turek [177]
capillary volume fraction (%)	5	De Souza [178]
	8	Anversa [175]
	10	Chen [174]
	12 ± 4	Inuwa [179]
	12.0 ± 0.1	Turek [177]
	22.2 ± 5.6	Watanabe [172]
capillaries:myocytes ratio	0.75	Smith [171]
	1.00 ± 0.04	Turek [177]
	1.12–1.70	Poole [173]
	1.135–1.376	Kayar [180]
	1.29 ± 0.04	Kano [176]
capillary density (mm^{-2})	2100	Huikeshoven [181]
	2321 ± 82	Turek [177]
	2589 ± 140	Kano [176]
	3121–5445	Poole [173]
	3955–4305	Kayar [180]
	4000	Anversa [175]
	4200	Chen [174]

sequence, in particular the diffusion time, affects the differences seen. As the diffusion time is increased, the effects of restriction will increase and so this could increase the differences found. In addition, the simulated results were compared with the experimental results, to investigate whether similar changes were seen.

7.2 Method

I extended the model described in Chapter 3 to include long cylindrical blood vessels interspersed regularly between the cuboidal cells (see Figure 7.1). I set the cells to a uniform size, with values close to the mid-range of those used in the sensitivity analysis in Chapter 3, as listed in Table 7.2. The vessels were modelled as cylinders

of 5 µm diameter extending the full length of the cells to which they run parallel (see Figure 7.1). To achieve different volume fractions of vessels (VF_{ves}), I used the arrangements shown in Figure 7.2 within each layer.

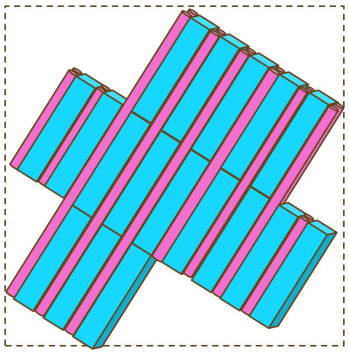

Figure 7.1: Model set-up of a single layer for vessels study. Cylindrical vessels (pink) interspersed between cuboidal cells (turquoise)

Volume fractions (%)				Set-up
vessels	cells	extra-cellular space	vessels:cells ratio	Key: cell vessel extracellular space
0.0	86.6	13.4	0	
4.4	83.6	12.3	0.5	
6.4	82.1	11.8	0.75	
8.4	80.8	11.3	1	
10.3	79.4	10.8	1.25	
12.1	78.1	10.4	1.5	
14.9	75.7	9.5	2	
20.6	69.8	9.6	3	

Figure 7.2: Model set-up within each layer for each VF_{ves}

I set the diffusivity in the cells and extra-cellular space to $1.5 \times 10^{-3}\,mm^2/s$. In discussion with colleagues from the National Heart and Lung Institute at Imperial College London and the Radcliffe Department of Medicine we considered that the restriction to diffusion in blood vessels could be less than in cells due to fewer sub-cellular structures; it is therefore possible that the diffusivity of water in vessels could be higher than that in cells. I therefore used two settings for the diffusivity in vessels: the same as the cells ($1.5 \times 10^{-3}\,mm^2/s$: 'DV1.5') and higher than in the cells ($2 \times 10^{-3}\,mm^2/s$: 'DV2'). These are both simulations of 'with vessels',

where the signal from the vessels contributes to the overall MRI signal. To simulate 'without vessels', where the signal from the vessels is suppressed, no molecules were placed in the vessels (signal from vessels = 0: 'SV0').

I carried out two studies. The first looked at the effect of filling the blood vessels for a range of volume fractions of vessels. The second investigated whether changing the acquisition sequence parameters, especially the diffusion time, affects the ability to discern between areas with and without blood vessels.

For the first study, I ran simulations for the DV1.5, DV2 and SV0 set-ups using a range of VF_{ves} and the parameters in Table 7.2, which I chose to match the experimental MRI sequence parameters. I simulated noisy data with Rician noise for 100 repetitions with an SNR of 50, which was approximately that found in the experimental data.

Table 7.2: Parameters for vessels studies

parameter	study 1	study 2A	study 2B	study 2C
diffusion pulse duration, δ (ms)	2.0	2.0–1.1	2.0	2.0
diffusion interval, Δ (ms)	5.5	5.5–16.4	5.5–17.5	5.5–17.5
bvalue ($s\,mm^{-2}$)	1000	1000	1000	1000–3500
gradient strength ($T\,m^{-1}$)	0.85	0.85	0.85–0.46	0.85
SNR	50	50–30	50–27	50–27
vessel volume fraction (VF_{ves})	0–20.6 %	6.4–10.3 %	6.4–10.3 %	6.4–10.3 %
voxel size		200 × 200× 200 µm		
simulation size		400 × 400× 400 µm		
cell length		120 µm		
cell cross-sectional area		200 μm^2		
aspect ratio		0.5		
helix angle range		75 $^\circ\,mm^{-1}$		
vessels diameters		5 µm		

For the second study, I again ran simulations for the DV1.5, DV2 and SV0 set-ups, but this time with different sequences and a smaller range of VF_{ves}. I carried out three studies, each increasing the diffusion interval (Δ), but keeping different parameters constant. For study 2A, the b-value and gradient strength were constant,

for study 2B the b-value and diffusion pulse duration (δ) were constant and for study 2C, the δ and gradient strength were constant. The parameters used are in Table 7.2. I varied the SNR with the diffusion time due to T2 relaxation, where the T2 relaxation time for cardiac tissue in this experimental set-up was measured by colleagues in the Radcliffe Department of Medicine to be around 20ms (see Figure 7.3). From the experimental data, the SNR for study 1 is 50, and so I varied the SNR for the other studies with the echo time (TE). Experimentally, the echo time is 1.9ms longer than ($\delta + \Delta$) so I used this echo time to determine the SNR:

$$SNR = SNR_1 \times \frac{exp(-TE/T2)}{exp(-TE_1/T2)} = 50 \times \frac{exp(-(\delta + \Delta + 1.9)/20)}{exp(-9.4/20)} \tag{7.1}$$

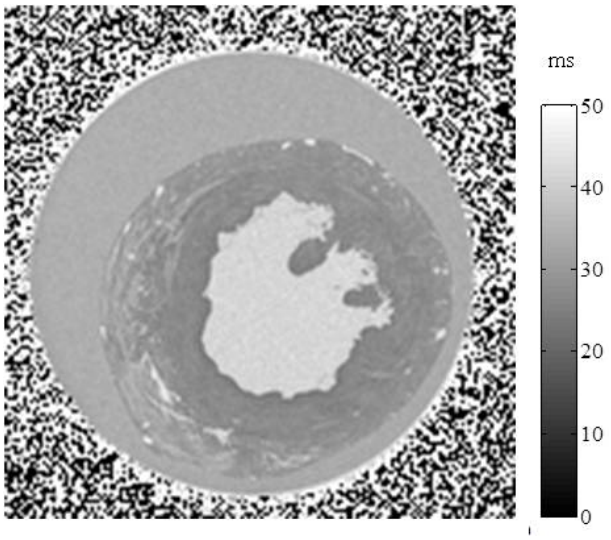

Figure 7.3: T2 relaxation times. An MRI image slice of an embedded rat heart showing T2 relaxation times. Tissue is approximately 20ms, gel 30ms and buffer 40ms

7.2.1 Experimental data

I was provided with pilot, unpublished data from one ex vivo rat heart by Dr Irvin Teh from the Radcliffe Department of Medicine. The heart had been casted with microfil through its right coronary artery, filling the vasculature on that side of the heart. The mean ADC and FA data was at 100 µm resolution, and the anatomical data at 33 µm resolution. Using the anatomical images for reference, I selected

areas from the LV wall where the blood vessels were not filled with microfil, and areas from the RV wall where the blood vessels were filled with microfil. From these areas I calculated the mean and standard deviation of the mean ADC and FA. The acquisition parameters were the same as for simulation study 1.

7.3 Results

7.3.1 Effect of filling volume fraction of vessels

Figure 7.4 shows the normalised MRI signals across each VF_{ves} for the 'without vessels' (SV0) and 'with vessels' (DV1.5 and DV2) simulations. The difference between the DV2 and DV1.5 signals is very small, especially at the lower VF_{ves}. At the highest VF_{ves}, the mean MRI signal for DV1.5 is slightly higher than that for DV2 with a smaller range. The mean MRI signal for SV0 is lower than DV1.5/DV2 with a smaller range and this difference increases as VF_{ves} increases.

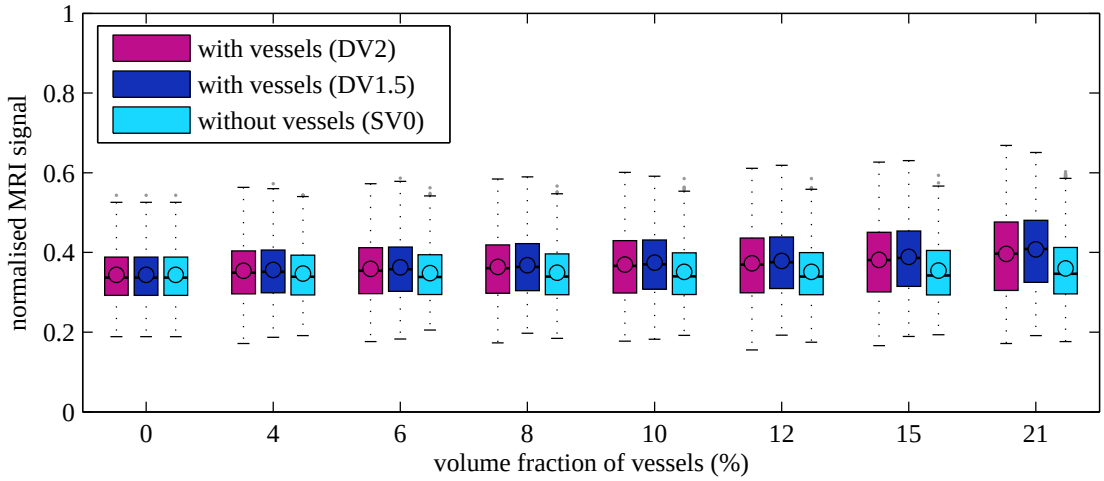

Figure 7.4: Study 1: Normalised MRI signals without vessels (pink), and with vessels with diffusivity of $1.5 \times 10^{-4}\,mm^2/s$ (turquoise) and $2 \times 10^{-4}\,mm^2/s$ (blue). Boxes are inter-quartile ranges with the median as a horizontal line and the circle indicating the mean; whiskers are 1.5 times the interquartile range, and outliers are beyond that.

Figure 7.5 shows the eigenvalues (λs), mean ADC and FA results for different vessel volume fractions (VF_{ves}). λ_1 remains approximately constant with VF_{ves} for SV0 and DV1.5, and increases for DV2. λ_2 remains approximately constant for SV0,

and decreases with increasing VF_{ves} for DV1.5 and DV2 at approximately the same rate. λ_3 decreases with VF_{ves} for all simulations; this decrease is steeper for DV1.5 and DV2 than for SV0. As the volume fraction of vessels increases, the mean ADC decreases for all simulations. This increase is more marked for the DV1.5 and DV2 simulations than the SV0. As the VF_{ves} increases, the FA increases. This increase is more marked for the DV1.5 and DV2 simulations than the SV0. The FA and mean ADC are higher for DV2 than DV1.5, although the differences are small. The difference between SV0 and DV1.5/DV2 increases with VF_{ves}.

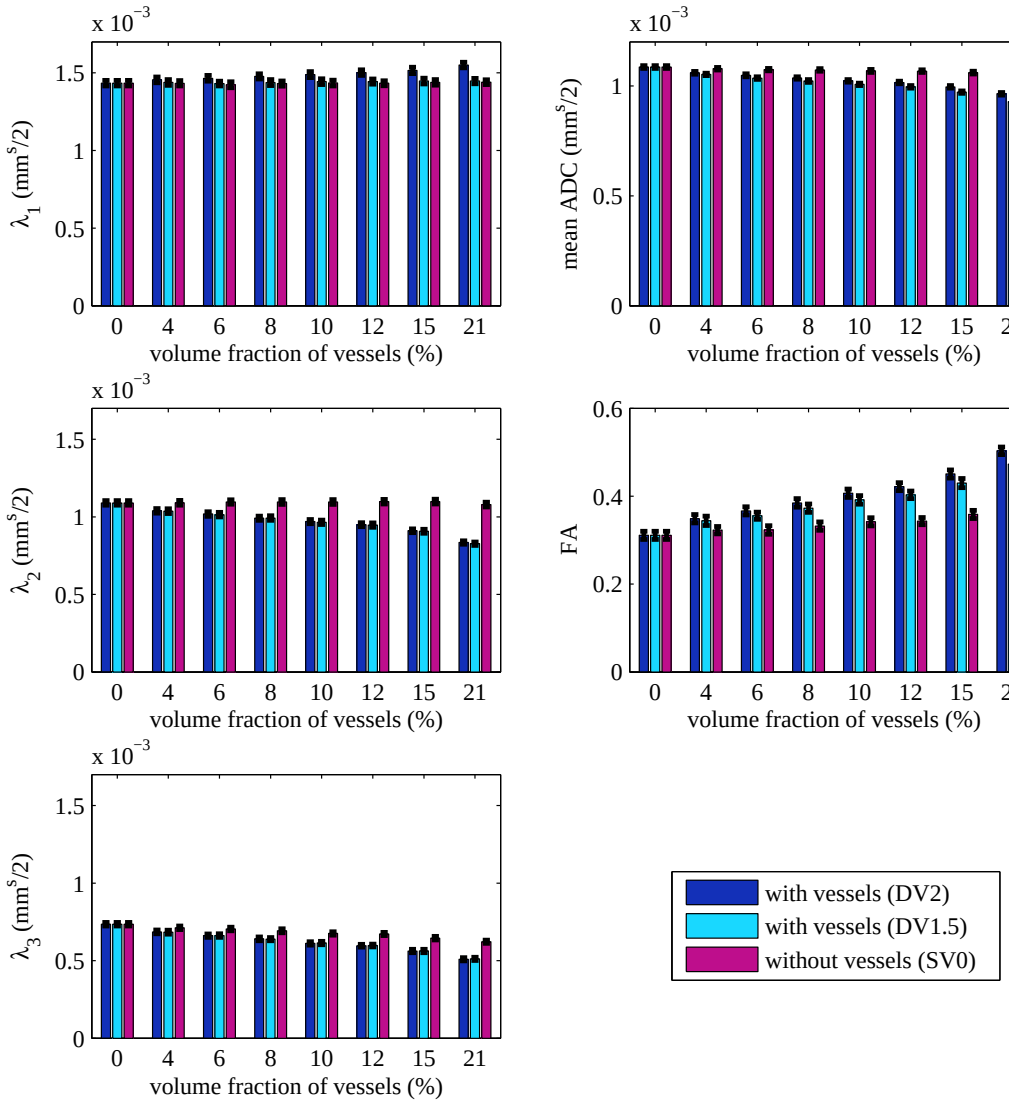

Figure 7.5: Study 1: eigenvalues (left, top - λ_1, middle - λ_2, bottom - λ_3), mean ADC (right, top) and FA (right, middle) without vessels (pink), and with vessels with diffusivity of $1.5 \times 10^{-4}\,\mathrm{mm}^2/\mathrm{s}$ (turquoise) and $2 \times 10^{-4}\,\mathrm{mm}^2/\mathrm{s}$ (blue). Error bars ± 1 standard deviation.

7.3.2 Effect of sequence

Figure 7.6 shows the effect of changing Δ on the MRI signals, while keeping the gradient strength and b-value constant (study 2A in Table 7.2). The figure shows the results for a volume fraction of 8%. As Δ increases, the mean and range of the MRI signals increase. The SV0 MRI signal is lower than the DV1.5 and DV2 signals.

Figure 7.7 shows the effect of changing Δ on the λs, mean ADC and FA for the same study. As Δ increases, all λs and the mean ADC decrease, while FA increases. The rates of increase/decrease are similar for each of the three studies (DV1.5, DV2 and SV0).

Very similar results were seen for studies 2B and 2C (Figures 7.8 to 7.11).

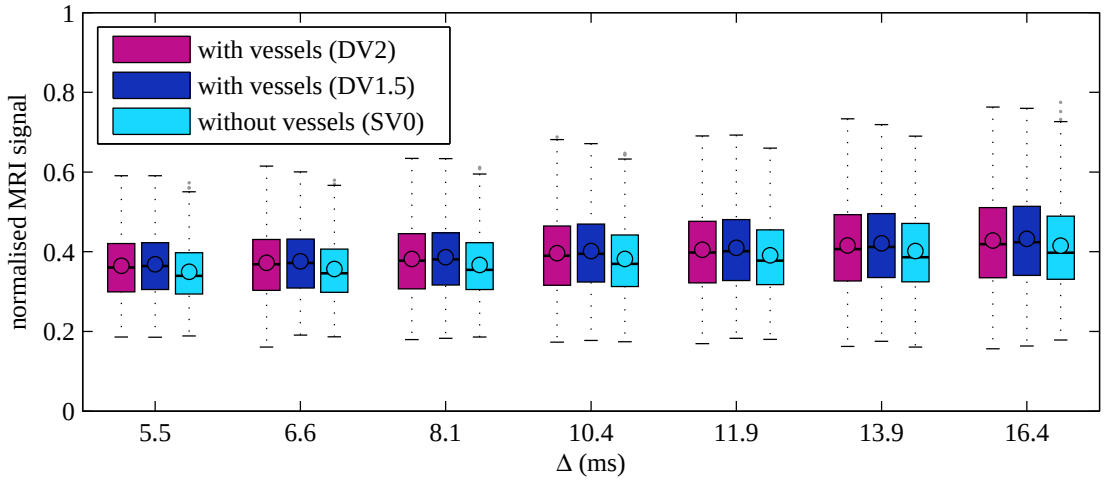

Figure 7.6: Study 2A: Effect of Δ on normalised MRI signal for volume fraction of 8%. Normalised MRI signals without vessels (pink), and with vessels with diffusivity of $1.5 \times 10^{-4}\,\mathrm{mm}^2/\mathrm{s}$ (turquoise) and $2 \times 10^{-4}\,\mathrm{mm}^2/\mathrm{s}$ (blue). Boxes are inter-quartile ranges with the median as a horizontal line and the circle indicating the mean; whiskers are 1.5 times the interquartile range, and outliers are beyond that.

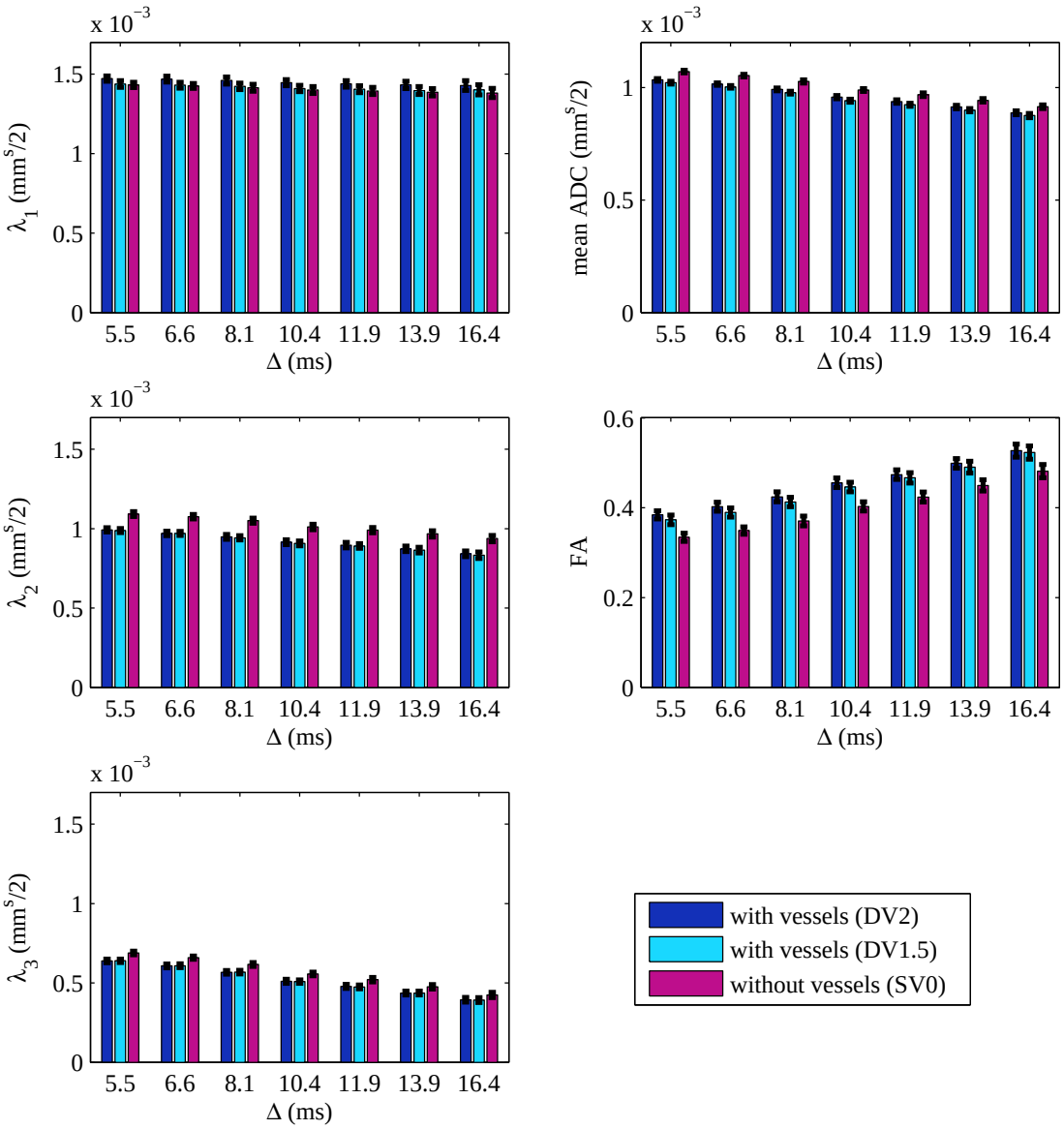

Figure 7.7: Study 2A: Effect of Δ on DT for volume fraction of 8% on eigenvalues (left, top - λ_1, middle - λ_2, bottom - λ_3), mean ADC (right, top) and FA (right, middle) without vessels (pink), and with vessels with diffusivity of $1.5 \times 10^{-4}\,\mathrm{mm}^2/\mathrm{s}$ (turquoise) and $2 \times 10^{-4}\,\mathrm{mm}^2/\mathrm{s}$ (blue). Error bars ±1 standard deviation.

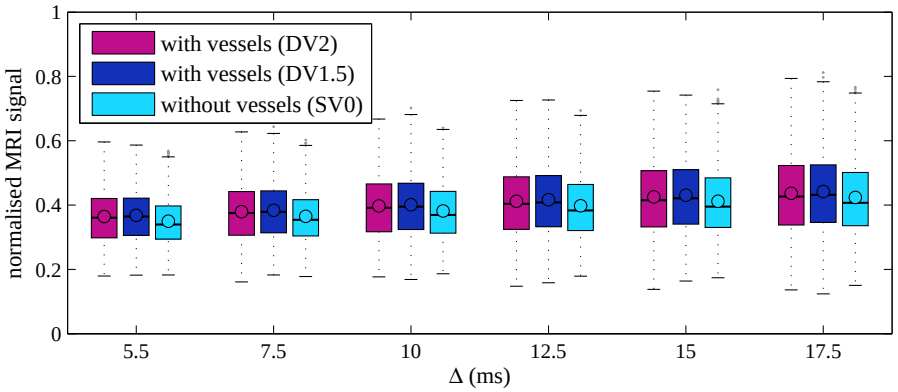

Figure 7.8: Study 2B: Effect of Δ on normalised MRI signal for volume fraction of 8%. Normalised MRI signals without vessels (pink), and with vessels with diffusivity of $1.5 \times 10^{-4}\,\mathrm{mm}^2/\mathrm{s}$ (turquoise) and $2 \times 10^{-4}\,\mathrm{mm}^2/\mathrm{s}$ (blue). Boxes are inter-quartile ranges with the median as a horizontal line and the circle indicating the mean; whiskers are 1.5 times the interquartile range, and outliers are beyond that.

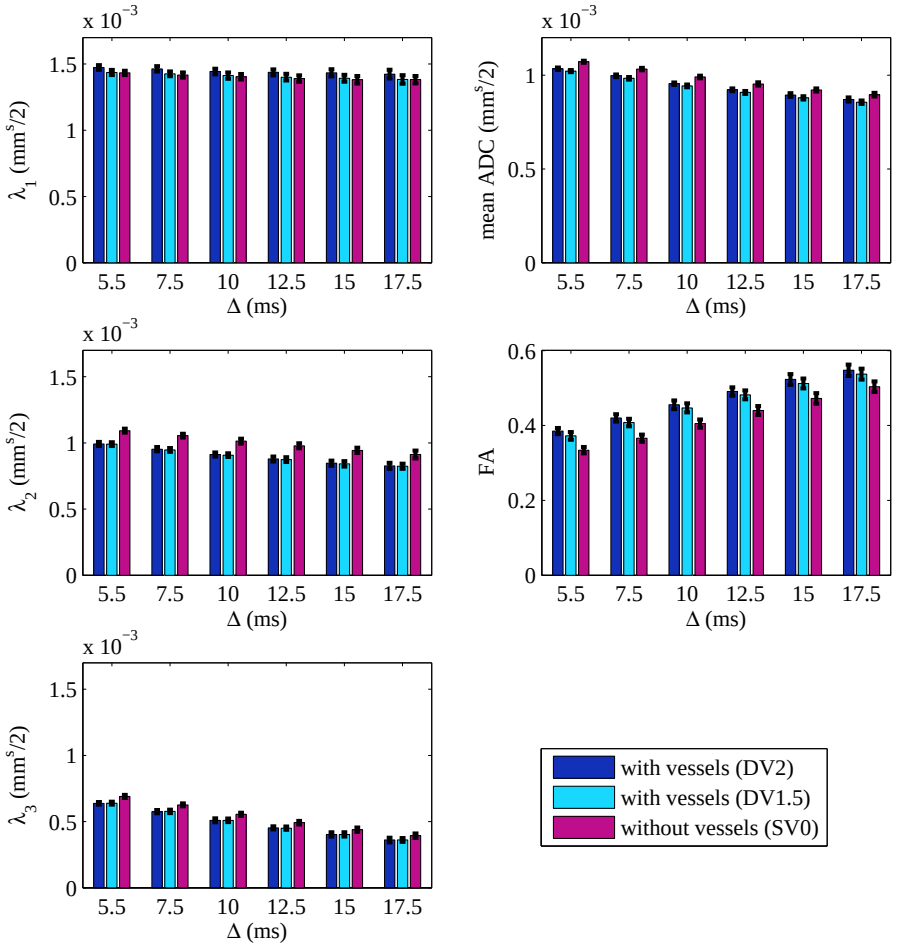

Figure 7.9: Study 2B: Effect of Δ on DT for volume fraction of 8% on eigenvalues (left, top - λ_1, middle - λ_2, bottom - λ_3), mean ADC (right, top) and FA (right, middle) without vessels (pink), and with vessels with diffusivity of $1.5 \times 10^{-4}\,\mathrm{mm}^2/\mathrm{s}$ (turquoise) and $2 \times 10^{-4}\,\mathrm{mm}^2/\mathrm{s}$ (blue). Error bars ±1 standard deviation.

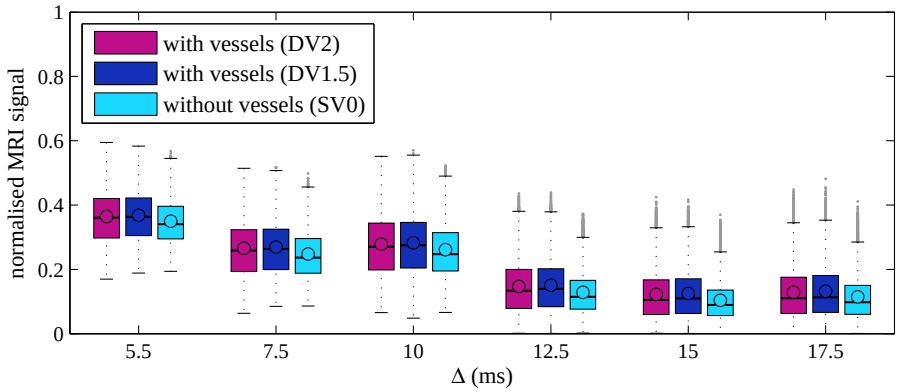

Figure 7.10: Study 2C: Effect of Δ on normalised MRI signal for volume fraction of 8%. Normalised MRI signals without vessels (pink), and with vessels with diffusivity of $1.5 \times 10^{-4}\,\mathrm{mm}^2/\mathrm{s}$ (turquoise) and $2 \times 10^{-4}\,\mathrm{mm}^2/\mathrm{s}$ (blue). Boxes are inter-quartile ranges with the median as a horizontal line and the circle indicating the mean; whiskers are 1.5 times the interquartile range, and outliers are beyond that.

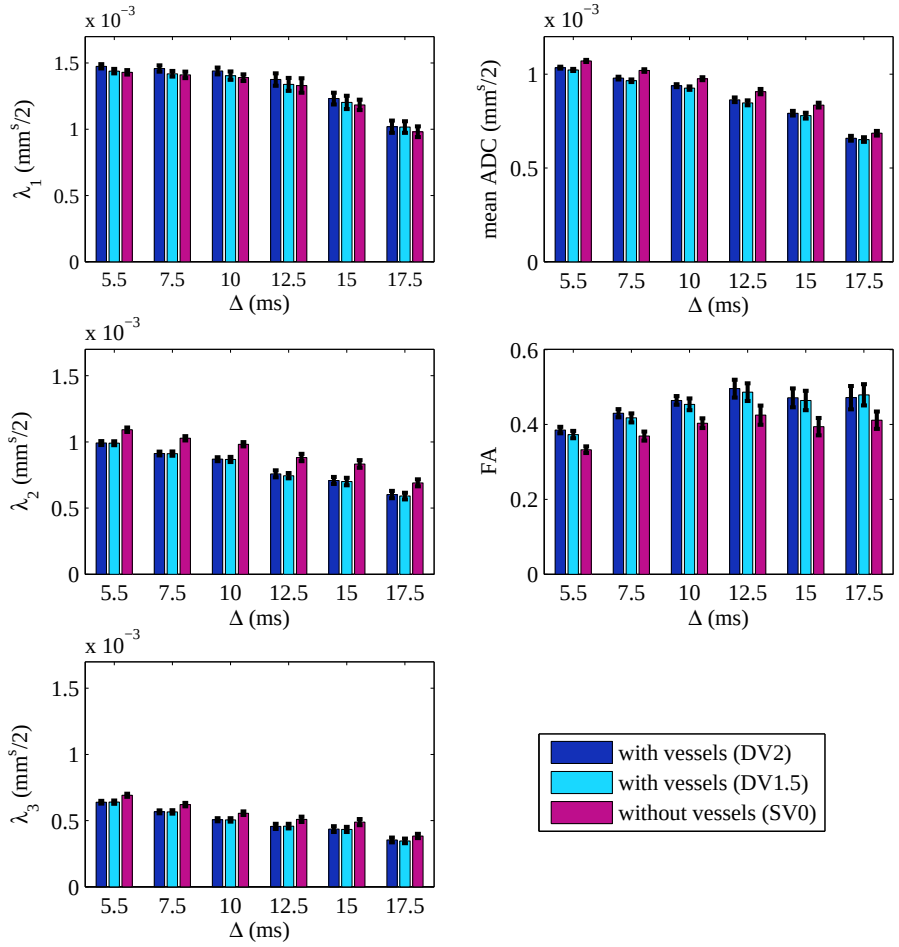

Figure 7.11: Study 2C: Effect of Δ on DT for volume fraction of 8% on eigenvalues (left, top - λ_1, middle - λ_2, bottom - λ_3), mean ADC (right, top) and FA (right, middle) without vessels (pink), and with vessels with diffusivity of $1.5 \times 10^{-4}\,\mathrm{mm}^2/\mathrm{s}$ (turquoise) and $2 \times 10^{-4}\,\mathrm{mm}^2/\mathrm{s}$ (blue). Error bars ±1 standard deviation.

7.3.3 Experimental results

The results from the experimental data are shown in Table 7.3, along with the simulated results from Study 1 for a volume fraction of 8%. The mean ADC is higher and the FA lower in the 'without vessels' than 'with vessels' for both the simulation and experiments.

Table 7.3: Experimental and simulated results of effect of filling vessels. Values are mean plus/minus the standard deviation. Simulated data is from study 1 with a VF of 8 %.

parameter		with vessels (unfilled vessels)	without vessels (filled vessels)
mean ADC ($10^{-3}\,\mathrm{mm^2\,s^{-1}}$)	expt	1.07 ± 0.03	1.12 ± 0.13
	sim	1.02 ± 0.01	1.07 ± 0.01
FA	expt	0.29 ± 0.03	0.25 ± 0.04
	sim	0.37 ± 0.01	0.33 ± 0.01

7.4 Discussion

As the volume fraction of vessels increases, the mean MRI signal increases, as does the range. The blood vessels are more restrictive than the cells across the cross-section and less restrictive along the long axis. This leads to a greater range of signals as VF_{ves} increases, since the signal becomes more dependent on the gradient direction. Overall, the vessels restrict diffusion more than the cells leading to less diffusion and higher MRI signals. These changes in the MRI signals lead to λ_2 and λ_3 decreasing as VF_{ves} increases due to increasing restriction across the vessels. λ_1 increases with VF_{ves}, especially for DV2, due to increased free diffusion. These changes in the λs lead to a decreasing mean ADC and increasing FA as VF_{ves} increases.

Without the blood vessels, the MRI signals, λs, mean ADC and FA are almost constant across the range of VF_{ves}. The small changes that occur are mainly a decrease in λ_3 and hence an increase in the FA and decrease in the mean ADC.

These would be expected to remain constant since the cells remain the same as VF_{ves} increases. The changes are due to the model geometry since the extracellular space around the vessels is more restrictive than that between the cells, especially in the direction perpendicular to the layers, that is, in the direction of λ_3.

The differences between the simulations with vessels of different diffusivities (DV1.5 and DV2) are only small, except for λ_1 where the higher diffusivity leads to increased diffusion along the long axis of the vessels and hence a higher λ_1. This higher λ_1 leads to slightly higher mean ADC and FA in the DV2 simulations compared with the DV1.5.

As VF_{ves} increases, the effect of these vessels increases, and therefore the differences between with and without vessels increases. The results suggest that λ_2 and λ_3, the mean ADC and the FA should all be able to discern differences between areas of myocardium with the vessels filled and unfilled for all the VF_{ves} from 4 % and above. In experimental data, there is likely to be a range of VF_{ves} across the voxels, as well as a variation in the microstructure leading to a wider variation in DT parameters. This variation is likely to mean that in experimental data it would be harder to discern differences between areas with filled and unfilled vessels, especially at the lower VF_{ves}.

Our previous work in Chapter 4 showed that the model tends to overestimate λ_2 and λ_3 and the FA, and has a lower variation in these parameters. From Figure 4.6 we can see that the standard deviation of λ_2 and λ_3 and the FA is approximately five times higher in the experimental data compared with the simulated data. Assuming a similar increase in standard deviation in the vessels results, the ability to discern differences becomes much harder.

To investigate whether the differences can be increased by changing the acquisition parameters, I increased Δ because as the diffusion time increases, there could be increased effects of restrictions. The λs and mean ADC decreased and the FA

increased with Δ for the three studies since there is a greater likelihood of reaching a barrier as the diffusion time increases and so diffusion decreases.

There was very little change in the relative values of the DT parameters as the diffusion time increased, and since the SNR worsens at longer diffusion times there is no increase in the ability to differentiate between the two areas of myocardium.

The simulated and experimental results are similar and show similar differences between areas with filled and unfilled vessels. The experimental data is from a single heart and therefore further validation with more hearts will be needed to confirm these results.

Although the changes with and without the vessels are fairly small, this is for a regular geometry with aligned capillaries. In pathological hearts, where the myocytes are disarrayed, the effect of the capillaries on the dMRI signals may be larger, especially if the capillaries remain straight and aligned with the original non-disarrayed cell orientations.

7.5 Summary of Chapter

In this chapter I introduced small blood vessels into the model. The purpose was threefold. Firstly, to determine whether the introduction of blood vessels affects the dMRI results, which could be important when analysing experimental results. Secondly, to assess whether changes in the acquisition sequence could help enhance the differences. Thirdly, to help corroborate experimental data where small changes were found.

The simulation results show that we would expect to be able to differentiate between areas with and without blood vessels. However, increasing the amount of variation to experimental levels would likely reduce these differences. Altering the acquisition sequence by increasing the diffusion interval does not affect the ability to discern

differences between areas with and without blood vessels. The experimental and simulated results are very similar and show small differences between areas with filled and unfilled vessels. This suggests that the small changes found in the experimental data are what we would expect, rather than being due to experimental protocol difficulties, although further validation with more hearts is needed.

8

Conclusions

The aim of this project was to create a model of diffusion MRI in cardiac tissue which could be used to investigate the relationship between the remodelling seen in disease and the diffusion MRI signal and thus to facilitate the design of MRI sequences and quantification measures to be used in the assessment of remodelling.

In this thesis, I have presented a model of diffusion MRI in simplified cardiac tissue. To my knowledge, this is the first model that simulates a realistic 3D geometry of cardiac tissue, and validates the results with experimental data. The results compare well with those from ex vivo rat hearts across a range of experimental gradient and diffusion time values, although there remain some differences which can be attributed to the increased regularity of the model's geometry compared with cardiac tissue. Neither adding membrane permeability nor increasing extracellular diffusivity had a marked effect on the results or improved the small differences with the experimental data. In addition to the comparison with the rat hearts, I compared the model results with a phantom. Although these results support the modelling method, some practical problems with modelling the phantom prevented the quantitative comparison that I had intended.

As a demonstration of the feasibility of the model for the assessment of the effects of cardiac remodelling, I modelled type IB disarray as found in hypertrophic cardiomyopathy. As either the degree or extent of disarray was increased, the fractional anisotropy decreased, which agrees with the existing literature, while the mean apparent diffusion coefficient remained constant. To my knowledge, this is the first simulation of cardiac remodelling and the effect of this remodelling on diffusion MRI results.

Studying the effect of the vasculature showed that the introduction of small blood vessels into the model increases the FA and decreases the mean ADC, which corresponds well with pilot experimental data. This is an important open question in the field, as diffusion and/or flow in the vessels may obscure diffusion changes due to structural changes in the myocardium.

The model presented in this thesis forms a good starting point for analysing the relationship between cardiac microstructure and diffusion MRI.

8.1 Future work

There remain some limitations in the model, in particular the regular arrangement and size of cells does not fully encapsulate the variation found even in healthy heart tissue. In addition, neither transverse nor sheet angles are modelled. These lead to increased anisotropy of the model compared with cardiac tissue. Accounting for the natural variation in healthy tissue is not, however, straightforward. The model at present consists of parallel layers of cells which effectively reduces arranging the cells to a 2D problem. Introducing variability in all three dimensions requires careful implementation to ensure that the required volume fraction of cells is maintained without cells overlapping each other. In addition, when stochasticity is introduced into the model, many repetitions will be required to average out potentially unrepresentative results. Neither of these problems is insurmountable, but both requite careful consideration.

8.1.1 Speeding up the simulations

As already mentioned in Chapter 3, my model requires substantial computational resources, and it would be beneficial to reduce this, especially if stochastic elements are introduced requiring multiple repetitions of simulations to be performed.

The two steps which currently require the most computational resources are running the Smoldyn simulations and converting the text output files from Smoldyn into Matlab files (see Table 3.1): future work on speeding up the simulations should focus on these areas. There are two graphics processing unit (GPU) implementations of Smoldyn which could be used to significantly decrease the runtime of step 2 [182, 183]. In addition, Smoldyn effectively has two stages: setting up the geometry and placing the molecules, and then simulating the diffusion. When the geometry is complicated, and whenever compartments need to be defined (for example, in Chapter 5 where extra and intra-cellular space have different parameters) the set-up time can be long. There is scope for maximising the number of molecules per simulation to limit the number of times the set-up needs to be done.

Improving the time for importing and converting the files into Matlab format offers less chance for improvement, as the majority of the time is simply to import the text file into Matlab. Using parallelisation should help with this. A better solution would be to have smaller or fewer text files to convert. In the studies in this thesis I use a boundary of 100 µm in all directions and therefore simulate a much larger volume and number of molecules than required. I chose this boundary since in the original set-up (Figure 8.1a) I only included cells which were fully inside the modelling volume which leads to large empty spaces. To ensure that these empty areas are not in the final voxel, a large boundary is needed. For the diffusivity study in Chapter 5 I wanted to ensure that the volume fraction within the modelling volume was close to that defined and I therefore kept all cells which had their majority within the volume (Figure 8.1b). Smoldyn allows surfaces to extend beyond the defined boundary; to prevent molecules from diffusing outside the simulation boundary

and slowing down the simulation, a reflective cube is defined coincident with the boundary (marked in pink in Figure 8.1). In retrospect, there was no need to keep such a large boundary once I had changed the set-up. The boundary could be much smaller, especially if I keep any cell which has any part in the volume (Figure 8.1c). The number of molecules and therefore the simulation time and size and number of files to be converted to Matlab format would be greatly reduced. The boundary should be chosen such that there is a very small probability of any molecule which finished inside the voxel having collided with the boundary. This will depend on the diffusivity and total diffusion time, and will require careful investigation.

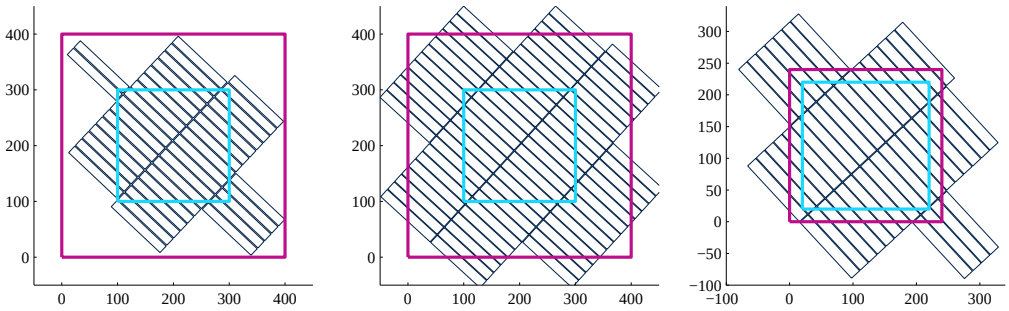

(a) original set-up **(b)** later set-up **(c)** proposed improvement

Figure 8.1: Single layer of geometry set-up for original studies (Chapters 3 & 4), for later studies (Chapters 5 & 6) and proposed improvement. Cells are marked in black, central voxel to be analysed is marked in turquoise. The molecules are placed in the pink area.

For the 100 µm voxel size for the sensitivity analysis, the original number of molecules was 2.7×10^6, with the boundary reduced to 20 µm, as an example, the number of molecules required would be 2.7×10^5. This reduces the computational time for steps 2 and 3 10-fold. The reduction will be smaller for a larger simulation volume as the boundary is a smaller proportion of the total volume, but even for the largest volume simulated (500 µm for the effect of diffusion time in Chapter 4), the number of molecules is halved.

Smoldyn was designed for modelling stochastic cellular reactions, of which diffusion and interactions with surfaces are only a part. It may therefore be possible to simplify certain aspects of its methodology to improve the speed while maintaining

the functionality and accuracy required. One potential option is the diffusion step length. Most Monte Carlo models use a fixed step length since this is quicker and no less accurate [98, 108]. Smoldyn uses a Gaussian distributed step length which although more realistic is likely to be slower: changing the Smoldyn code to use a fixed step length could therefore speed up the simulations.

The text output files are very large and take a long time to import into Matlab and convert into Matlab format. Any format which stores the 3D position for each of such a large number of molecules for every one of so many timesteps will inevitably produce large files, but it is possible that an alternative file output format may be smaller and/or quicker to import into Matlab.

Matlab itself is not an especially fast environment, and therefore writing the code to perform the MRI signal modelling and DT calculations in an alternative program or language could improve the simulation time.

8.1.2 Validation by synchrotron imaging

Acquiring DT and synchrotron data on the same hearts offers exciting prospects for both increasing the understanding of the relationship between cardiac microstructure and DT results, and using the data to further validate my modelling technique.

Synchrotron imaging gives 3D high resolution images where individual myocytes can be seen. If the same heart also has DT imaging then the exact correlation between the structure and diffusion MRI can be seen. This offers the potential for improved validation of the modelling technique by creating a 3D mesh from the synchrotron images and using this as the model geometry. The model outputs can then be directly compared with the DT imaging results for validation.

Synchrotron images of pathological hearts could be used as a partial alternative to modelling: the amount of disarray, fibrosis or hypertrophy could be measured from the synchrotron images and correlated with the DT results. However, the disease

changes cannot be controlled and this would be a very expensive method due to the large number of animals required, and the synchrotron and MRI scanner time. Monte Carlo modelling offers a quicker, more controlled and less expensive option, with far fewer animals required. It is also only an ex vivo technique.

8.1.3 Disarray and remodelling

In Chapter 6 I modelled type IB disarray as found in hypertrophic cardiac myopathy and the effect this has on the MRI signal and DT derivatives. I believe that the most useful application of Monte Carlo models is to explore and understand the effects of pathology on the results. In particular, to investigate the interactions of pathological changes. In addition to types of disarray, diseased hearts may have remodelling including increased fibrosis, cell hypertrophy, changes in LV wall thickness, and alterations to IC structures. Each of these will affect the results of diffusion MRI in some way, and in combination the changes could be amplified or cancelled out. Without understanding these effects we cannot use diffusion MRI to quantify and classify disease changes in vivo, which could play an important role in assessing and treating patients.

8.1.4 In vivo imaging and modelling

At present the model is of ex vivo rat myocardial tissue. For it to be of use in furthering the detection and quantification of pathology, an in vivo version will be required. In vivo modelling has several challenges, especially cardiac and respiratory motion, which will need to be included in the modelling. Due to clinical time constraints, in vivo imaging is lower resolution than ex vivo; the SNR is also poorer. In vivo acquisition sequences and gradient values are substantially different to those used in ex vivo imaging. All these factors will be particularly important if the model is to be successfully used to optimise MRI sequences for the acquisition of in vivo images.

The first step in modelling in vivo sequences, for example to determine their effect on the changes seen in Chapter 6 or 7, would be to implement the standard PGSE sequence with realistic in vivo parameters. The maximum gradient strength for in vivo scanners is lower than ex vivo ones (typically one-third of ex vivo strength), and the pulse timings are determined by the subject's heart rate since measurements are either made within a single heart beat, or at are gated so that pulse are applied at the same time in sequential heart beats [90]. These lead to lower b-values than in ex vivo imaging (typically no higher than $1000\,\mathrm{s\,mm^{-2}}$).

Subsequently, more realistic in vivo sequences, such as the STEAM (stimulated echo acquisition mode) or spin-echo (SE) sequences. These sequences have been designed to overcome in vivo difficulties such as cardiac and respiratory motion. STEAM occurs over two heartbeats and therefore relies on the heart being in the same position in each cardiac cycle. The data is therefore acquired with the breath held, and with a gated acquisition to collect the data at the same time in the cardiac cycle. Strain compensation is usually required by collecting separate strain data, although data acquisition at certain times in the cardiac cycle can overcome this need. SE is acquired within a single heart beat and motion correction is therefore required; the advantage of this method is its higher SNR. [90] Whether these sequences can be usefully modelled without also modelling cardiac and respiratory motion will be a matter for investigation.

The in vivo model would be useful for simulating the effects of factors which cannot currently be quantified, such as the effect of irregular heartbeats.

8.1.5 Diastole and systole

dMRI can be used to measure the microstructural changes that occur in the transition from systole to diastole, for example changes in the helix and sheet angles [10, 75]. Modelling these two states could be useful in the understanding of pathological remodelling since an initial study of HCM patients showed that

it is only in diastole that HCM changes are seen [96]. The introduction into the model of two or more contraction states and the relationship between them could be essential in fully understanding and modelling disease changes. The sheet structure is fundamental to the changes in the shape of the heart between these two states and it will therefore be necessary to introduce this sheet structure into the model.

8.1.6 Diffusivity

The diffusion of water in biological tissue is complex and fascinating. It is affected not only by restrictions from cell membranes, but by interactions with IC and EC structures such as organelles and proteins. In addition, the interaction with the cell membrane appears to extend some distance from the membrane and to have an anisotropic effect [65].

As the accuracy of several models [98, 106], including my own, has shown, it may be possible to encapsulate these effects with a single diffusivity value and impermeable or semi-permeable membranes. Models should not be made unnecessarily complex, but rather should be 'as simple as possible, but not simpler'. Nevertheless, better understanding and modelling of diffusion may increase understanding of pathological changes.

The theory that slow diffusion occurs either side of the cell membrane, as well as in water bound to proteins within the intracellular space echoes the 'trapped water' theory of the 1970s. Le Bihan's [65] exploration of membrane biology gives estimates for some parameters such as the thickness of the slow layer next to the membrane in the brain, but whether these are similar in heart tissue is not known.

From a modelling perspective, it would be relatively simple to have a layer either side of the membrane where the diffusivity is lower and probably anisotropic (slower perpendicular to the membrane than parallel to it. Indeed, Smoldyn allows for

molecules to bind to surfaces and to exchange between this state and the faster diffusion away from the membranes.

Care must be taken in modelling that the parameter values used are as accurate as possible. When there are many parameters in a model, there is the potential that almost any output value is achievable if the input parameters are adjusted enough. Further biexponential analysis of heart diffusion MRI data may help to derive appropriate parameter values for the diffusivities and volume fractions of the fast and slow components, including anisotropy of diffusion.

References

[1] Victoria C. Garside, Alex C. Chang, Aly Karsan, and Pamela A. Hoodless. "Co-ordinating Notch, BMP, and TGF β Signalling During Heart Valve Development". In: *Cellular and molecular life sciences : CMLS* 70.16 (2013), pp. 2899–2917.

[2] Henry M. Spotnitz. "Macro design, structure, and mechanics of the left ventricle". In: *The Journal of Thoracic and Cardiovascular Surgery* 119.5 (2000), pp. 1053–1077.

[3] Karen May-Newman, Odile Mathieu-Costello, Jeffrey H. Omens, Katherine Klumb, and Andrew D. McCulloch. "Transmural Distribution of Capillary Morphology as a Function of Coronary Perfusion Pressure in the Resting Canine Heart". In: *Microvascular Research* 50.3 (1995), pp. 381–396.

[4] Leonid Zhukov and Alan Barr. "Heart-Muscle Fiber Reconstruction from Diffusion Tensor MRI". In: *IEEE Visualization Conference*.

[5] I. J. LeGrice, B. H. Smaill, L. Z. Chai, S. G. Edgar, J. B. Gavin, and P. J. Hunter. "Laminar structure of the heart: ventricular myocyte arrangement and connective tissue architecture in the dog". In: *American Journal of Physiology - Heart and Circulatory Physiology* 269.2 (1995), H571–H582.

[6] DD Streeter, H. M. Spotnitz, D. P. Patel, J. Ross, and E. H. Sonnenblick. "Fiber orientation in the canine left ventricle during diastole and systole". In: *Circulation Research* 24.3 (1969), pp. 339–47.

[7] H. Lombaert, J. M. Peyrat, P. Croisille, S. Rapacchi, L. Fanton, F. Cheriet, P. Clarysse, I. Magnin, H. Delingette, and N. Ayache. "Human atlas of the cardiac fiber architecture: study on a healthy population". In: *IEEE Transactions on Medical Imaging* 31.7 (2012), pp. 1436–47.

[8] Manuel D. Cerqueira, Neil J. Weissman, Vasken Dilsizian, Alice K. Jacobs, Sanjiv Kaul, Warren K. Laskey, Dudley J. Pennell, John A. Rumberger, Thomas Ryan, and Mario S. Verani. "Standardized Myocardial Segmentation and Nomenclature for Tomographic Imaging of the Heart: A Statement for Healthcare Professionals From the Cardiac Imaging Committee of the Council on Clinical Cardiology of the American Heart Association". In: *Circulation* 105.4 (2002), pp. 539–542.

[9] Henry M. Spotnitz, William D. Spotnitz, Thomas S. Cottrell, David Spiro, and Edmund H. Sonnenblick. "Cellular basis for volume related wall thickness changes in the rat left ventricle". In: *Journal of Molecular and Cellular Cardiology* 6.4 (1974), pp. 317–331.

[10] Patrick W. Hales, Jürgen E. Schneider, Rebecca A. B. Burton, Benjamin J. Wright, Christian Bollensdorff, and Peter Kohl. "Histo-anatomical structure of the living isolated rat heart in two contraction states assessed by diffusion tensor MRI". In: *Progress in Biophysics and Molecular Biology* 110.2-3 (2012), p. 319.

[11] Yasuo Takayama, Kevin D. Costa, and James W. Covell. "Contribution of laminar myofiber architecture to load-dependent changes in mechanics of LV myocardium". In: *American Journal of Physiology - Heart and Circulatory Physiology* 282.4 (2002), H1510–H1520.

[12] Stephen H. Gilbert, David Benoist, Alan P. Benson, Ed White, Steven F. Tanner, Arun V. Holden, Halina Dobrzynski, Olivier Bernus, and Aleksandra Radjenovic. "Visualization and quantification of whole rat heart laminar structure using high-spatial resolution contrast-enhanced MRI". In: *American Journal of Physiology - Heart and Circulatory Physiology* 302.1 (2012), H287–H298.

[13] N. J. Severs. "The cardiac muscle cell". In: *BioEssays* 22.2 (2000), pp. 188–199.

[14] Gerald J. Tortora and Sandra Reynolds Grabowski. *Principles of Anatomy and Physiology*. 10th. Hoboken, New Jersey: John Wiley, 2003.

[15] R. Ferrari. "Healthy versus sick myocytes: Metabolism, structure and function". In: *European Heart Journal, Supplement* 4.G (2002), G1–G12.

[16] M. Golob, R. L. Moss, and N. C. Chesler. "Cardiac Tissue Structure, Properties, and Performance: A Materials Science Perspective". In: *Annals of Biomedical Engineering* 42.10 (2014), pp. 2003–2013.

[17] Barry J. Maron, Julius M. Gardin, John M. Flack, Samuel S. Gidding, Tom T. Kurosaki, and Diane E. Bild. "Prevalence of Hypertrophic Cardiomyopathy in a General Population of Young Adults: Echocardiographic Analysis of 4111 Subjects in the CARDIA Study". In: *Circulation* 92.4 (1995), pp. 785–789.

[18] BJ Gersh, BJ Maron, RO Bonow, JA Dearani, MA Fifer, MS Link, SS Naidu, RA Nishimura, SR Ommen, H Rakowski, CE Seidman, JA Towbin, JE Udelson, and CW Yancy. "2011 AACF/AHA guideline for the diagnosis and treatment of hypertrophic cardiomyopathy". In: *Journal of the American College of Cardiology* 58 (2011), e212 –60.

[19] B. J. Maron. "Contemporary insights and strategies for risk stratification and prevention of sudden death in hypertrophic cardiomyopathy". In: *Circulation* 121.3 (2010), p. 445.

[20] B. J. Maron and M. S. Maron. "Hypertrophic cardiomyopathy". In: *The Lancet* 381.9862 (2013), pp. 242–255.

[21] Kristian Thygesen, Joseph S. Alpert, Allan S. Jaffe, Maarten L. Simoons, Bernard R. Chaitman, and Harvey D. White. "Third Universal Definition of Myocardial Infarction". In: *Circulation* 126.16 (2012), p. 2020.

[22] N. Townsend, P. Bhatnagar, E. Wilkins, K. Wickramasinghe, and M. Rayner. *Cardiovascular Disease Statistics 2015*. Report. British Heart Foundation, 2015.

[23] C. Cuspidi, M. Rescaldani, C. Sala, F. Negri, G. Grassi, and G. Mancia. "Prevalence of electrocardiographic left ventricular hypertrophy in human hypertension: An updated review". In: *Journal of Hypertension* 30.11 (2012), pp. 2066–2073.

[24] E. D. Frohlich, A. González, and J. Díez. "Hypertensive left ventricular hypertrophy risk: Beyond adaptive cardiomyocytic hypertrophy". In: *Journal of Hypertension* 29.1 (2011), pp. 17–26.

[25] Lewis K. Waldman, David Nosan, Francisco Villarreal, and James W. Covell. "Relation Between Transmural Deformation and Local Myofiber Direction in Canine Left Ventricle". In: *Circulation Research* 63.3 (1988), pp. 550–562.

[26] Anthony Kanai and Guy Salama. "Optical Mapping Reveals That Repolarization Spreads Anisotropically and Is Guided by Fiber Orientation in Guinea Pig Hearts". In: *Circulation Research* 77.4 (1995), pp. 784–802.

[27] D. Teare. "Asymmetrical hypertrophy of the heart in young adults". In: *British heart journal* 20.1 (1958), pp. 1–8.

[28] B J Maron and W C Roberts. "Quantitative analysis of cardiac muscle cell disorganization in the ventricular septum of patients with hypertrophic cardiomyopathy". In: *Circulation* 59.4 (1979), pp. 689–706.

[29] BJ Maron, TJ Anan, and WC Roberts. "Quantitative analysis of the distribution of cardiac muscle cell disorganization in the left ventricular wall of patients with hypertrophic cardiomyopathy". In: *Circulation* 63 (1981), pp. 882 –94.

[30] T Kuribayashi and WC Roberts. "Myocardial disarray at junction of ventricular septum and left and right ventricular free walls in hypertrophic cardiomyopathy". In: *American Journal of Cardiology* 70 (1992), pp. 1333 –40.

[31] B J Maron, N Sato, W C Roberts, J E Edwards, and R S Chandra. "Quantitative analysis of cardiac muscle cell disorganization in the ventricular septum. Comparison of fetuses and infants with and without congenital heart disease and patients with hypertrophic cardiomyopathy". In: *Circulation* 60.3 (1979), pp. 685–96.

[32] Kikuko Imamura. "Ultrastructural aspect of left ventricular hypertrophy in spontaneously hypertensive rats : a qualitative and quantitative study". In: *Japanese Circulation Journal* 42.8 (1978), pp. 979–1002.

[33] Masaru Tanaka, Hisayoshi Fujiwara, Tomoya Onodera, Der-Jinn Wu, Mitsuo Matsuda, Yoshihiro Hamashima, and Chuichi Kawai. "Pathogenetic role of myocardial fiber disarray in the progression of cardiac fibrosis in normal hearts, hypertensive hearts and hearts with hypertrophic cardiomyopathy". In: *Japanese Circulation Journal* 51.6 (1987), pp. 624–630.

[34] V. Fineschi, M. D. Silver, S. B. Karch, M. Parolini, E. Turillazzi, C. Pomara, and G. Baroldi. "Myocardial disarray: an architectural disorganization linked with adrenergic stress?" In: *International Journal of Cardiology* 99.2 (2005), pp. 277–282.

[35] J. Milei, R. Migliore, F. Guerrero, C. Pedroza, and R. Storino. "Muscle fiber disarray in patients without hypertrophic cardiomyopathy". In: *Cardiology (Switzerland)* 72.3 (1985), pp. 105–112.

[36] T. Masuda, S. I. Sato, G. Muro-Oka, I. Segawa, A. Tashiro, K. Hiramori, and R. Satodate. "Simple method for quantifying disorientation of myofiber in endomyocardial biopsy specimens using an image analyzer". In: *Tohoku Journal of Experimental Medicine* 178.3 (1996), pp. 217–223.

[37] M. Pop, N. R. Ghugre, V. Ramanan, L. Morikawa, G. Stanisz, A. J. Dick, and G. A. Wright. "Quantification of fibrosis in infarcted swine hearts by ex vivo late gadolinium-enhancement and diffusion-weighted MRI methods". In: *Physics in Medicine and Biology* 58.15 (2013), pp. 5009–5028.

[38] Shinichiro Noda. "Histopathology of endomyocardial biopsies from patients with idiopathic cardiomyopathy; quantitative evaluation based on multivariate statistical analysis." In: *Japanese Circulation Journal* 44.2 (1980), pp. 95–116.

[39] S. I. Morimoto, M. Sekiguchi, S. Hiramitsu, A. Uemura, T. Nishikawa, and H. Hishida. "Contribution of cardiac muscle cell disorganization to the clinical features of hypertrophic cardiomyopathy". In: *Heart and Vessels* 15.4 (2000), pp. 149–158.

[40] A. M. Varnava, P. M. Elliott, S. Sharma, W. J. McKenna, and M. J. Davies. "Hypertrophic cardiomyopathy: The interrelation of disarray, fibrosis and small vessel disease". In: *Heart* 84.5 (2000), pp. 476–482.

[41] B Schwartzkopff, W Motz, H Frenzel, M Vogt, S Knauer, and B E Strauer. "Structural and functional alterations of the intramyocardial coronary arterioles in patients with arterial hypertension". In: *Circulation* 88.3 (1993), pp. 993–1003.

[42] C G Brilla, J S Janicki, and K T Weber. "Impaired diastolic function and coronary reserve in genetic hypertension. Role of interstitial fibrosis and medial thickening of intramyocardial coronary arteries". In: *Circulation Research* 69.1 (1991), pp. 107–15.

[43] G L Engelmann, J C Vitullo, and R G Gerrity. "Morphometric analysis of cardiac hypertrophy during development, maturation, and senescence in spontaneously hypertensive rats". In: *Circulation Research* 60.4 (1987), pp. 487–94.

[44] A. Martin Gerdes, Tatsuyuki Onodera, Xuejun Wang, and Sylvia A. McCune. "Myocyte Remodeling During the Progression to Failure in Rats With Hypertension". In: *Hypertension* 28.4 (1996), pp. 609–614.

[45] BJ Maron, JK Wolfson, and WC Roberts. "Relation between extent of cardiac muscle cell disorganization and left ventricular wall thickness in hypertrophic cardiomyopathy". In: *American Journal of Cardiology* 70 (1992), pp. 785 –90.

[46] A. M. Varnava, P. M. Elliott, N. Mahon, M. J. Davies, and W. J. McKenna. "Relation between myocyte disarray and outcome in hypertrophic cardiomyopathy". In: *American Journal of Cardiology* 88.3 (2001), pp. 275–279.

[47] A. M. Varnava, P. M. Elliott, C. Baboonian, F. Davison, M. J. Davies, and W. J. McKenna. "Hypertrophic cardiomyopathy: Histopathological features of sudden death in cardiac troponin T disease". In: *Circulation* 104.12 (2001), pp. 1380–1384.

[48] K. P. Anderson, R. Walker, P. Urie, P. R. Ershler, R. L. Lux, and S. V. Karwandee. "Myocardial electrical propagation in patients with idiopathic dilated cardiomyopathy". In: *The Journal of Clinical Investigation* 92.1 (1993), pp. 122–140.

[49] S M Dillon, M A Allessie, P C Ursell, and A L Wit. “Influences of anisotropic tissue structure on reentrant circuits in the epicardial border zone of subacute canine infarcts”. In: *Circulation Research* 63.1 (1988), pp. 182–206.

[50] P. S. Chen, Y. M. Cha, B. B. Peters, and L. S. Chen. “Effects of myocardial fiber orientation on the electrical induction of ventricular fibrillation”. In: *American Journal of Physiology - Heart and Circulatory Physiology* 264.6 (1993), H1760–H1773.

[51] Adolf Fick. “Ueber Diffusion”. In: *Annalen der Physik* 170.1 (1855), pp. 59–86.

[52] Robert Brown. “XXVII. A brief account of microscopical observations made in the months of June, July and August 1827, on the particles contained in the pollen of plants; and on the general existence of active molecules in organic and inorganic bodies”. In: *Philosophical Magazine Series 2* 4.21 (1828), pp. 161–173.

[53] A. Einstein. “Über die von der molekularkinetischen Theorie der Wärme geforderte Bewegung von in ruhenden Flüssigkeiten suspendierten Teilchen”. In: *Annalen der Physik* 322.8 (1905), pp. 549–560.

[54] Robert A. Pooley. “Fundamental Physics of MR Imaging”. In: *Radiographics* 25.4 (2005), pp. 1087–1099.

[55] Stuart Currie, Nigel Hoggard, Ian J Craven, Marios Hadjivassiliou, and Iain D Wilkinson. “Understanding MRI: basic MR physics for physicians”. In: *Postgraduate Medical Journal* 89.1050 (2013), pp. 209–223.

[56] Peter J. Basser and Carlo Pierpaoli. “Microstructural and Physiological Features of Tissues Elucidated by Quantitative Diffusion Tensor MRI”. In: *Journal of Magnetic Resonance, Series B* 111.3 (1996), p. 209.

[57] E. O. Stejskal and J. E. Tanner. “Spin Diffusion Measurements: Spin Echoes in the Presence of a Time-Dependent Field Gradient”. In: *The Journal of Chemical Physics* 42.1 (1965), pp. 288–292.

[58] P. J. Basser, J. Mattiello, and D. LeBihan. “MR diffusion tensor spectroscopy and imaging”. In: *Biophysical Journal* 66.1 (1994), p. 259.

[59] P. Hagmann, L. Jonasson, P. Maeder, J. P. Thiran, J. V. Wedeen, and R. Meuli. “Understanding diffusion MR imaging techniques: From scalar diffusion-weighted imaging to diffusion tensor imaging and beyond”. In: *Radiographics* 26 (2006), S205.

[60] Van J. Wedeen, Patric Hagmann, Wen-Yih Isaac Tseng, Timothy G. Reese, and Robert M. Weisskoff. “Mapping complex tissue architecture with diffusion spectrum magnetic resonance imaging”. In: *Magnetic Resonance in Medicine* 54.6 (2005), pp. 1377–1386.

[61] C. Mekkaoui, T. G. Reese, M. P. Jackowski, H. Bhat, and D. E. Sosnovik. “Diffusion MRI in the heart”. In: *NMR in Biomedicine* (2015).

[62] Denis Le Bihan, Shin-ichi Urayama, Toshihiko Aso, Takashi Hanakawa, and Hidenao Fukuyama. “Direct and fast detection of neuronal activation in the human brain with diffusion MRI”. In: *Proceedings of the National Academy of Sciences* 103.21 (2006), pp. 8263–8268.

[63] Jonathan V. Sehy, Joseph J. H. Ackerman, and Jeffrey J. Neil. “Evidence that both fast and slow water ADC components arise from intracellular space”. In: *Magnetic Resonance in Medicine* 48.5 (2002), pp. 765–770.

[64] Jean-Philippe Galons, Silvia Lope-Piedrafita, Joseph L. Divijak, Curt Corum, Robert J. Gillies, and Theodore P. Trouard. “Uncovering of intracellular water in cultured cells”. In: *Magnetic Resonance in Medicine* 54.1 (2005), pp. 79–86.

[65] D Le Bihan. “The ‘wet mind’: water and functional neuroimaging”. In: *Physics in Medicine and Biology* 52.7 (2007), R57.

[66] Kevin M. Bennett, Kathleen M. Schmainda, Raoqiong Bennett, Daniel B. Rowe, Hanbing Lu, and James S. Hyde. “Characterization of continuously distributed cortical water diffusion rates with a stretched-exponential model”. In: *Magnetic Resonance in Medicine* 50.4 (2003), pp. 727–734.

[67] A. Bueno-Orovio, I. Teh, J. E. Schneider, K. Burrage, and V. Grau. “Anomalous diffusion in cardiac tissue as an index of myocardial microstructure”. In: *IEEE Transactions on Medical Imaging* 35.9 (2016), pp. 2200–2207.

[68] Jens H. Jensen, Joseph A. Helpern, Anita Ramani, Hanzhang Lu, and Kyle Kaczynski. “Diffusional kurtosis imaging: The quantification of non-gaussian water diffusion by means of magnetic resonance imaging”. In: *Magnetic Resonance in Medicine* 53.6 (2005), pp. 1432–1440.

[69] Eleftheria Panagiotaki, Torben Schneider, Bernard Siow, Matt G. Hall, Mark F. Lythgoe, and Daniel C. Alexander. “Compartment models of the diffusion MR signal in brain white matter: A taxonomy and comparison”. In: *Neuroimage* 59.3 (2012), pp. 2241–2254.

[70] E. W. Hsu, A. L. Muzikant, S. A. Matulevicius, R. C. Penland, and C. S. Henriquez. “Magnetic resonance myocardial fiber-orientation mapping with direct histological correlation”. In: *American Journal of Physiology - Heart and Circulatory Physiology* 274.5 (1998), H1627–H1634.

[71] J. Chen, S. K. Song, W. Liu, M. McLean, J. S. Allen, J. Tan, S. A. Wickline, and X. Yu. “Remodeling of cardiac fiber structure after infarction in rats quantified with diffusion tensor MRI”. In: *American Journal of Physiology - Heart and Circulatory Physiology* 285.3 54-3 (2003), H946–H954.

[72] A. A. Holmes, D. F. Scollan, and R. L. Winslow. “Direct histological validation of diffusion tensor MRI in formaldehyde-fixed myocardium”. In: *Magnetic Resonance in Medicine* 44.1 (2000), pp. 157–61.

[73] D. F. Scollan, A. Holmes, R. Winslow, and J. Forder. “Histological validation of myocardial microstructure obtained from diffusion tensor magnetic resonance imaging”. In: *American Journal of Physiology - Heart and Circulatory Physiology* 275.6 Pt 2 (1998), H2308–18.

[74] W. Li, M. Lu, S. Banerjee, J. Zhong, A. Ye, J. Molter, and X. Yu. “Ex vivo diffusion tensor MRI reflects microscopic structural remodeling associated with aging and disease progression in normal and cardiomyopathic Syrian hamsters”. In: *NMR in Biomedicine* 22.8 (2009), pp. 819–825.

[75] J. Chen, W. Liu, H. Zhang, L. Lacy, X. Yang, S. K. Song, S. A. Wickline, and X. Yu. "Regional ventricular wall thickening reflects changes in cardiac fiber and sheet structure during contraction: quantification with diffusion tensor MRI". In: *American Journal of Physiology - Heart and Circulatory Physiology* 289.5 (2005), H1898–907.

[76] G. Seemann, D. U. J. Keller, D. L. Weiss, and O. Dössel. "Modeling human ventricular geometry and fiber orientation based on diffusion tensor MRI". In: *Computers in Cardiology Conference*. Vol. 33, pp. 801–804.

[77] Y. Jiang, K. Pandya, O. Smithies, and E. W. Hsu. "Three-dimensional diffusion tensor microscopy of fixed mouse hearts". In: *Magnetic Resonance in Medicine* 52.3 (2004), pp. 453–460.

[78] J. M. Peyrat, M. Sermesant, X. Pennec, H. Delingette, C. Xu, E. McVeigh, and N. Ayache. "Towards a statistical atlas of cardiac fiber structure". In: *Med Image Comput Comput Assist Interv* 9.Pt 1 (2006), pp. 297–304.

[79] J. M. Peyrat, M. Sermesant, X. Pennec, H. Delingette, C. Xu, E. McVeigh, and N. Ayache. "Statistical comparison of cardiac fibre architectures". In: *International Conference on Functional Imaging and Modeling of the Heart*. Vol. 4466 LNCS, pp. 413–423.

[80] B. Schmitt, K. Fedarava, J. Falkenberg, K. Rothaus, N. K. Bodhey, C. Reischauer, S. Kozerke, B. Schnackenburg, D. Westermann, P. P. Lunkenheimer, R. H. Anderson, F. Berger, and T. Kuehne. "Three-dimensional alignment of the aggregated myocytes in the normal and hypertrophic murine heart". In: *Journal of Applied Physiology* 107.3 (2009), pp. 921–927.

[81] E.X. Wu, Y. Wu, J.M. Nicholls, J. Wang, S. Liao, S. Zhu, C.P. Lau, and H.F. Tse. "MR diffusion tensor imaging study of postinfarct myocardium structural remodeling in a porcine model". In: *Magnetic Resonance in Medicine* 58 (2007), pp. 687 –95.

[82] G. J. Strijkers, A. Bouts, W. M. Blankesteijn, T. H. J. M. Peeters, A. Vilanova, M. C. van Prooijen, H. M. H. F. Sanders, E. Heijman, and K. Nicolay. "Diffusion tensor imaging of left ventricular remodeling in response to myocardial infarction in the mouse". In: *NMR in Biomedicine* 22.2 (2009), pp. 182–190.

[83] D. E. Sosnovik, R. Wang, G. Dai, T. Wang, E. Aikawa, M. Novikov, A. Rosenzweig, R. J. Gilbert, and V. J. Wedeen. "Diffusion spectrum MRI tractography reveals the presence of a complex network of residual myofibers in infarcted myocardium". In: *Circulation: Cardiovascular Imaging* 2.3 (2009), pp. 206–212.

[84] R.R. Edelman, J. Gaa, V.J. Wedeen, E. Loh, J.M. Hare, P. Prasad, and W. Li. "In vivo measurement of water diffusion in the human heart". In: *Magnetic Resonance in Medicine* 32 (1994), pp. 423 –8.

[85] C. Nguyen, Z. Fan, B. Sharif, Y. He, R. Dharmakumar, D. S. Berman, and D. Li. "In vivo three-dimensional high resolution cardiac diffusion-weighted MRI: A motion compensated diffusion-prepared balanced steady-state free precession approach". In: *Magnetic Resonance in Medicine* 72.5 (2014), pp. 1257–1267.

[86] Sonia Nielles-Vallespin, Choukri Mekkaoui, Peter Gatehouse, Timothy G. Reese, Jennifer Keegan, Pedro F. Ferreira, Steve Collins, Peter Speier, Thorsten Feiweier, Ranil de Silva, Marcel P. Jackowski, Dudley J. Pennell, David E. Sosnovik, and David Firmin. "In vivo diffusion tensor MRI of the human heart: Reproducibility of breath-hold and navigator-based approaches". In: *Magnetic Resonance in Medicine* 70.2 (2013), pp. 454–465.

[87] Laura-Ann McGill, Tevfik Ismail, Sonia Nielles-Vallespin, Pedro Ferreira, Andrew Scott, Michael Roughton, Philip Kilner, S Yen Ho, Karen McCarthy, Peter Gatehouse, Ranil de Silva, Peter Speier, Thorsten Feiweier, Choukkri Mekkaoui, David Sosnovik, Sanjay Prasad, David Firmin, and Dudley Pennell. "Reproducibility of in-vivo diffusion tensor cardiovascular magnetic resonance in hypertrophic cardiomyopathy". In: *Journal of Cardiovascular Magnetic Resonance* 14.1 (2012), p. 86.

[88] Elizabeth Tunnicliffe, Andrew Scott, Pedro Ferreira, Rina Ariga, Laura-Ann McGill, Sonia Nielles-Vallespin, Stefan Neubauer, Dudley Pennell, Matthew Robson, and David Firmin. "Intercentre reproducibility of cardiac apparent diffusion coefficient and fractional anisotropy in healthy volunteers". In: *Journal of Cardiovascular Magnetic Resonance* 16.1 (2014), p. 31.

[89] N. Toussaint, M. Sermesant, C. T. Stoeck, S. Kozerke, and P. G. Batchelor. "In vivo human 3D cardiac fibre architecture: reconstruction using curvilinear interpolation of diffusion tensor images". In: *Medical Image Computing and Computer-Assisted Intervention Conference*. Vol. 13, pp. 418–25.

[90] C. von Deuster, C. T. Stoeck, M. Genet, D. Atkinson, and S. Kozerke. "Spin echo versus stimulated echo diffusion tensor imaging of the in vivo human heart". In: *Magnetic Resonance in Medicine* 76.3 (2016), pp. 862–72.

[91] U. Gamper, P. Boesiger, and S. Kozerke. "Diffusion imaging of the in vivo heart using spin echoes–considerations on bulk motion sensitivity". In: *Magnetic Resonance in Medicine* 57.2 (2007), pp. 331–7.

[92] C. T. Stoeck, C. von Deuster, M. Genet, D. Atkinson, and S. Kozerke. "Second-order motion-compensated spin echo diffusion tensor imaging of the human heart". In: *Magnetic Resonance in Medicine* 75.4 (2016), pp. 1669–76.

[93] C. L. Welsh, E. V. R. Di Bella, and E. W. Hsu. "Higher-Order Motion-Compensation for in Vivo Cardiac Diffusion Tensor Imaging in Rats". In: *IEEE Transactions on Medical Imaging* 34.9 (2015), pp. 1843–1853.

[94] C. T. Stoeck, A. Kalinowska, C. von Deuster, J. Harmer, R. W. Chan, M. Niemann, R. Manka, D. Atkinson, D. E. Sosnovik, C. Mekkaoui, and S. Kozerke. "Dual-phase cardiac diffusion tensor imaging with strain correction". In: *PLoS ONE* 9.9 (2014), e107159.

[95] WY Tseng, J Dou, TG Reese, and VJ Wedeen. "Imaging myocardial fiber disarray and intramural strain hypokinesis in hypertrophic cardiomyopathy with MRI". In: *Journal of Magnetic Resonance Imaging* 23.1 (2006), pp. 1 –8.

[96] P. F. Ferreira, P. J. Kilner, L. A. McGill, S. Nielles-Vallespin, A. D. Scott, S. Y. Ho, K. P. McCarthy, M. M. Haba, T. F. Ismail, P. D. Gatehouse, R. de Silva, A. R. Lyon, S. K. Prasad, D. N. Firmin, and D. J. Pennell. "In vivo cardiovascular magnetic resonance diffusion tensor imaging shows evidence of abnormal myocardial laminar orientations and mobility in hypertrophic cardiomyopathy". In: *Journal of Cardiovascular Magnetic Resonance* (2014), p. 87.

[97] M. T. Wu, M. Y. M. Su, Y. L. Huang, K. R. Chiou, P. Yang, H. B. Pan, T. G. Reese, V. J. Wedeen, and W. Y. I. Tseng. "Sequential changes of myocardial microstructure in patients postmyocardial infarction by diffusion-tensor cardiac mr correlation with left ventricular structure and function". In: *Circulation: Cardiovascular Imaging* 2.1 (2009), pp. 32–40.

[98] M. G. Hall and D. C. Alexander. "Convergence and Parameter Choice for Monte-Carlo Simulations of Diffusion MRI". In: *IEEE Transactions on Medical Imaging* 28.9 (2009), p. 1354.

[99] B. Balinov, B. Jonsson, P. Linse, and O. Soderman. "The NMR Self-Diffusion Method Applied to Restricted Diffusion. Simulation of Echo Attenuation from Molecules in Spheres and between Planes". In: *Journal of Magnetic Resonance, Series A* 104.1 (1993), pp. 17–25.

[100] P. Linse and O. Soderman. "The Validity of the Short-Gradient-Pulse Approximation in NMR Studies of Restricted Diffusion. Simulations of Molecules Diffusing between Planes, in Cylinders and Spheres". In: *Journal of Magnetic Resonance, Series A* 116.1 (1995), pp. 77–86.

[101] Congbo Cai, Zhong Chen, Shuhui Cai, and Jianhui Zhong. "Propagator formalism and computer simulation of restricted diffusion behaviors of inter-molecular multiple-quantum coherences". In: *Physica B: Condensed Matter* 366.1–4 (2005), pp. 127–137.

[102] Andrej Duh, Aleš Mohorič, and Janez Stepišnik. "Computer Simulation of the Spin-Echo Spatial Distribution in the Case of Restricted Self-Diffusion". In: *Journal of Magnetic Resonance* 148.2 (2001), pp. 257–266.

[103] Mu Lin, Hongjian He, Giovanni Schifitto, and Jianhui Zhong. "Simulation of changes in diffusion related to different pathologies at cellular level after traumatic brain injury". In: *Magnetic Resonance in Medicine* 76.1 (2016), pp. 290–300.

[104] J. Chetley Ford and David B. Hackney. "Numerical model for calculation of apparent diffusion coefficients (ADC) in permeable cylinders-comparison with measured ADC in spinal cord white matter". In: *Magnetic Resonance in Medicine* 37.3 (1997), pp. 387–394.

[105] Hans-Gerd Lipinski. "Monte Carlo simulation of extracellular diffusion in brain tissues". In: *Physics in Medicine and Biology* 35.3 (1990), p. 441.

[106] Michal Plotkowiak, Kelly Burrowes, Jan Wolber, Christopher Buckley, Robert Davies, Fergus Gleeson, David Gavaghan, and Vicente Grau. "Relationship between Structural Changes and Hyperpolarized Gas Magnetic Resonance Imaging in Chronic Obstructive Pulmonary Disease Using Computational Simulations with Realistic Alveolar Geometry". In: *Philosophical Transactions of the Royal Society of London. Series A:* 367.1896 (2009), pp. 2347–2369.

[107] A. L. Sukstanskii and D. A. Yablonskiy. “In vivo lung morphometry with hyperpolarized 3He diffusion MRI: Theoretical background”. In: *Journal of Magnetic Resonance* 190.2 (2008), pp. 200–210.

[108] Lihui Wang, Yue-Min Zhu, Hongying Li, Wanyu Liu, and Isabelle E. Magnin. “Simulation of Diffusion Anisotropy in DTI for Virtual Cardiac Fiber Structure”. In: *Lecture Notes in Computer Science* 6666 (2011), pp. 95–104.

[109] Lihui Wang, Yuemin Zhu, Hongying Li, Yang Liu, and I. E. Magnin. “Multiscale Modeling and Simulation of the Cardiac Fiber Architecture for DMRI”. In: *IEEE Transactions on Biomedical Engineering* 59.1 (2012), pp. 16–19.

[110] C. H. Yeh, B. Schmitt, D. Le Bihan, J. R. Li-Schlittgen, C. P. Lin, and C. Poupon. “Diffusion Microscopist Simulator: A General Monte Carlo Simulation System for Diffusion Magnetic Resonance Imaging”. In: *PLoS ONE* 8.10 (2013).

[111] L. H. Wang, Y. M. Zhu, F. Yang, W. Y. Liu, and I. E. Magnin. “Simulation of dynamic DTI of 3D cardiac fiber structures”. In: *2014 IEEE 11th International Symposium on Biomedical Imaging (ISBI)*, pp. 714–717.

[112] Scott N. Hwang, Chih-Liang Chin, Felix W. Wehrli, and David B. Hackney. “An image-based finite difference model for simulating restricted diffusion”. In: *Magnetic Resonance in Medicine* 50.2 (2003), pp. 373–382.

[113] S. R. Arridge, M. Schweiger, M. Hiraoka, and D. T. Delpy. “A finite element approach for modeling photon transport in tissue”. In: *Med Phys* 20.2 Pt 1 (1993), pp. 299–309.

[114] Chih-Liang Chin, Felix W. Wehrli, Scott N. Hwang, Masaya Takahashi, and David B. Hackney. “Biexponential diffusion attenuation in the rat spinal cord: Computer simulations based on anatomic images of axonal architecture”. In: *Magnetic Resonance in Medicine* 47.3 (2002), pp. 455–460.

[115] L. Beltrachini, Z. A. Taylor, and A. F. Frangi. “A parametric finite element solution of the generalised Bloch-Torrey equation for arbitrary domains”. In: *Journal of Magnetic Resonance* 259 (2015), pp. 126–34.

[116] Joanne Bates, Irvin Teh, Peter Kohl, Jürgen E Schneider, and Vicente Grau. “Sensitivity Analysis of Diffusion Tensor MRI in Simulated Rat Myocardium”. In: *Lecture Notes in Computer Science* 9126 (2015), pp. 120–128.

[117] C. H. Neuman. “Spin echo of spins diffusing in a bounded medium”. In: *The Journal of Chemical Physics* 60.11 (1974), pp. 4508–4511.

[118] P. T. Callaghan. “Pulsed-Gradient Spin-Echo NMR for Planar, Cylindrical, and Spherical Pores under Conditions of Wall Relaxation”. In: *Journal of Magnetic Resonance, Series A* 113.1 (1995), pp. 53–59.

[119] P. Vangelderen, D. Despres, P. C. M. Vanzijl, and C. T. W. Moonen. “Evaluation of Restricted Diffusion in Cylinders. Phosphocreatine in Rabbit Leg Muscle”. In: *Journal of Magnetic Resonance, Series B* 103.3 (1994), pp. 255–260.

[120] Steven S Andrews and Dennis Bray. “Stochastic simulation of chemical reactions with spatial resolution and single molecule detail”. In: *Physical Biology* 1.3 (2004), p. 137.

[121] P. A. Cook, Y. Bai, S. Nedjati-Gilani, K. K. Seunarine, M. G. Hall, G. J. Parker, and D. C. Alexander. "Camino: Open-Source Diffusion-MRI Reconstruction and Processing," in: *Scientific Meeting of the International Society for Magnetic Resonance in Medicine*, p. 2759.

[122] Chunlei Liu, Roland Bammer, Burak Acar, and Michael E. Moseley. "Characterizing non-gaussian diffusion by using generalized diffusion tensors". In: *Magnetic Resonance in Medicine* 51.5 (2004), pp. 924–937.

[123] Emmanuel Caruyer. *Emmanuel Caruyer homepage*. Web Page. 2016.

[124] Peter B. Kingsley. "Introduction to diffusion tensor imaging mathematics: Part III. Tensor calculation, noise, simulations, and optimization". In: *Concepts in Magnetic Resonance Part A* 28A.2 (2006), p. 155.

[125] Jonathan Guy Bensley, Robert De Matteo, Richard Harding, and Mary Jane Black. "Three-dimensional direct measurement of cardiomyocyte volume, nuclearity, and ploidy in thick histological sections". In: *Scientific Reports* 6 (2016), p. 23756.

[126] H. Satoh, L. M. Delbridge, L. A. Blatter, and D. M. Bers. "Surface:volume relationship in cardiac myocytes studied with confocal microscopy and membrane capacitance measurements: species-dependence and developmental effects". In: *Biophysical Journal* 70.3 (1996), pp. 1494–504.

[127] W. Kromen, H. Korkusuz, Y. Korkusuz, P. Esters, R. W. Bauer, F. Huebner, S. Lindemayr, and T. J. Vogl. "Correlation of left ventricular wall thickness, heart mass, serological parameters and late gadolinium enhancement in cardiovascular magnetic resonance imaging of myocardial inflammation in an experimental animal model of autoimmune myocarditis". In: *International journal of cardiovascular imaging* 28.8 (2012), pp. 1983–97.

[128] R. M. McAdams, R. J. McPherson, N. M. Dabestani, C. A. Gleason, and S. E. Juul. "Left ventricular hypertrophy is prevalent in Sprague-Dawley rats". In: *Comparative medicine* 60.5 (2010), pp. 357–63.

[129] David Benoist, Rachel Stones, Mark J. Drinkhill, A. P. Benson, Zhaokang Yang, Cecile Cassan, Stephen H. Gilbert, David A. Saint, Olivier Cazorla, Derek S. Steele, O. Bernus, and Ed White. "Cardiac arrhythmia mechanisms in rats with heart failure induced by pulmonary hypertension". In: *American Journal of Physiology - Heart and Circulatory Physiology* 302.11 (2012), H2381–H2395.

[130] S. E. Campbell, K. Rakusan, and A. M. Gerdes. "Change in cardiac myocyte size distribution in aortic-constricted neonatal rats". In: *Basic Research in Cardiology* 84.3 (1989), pp. 247–258.

[131] Yue-Feng Chen, Rebecca A. Redetzke, Ryan M. Sivertson, Tamora S. Coburn, Luke R. Cypher, and Anthony Martin Gerdes. "Post-myocardial infarction left ventricular myocyte remodeling: are there gender differences in rats?" In: *Cardiovascular Pathology* 20.5 (2011), e189–e195.

[132] A. M. Gerdes, J. A. Moore, J. M. Hines, P. A. Kirkland, and S. P. Bishop. "Regional differences in myocyte size in normal rat heart". In: *The Anatomical record* 215.4 (1986), pp. 420–6.

[133] Scott E. Campbell, A. Martin Gerdes, and Teri D. Smith. “Comparison of regional differences in cardiac myocyte dimensions in rats, hamsters, and guinea pigs”. In: *The Anatomical record* 219.1 (1987), pp. 53–59.

[134] Sanford P. Bishop and Janice L. Drummond. “Surface morphology and cell size measurement of isolated rat cardiac myocytes”. In: *Journal of Molecular and Cellular Cardiology* 11.5 (1979), pp. 423–433.

[135] Alejandra M. Yeves, María C. Villa-Abrille, Néstor G. Pérez, Andrés J. Medina, Eduardo M. Escudero, and Irene L. Ennis. “Physiological cardiac hypertrophy: Critical role of AKT in the prevention of NHE-1 hyperactivity”. In: *Journal of Molecular and Cellular Cardiology* 76.0 (2014), pp. 186–195.

[136] P. Kohl. *Discussion of myocyte shape and size*. Personal Communication. 2014.

[137] Robert L. Cooper, David B. Chang, Allan C. Young, Carroll J. Martin, and Betsy Ancker-Johnson. “Restricted Diffusion in Biophysical Systems: Experiment”. In: *Biophysical Journal* 14.3 (1974), pp. 161–177.

[138] L. Garrido, V. J. Wedeen, K. K. Kwong, U. M. Spencer, and H. L. Kantor. “Anisotropy of water diffusion in the myocardium of the rat”. In: *Circulation Research* 74.5 (1994), pp. 789–93.

[139] R. E. Safford, E. A. Bassingthwaighte, and J. B. Bassingthwaighte. “Diffusion of water in cat ventricular myocardium”. In: *Journal of General Physiology* 72.4 (1978), pp. 513–538.

[140] John Georg Seland, Morten Bruvold, Henrik Anthonsen, Heidi Brurok, Wibeke Nordhøy, Per Jynge, and Jostein Krane. “Determination of water compartments in rat myocardium using combined D–T1 and T1–T2 experiments”. In: *Magnetic Resonance Imaging* 23.2 (2005), pp. 353–354.

[141] John Georg Seland, Morten Bruvold, Heidi Brurok, Per Jynge, and Jostein Krane. “Analyzing equilibrium water exchange between myocardial tissue compartments using dynamical two-dimensional correlation experiments combined with manganese-enhanced relaxography”. In: *Magnetic Resonance in Medicine* 58.4 (2007), pp. 674–686.

[142] P. Anversa, B. Hiler, R. Ricci, G. Guideri, and G. Olivetti. “Myocyte cell loss and myocyte hypertrophy in the aging rat heart”. In: *Journal of the American College of Cardiology* 8.6 (1986), pp. 1441–8.

[143] M. A. Rossi and L. C. Peres. “Effect of captopril on the prevention and regression of myocardial cell hypertrophy and interstitial fibrosis in pressure overload cardiac hypertrophy”. In: *American Heart Journal* 124.3 (1992), pp. 700–709.

[144] Manfred Holz, Stefan R. Heil, and Antonio Sacco. “Temperature-dependent self-diffusion coefficients of water and six selected molecular liquids for calibration in accurate 1H NMR PFG measurements”. In: *Physical Chemistry Chemical Physics* 2.20 (2000), pp. 4740–4742.

[145] Christian Beaulieu. “The basis of anisotropic water diffusion in the nervous system – a technical review”. In: *NMR in Biomedicine* 15.7-8 (2002), pp. 435–455.

[146] A. Saltelli, Stefano Tarantolo, Francesca Campolongo, and Marco Ratto. *Sensitivity analysis in practice: a guide to assessing scientific models*. Chichester, UK: John Wiley & Sons, 2004.

[147] Max D. Morris. “Factorial Sampling Plans for Preliminary Computational Experiments”. In: *Technometrics* 33.2 (1991), pp. 161–174.

[148] F. Campolongo, J. Cariboni, and A. Saltelli. “An effective screening design for sensitivity analysis of large models”. In: *Environmental Modelling and Software* 22.10 (2007), pp. 1509–1518.

[149] Joint Research Centre: Institute for the Protection Citizen and Security of the. *SIMLAB and other software*. Web Page. 2014.

[150] D. McClymont, I. Teh, H. J. Whittington, V. Grau, and J. E. Schneider. “Prospective acceleration of diffusion tensor imaging with compressed sensing using adaptive dictionaries”. In: *Magnetic Resonance in Medicine* 76.1 (2016), pp. 248–258.

[151] HáKon Gudbjartsson and Samuel Patz. “The Rician distribution of noisy MRI data”. In: *Magnetic Resonance in Medicine* 34.6 (1995), pp. 910–914.

[152] J. Weinreb, P. A. Wilcox, J. Hayden, R. Lewis, and J. Froelich. “ACR MRI accreditation: Yesterday, today, and tomorrow”. In: *Journal of the American College of Radiology* 2.6 (2005), pp. 494–503.

[153] Ching-Po Lin, Van Jay Wedeen, Jyh-Horng Chen, Ching Yao, and Wen-Yih Isaac Tseng. “Validation of diffusion spectrum magnetic resonance imaging with manganese-enhanced rat optic tracts and ex vivo phantoms”. In: *Neuroimage* 19.3 (2003), pp. 482–495.

[154] Els Fieremans, Yves De Deene, Steven Delputte, Mahir S. Özdemir, Yves D’Asseler, Jelle Vlassenbroeck, Karel Deblaere, Eric Achten, and Ignace Lemahieu. “Simulation and experimental verification of the diffusion in an anisotropic fiber phantom”. In: *Journal of Magnetic Resonance* 190.2 (2008), pp. 189–199.

[155] Irvin Teh, Feng-Lei Zhou, Penny L. Hubbard Cristinacce, Geoffrey J. M. Parker, and Jürgen E. Schneider. “Biomimetic Phantom for Cardiac Diffusion MRI”. In: *Journal of Magnetic Resonance Imaging* 43.3 (2015), pp. 594–600.

[156] Toshitsugu Ogura, Sunao Imanishi, and Toshishige Shibamoto. “Osmometric and Water-Transporting Properties of Guinea Pig Cardiac Myocytes”. In: *The Japanese Journal of Physiology* 52.4 (2002), pp. 333–342.

[157] M A Suleymanian and C M Baumgarten. “Osmotic gradient-induced water permeation across the sarcolemma of rabbit ventricular myocytes”. In: *The Journal of General Physiology* 107.4 (1996), pp. 503–514.

[158] Greg J. Stanisz. “Diffusion MR in Biological Systems: Tissue Compartments and Exchange”. In: *Israel Journal of Chemistry* 43.1-2 (2003), pp. 33–44.

[159] D. Le Bihan. “Molecular diffusion, tissue microdynamics and microstructure”. In: *NMR Biomedicine* 8.7-8 (1995), pp. 375–86.

[160] L. Zhao, A. L. Sukstanskii, C. D. Kroenke, J. Song, D. Piwnica-Worms, J. J. H. Ackerman, and J. J. Neil. “Intracellular water specific MR of microbead-adherent cells: Hela cell intracellular water diffusion”. In: *Magnetic Resonance in Medicine* 59.1 (2008), pp. 79–84.

[161] Christian Beaulieu and Peter S. Allen. “Water diffusion in the giant axon of the squid: Implications for diffusion-weighted MRI of the nervous system”. In: *Magnetic Resonance in Medicine* 32.5 (1994), pp. 579–583.

[162] Matthew D. Silva, Tsuyoshi Omae, Karl G. Helmer, Fuhai Li, Marc Fisher, and Christopher H. Sotak. “Separating changes in the intra- and extracellular water apparent diffusion coefficient following focal cerebral ischemia in the rat brain”. In: *Magnetic Resonance in Medicine* 48.5 (2002), pp. 826–837.

[163] Timothy Q. Duong, Joseph J. H. Ackerman, Howard S. Ying, and Jeffrey J. Neil. “Evaluation of extra- and intracellular apparent diffusion in normal and globally ischemic rat brain via 19F NMR”. In: *Magnetic Resonance in Medicine* 40.1 (1998), pp. 1–13.

[164] Ingrid Åslund and Daniel Topgaard. “Determination of the self-diffusion coefficient of intracellular water using PGSE NMR with variable gradient pulse length”. In: *Journal of Magnetic Resonance* 201.2 (2009), pp. 250–254.

[165] E. W. Hsu, D. L. Buckley, J. D. Bui, S. J. Blackband, and J. R. Forder. “Two-component diffusion tensor MRI of isolated perfused hearts”. In: *Magnetic Resonance in Medicine* 45.6 (2001), pp. 1039–1045.

[166] J. R. Forder, J. D. Bui, D. L. Buckley, and S. J. Blackband. “MR imaging measurement of compartmental water diffusion in perfused heart slices”. In: *American Journal of Physiology - Heart and Circulatory Physiology* 281.3 (2001), H1280–5.

[167] G. G. Cleveland, D. C. Chang, C. F. Hazlewood, and H. E. Rorschach. “Nuclear magnetic resonance measurement of skeletal muscle: anisotrophy of the diffusion coefficient of the intracellular water”. In: *Biophysical Journal* 16.9 (1976), pp. 1043–1053.

[168] S. T. Kinsey, B. R. Locke, B. Penke, and T. S. Moerland. “Diffusional anisotropy is induced by subcellular barriers in skeletal muscle”. In: *NMR in Biomedicine* 12.1 (1999), pp. 1–7.

[169] Ingrid Åslund, Agnieszka Nowacka, Markus Nilsson, and Daniel Topgaard. “Filter-exchange PGSE NMR determination of cell membrane permeability”. In: *Journal of Magnetic Resonance* 200.2 (2009), pp. 291–295.

[170] I Teh, D McClymont, MC Zdora, V Davidoiu, H Whittington, C Rau, I Zanette, and J Schneider. “Validation of Diffusion Tensor MRI with Structure Tensor Synchrotron Imaging”. In: *Proceedings of the 24th Annual Meeting of ISMRM, Singapore* (2016).

[171] P. Smith and D. R. Clark. “Myocardial capillary density and muscle fibre size in rats born and raised at simulated high altitude”. In: *British journal of experimental pathology* 60.2 (1979), pp. 225–230.

[172] N. Watanabe, T. Akasaka, E. Toyota, K. Fujimoto, T. Kajita, F. Shigeto, Y. Ogasawara, and K. Yoshida. “Three-dimensional microstructural abnormality of the coronary capillary network after myocardial reperfusion - Comparison between ’reflow’ and ’no-reflow’”. In: *Circulation Journal* 68.9 (2004), pp. 868–872.

[173] D. C. Poole, S. Batra, O. Mathieu-Costello, and K. Rakusan. "Capillary geometrical changes with fiber shortening in rat myocardium". In: *Circulation Research* 70.4 (1992), pp. 697–706.

[174] Y. Chen, R. J. Torry, G. L. Baumbach, and R. J. Tomanek. "Proportional arteriolar growth accompanies cardiac hypertrophy induced by volume overload". In: *American Journal of Physiology - Heart and Circulatory Physiology* 267.6 36-6 (1994), H2132–H2137.

[175] P Anversa, C Beghi, Y Kikkawa, and G Olivetti. "Myocardial infarction in rats. Infarct size, myocyte hypertrophy, and capillary growth". In: *Circulation Research* 58.1 (1986), pp. 26–37.

[176] Y. Kano, S. Shimegi, K. Masuda, H. Sakato, H. Ohmori, and S. Katsuta. "Effects of different intensity endurance training on capillary network in rat left ventricular myocardium". In: *Japanese Journal of Physical Fitness and Sports Medicine* 45.5 (1996), pp. 511–518.

[177] Z. Turek, M. Grandtner, and F. Kreuzer. "Cardiac hypertrophy, capillary and muscle fiber density, muscle fiber diameter, capillary radius and diffusion distance in the myocardium of growing rats adapted to a simulated altitude of 3500 m". In: *Pflügers Archiv* 335.1 (1972), pp. 19–28.

[178] M. R. De Souza, L. Pimenta, T. C. Pithon-Curi, M. Bucci, R. G. Fontinele, and R. R. De Souza. "Effects of aerobic training, resistance training, or combined resistance-aerobic training on the left ventricular myocardium in a rat model". In: *Microscopy Research and Technique* 77.9 (2014), pp. 727–734.

[179] Ibrahim Inuwa, Badreldin H Ali, Intisar Al-Lawati, Sumaya Beegam, Amal Ziada, and Gerald Blunden. "Long-term ingestion of Hibiscus sabdariffa calyx extract enhances myocardial capillarization in the spontaneously hypertensive rat". In: *Experimental Biology and Medicine* 237.5 (2012), pp. 563–569.

[180] S. R. Kayar, K. E. Conley, H. Claassen, and H. Hoppeler. "Capillarity and mitochondrial distribution in rat myocardium following exercise training". In: *Journal of Experimental Biology* 120.1 (1986), pp. 189–199.

[181] M. Huikeshoven, J. A. M. Beliën, R. Tukkie, and J. F. Beek. "The vascular response induced by transmyocardial laser revascularization is determined by the size of the channel scar: Results of CO_2, holmium and excimer lasers". In: *Lasers in Surgery and Medicine* 35.1 (2004), pp. 35–40.

[182] Lorenzo Dematte. *GPU implementation of Smoldyn*. Web Page. 2013.

[183] Denis V. Gladkov, Samuel Alberts, Roshan M. D'Souza, and Steven Andrews. "Accelerating the smoldyn spatial stochastic biochemical reaction network simulator using GPUs". In: *Proceedings of the 19th High Performance Computing Symposia*. 2048597: Society for Computer Simulation International, pp. 151–158.